Electronic spin manipulation in all solid state devices

Valentin Desbuis

Thèse

Présentée et soutenue publiquement pour l'obtention du titre de

DOCTEUR DE L'UNIVERSITE DE LORRAINE

en Physique

par Valentin DESBUIS

Sous la direction de Michel HEHN et Daniel LACOUR

Manipulation du spin électronique dans des dispositifs tout solide

Soutenue le 2 novembre 2023

Membres du jury, présidé par M Nicolas Rougemaille :

Directeurs de thèse :	**M Michel Hehn**	**Professeur (IJL, Nancy)**
	M Daniel Lacour	**Directeur de recherche (IJL, Nancy)**
Rapporteurs :	**Mme Claire Baraduc**	**Ingénieure HDR, (CEA, Grenoble)**
	M Nicolas Rougemaille	**Directeur de recherche (Institut Néel, Grenoble)**
Examinateurs :	**Mme Marie Hervé**	**Chargée de recherche (INSP, Paris)**
	M Wolfgang Weber	**Professeur (IPCMS, Strasbourg)**

Thèse préparée à l'Institut Jean Lamour, UMR CNRS 7198, Université de Lorraine, France

Résumé

Les électrons sont dits "chauds" lorsqu'ils sont excités au-dessus du niveau de Fermi. Ils ont une énergie cinétique supérieure à celle des électrons de la mer de Fermi. Les électrons chauds peuvent être créés en injectant de l'énergie dans un matériau, par exemple par exposition à une lumière intense, en appliquant une tension ou même en chauffant le matériau. Une fois que ces électrons sont excités au-dessus du niveau de Fermi, ils peuvent se déplacer à l'intérieur du matériau. Plusieurs facteurs peuvent affecter le transport des électrons chauds, tels que la température, la structure cristalline ou la présence de défauts, induisant des mécanismes de diffusion qui conduisent à des processus de relaxation. Le transport des électrons chauds est crucial dans plusieurs domaines tels que l'électronique haute fréquence, les dispositifs optoélectroniques (photovoltaïques, photodétecteurs) ou même en magnétisme (transfert de spin, démagnétisation ultra-rapide). Comprendre le transport des électrons chauds nécessite une connaissance détaillée des propriétés électroniques et structurales du matériau. De plus, la connaissance des interactions entre les électrons et entre les électrons et d'autres particules est cruciale pour décrire le transport des électrons chauds.

Les électrons sont l'une des nombreuses particules élémentaires. Les électrons sont des porteurs de charge avec une masse donnée et un spin. Le spin est une propriété fondamentale qui décrit le moment angulaire intrinsèque d'un électron. Le spin électronique est un concept clé en mécanique quantique et joue un rôle significatif dans divers domaines de la physique. Le spin d'un électron est quantifié, ce qui signifie qu'il ne peut avoir que deux états : +1/2 ou -1/2. Ces valeurs sont désignées comme spin "haut" (ou majoritaire) et spin "bas" (minoritaire). Le spin est responsable des propriétés magnétiques des matériaux. En raison de l'interaction d'échange locale, les spins électroniques voisins peuvent s'aligner dans la même direction. C'est la base du ferromagnétisme. En manipulant les états de spin des électrons, les chercheurs peuvent créer des dispositifs améliorés dotés de plus de puissance de calcul appelés « ordinateurs quantiques ».

Le domaine de la spintronique combine à la fois le transport de charge des électrons et les propriétés du spin. Il vise à développer un nouveau type de dispositifs électroniques pour stocker, traiter ou transmettre des informations de manière plus efficace que l'électronique conventionnelle. Ici, le spin est utilisé pour représenter l'information binaire (0/1). Le transport des électrons est affecté par leur spin. Plusieurs phénomènes ont été étudiés, tels que la polarisation du spin, l'injection de spin et les effets de filtrage du spin dans divers matériaux, y compris les semi-conducteurs et les métaux. Parmi les nombreuses applications découlant de la spintronique, les plus notables sont les dispositifs à vanne de spin, les mémoires magnétiques à accès aléatoire (MRAM) et les structures utilisant le couple de transfert de spin (STT) pour manipuler l’aimantation des matériaux magnétiques.

Les dernières années ont vu le développement de structures de spin non colinéaires pour des dispositifs avancés. Les plus célèbres sont les skyrmions, qui ont suscité un immense intérêt au sein de la communauté scientifique tant du point de vue fondamental qu'appliqué. Les skyrmions sont des textures de spin qui peuvent être manipulées avec un courant électrique. Cette manipulation est effectuée par interaction entre les spins des électrons injectés et les moments magnétiques constituant le skyrmion. De plus, de nouveaux matériaux sont développés et intégrés dans des dispositifs spintroniques actuels pour améliorer encore leur efficacité. Cependant, le contrôle du spin électronique est souvent régi par des interactions avec

des électrons chauds d'environ 1 eV dans les structures spintroniques actuelles. Par conséquent, la manipulation du spin électronique de ces électrons chauds pourrait améliorer l'efficacité de tous les dispositifs utilisant ce type d'interactions. L'objectif serait de contrôler l'orientation du spin avec un paramètre choisi.

La manipulation du spin électronique est un défi à relever à la fois d'un point de vue scientifique, avec des mécanismes de transition complexes régissant le transport, mais aussi par rapport aux perspectives d'application dans le domaine de la spintronique. Le contrôle de l'orientation du spin des électrons dans les matériaux pourrait permettre d'aller plus loin dans la conception de dispositifs spintroniques peu énergivores. La manipulation du spin électronique est étroitement liée aux mécanismes de transport qui se déroulent dans les matériaux traversés par les porteurs de charge. Ces derniers peuvent être affectés et subir des interactions pour finalement voir leur trajectoire et l'orientation de leur spin être modifiées. Comprendre la physique qui se cache derrière ces différentes interactions peut être la clé pour permettre la manipulation du spin électronique.

Dans ce travail, nous avons cherché à étudier la manipulation du spin électronique pour des électrons balistiques chauds. Le terme "chauds" fait référence à des porteurs de charge hors équilibre dont l'énergie dépasse le niveau de Fermi du métal, tandis que "balistique" signifie que la particule s'est déplacée sans subir d'interactions. Pour ce faire, un transistor tunnel magnétique (MTT) a été conçu. Il se compose d'une vanne de spin insérée entre une barrière tunnel pour injecter des électrons chauds polarisés en spin d'un côté, et d'une barrière Schottky avec un contact Cu/Si pour collecter uniquement les électrons balistiques chauds de l'autre côté. La structure du MTT a été utilisée pour cette étude afin d'explorer la physique des électrons chauds dans la plage d'énergie basse. D'autres méthodes pour injecter des électrons chauds dans les métaux sont limitées par le niveau de vide du matériau. Notre dispositif tout solide permet également de filtrer les électrons non balistiques à travers la barrière Schottky.

Le premier aspect exploré dans ce travail est l'effet des interactions électron-électron sur le transport des électrons chauds. Lorsqu'ils traversent un métal, les électrons peuvent interagir avec ceux de la bande de conduction du métal, ce qui les amène à perdre une partie significative de leur énergie initiale. Sur la base de résultats expérimentaux, un modèle tenant compte de ces effets a été développé. Il est possible de montrer que les électrons secondaires générés lors de ces interactions contribuent au signal à des tensions d'injection élevées. Lorsque les électrons chauds traversent des matériaux ferromagnétiques, les interactions électron-électron dépendent du spin. En se basant sur des calculs de la densité d'états des matériaux étudiés insérés dans ce MTT, il est possible de relier ces caractéristiques aux mécanismes de diffusion dans notre modèle. Ce travail ouvre des perspectives pour des études approfondies de la diffusion électron-électron, y compris les processus éventuels de retournement de spin, et permet un meilleur contrôle de la polarisation en spin du courant d'électrons chauds.

Une autre stratégie pour manipuler le spin électronique consiste à induire une précession. Cet effet a déjà été démontré pour plusieurs classes de matériaux, y compris les ferromagnétiques. Cependant, seule une étude, menée par notre équipe, a prouvé l'existence de cet effet pour les électrons de faible énergie dans la gamme des dispositifs spintroniques actuels. Dans le but de compléter les travaux de Vautrin *et al.*[1], une nouvelle série de MTT utilisant une couche de CoFeB comme couche de précession a été développée. Dans cette étude, nous nous sommes concentrés sur la vérification du bon contrôle de toutes les configurations magnétiques

accessibles (5 au total) en inversant les aimantations non biaisées. Ces configurations peuvent être observées expérimentalement via le signal de précession, qui change de signe lorsque l'aimantation est inversée, passant ainsi d'une configuration directe à une configuration inverse, ou vice versa.

De plus, une étude sur l'effet d'un possible désalignement a été menée. Lorsqu'une aimantation s'écarte d'une configuration perpendiculaire parfaite, on peut s'attendre à un changement dans le signal de précession mesuré. Cette rotation de l'aimantation peut être évaluée en mesurant la résistance tunnel du dispositif. Ainsi, il est possible de contrôler artificiellement ce désalignement en appliquant un faible champ magnétique dans le plan de l'échantillon. Les résultats de cette étude semblent indiquer que ce désalignement provoque des variations significatives du signal de précession mesuré. Cependant, lorsque le même désalignement est présent dans les configurations perpendiculaires horaire et antihoraire, les deux erreurs "s'annulent", et l'erreur dans le signal par rapport à une configuration parfaite n'est pas ressentie sur une plage d'environ 20 degrés. Pour des écarts plus importants, le signal diminue progressivement jusqu'à devenir nul lorsque les aimantations sont parfaitement alignées.

Des caractérisations magnétiques et électriques ont été réalisées sur les films minces déposés et sur les MTT développés en utilisant le même processus de lithographie que celui utilisé par Vautrin *et al.*[1]. Les nouveaux dispositifs, mesurés en injectant des électrons chauds dans différentes configurations magnétiques, sont cohérents avec ceux étudiés par Vautrin *et al.*[1]. Sur la base d'un modèle théorique proposé dans le travail précédent, les nouveaux échantillons ont des épaisseurs de CoFeB allant de 3 nm à 4 nm. L'objectif est de confirmer le résultat de l'oscillation du signal de précession en fonction de l'épaisseur de la couche de précession en sondant une seule période d'oscillation. Les nouvelles données s'alignent parfaitement sur le modèle théorique. Ces nouveaux ajouts démontrent à la fois l'exactitude du modèle proposé et la robustesse du processus de fabrication des dispositifs. En effet, les mêmes paramètres matériels (rugosité) ont permis un ajustement simultané du modèle à tous les résultats expérimentaux (ceux de 2021[1] et ceux de 2023).

Les calculs ab initio servant de base au modèle théorique proposé montrent que, pour une énergie de 1,95 eV, la précession par unité de longueur devrait diminuer brusquement. Cela est dû à l'accès à la bande minoritaire des électrons de conduction à cette énergie. Un accord qualitatif peut être observé entre les mesures expérimentales et les prédictions théoriques du modèle. Dans l'espoir d'observer expérimentalement la diminution de la précession par unité de longueur, un échantillon a été mesuré à une tension très élevée (jusqu'à 2,5 V). La précession extraite de ces mesures ne correspond pas à un changement abrupt du phénomène de précession. Un dispositif plus adapté est nécessaire pour mener une telle étude de manière fiable, avec une barrière Schottky plus élevée pour filtrer les contributions des électrons secondaires.

Suite à ce travail exploratoire, une stratégie a été mise en place pour contrôler l'angle de précession associé en utilisant la température. En faisant varier la température dans notre dispositif, il est possible d'ajuster le mécanisme de précession dans une couche ferromagnétique. En utilisant un MTT spécifique avec une configuration tridimensionnelle de la magnétisation, des angles de précession ont été extraits à plusieurs températures et ont pu être expliqués dans le cadre du mouvement de précession du spin électronique dépendant de la température.

Deux matériaux différents ont été choisis pour étudier ce phénomène avec la température : le CoAl et le CoCu. Ce sont deux alliages de cobalt qui peuvent être facilement déposés par co-pulvérisation. Ainsi, en faisant varier la vitesse de dépôt de l'un des deux éléments, on peut avoir accès à une large gamme de concentrations en alliages. La première étude porte sur le CoAl. Ce matériau avait déjà été étudié dans le cadre de la thèse de C. Vautrin. Cependant, un rapport signal/bruit trop faible avait empêché toute interprétation des mesures de précession dans de tels MTT. Ici, nous avons revisité l'étude en complétant la caractérisation du matériau par des mesures magnétiques, électriques et structuraux. Initialement, la caractérisation structurale par diffraction des rayons X n'a pas permis d'identifier la phase dans laquelle le CoAl avait tendance à cristalliser. Par conséquent, une analyse complémentaire a été réalisée après avoir préparé des lames à l'aide de la technique de faisceau d'ions focalisés (FIB) et les avoir examinées au microscope électronique en transmission (MET). Cette technique permet une large gamme de caractérisations de la structure des couches déposées, de l'imagerie haute résolution des différentes couches composant l'échantillon à l'analyse chimique des éléments présents. Ainsi, un mécanisme de diffusion de l'aluminium vers la barrière tunnel a pu être mis en évidence. Ce transfert d'aluminium vers l'oxygène du MgO explique les valeurs de la magnétorésistance tunnel (TMR) obtenues au niveau de la jonction tunnel du MTT, en comparaison avec les cycles magnétiques obtenus par SQUID.

Après avoir stabilisé les différentes configurations magnétiques sur une plage de température de 50K à 110K, des mesures de précession ont été effectuées. Ces mesures montrent une oscillation du signal de précession avec la température. Le modèle précédemment développé dans l'étude de CoFeB peut être utilisé en introduisant une énergie d'échange dépendante de la température dans le matériau, similaire à la dépendance en température de l'aimantation. Ainsi, les données expérimentales peuvent être ajustées en ne permettant que deux paramètres libres : l'asymétrie en spin des libres parcours moyens inélastiques et l'angle de précession par unité de longueur à 0K. La dépendance en énergie de ces deux paramètres correspond bien à celle fournie par un modèle simple de diffusion inélastique des libres parcours moyens d'une part, et par l'expression de la vitesse de précession dans un échantillon polycristallin d'autre part.

En ce qui concerne l'alliage CoCu, un travail complet a dû être réalisé pour étudier la qualité du dépôt à l'aide de notre technique de pulvérisation cathodique. Le paramètre de maille, l'orientation cristallographique, l'aimantation en fonction de la concentration et de la température ont été mesurés sur divers échantillons pour observer d'éventuelles différences liées aux changements d'interface ou aux effets de recuit. Contrairement à ce qui a été observé dans la littérature, nos échantillons de CoCu semblent rester homogènes sans formation d'agrégats de Co. Cela a été confirmé par une analyse chimique au MET d'un échantillon multicouche utilisé pour un MTT. Cependant, la caractérisation de la TMR du dispositif à base de CoCu a montré un cycle d'hystérésis très faible. L'explication la plus probable de ce résultat surprenant est la complexité du magnétisme du CoCu. Contrairement au CoAl, ce matériau n'est pas entièrement saturé sous l'influence d'un champ magnétique faible.

Les mesures de précession pour ce MTT sur une plage de température de 90K montrent plusieurs différences par rapport au CoAl. Tout d'abord, la période est différente. Ici, deux périodes peuvent être observées à 70K, ce qui démontre la robustesse de la mesure. De plus, au-delà de 140K, le signal de précession reste proche de 0. Cela correspond bien à ce qui est

attendu compte tenu de la température de Curie du matériau dans cette région. Enfin, l'amplitude des oscillations est plus faible que dans le cas du CoAl.

Mots-clefs: *Spintronique, Basses énergies, Transistor, Précession*

Abstract

Manipulating electronic spin is a challenge both from a scientific point of view, with complex physics governing transport mechanisms, and from the perspective of applications in the field of spintronics. Full control of the orientation of electron spin in materials could lead to a more advanced three-dimensional design of energy-efficient next-generation memory bits or even computing systems. Manipulating electronic spin is closely linked to the transport mechanisms occurring in the materials traversed by charge carriers. These charge carriers can be affected by both electric fields and other particles, thereby altering both their trajectory and their spin orientation. Understanding the underlying physics of these interactions can be the key to gaining further control over electronic spin.

In this work, we aimed to study the manipulation of electronic spin for hot ballistic electrons. The term "hot" refers to out-of-equilibrium charge carriers whose energy is higher than the Fermi level of the metal, while "ballistic" means the particle has traveled without undergoing any interactions. To do this, a Magnetic Tunnel Transistor (MTT) was designed with specific features required for this study. It consists of a spin valve structure sandwiched between a tunnel barrier for injecting spin-polarized hot electrons on one side and a Schottky barrier with a Cu/Si contact to collect only hot ballistic electrons on the other side. The MTT structure was used for this study to explore the physics of hot electrons in the low-energy range. Other methods of injecting hot electrons into metals are limited by the vacuum level of the materials, thus setting a physical lower boundary for such studies. Our solid-state device also allows precise filtering of non-ballistic electrons due to the presence of the Schottky barrier for collecting hot electrons.

The first aspect investigated in this study concerns the effect of electron-electron interactions on the transport of hot electrons. As they pass through a metal, electrons can interact with those from the Fermi sea of the material. When they do so, they lose a significant portion of their initial energy. Our MTT measurements reveal distinct features related to electron-electron interactions. Based on experimental results, a model is developed to account for these effects. We demonstrated that secondary electrons generated during such interactions contribute to the signal at high injection voltage. When hot electrons traverse ferromagnetic materials, electron-electron interactions and the generation of secondary electrons become spin-dependent. By utilizing density of states calculations of the studied materials integrated into this MTT, it is possible to correlate these features with scattering mechanisms in our model. This work paves the way for in-depth studies of electron-electron scattering, including potential spin-flip processes and the enhancement of spin polarization in hot electron currents.

Another strategy for manipulating electronic spin is to induce precessional motion. Under the influence of a magnetic field, the spin of hot electrons can initiate a precessional motion while traveling through a material. This effect has already been demonstrated for various types of materials, including ferromagnets. However, only one study, conducted by our team, has proven this effect to exist for low-energy electrons within the energy range of current spintronic devices. Following this pioneering work, a new strategy was implemented to control the associated precession angle using an external parameter, temperature. Temperature variation in our device allows the tuning of the precession mechanism in a ferromagnetic layer. By employing a specific MTT with a three-dimensional magnetization configuration,

precession angles were extracted at various temperatures and could be explained within the context of temperature-dependent precessional motion of electronic spin.

Keywords: *Spintronics, Low energies, Transistor, Precession*

Remerciements

Tout d'abord, je tiens à remercier Claire Baraduc et Nicolas Rougemaille qui ont accepté de rapporter cette thèse. Je remercie également Marie Hervé d'avoir fait partie du jury tout comme Wolfgang Weber que j'ai eu le plaisir de connaître dans le cadre de mon comité de suivi.

En 2019, à la recherche d'un stage, je rencontrais un de mes professeurs à l'école des Mines, Stéphane Mangin. Sa proposition de m'envoyer trois mois à Sendai pour travailler avec Junta Igarashi m'a directement enthousiasmé. Si au début il s'agissait plus de partir au Japon quelques mois que d'étudier la spintronique, ce stage m'a complètement fait changé d'avis. A mon retour en France, je demandais à Stéphane s'il y aurait des possibilités de commencer une thèse dans l'équipe 101 de l'Institut Jean Lamour, une fois diplômé de l'école des Mines, et c'est ainsi que j'ai fait la rencontre de Michel et Dan.

Un grand merci à tous les deux pour ces trois (quasiment quatre) années passées ensemble. Je ne vous remercierai jamais assez d'avoir été là, dans les bons moments comme dans les compliqués. Il est évident que je n'en serais pas là aujourd'hui sans votre soutien. J'ai énormément appris à votre contact et je garderai toujours des bons souvenirs des longues discussions qu'on a pu avoir dans votre bureau.

Je tiens également à remercier toutes les personnes qui m'ont aidé au cours de ma thèse. Les membres du C.C Minalor avec Gwladys Lengaigne et Laurent Badie pour me former et réparer mes bêtises, ceux du C.C Magnétisme avec Thomas Hauet et Stéphane Suire. Je pense aussi à Sylvie Migot et Jaafar Ghanbaja pour les images TEM. Cela a été un vrai plaisir de plaisir d'échanger avec vous. Merci également à Isabelle Fournelle pour sa gentillesse et sa disponibilité. Enfin je n'oublie pas Pascal Boulet qui m'a formé et aidé pour les expériences de rayons X.

J'ai été incroyablement chanceux de faire partie d'une équipe aussi vivante. Je pense en premier lieu aux anciens, Mariam et Koss qui sont partis longtemps avant moi. Quentin, avec qui j'ai eu des conversations intéressantes, souvent avec quelques bières. Junta qui m'a connu encore étudiant jusqu'à aujourd'hui. Comment oublier tous ceux avec qui j'ai passé des heures à jouer au tarot et à la coinche : Maxime, Sandrine, Héloïse, Jon, Séb, Guillaume, Yann, Jude. J'espère que je vais trouver d'autres personnes pour entretenir mon addiction aux jeux de cartes dans la futur ! Je pense également au reste des doctorants avec qui j'ai passé des moments incroyables Eva, Corentin, Yi, Mariam, Léo. Alberto qui avec Jon et Maxime m'ont fait passé des heures sur Baldur's Gate quand j'aurais du être en train de rédiger mon manuscrit. Je pense aussi à Anna, avec qui j'ai partagé de longues heures à discuter avec un tisane sur son canapé.

Plus généralement, je remercie toutes les personnes qui ont partagé un bout de ma vie durant ces trois années de thèse. Merci beaucoup.

Table of contents

Table of figures and tables

Introduction

Electrons are said to be “hot” when excited above the Fermi level. They have a kinetic energy above that of the electrons of the Fermi sea. Hot electrons can be created by injecting energy in a material with exposition to an intense light, by applying a voltage or even heating the material. Once, these electrons are excited above the Fermi level they can travel within the material. Several factors can affect the transport of hot electrons such as temperature, crystalline structure or the presence of defects, inducing scattering mechanisms that lead to relaxation processes. Transport of hot electrons is crucial in several fields such as high-frequency electronics[2–4], optoelectronic devices (photovoltaics[5], photodetectors[6,7]) or even in magnetism (spin transfer torque[8], ultrafast demagnetization[9]). Understanding the transport of hot electrons requires a detailed knowledge of both electronic and structural properties of the material. Furthermore, knowledge about interactions between electrons and between electrons and other particles is critical to describe hot electrons transport.

Electrons are one of the numerous elementary particles. Electrons are charge carriers with a given mass and a spin. The spin is fundamental property that describes the intrinsic angular momentum of an electron. Electronic spin is a key concept in quantum mechanics and plays a significant role in various areas of physics. The spin of an electron is quantified, thus it can have only two states: +1/2 or -1/2. These values are noted as spin-up (or majority) and spin-down (minority). The spin is responsible for the magnetic properties of materials. Due to local exchange interaction, neighboring electronic spins can align in the same direction. This is the basis for ferromagnetism.

The field of spintronics combines both charge transport of electrons and properties of the spin. It aims to develop a new kind of electronic devices for storing, processing or transmitting information more efficiently than conventional electronics. Here, the spin is used to represent binary information (0/1). Here, transport of electrons is affected by their spin. Several phenomena have been investigated such as spin polarization, spin injection and spin-filtering effects in various materials, including semiconductors and metals. Among the numerous applications arising from spintronics, the most notable ones are spin valve devices[10], magnetic random-access memories (MRAM)[11] and structures using the spin-transfer torque (STT)[12] to manipulate magnetic materials.

In order to investigate the possibility of manipulating electronic spin, several points concerning the transport of hot electrons through heterostructures have been tackled.

In the first chapter, the structure of our magnetic tunnel transistor (MTT) is proposed with definitions and descriptions of mechanisms related to hot electrons transport in the different parts. Advantages of using an all solid state device for low-energy electrons investigations are given from both filtering and collection points of view. A detailed review on the different scattering mechanisms that electrons can suffer with other particles in metals for this energy range is proposed.

In the second chapter, transport measurement of hot electrons in our typical device is explained in the scope of electron-electron interactions. A model for the low-energy range describes accurately experimental data. Extension of our model to higher energy includes contribution of secondary electrons generated by electron-electron interactions. Scattering

mechanisms and spin-flip processes are discussed. A planar MTT can give further detail about spin-dependent transport and scattering of hot electrons.

In the third chapter, spin precession in a CoFeB layer is presented. Expressions derived from Schrödinger equation are given in the case of a precession phenomenon. Control of the magnetic configurations of our device is ensured with both 5 configurations stabilized and misalignment errors evaluated. Previous study on spin precession in CoFeB is completed with additional data and energy dependence of this phenomena is discussed.

In the fourth chapter, similar precession measurements are performed with two different materials inserted as a precession layer: CoAl and CoCu. Characterizations of both materials allowed optimized integration in the MTT. By changing the temperature, the internal molecular field of the ferromagnet is tuned. Thus, precession speed can be controlled with temperature. A model reproduces oscillations for both materials using only their magnetic properties.

Finally, the conclusion summarizes the results of this work and give few perspectives to further investigate and develop such kind of studies.

Chapter I: Magnetic Tunnel Transistor

I. Magnetic Tunnel Transistor

A magnetic tunnel transistor (MTT) is a three terminals device. Combining a magnetic tunnel junction deposited on top of a semiconductor, it opens a path to the development of new magnetoelectronic devices. In this magnetic transistor, the current is extracted from a tunnel barrier resulting in high energy electrons injected into the base. By inserting ferromagnetic layers inside the metallic base, one can form a spin valve. Thus, by stabilizing different magnetic configurations, attenuation of hot electrons beam (electrons above the Fermi level) can be tuned with an external applied field. Finally, a Schottky barrier is formed by a metal/semiconductor interface which filters incoming electrons in term of both energy and wave vector. Only electrons which did not keep a high enough energy with a right wave vector can be collected. They are called ballistic electrons.

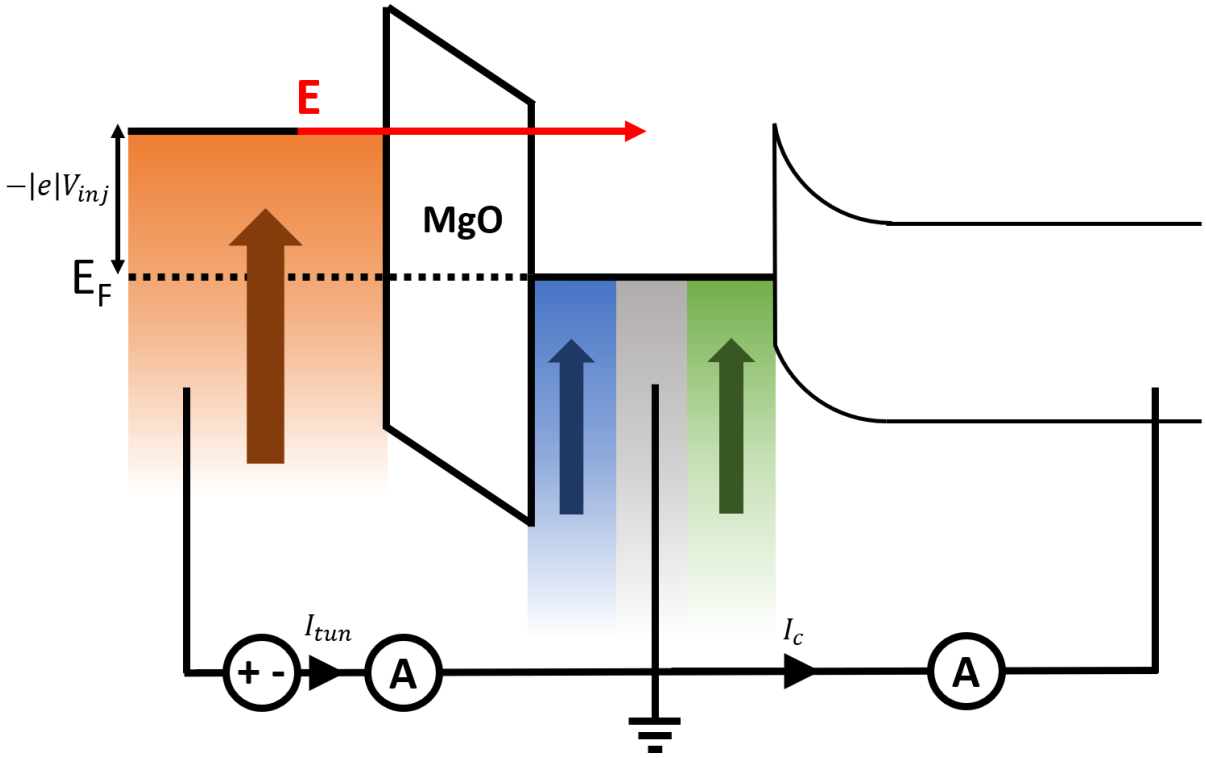

Figure I.1: All solid state device based on a magnetic tunnel transistor. Ferromagnetic layers are represented with different colors. The magnetic configuration shown here is colinear. During measurements, two current are collected: the tunnel current I_{tun} and the hot electron ballistic current crossing the Schottky barrier I_c.

I.1 – Magnetic Tunnel Junction

I.1 – 1. Introduction

A magnetic tunnel junction (MTJ) consists of two magnetic layers spaced by an insulator. The insulating layer is generally an oxide layer such as Al_2O_3 or MgO, several nanometer thick to allow tunneling of the electrons from one magnetic layer to the other one. Most used materials for magnetic electrodes are ferromagnetic alloys of transition metals as Co, Fe or CoFeB. When a voltage bias is applied across the two metallic electrodes, electrons can flow through the insulating layer. This effect, called tunnel effect, arises when the barrier is thin enough and is explained by quantum mechanics. Improvement of growth techniques made this

effect experimentally observable. Indeed, as the tunneling current is exponentially attenuated with the insulating layer thickness, growth techniques to reach nanometric scale deposition was necessary.

The tunneling current is also affected by the relative orientation of magnetization of the ferromagnetic electrodes. Therefore, the resistance of the device can be changed by an applied magnetic field. Generally speaking, the tunnel resistance is minimum when the magnetizations configuration is parallel (P) and maximum when antiparallel (AP). A typical figure of merit to characterize this effect of tunnel magnetoresistance (TMR) is expressed as:

$$TMR = \frac{R_{AP} - R_P}{R_P} \qquad (I.1)$$

where $R_{P(AP)}$ is the resistance state in the P (resp. AP) configuration.

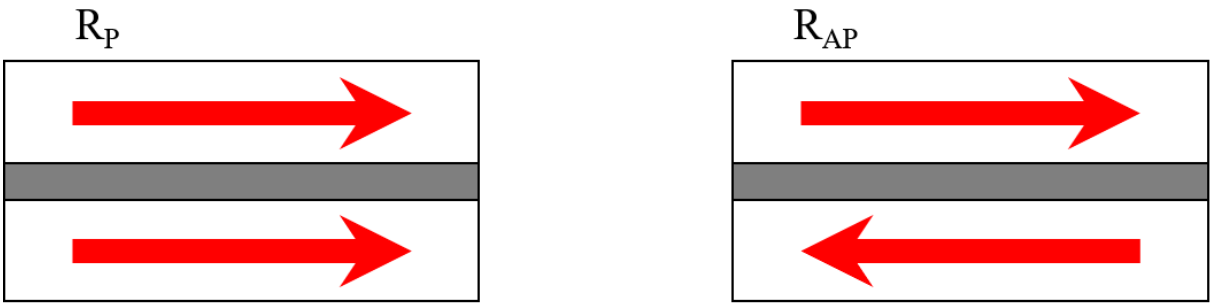

Figure I.2: Magnetic tunnel junction with two ferromagnetic electrodes separated by an insulating layer. Magnetizations are depicted by red arrows. In the parallel configuration (left), the tunnel resistance is lower than in the antiparallel one (right).

I.1 – 2. Tunnel Effect

Quantum mechanics predicts that a particle has a non-zero probability of crossing a potential barrier, even though its own energy is lower than the barrier height. This phenomenon is called "tunnel effect" and is shown on figure I.3. Considering a one dimensional problem, an electron of mass *m* and energy E crosses a rectangular potential of height U_0 and width *d* along the x-axis. By considering that the electron is free in the y and z directions, its wavefunction can be written $\Psi(x,y,z) = e^{i(k_y y + k_z z)}\Phi(x)$. Therefore, one dimensional Schrödinger equation can be solved:

$$-\frac{\hbar^2}{2m}\frac{\partial^2\Phi(x)}{\partial x^2} + V(x)\Phi(x) = E\Phi(x) \qquad (I.2)$$

To find analytical solutions for this problem, one has to separate three regions:

- In I and III regions, the electron is not affected by any potential ($V(x) = 0$). Thus, Schrödinger equation has a well-known form of solutions: $\Phi(x) = Ae^{ikx} + A'e^{-ikx}$, with $k = \frac{\sqrt{2mE}}{\hbar}$.
- In II region, the potential barrier $V(x)$ = U_0 is higher than the electron energy E. Solutions of Schrödinger equation then takes the form $Be^{\kappa x} + B'e^{-\kappa x}$ ($\kappa = \frac{\sqrt{2m(U_0 - E)}}{\hbar}$) which leads to exponential decay of the wavefunction along the tunnel barrier.

The transmission through the barrier can also be calculated by considering the continuity of the wavefunction and its derivative at interfaces between all three regions and assuming that $\kappa d \ll 1$:

$$T \approx 16 \frac{E(U_0 - E)}{U_0^2} e^{-2d\frac{\sqrt{2m(U_0-E)}}{\hbar}} \qquad (I.3)$$

Even though actual tunnel effect is more complicated than this simple model (due to distortion of barrier potential with applied voltage), this solution highlights the possibility of injecting electrons with an energy E, $E_F < E < U_0$, E_F being the Fermi level of the metals (regions I and III), through a potential barrier.

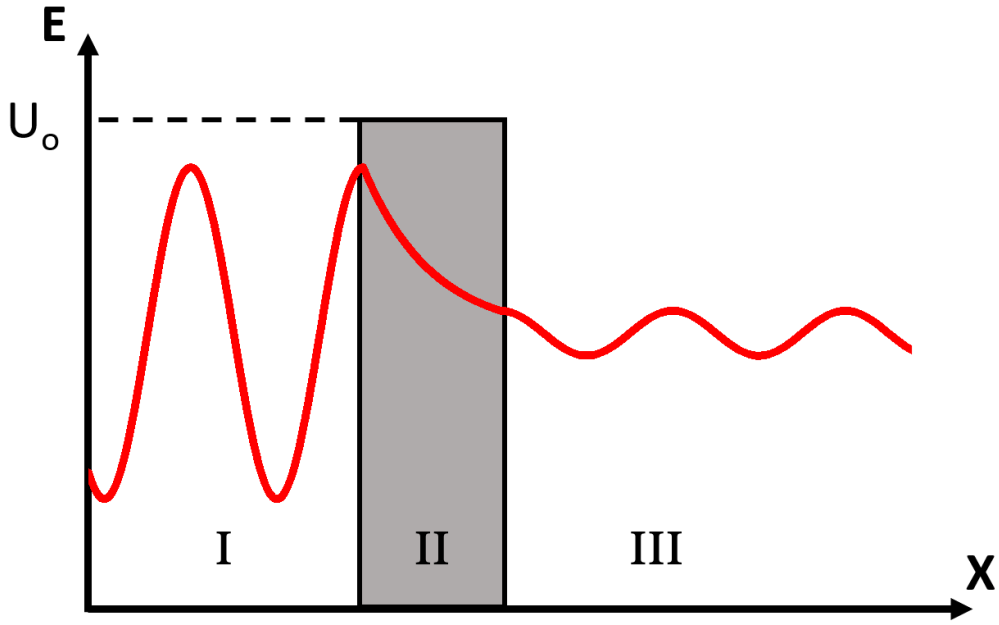

Figure I.3: Diagram of the tunnel effect. The wavefunction of an electron crossing a tunnel barrier (Region II) is represented in red. Its energy is lower than the barrier height (U_0).

I.1 – 3. Jullière's model

Shortly after the first experiments of tunneling[13], spin-dependence of tunnel effect has been demonstrated by Meservey and Tedrow in a ferromagnet/insulator/superconductor heterostructure[14]. An external magnetic field is applied on the structure to saturate the ferromagnet magnetization. Thus, Zeeman effect will lead to a shift in the density of state of quasiparticles of the superconductor (Fig.I.4.a). Electrons flowing from the ferromagnet can be spin-polarized for a given energy (Fig.I.4.b) and will be filtered when crossing the tunnel barrier. Therefore, variations in the measured conductance can be observed while changing injection

energy (Fig.I.4.c). Local maximums correspond to the opening of new conduction channels in the superconductor.

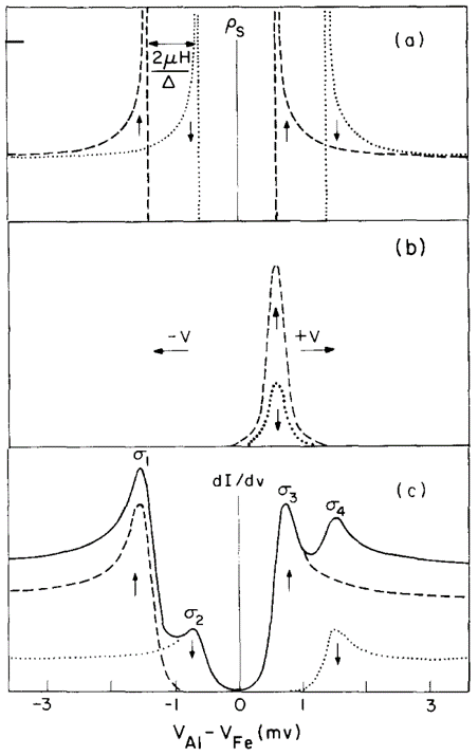

Figure I.4: Superconductor-ferromagnetic metal tunneling. (a) DOS of a superconductor as function of voltage in a magnetic field. (b) spin-resolved derivative of the DOS for a ferromagnet. (c) Theoretical normalized conductance for each spin direction (dotted and dashed curves) and the total conductance (solid line). Taken from Merservey and Tedrow[14].

Through this asymmetric conductance curve, Tedrow and Meservey were able to access the spin-polarization of several ferromagnetic materials inserted in a F/I/S heterostructure[15]. This spin-polarization is defined as :

$$P = \frac{N^{\uparrow}(E_F) - N^{\downarrow}(E_F)}{N^{\uparrow}(E_F) + N^{\downarrow}(E_F)} \qquad (I.4)$$

where $N^{\uparrow,\downarrow}(E_F)$ are the electron density of states of the ferromagnetic electrode for majority spin and minority spin at the Fermi level, respectively. Discrepancies between measurements and theoretical predictions also showed presence of spin-flip mechanisms during tunneling phenomena which leads to a experimental spin-polarization lower than expected.

Few years after, Jullière performed conductance measurements on a Fe-Ge-Co (F/I/F) and observed a difference of resistance between parallel and antiparallel magnetizations configurations in the structure[16]. This report of the first experimental demonstration of Tunnel Magneto-Resistance (14%) was limited both by temperature (4.2K) or energy of injection (TMR measured with less than 10mV). Following Tedrow and Meservey's analysis, Jullière explained his work by assuming spin conservation during tunneling and dependence of the relative resistance of the density of state of electrodes. Therefore, associated Tunnel Magneto-Resistance (TMR) can be expressed as a function of the spin-polarization from both electrodes:

$$TMR = \frac{R_{AP} - R_P}{R_P} = \frac{\left(N_1^{\uparrow}N_2^{\downarrow} + N_1^{\downarrow}N_2^{\uparrow}\right) - \left(N_1^{\uparrow}N_2^{\uparrow} + N_1^{\downarrow}N_2^{\downarrow}\right)}{\left(N_1^{\uparrow}N_2^{\uparrow} + N_1^{\downarrow}N_2^{\downarrow}\right)} = \frac{2P_1P_2}{1 - P_1P_2} \qquad (I.5)$$

Where R_k represents the electrical resistance of the structure in either parallel (k=P) or antiparallel (k=AP) configuration of the magnetizations, P_i is the spin polarization of electrode i, and $N_i^{\uparrow}$ and $N_i^{\downarrow}$ are the densities of states at the Fermi level of electrodes for majority and minority respectively. Figure I.5 illustrates relationships between the two resistance states and the density of state for each electrodes.

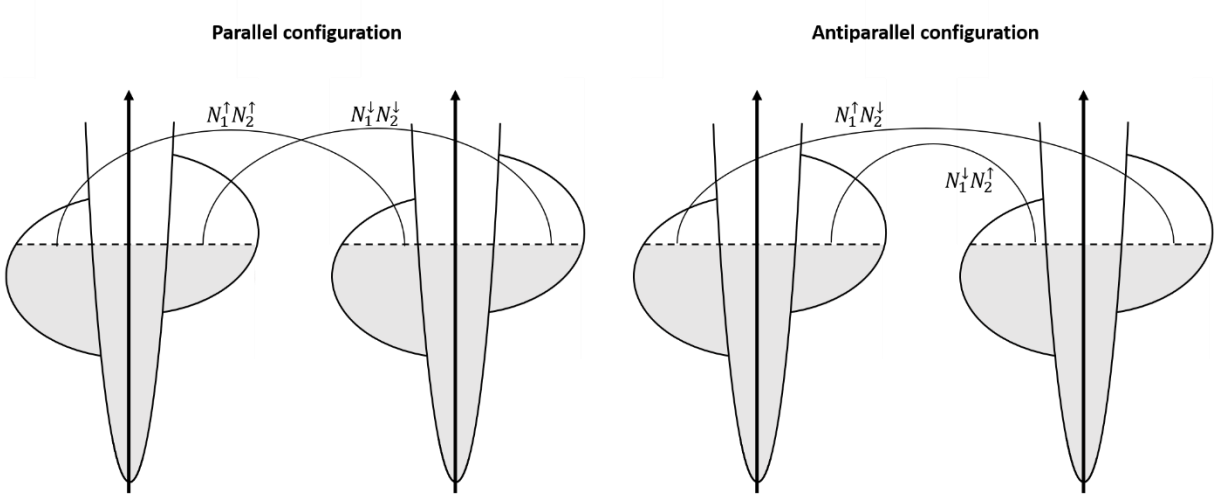

Figure I.5: Jullière's model for tunnel magneto-resistance. The density of state for each electrodes is described by two bands: majority spins (↑) and minority spins (↓) splitted by exchange interaction. Associated resistance for each configuration state is calculated by summing two independent conduction channels.

From Tedrow and Meservey spin-polarization results on Fe and Co[15], Jullière calculated a predicted TMR of 26%, close to the value actually measured. However, this interpretation is based exclusively on density of states of electrodes at the Fermi level and is neglecting both the tunnel barrier characteristics (height, width,…) and processes that could alter ballistic transport during tunneling such as inelastic interactions.

Measurements of electrons tunneling from several ferromagnetic materials[15,17] showed positive values for spin-polarization. If spin-polarizations of tunnel electrons flowing from Fe, Co or Ni followed their bulk magnetization, that of Co and Ni did not match with the materials spin-polarization at the Fermi level. Indeed, they both are strong ferromagnets whose spin-polarization in negative at the Fermi level. Based on band structure calculations, Stearn[18] proposed to distinguish contributions from d-like localized electrons and s-like itinerant ones – based on hybridization of electrons. s-like electrons are supposed to dominate tunneling due to their high velocity at the Fermi level, even though they are fewer than d-like ones. This model of free electron tunneling gives a more accurate interpretation for spin-polarization experiments on MTJ[19].

I.1 – 4. Slonczweski's model

In 1989, Slonczewski went a step further to model spin-dependent tunnel transport[20]. Slonczewski considered the whole junction to integrate the impact of oxide barrier properties

on the tunnel transport. His analytical calculation assume that only electrons close to the Fermi level and with a wave vector perpendicular to interfaces ($k_{\parallel} \approx 0$) contributes to the tunneling.

A diagram of a MTJ as modeled by Slonczweski is shown on Figure I.6. The junction consists of a stack Ferromagnet 1 / Insulator / Ferromagnet 2 with the three different regions with different potentials for spin up (resp. down) electrons: $V_{1\uparrow}$ (resp. $V_{1\downarrow}$) for the left ferromagnet, U_0 for the insulating layer and $V_{2\uparrow}$ (resp. $V_{2\downarrow}$) for the right ferromagnet. In this model, spin-dependent tunnel effect is explained by the difference of energy states in each electrodes assuming a parabolic dispersion shifted in energy (see Fig.I.5).

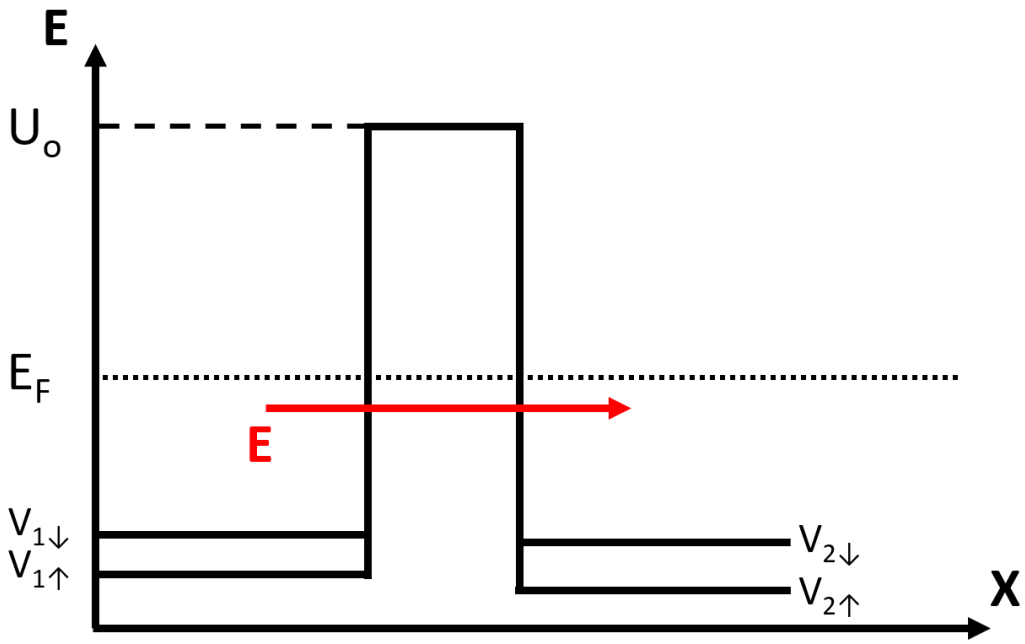

Figure I.6: Energy profile in a MTJ. Potential are spin-dependent in each ferromagnetic electrodes (indexed 1 and 2). An electron of energy E crossing the tunnel barrier is represented with the red arrow.

Assumptions are made that the system temperature is zero, electrons are injected with a low energy (only states close to E_F are contributing to the tunnel current) and barrier is thick enough so that $\kappa d \gg 1$. By solving Schrödinger equation for both conduction channels (majority and minority spins), spin-dependent transmission coefficients were calculated :

$$T^s = 16\frac{\kappa^2 k_1^s k_2^s}{[\kappa(k_1^s + k_2^s)]^2 + (\kappa^2 - k_1^s k_2^s)^2} e^{-2d\kappa} \qquad (I.6)$$

where k_i^s is the wave vector of s-spin electrons in the electrode i and κ is the imaginary part of the evanescent wave vector in the tunnel barrier. Associated conductance for each conduction channel can be expressed for each magnetic states:

$$G_P \propto \frac{\kappa}{d}(T_{\uparrow\uparrow} + T_{\downarrow\downarrow}) \;\&\; G_{AP} \propto \frac{\kappa}{d}(T_{\uparrow\downarrow} + T_{\downarrow\uparrow}) \qquad (I.7 \;\&\; I.8)$$

Furthermore, wave vectors of electrons tunneling can be expressed as for the normal tunnel effect but with spin-dependent energies (wave vector in the barrier is left unchanged):

$$k_{1(2)}^{s} = \frac{\sqrt{2m\left(E_F - V_{1(2)}^{s}\right)}}{\hbar} \qquad (I.9)$$

Following Jullière's expression of the Tunnel Magneto-Resistance, Slonczewski finds a similar formulation:

$$TMR = \frac{G_P - G_{AP}}{G_{AP}} = \frac{2P_1^{eff}P_2^{eff}}{1-P_1^{eff}P_2^{eff}}, \text{ with } P_i^{eff} = \frac{k_i^{\uparrow} - k_i^{\downarrow}}{k_i^{\uparrow} + k_i^{\downarrow}} \times \frac{\kappa^2 - k_i^{\uparrow}k_i^{\downarrow}}{\kappa^2 + k_i^{\uparrow}k_i^{\downarrow}}$$

Where P_i^{eff} represents the effective polarization in the electrode *i*. Unlike Jullière's expression of the polarization, this term includes influence of the barrier characteristics on tunneling via κ. In case of a high tunnel barrier ($\kappa \gg k_i^{\uparrow}k_i^{\downarrow}$), one retrieves Jullière's TMR formula. Even though further characteristics of the tunnel barrier are still ignored, this model proves the importance of band structure of materials concerning tunneling, especially the electrode/barrier influence on the TMR.

I.1 – 5. General models for tunnel transport

Slonczewski's model assuming free-electron behavior is based on three assumptions:

1. Applied voltage on the junction is low
2. Temperature is taken equal as zero
3. Electrons have wave vectors perpendicular to interfaces ($k_{\parallel} \approx 0$)

However, in real systems those hypothesis may not be verified. Corrections can be made to generalize Slonczewski's model and thus, lifting one of the three items.

Low voltage

Voltage applied between MTJ electrodes can modify the energy profile of the tunnel barrier. During distortion of the barrier, the potential becomes trapezoidal or even triangular if the voltage is high compared to the barrier height (Fowler-Nordheim tunneling). The different regimes are shown on Figure I.7.

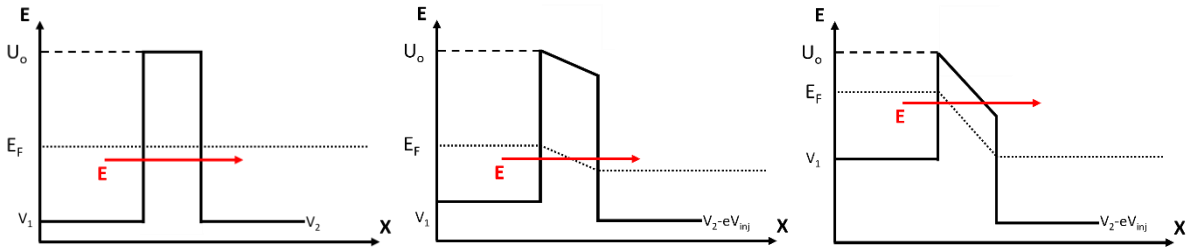

Figure I.7: Three distortion states under the effect of voltage. a) Almost no voltage is applied and the barrier remains rectangular. b) Applied voltage V_{inj} makes the barrier trapezoidal. c) Under V_{inj}, the barrier becomes triangular and electrons tunnel only partially in the insulating layer.

When the barrier is distorted, Fermi levels are shifted by $-eV_{inj}$ due to the applied voltage. Therefore, electrons from occupied states of the first electrode are injected into vacancy states of the second. Some analytical models have been proposed in order to overcome effects of voltages on barrier distortion. Most known are Simmons[21] and Brinkman[22] models. These

models showed the strong dependence of tunnel transport on barrier thickness and height. An estimation of the two parameters can also be made from I-V curve of the MTJ. However, the two models do not include more complex effects such zero-bias anomaly (ZBA)[23–25] that takes place at low voltages.

For spin-dependent tunnel transport, those analytical models predict variations of the magnetoresistance with voltage. In this approach, the TMR always decreases by increasing injection energy as observed experimentally[23,26]. Still, it cannot be used for a quantification of magnetoresistance voltage-dependence nor for more complex MTJ structures. Indeed, only the tunnel barrier is taken into account. As the density of states of ferromagnetic electrodes, phenomena are ignored in this model. More detailed methods taking into account electronic structure of ferromagnetic electrodes have modeled band structure impact on spin-dependent transport[27].

Zero temperature

So far, temperature has always been taken equal to zero kelvin. However, several effects are neglected. Indeed, with increasing temperature, an enlargement of the Fermi-Dirac distribution needs to be considered. Stratton studied voltage-current characteristics of tunneling across an insulating layer for various temperatures[28]. He developed a model for tunnel transport in defect-free structures to support experimental measurements. By including the smearing of electronic states close to the Fermi level in the free electron model, he was able to reproduce temperature-dependence of the tunnel resistance for an $Al/Al_2O_3/Al$ structure, varying by less than 10% from 4.2K to room temperature.

For MTJs, the change of resistance is stronger with Co electrodes over the same temperature range[29]. Shang *et al.* explained this difference by the impact of spin-wave excitation. In this phenomenological model, two canals are assumed for tunneling: a direct contribution and a second one for electrons assisted in the tunneling which is spin-independent. The total conductance of the structure is then expressed as:

$$G(\theta) = G_T(1 + P_1P_2\cos(\theta)) + G_{SI} \qquad (I.10)$$

Where θ is the angle between the electrodes magnetizations, G_T is a prefactor for direct tunneling, G_{SI} is the spin-independent contribution and P_1 and P_2 are the effective polarizations of the ferromagnets. Due to spin-wave excitations (see I.3 – 2. **Electron-magnon interaction**), the polarizations decrease with increasing temperature, following a Bloch's law:

$$P(T) = P_0\left(1 - \alpha T^{\frac{3}{2}}\right) \qquad (I.11)$$

With P_0 being the effective polarization at 0K and α, a material-dependent constant. By fitting α, a satisfactory explanation for both tunnel resistance and TMR temperature-dependence could be obtained. MacDonald *et al.* theoretical calculations confirmed these ideas with a rigorous link between $M(T)$ and $P(T)$[30].

The second contribution G_{SI} is not dependent on the magnetizations but can also impact tunnel resistance temperature-dependence. Among all the possible contributions that can lead to spin-independent tunneling, the presence of vacancies and/or metallic impurities inside the barrier is usually dominant. These defects are responsible for localized states leading to hopping

for electrons[31]. This hopping mechanism leads to an exponential increase of the resistance with decreasing temperature.

Perpendicular wave vector

In the Slonczewski's model, only electrons with a perpendicular wave vector to the interfaces are considered ($k_{\parallel} \approx 0$). However, this assumption is only verified for thick tunnel barrier. The generalized wave vectors can be expressed as:

$$k_{1(2)}^{S} = \sqrt{\frac{2m(E_F - V_{1(2)}^{S})}{\hbar} - k_{\parallel}^{2}} \text{ and } \kappa = \sqrt{\frac{2m(U_0 - E)}{\hbar} + k_{\parallel}^{2}}$$

and the probability for tunnel transmission,

$$T^{S} = 16\frac{\kappa^2 k_1^S k_2^S}{\left[\kappa(k_1^S + k_2^S)[1 + \exp(2\kappa d)]\right]^2 + \left[(\kappa^2 - k_1^S k_2^S)[1 - \exp(-2\kappa d)]\right]^2} e^{-2d\kappa} \quad (I.12)$$

The attenuation in the tunnel barrier κ is higher for electrons with non-perpendicular wave vectors. The latter expression shows that with a thick tunnel barrier, those electrons are strongly attenuated. This model shows that the TMR increases when the barrier thickness is decreased and to increase when the barrier height increases[32].

For MTJs, taking into account electrons with non-perpendicular wave vectors can be critical to understand tunnel transport. Calculations have studied their impact on conductance of tunnel barrier. Here, all diffusion processes that can help electrons to overcome the tunnel barrier are neglected. The system modeled is supposed to be monocrystalline. MacLaren *et al.* computed calculations on a Fe(001)/barrier/Fe(001) MTJ where the barrier is described as a rectangular energy step[33]. They calculate the conductance resolved in $k_{\parallel}$. The results are shown on Fig.I.8 for parallel and antiparallel configurations.

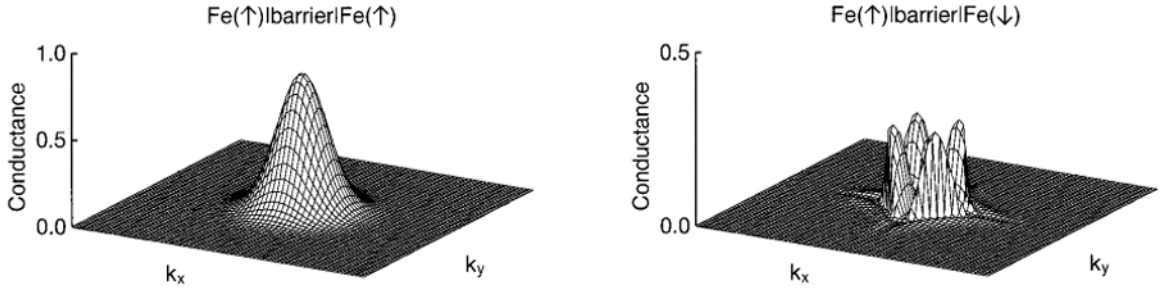

Figure I.8: Tunnel conductance resolved in $k_{\parallel}$ for parallel (left) and antiparallel (right) configuration of a Fe(001)/barrier/Fe(001) junction. From MacLaren et al.[33].

In the parallel configuration, the conductance is maximum when $k_{\parallel} = 0$ and the distribution is similar to the free-electron model. However, in the antiparallel configuration, the conductance is dominated by electrons whose wave vectors is different from 0, which are not free-electrons. Therefore, reaching more realistic models for electronic states is critical for understanding spin-dependent tunnel transport.

I.1 – 6. Interface dependence: effect of electronic structure

The dependence of tunnel current on electronic structure at the oxide/ferromagnet interfaces is strong. In order to explore its effects over bulk ones to the tunneling, is to insert

ultrathin layers at the electrode-barrier interface. In 1975, Tedrow and Meservey[34] showed that spin-polarization of tunneling electrons results from the first monolayers of Co. In the same way, Moodera *et al.* studied the decrease of spin-polarization as a function of gold thickness in a $Al/Al_2O_3/Au(d)/Fe$ structure[35]. The growth of interface layers is critical for reaching ideal tunnel transport[36]. In a $Co/Al_2O_3/Co$ junction, LeClair *et al.* inserted non-magnetic Cr between an electrode and the oxide layer and got an exponential decay the TMR with the Cr thickness[37]. With only 3Å of Cr deposited, the TMR can be reduced by 90% as shown on figure I.10. Still, the magnetoresistance was almost completely restored by reinserting 1nm of Co between the Cr layer and the tunnel barrier. This study further confirmed that ferromagnetic-insulator interfaces dominate MTJs properties, in good agreement with precedent spin-dependent spectroscopies with ultrathin magnetic layers.

The development of improved deposition with a better control of epitaxy along with new measurement techniques led to further investigation on band structure matching at the metal-barrier interface during tunneling. Binning introduced Scanning Tunneling Microscopy where a tip is used to inject tunneling electron locally through a vacuum gap[38]. Before that, tunneling spectroscopy was performed exclusively with solid tunnel junctions. Replacing oxide barrier by a vacuum brings interesting advantages as using a defect-less and tunable tunnel barrier or studying specific physical or chemical regions on a material. Several materials have been used as bottom electrodes in STM-based tunneling experiments. Atomic resolution measurements on ferromagnetic thin films[39–41] enabled to probe local electronic states of the materials. Sharp features have been associated with band structure calculations, thus exhibiting its importance to understand tunnel transport (see Fig.I.9).

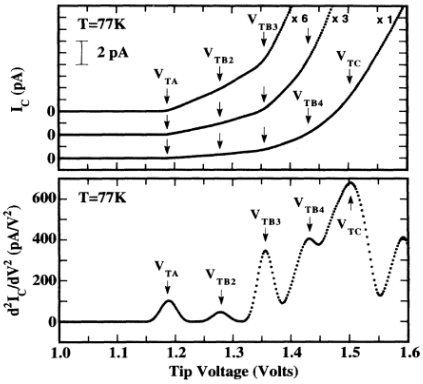

Figure I.9: BEEM I_c-V and its second derivative in a double barrier structure. All resonant states resulting from specific energy states are identified. From Sajoto et al.[42].

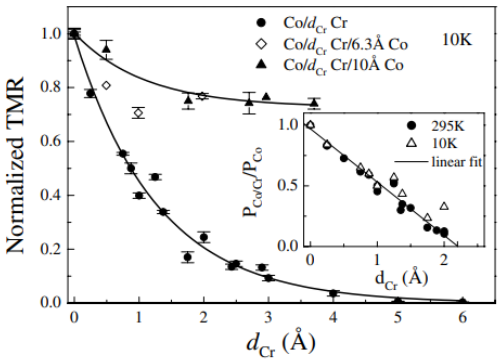

Figure I.10: Normalized TMR as a function of Cr interlayer thickness in $Co/Cr(d_{Cr})/Al_2O_3/Co$ and $Co/Cr(d_{Cr})/Co/A_{l2}O_3/Co$ junctions. From LeClair et al.[37].

Interfacial effects on tunnel transport is also highly impacted by chemical bonds between elements between the ferromagnetic and insulating layers. Indeed, bonds can involve preferentially sp or d states. In the case of Fe or Co, the first kind results in a positive polarization when the latter, gives rise to negative polarization for a same material[43]. Therefore, one can play with ferromagnetic electrodes and oxide barrier combination to tune the sign of the TMR[44]. However, theoretical work shows that interface is not enough to explain those experimental results. *Ab initio* calculations tends to prove that if the polarization is indeed positive inside the tunnel barrier, it is negative at the Co/Al_2O_3 itself[45]. The tunnel barrier also filter electrons depending on their orbital behavior.

I.1 – 7. MgO tunnel barrier

Butler *et al.* and Mathon *et al.* simultaneously calculated conductance of the Fe/MgO/Fe(001) using different approaches[46,47]. Similar results have been obtained, predicting a TMR above 1000% at 0K. Mathon's work tends to show that this high TMR comes from the difference of conductance at the gamma point. It is surprising to have $G^{\uparrow\downarrow}(k_{\parallel})$ reaching a minimum at this point because the density for minority states in Fe is different from 0. Butler *et al.* showed an additional effect of the MgO, the symmetry filtering.

By considering that only states around the gamma point are contributing to the tunnel transport, it is possible to describe tunneling with a finite number of Bloch states Δ. Here, the states are no longer described by their orbital behavior (sp or d) but by their symmetry. Indeed, the states s, p and d are hybridized. Still, the Bloch states Δ have a behavior that correspond to a certain extent to a sp or d one. The table I-1. summarizes the correspondence between orbital and Δ states.

Symmetry	Compatible orbitals
Δ_1	s, p_z, d_{z^2}
Δ_5	p_x, p_y, d_{xz}, d_{yz}
Δ_2	$d_{x^2-y^2}$
$\Delta_{2'}$	d_{xy}

Table I.1: Atomic orbital classified with their symmetry in the Δ direction

The zone $\Gamma - \Delta - H$ of the Fe band diagram is shown on Fig.I.11. For a Fe layer oriented in the [001] direction, Δ states have a perpendicular wave vector. The magnetic exchange results in the shift of majority/minority bands by about 2eV.

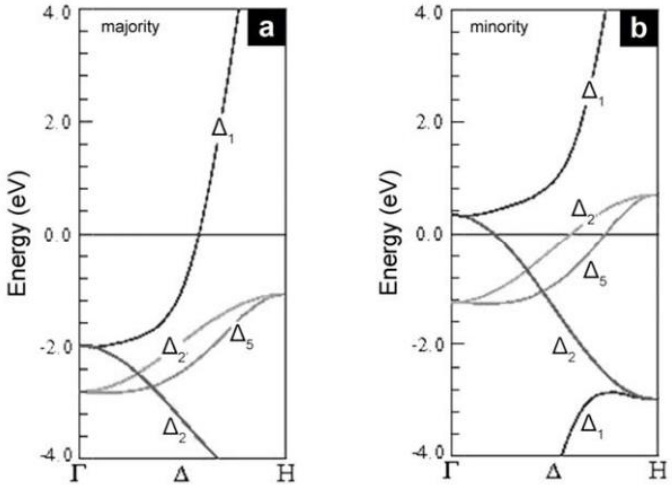

Figure I.11: Band diagram for bcc Fe in the $\Gamma - \Delta - H$ direction in the case of a) majority and b) minority spins. All the bands are labeled with their symmetry[48].

At low energies, the only states that can contribute to the transport are those available at the Fermi level. For majority spins, they are $\Delta_1^{\uparrow}, \Delta_5^{\uparrow}$ and $\Delta_2^{\uparrow}$, and for minority spins

$\Delta_5^{\uparrow}, \Delta_2^{\uparrow}$ and $\Delta_{2'}^{\uparrow}$,. Fe has a half-metallicity behavior for the Δ_1 symmetry: states are available for the majority spins but not for the minority ones. Therefore, in case of ballistic ($k_{\parallel}$ is conserved) and coherent (symmetry conservation) transport, the canal $\Delta_1^{\uparrow} \rightarrow \Delta_1^{\downarrow}$ does not exist.

In the same direction, band structure of MgO can be calculated. One can retrieve the same states $\Delta_1, \Delta_5, \Delta_2$ and $\Delta_{2'}$. For each one of those states, attenuation factor can be estimated, thus leading to the following relationship:

$$\kappa_2 > \kappa_{2'} > \kappa_5 > \kappa_1 \qquad (I.13)$$

The filtering of MgO is dependent on the symmetry of each state in the Γ-Δ-X direction. The states Δ_1 are the less attenuated ones. Other states Δ_5, Δ_2 and $\Delta_{2'}$ which can allow the tunnel transport in MgO of minority spins are strongly attenuated.

I.1 – 8. Decoherence length and injection/attenuation cones

In order to study manipulation of electronic spin, spin conservation during the whole travel of hot electrons is crucial. Absorption of a spin current has been predicted for ferromagnetic materials. In typical spin valve structure (see Fig. I.12 – a), theoretical predictions[49–51] evaluated this lengths to lie around 1nm or 2nm. This value was confirmed by experimental work[52]. After electrons crossed this thickness of ferromagnetic material, all information concerning their initial spin orientation is lost and thus, no further details can be extracted from such measurements.

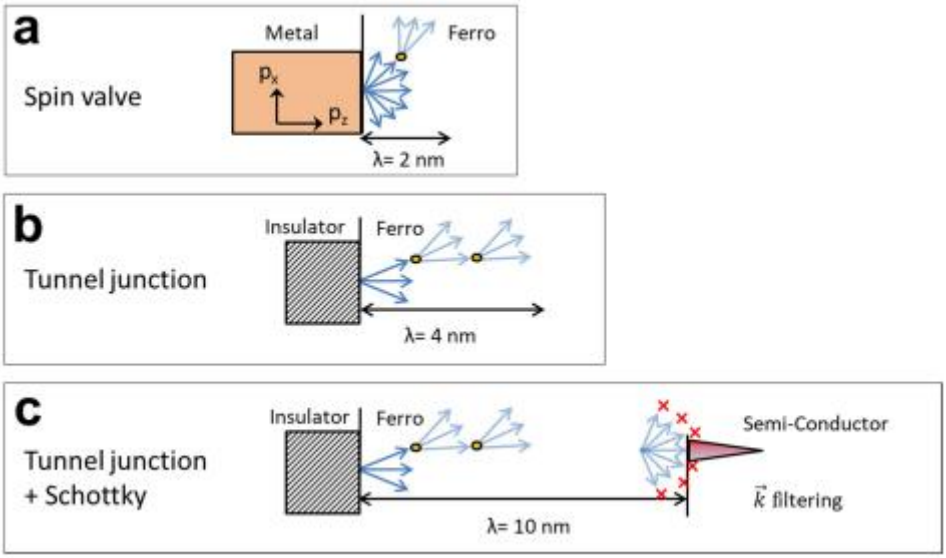

Figure I.12: Classical decoherence processes for different spintronics devices in the literature: a) spin valve, b) magnetic tunnel junction, c) Combinaison of tunnel junction and Schottky barrier as present in a magnetic tunnel transistor. From Vautrin[1].

When electrons are injected from a magnetic tunnel junction (see Fig. I.12 – b), the spin transverse component is damped by 50% within the first few nanometers[53,54]. This decay length is here evaluated around 4nm, larger than similar studies on spin valves. This is explained by an injection cone reduced in the case of a tunnel barrier due to k-vector selection.

Adding a Schottky barrier in the device (see Fig.12 – c) results in additional filtering of incoming electrons. Here not only injection cone is more narrow due to the tunnel barrier, but

electrons are also filtered by the Schottky acceptance cone. Experimental results suggest that the effective decay length of collected electrons can then be increased to 10nm[1]. The following section will focus on Schottky barrier to show how it contributes to selection of hot ballistic electrons.

I.2 Schottky barrier

I.2 – 1. Shape of a Schottky barrier

Schottky barrier formation

A Schottky barrier is a potential energy barrier formed at a metal-semiconductor contact (see Fig. I.13). The discontinuity of electronic states responsible for conduction in the two materials results in a non-linear behavior against applied voltage. The work function (Φ) is defined as the energy difference between the Fermi level (E_F) and the vacuum level of the material. When the metal and the semiconductor are in contact, the Fermi levels of both materials ($E_{F,M}$ & $E_{F,SC}$) will align, producing a curvature of conduction and valence bands. The presence of an energy gap in the semiconductor results in an offset known as the Schottky barrier height (ϕ_{Sch}). This barrier is defined through the formula :

$$\phi_{Sch} = \Phi_M - e\chi \qquad (I.14)$$

The Schottky barrier leads to a rectifying behavior of the contact: the flow of electrons is easier coming from the semiconductor than from the metal. Thus, this system can be used as a diode conducting the current in one direction and blocking electrons in the other.

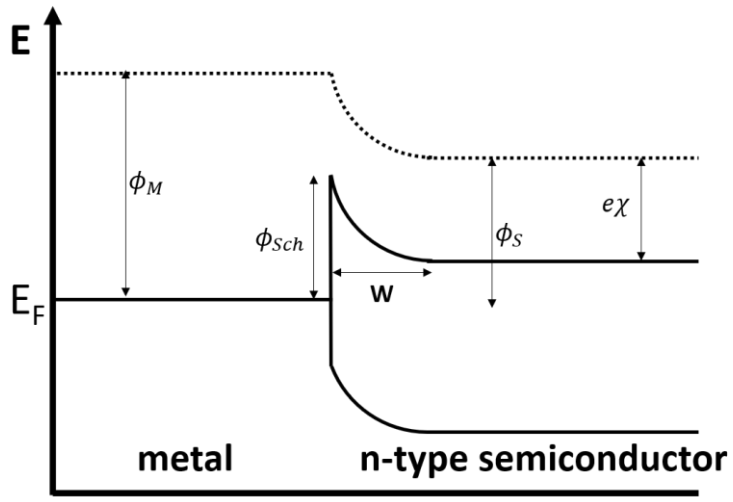

Figure I.13: Energy diagram of a Schottky barrier.

Depletion Zone

The curvature of the bands in the semiconductor takes place on a region called depletion zone. The width of this region can be expressed as follows[55]:

$$W = \sqrt{\frac{2\varepsilon_S}{e^2 N_D}(\Phi_M - \Phi_S)} \qquad (I.15)$$

Where ε_S is the semiconductor permittivity, N_D the charge carriers in the semiconductor and e electronic charge.

Schottky Resistance

At room temperature, a direct I-V measurement of a Schottky diode shows a non-zero current flowing through the metal-semiconductor contact even under reverse bias. This signal comes from diffusive current crossing the interface. This contribution to the collected current can be reduced with an enhanced Schottky resistance under zero-bias[56]:

$$R_0 = \frac{k_b}{eA^*TS}\exp\left(\frac{\phi_{Sch}}{k_bT}\right) \qquad (I.16)$$

With T the temperature, k_b the Boltzmann constant, S the Schottky diode area and A* the Richardson constant that can be expressed:

$$A^* = \frac{4\pi e m^* k_b^2}{h^3} \qquad (I.17)$$

Where h is the Planck constant and m* the electronic effective mass in the semiconductor.

I.2 – 2. Hot electron current with a free-electron model

Previous studies on Ballistic Electrons Emission Microscopy (BEEM) structures paved the way for giving expressions for hot electron transport in such devices. Ludeke and Prietsch[57–59] divided transport in 3 separate steps. First, hot electrons are extracted from the tunnel barrier into the base. This generates a peaky electronic distribution around the energy of injection at the base entrance (e is the elementary charge and V_{inj}, the applied voltage). The injected electron beam will be considered mono-cinetic with wave vector $\boldsymbol{k}$ perpendicular to the interfaces[60]. In a second step, the charge carriers travel in the base towards the Schottky barrier. As the metallic layers thicknesses are smaller or of the same order of magnitude as attenuation lengths, scattering can be accurately described using an exponential decay of the ballistic electron population all along the base. In the last step, electrons that overcome the Schottky barrier height are collected in the semiconductor conduction band.

The shape of the BEEM spectra was determined analytically initially by Kaiser and Bell[61,62], followed by the work of Prietsch and Ludeke. A general expression of the collected current can be given by:

$$I_C \propto \int_{-\infty}^{\infty}\int_{0}^{4\pi}\left[F(E,T) - F\left(E - eV_{inj},T\right)\right]D\left(E,V_{inj},\boldsymbol{u}\right)e^{-\frac{d(\boldsymbol{u})}{\lambda(E)}}T(E,\boldsymbol{u})d\Omega dE \qquad (I.18)$$

where $F(E - V_{inj},T)$ represents the Fermi function of the tip electrons at temperature T, $D(E,V_{inj},\boldsymbol{u})$ is the tunneling probability from the tip to the metal for electrons at energy E at a tip voltage V_{inj}, **u** is the direction of electrons in the base, dΩ is the solid-angle in the direction **u**, d(**u**) is the path length of an electron traveling in the direction **u** and $\lambda(E)$ is the mean-free path in the base and $T(E,\boldsymbol{u})$ the transmission probability at the metal-semiconductor interface.

Free-electron behavior

The transmission probability of the Schottky barrier can be expressed as function of the perpendicular component of wavevectors relative to the metal-semiconductor interface:

$$T\left(k_{\perp,M}, k_{\perp,SC}\right) = \frac{4k_{\perp,M}k_{\perp,SC}}{\left(k_{\perp,M} + k_{\perp,SC}\right)^2} \qquad (I.19)$$

With $k_{\perp,M}$ representing the perpendicular component of the wave vector in the metal and $k_{\perp,SC}$, the one in the semiconductor.

Assuming both free-electron behavior and conservation of the parallel component of the wavevector, $k_{\perp,M}$ and $k_{\perp,SC}$ can be expressed as follows:

$$k_{\perp,M} = \sqrt{\frac{2m_M(E - E_M^0)}{\hbar^2} - k_{\parallel}^2} \qquad (I.20)$$

$$k_{\perp,SC} = \sqrt{\frac{2m_{SC}(E - \phi_{Sch})}{\hbar^2} - k_{\parallel}^2} \qquad (I.21)$$

with m_M (resp. m_{SC}) is the effective mass in the metal (resp. semiconductor), E_M^0 (resp. ϕ_{Sch}) is the conduction band-minima in the metal (resp. semiconductor) and $k_{\parallel}$, the parallel component of the wavevector.

Low energies

Close to the threshold ($E \approx \phi_{Sch}$), $k_{\perp,M} \gg k_{\perp,SC}$ and $k_{\perp,M}$ varies slightly with energy therefore, the energy dependence of the transmission probability is mostly that of $k_{\perp,SC}$:

$$T(E, k_{\parallel}) \propto k_{\perp,SC} = \sqrt{\frac{2m_{SC}(E - \phi_{Sch})}{\hbar^2} - k_{\parallel}^2} \qquad (I.22)$$

Angular distribution

By assuming equal angular distribution and equal path lengths of the ballistic electrons crossing the base, a substitution can be applied in equation I.18 with $D(E, V_{inj}, \boldsymbol{u})d\Omega$ being proportional to $D(E, V_{inj})k_{\parallel}dk_{\parallel}$. The distance of travel d(**u**) can also be taken equal to a constant.

By taking into account those three assumptions, equation I.18 can be rewritten as function of the parallel wave vector of incoming electrons:

$$I_C \propto \int_{E_F}^{eV_{inj}} \int_{0}^{k_{\parallel,max}} D\left(E, V_{inj}\right) e^{-\frac{d}{\lambda(E)}} k_{\parallel} T(E, k_{\parallel}) dk_{\parallel} dE \qquad (I.23)$$

In the first theoretical model proposed by Kaiser and Bell, a simplified expression of the collected current was given by:

$$I_C \propto \int_{E_F}^{eV_{inj}} \theta\left(E - \left(E_F - eV_{inj} + eV_b\right)\right) dE \int_0^{k_{\parallel,max}} k_\parallel dk_\parallel \qquad (I.24)$$

where $\theta(E - (E_F - eV_{inj} + eV_b))$ is the Heaviside function. This Heaviside function is introduced to model the transmission at the metal-semiconductor interface. The transmission coefficient is supposed to be independent of energy and of incoming electrons wavevectors: if the particle has an energy below ϕ_{Sch} it has a zero probability to overcome the Schottky barrier. If its energy is above this height, the probability is equal to 1. Integration of equation leads to the square law on the energy:

$$I_c \propto \left(eV_{inj} - \phi_{Sch}\right)^2 \qquad (I.25)$$

The modified version of Kaiser and Bell was proposed Ludeke and Prietsch few years later. It takes into account the dependence of the transmission probability of the Schottky barrier on both energy and parallel wave vector (equation I.22). Then, calculation of the integral (Eq. I.18) on $k_\parallel$ makes the power law appear:

$$I_C \propto \int_{\phi_{Sch}}^{eV_{inj}} (E - \phi_{Sch})^{\frac{3}{2}} dE \qquad (I.26)$$

Therefore, we obtain:

$$I_C \propto \left(eV_{inj} - \phi_{Sch}\right)^{\frac{5}{2}} \qquad (I.27)$$

Equation I.22 set a condition for electrons to enter the semiconductor: $k_{\perp,SC} > 0$. This condition is equivalent to defining a critical parallel wavevector for the square root to be strictly positive:

$$k_\parallel < k_{\parallel,max}(E) \; with \; k_{\parallel,max}(E) = \sqrt{\frac{2m_{SC}}{\hbar^2}(E - \phi_{Sch})} \qquad (I.28)$$

This restriction is equivalent to geometrical cone of acceptance at the metal-semiconductor. This cone will open more and more with increasing energy E. For a given energy $E > \phi_{Sch}$, only electrons with a low enough parallel wavevector component will be allowed to cross the Schottky barrier. Other electrons will be completely reflected towards the base.

The critical angle defining the acceptance can be introduced to express the relationship between the wavevector of incoming electron in the metal and its parallel component:

$$k_\parallel = \sin(\theta_C)\, k_M \qquad (I.29)$$

where θ_c is the critical angle that restricts the entering of electrons in the semiconductor (see Fig. I.14). This expression can be modified with equations I.22 and I.28 to introduce energy dependence of the critical angle:

$$sin^2(\theta_c) = \frac{m_{SC}}{m_M}\frac{V_{inj} - \phi_{Sch}}{E_F + V_{inj}} \qquad (I.30)$$

This model was initially introduced by Kaiser and Bell[62] to estimate the BEEM lateral resolution.

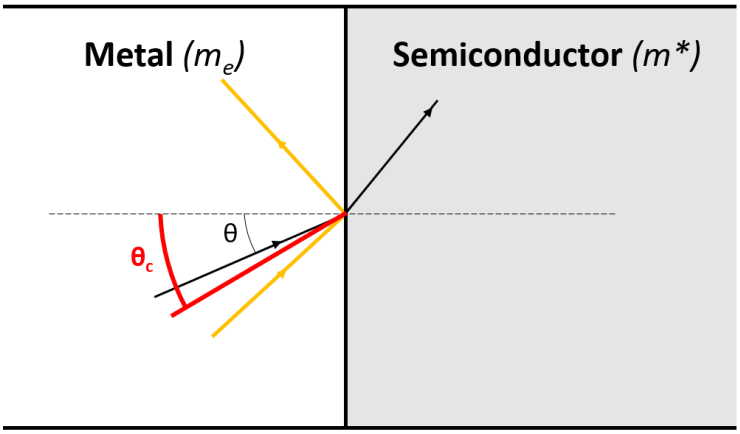

Figure I.14: Diagram of refraction/reflection at the Schottky interface. Depending on the incidence angle of wave vectors in relation to the interface normal, electrons with an angle below the critical angle (black) are transmitted while electrons out of the acceptance cone (orange) are reflected. This effect is due to the difference of effective masses on each side of the interface.

In the case of Si, the ratio of electronic masses is estimated to 0.2. The Schottky barrier height of the devices lies around 0.7eV and the Fermi level is taken at 7.1eV above the conduction band minimum. Therefore, an injection voltage of 1V gives a critical angle θ_c equal to 4.5°. Only electrons with an almost normal incidence can enter the collector.

I.2 – 3. Towards a more complex description

This description of BEEM spectra using free-electron like behavior proved to be unable to explain some experimental results[61–66]. For those studies, the transmission of electrons across the Schottky barrier was observed for electrons with wavevectors out of the acceptance cone, as defined in equation I.27.

In the case of diffuse or polycrystalline interfaces, these results could be explained by the presence of elastic interactions at the Schottky barrier leading to a reorientation of the wavevector towards the acceptance cone (i.e. a modification of parallel component between metallic and semiconductor regions). However, in the case of epitaxial interfaces, such explanation is not valid anymore. The ordering of the metal-semiconductor interface should actually make ideal models more accurate. Theoretical works showing the importance of band structure on ballistic transmission was carried by the group of Flores and de Andres[67–70]. This new model applied for epitaxial heterostructures considered Bloch electrons to describe the transport.

During the propagation of electrons in the base, hot electrons are diffused elastically by the crystal periodical potential. After travelling few nanometers, the electrons can be considered to occupy Bloch states of the band structure of the metal. Therefore, electrons parallel component of their wavevector can be affected. Once at the metal-semiconductor interface, this new transverse momentum can cross the Schottky barrier using conduction channels that were

not considered using the acceptance cone model based on free-electron behavior. Some experimental studies have showed good agreement between this Bloch electrons model and epitaxial Schottky barrier measurement.

Study of metal/Silicium interfaces

This distinction was of particular importance in the study of ballistic transport based on silicon collectors. Several groups have been comparing transport measurement on structures using Si(100) and Si(111). Studies focusing on epitaxial Au/Si with the two orientations for the substrates will be presented to illustrate the importance of the Bloch approach.

Figure I.15 shows the Brillouin zones of silicon with 2D-projections on the orientations considered for Si. The conduction band minimum are represented by a cross (+). The two open-state pockets are shown at 0.2eV (dashed line) and 0.6eV (dotted line) above the minimum. The Si(111) orientation presents no available state for incoming electrons at $\bar{\Gamma}$ point, unlike Si(100). Therefore, almost no current should be transmitted with this Si(111) orientation if considering a free-electron model with $k_{\parallel}$ conservation at the interface. However, some studies[53–55,57,60] showed the collected current to be almost independent of Si orientation, testifying of the limits of free-electron approach concerning the description of transport in the base.

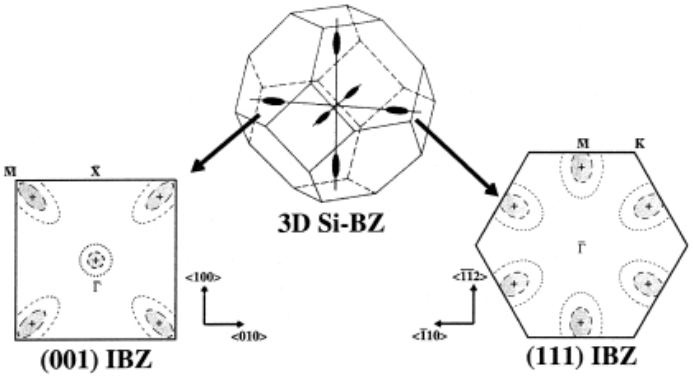

Figure I.15: Constant energy surface of Si conduction band (middle panel) and its respective projections onto (100) and (111) orientation (left and right panels). Conduction band minima are indicated by crosses (+) and open-state pockets at 0.2eV and 0.6eV above minimum by dashed and dotted line. From de Andres et al.[70].

Addition of a Schottky barrier leads to further filtering of incoming hot electrons crossing the base. Yet, while electron spin coherence is increased up to several nanometers, it is crucial to understand the transport physics taking place between the tunnel barrier and the Schottky contact. In our study, it consists in a spin valve allowing much flexibility over the choice of materials for investigated spin-dependent phenomena.

I.3 Spin Valve

I.3 – 1. Introduction

A spin valve is a trilayer composed of a non-magnetic metal sandwiched by two ferromagnetic layers. Depending on the relative orientation of the ferromagnets magnetizations, a change of conductance can be observed. At the Fermi level, this magnetoresistance effect is called giant magnetoresistance (GMR). The normal metal is used to space the two ferromagnets

in order for them not to interact with each other and to transmit the spin-polarized current from one ferromagnetic electrode to the other.

Unlike conventional spin valves, ours is crossed by hot electrons with an energy far above the Fermi level. Therefore, the injected beam will be attenuated while crossing the different layers of the spin valve. Furthermore, those electrons may suffer several interactions during their travel towards the Schottky barrier. Due to the high number of interfaces, defects, quasi-particles, it is necessary to review their possible interactions with hot electrons in order to characterize the collected current (wave vector, spin, energy).

I.3 – 2. Scattering mechanisms

Electron-electron interaction

Several calculations and experiments have shown that inelastic interactions of hot electrons can be described by only considering electron-electron scattering in our energy range. Indeed, electron-plasmon interactions affect electrons which have an energy of several eVs. For this process, primary hot electrons above the Fermi level feel Coulomb potential from the bath of "cold" electrons. During this collision, the hot electron will transfer part of his energy and momentum to the thermalized electrons (see Fig. I.16). Therefore, the result of this interaction is the creation of another hot electron coming from the Fermi level. This excited new electron also leaves a hot hole in the conduction band at its previous energy level below E_F. All electrons involved in this process are called secondary electrons after the collision. Those secondary electrons have an energy lower than that of the initial hot electron but higher than the Fermi level.

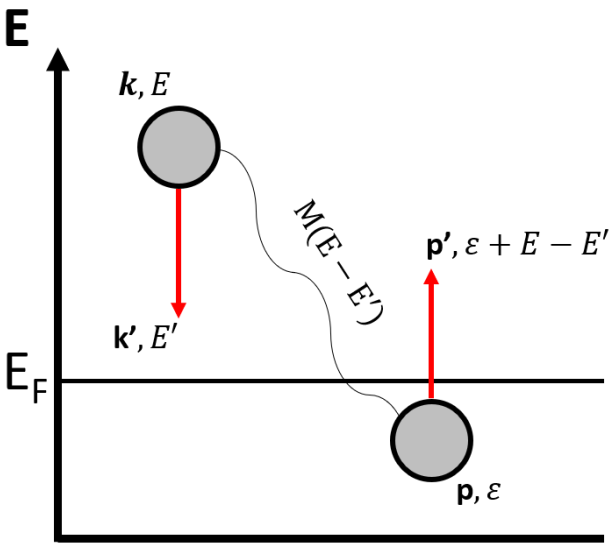

Figure I.16: Energy diagram of an electron-electron interaction. An incoming hot electron of energy E is scattered by an electron below the Fermi level. This interaction results in an energy transfer E-E'. This interaction is ruled by the transition probability M(E-E') for this interaction to happen. The newly excited electron will leave a hole after being excited.

Two conditions are required for electron-electron interactions to happen. First, incoming hot electrons can only be scattered by conductions electrons in an energy larger than $2E_F - E$

(for T=0K) due to Pauli's principle (all states below E_F are filled). Thus, the rate of scattering for inelastic collisions can be reduced with a presence of a gap in electronic density below the Fermi level. Secondly, secondary electrons must have empty electronic states to be scattered into. When, such states do not exist for a specific (E,**k**) couple, no interactions can be observed.

The Fermi golden rule can be used to expressed the electron-electron relaxation rate for a given electron of energy E. In this approach, all energy of the final states for primary and secondary electrons are summed with weights for the densities[71]:

$$\tau^{-1}{}_{e-e} = \frac{2\pi}{\hbar}\int_{E_F}^{E}\big(1-f(E')\big)\rho(E')\int_{0}^{E_F} f(\varepsilon)\rho(\varepsilon)\big(1-f(\varepsilon+E-E')\big)\times|M(E-E')|^2 dE'd\varepsilon \quad (I.31)$$

Here, the energy transfer for the primary electron is equal to E-E' for this single event, $M(E-E')$ is the matrix element for the transfer between initial and final states and ρ is the density of state for the given energy level. The latter equation I.3 is valid for normal metals. In the case of ferromagnets, the presence of spin-asymmetry between spin-up and spin-down in density of states and also the scattering itself gives rise to addition spin-dependent terms in equation I.3.

In addition, if one assumes energy independence of both matrix element and density of states, a simple expression for equation I.3 can be given by:

$$\tau^{-1}{}_{e-e} = \frac{\pi}{\hbar^3}\rho^3|M|^2(E-E_F)^2 \quad (I.32)$$

For simple metals like, this model reproduces well measurements of inelastic lifetime of hot electrons for an energy range of few eVs[72], thus showing that the main contribution to the inelastic interaction is electron-electron scattering. However, transition metals have a much more complex band structure with d-bands pockets opening and/or closing near the Fermi level. Therefore, the energy dependence of matrix elements and densities of states need to be taken into account[71,73].

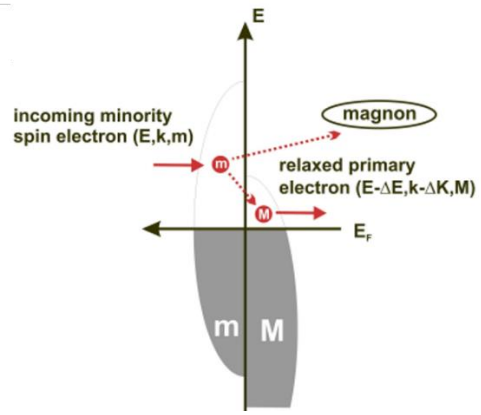

Figure I.17: Energy diagram of spontaneous magnon emission. An incoming spin down electron emits a magnon and thus, lose both angular momentum and energy during the spin-flip. From Heindl et al.[74].

Electron-magnon interaction

A magnon is a collective excitation of electronic spins in a magnetic material. Magnons are quasiparticles associated with vibration of the magnetization. They carry a certain amount

of energy, momentum and also a spin (-1 being associated to the minority spin orientation of the material). Some experiments have demonstrated the possibility of interactions between electrons and magnons[75]. There are two different processes of interaction for electrons and magnons: either a spin-wave can be emitted by a hot electron transferring a part of its energy, momentum and spin to the newly created magnon, or it can be absorbed by another electron with similar transfers.

At 0K, magnons can only result from spontaneous emission of a hot electron[76]. Therefore, electron-magnon scattering can only make a spin down hot electron turning into a spin up, resulting in a source of spin asymmetry in relaxation processes. For finite temperature (T≠0), thermal magnons of energy $k_B T$ can exist in the metals. Thus, spin up hot electron can now absorb some magnons to turn into spin down electrons. The emission of magnons by spin down hot electrons is still present. In the case of magnon emissions, larger energy loss can be expected ($\gg k_B T$). Hong and Mills have shown that electron-magnon interaction can be as strong for minority electron as electron-electron interaction around 1eV[77].

Electron-magnon interaction can have a strong impact on momentum relaxation. Hot electrons may reach energy states due to the large momentum exchange provided by the emission of large wave vector magnons. Therefore, spontaneous magnon emission is believed to enhance magnetocurrent as it decrease the population of ballistic minority electrons. In the case of thermal magnons with low energy and a vanishing parallel wave vector, scattered electrons can become a quasi-ballistic contribution to the collected current. However, as the electron-magnon scattering rate is much slower than electron-electron one, a low influence of this effect on hot electron transport is expected[78].

Electron-phonon interaction

A phonon is a collective excitation in an arrangement of atoms in condensed matter. Phonons are quasiparticles associated with vibration of the elastic structure formed by the interacting atoms. Phonons play a major role in both thermal and electrical conductivities, especially by their interactions with electrons of the system. In the same way as magnons, phonons can be either emitted or absorbed by electrons.

The order of magnitude for electron-phonon energy exchange is around 10meV per scattering event. Therefore, this energy transfer will not enable relaxation for scattered electrons. On the other hand, the impact on momentum is larger. Electrons suffering an electron-phonon interaction have high probability of being backscattered. As the electron-phonon interaction is spin-independent it does not influence much the magnetocurrent compared to electron-electron scattering. However, a fingerprint of electron-phonon process could be seen in the temperature-dependence of the magnetocurrent.

Electron-defect and electron-interface interactions

Improvement of growth techniques cannot get rid of the presence of defects in spintronic devices. The presence of impurities, vacancies, stacking or crystallographic quality of materials can have a huge impact on electron transport. These defects will be considered as non-magnetic (no spin) and neutral (no charge). Thus, electron-defect are elastic processes that changes the wave vector of incoming electrons but without energy transfer. They are both temperature and energy independent. The quality of deposited layers can reduce the density of those defect and so, increase the number of ballistic that can be collected.

Interfaces also contribute to elastic scattering. It cannot be tuned by changing the temperature of the system or the energy of incoming electrons. Mismatches between two layers having two different orientation will also participate to electrons deviation. A huge fraction of ballistic electrons transported through the base is attenuated by interfaces[79].

I.3 – 3. Magneto-current with colinear geometry

Tunnel current emitted from the barrier enters the spin valve by being directly injected into a first ferromagnetic layer. Figure I.18 shows the travel of incoming electrons depending both on their spin and on the spin valve configuration. For simplicity, only parallel and antiparallel configurations are taken into account.

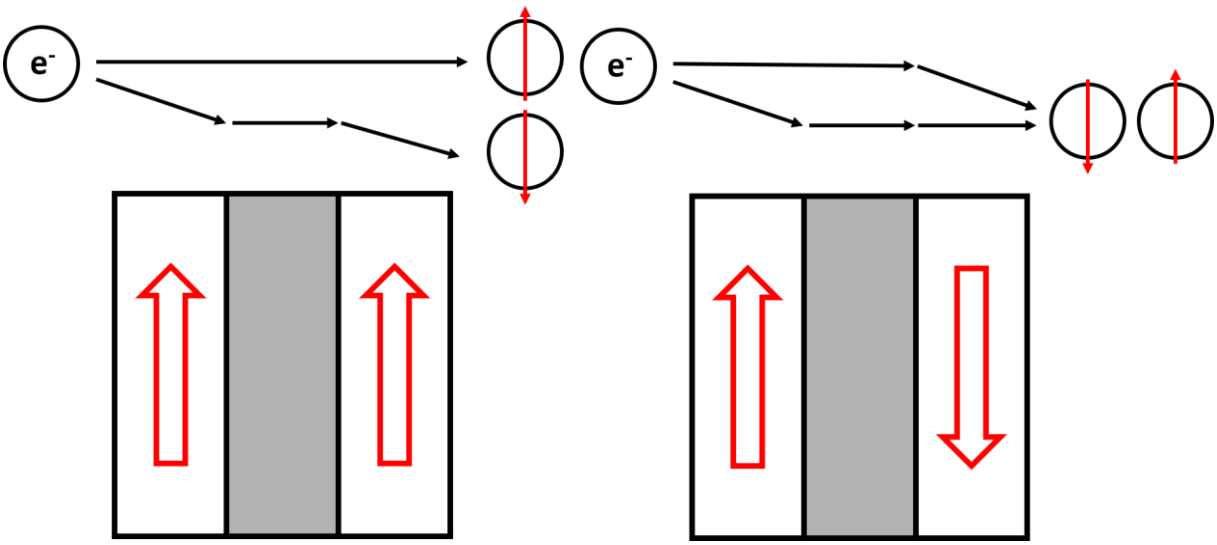

Figure I.18: Diagram of a spin valve crossed by hot electrons emitted from the tunnel barrier. On the left, P configuration scatters spin down electrons, thus giving a spin-polarized collected current at the Schottky barrier. On the left, both spin directions are affected by AP configuration, thus almost no current can be collected.

In the parallel configuration, hot electrons will cross both ferromagnets. Depending on their spin direction, they may suffer several scattering events. Therefore, scattered eletrons will relax to the Fermi sea and will not be collected. At the Schottky interface, the collected current will be mainly composed of spin up electrons. In the antiparallel configuration, both spin direction will relax, losing energy (or adequate wave vector) to cross the Schottky barrier. Therefore, a weak collected current is expected.

To characterize the efficiency of such structure, a figure of merit is given by the magnetocurrent (MC), defined as:

$$MC = \frac{I_C^P - I_C^{AP}}{I_C^{AP}} \qquad (I.33)$$

As the collected current I_{AP} in the AP configuration is very low, a huge MC is expected. Lu *et al.* have measured for a Co/Cu/NiFe structure with a Cu/MgO emitter that a MC of 2700% could be reached at low temperature[80].

Collected currents can be further modeled based on a formalism derived from classical Boltzmann equation. In a colinear geometry, spin-dependent transport can be expressed in term

of majority and minority spins. No spin-mixing is considered, meaning that the two spin channels (up and down) flow independently in the spin valve. If the incoming hot electron beam is not polarized (as much spin up electrons as spin down), then the collected current in P (resp. AP) configuration can be expressed as follows:

$$I_C^P = 0.5\ (T_M^{FM1}T_M^{FM2} + T_m^{FM1}T_m^{FM2})T^{Cu} \qquad (I.34)$$

$$I_C^{AP} = 0.5\ (T_M^{FM1}T_m^{FM2} + T_m^{FM1}T_M^{FM2})T^{Cu} \qquad (I.35)$$

with M (resp. m) label for majority (resp. minority) spins. In the previous expression, the 0.5 factor takes into account the 50/50 proportion of spin up / spin down populations in the injected current. The spacer is indicated by Cu and is supposed to be spin-independent, thus it is factored in the previous expressions.

The transmission factors have to take into account scattering coming from both interfaces and from the bulk of the ferromagnets. Exponential attenuation of ballistic electron populations is expected leading to transmission factors given by:

$$T_{M(m)}^i = \Gamma_{M(m)}^{in} \exp\left(-\frac{d_i}{\lambda_{M(m)}^i}\right)\Gamma_{M(m)}^{out} \qquad (I.36)$$

where in/out designate the ferromagnet/normal metal interface considered and i, the layer considered with a thickness d_i. $\lambda_{M(m)}$ is the hot-electron attenuation length for the majority/minority spins in the ferromagnet i. This λ represents the "average" length on which a hot electron is scattered. Therefore, each electron undergoing such event is eliminated from the collected beam. The interface factors Γ can be spin-dependent due to the mismatch in the band structure of the magnetic and non-magnetic metals.

A difference is made between mean free path and attenuation length. Mean free path is defined for a given material for a certain energy. It represents the distance between two interactions. While attenuation length also depends on the device geometry and on energy/momentum selection of the Schottky barrier, the mean free path depends only on the material considered. Therefore, measured attenuation length differs from theoretical mean free path[79].

I.3 – 3. Magneto-current with crossed geometry

Most magnetic tunnel transistors developed so far have used colinear geometries. If interesting information about hot electron transport and scattering mechanisms can be extracted from such experiments[81,82], a crossed geometry is required to measure spin precession in ferromagnets[1].

Previous equations for collected currents in the colinear configuration can be adapted to express this current but when magnetizations of the spin valve are perpendicular to each other :

$$I_C^{\perp} = 0.5\left[T_M^{FM1}\left(\frac{T_M^{FM2}}{2}+\frac{T_m^{FM2}}{2}\right) + T_m^{FM1}\left(\frac{T_M^{FM2}}{2}+\frac{T_m^{FM2}}{2}\right)\right]T^{Cu} \qquad (I.37)$$

A new magnetocurrent can be defined in this crossed configuration:

$$MC^{\perp} = \frac{I_C^P - I_C^{\perp}}{I_C^{\perp}} \qquad (I.38)$$

This perpendicular magnetocurrent can be expressed as the one in colinear configuration as follows:

$$MC^{\perp} = MC\left(\frac{I_C^{AP}}{I_C^{AP} + I_C^{P}}\right) \qquad (I.39)$$

If magnetocurrent exceeding 1000% could be obtained with a colinear configuration, it is no longer the case with crossed geometry. Calculations with previous expressions shown on Fig.I.19 proves that $MC^{\perp}$ cannot exceed 100%, no matter the current asymmetry[83].

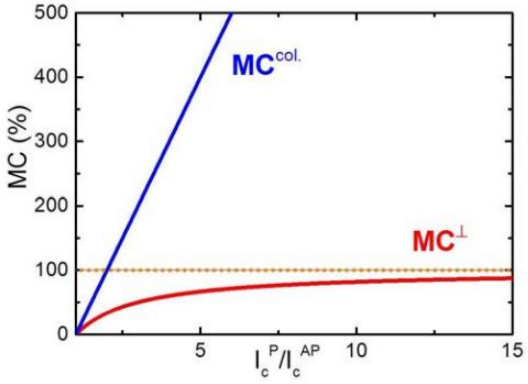

Figure I.19: Simulation of the magnetocurrent as function of I_C^P/I_C^{AP}. *The blue curve shows MC for a colinear configuration while the red one represents* $MC^{\perp}$ *for a spin valve with a crossed configuration. From Vautrin* et al.[83].

Key takeaways for Chapter I:

- **Magnetic tunnel junction allow injection of spin-polarized current of hot electrons with a narrow injection cone**
- **Schottky barrier filters incoming hot electrons both in energy and wavevector and enables collection of only ballistic electrons**
- **Several scattering mechanisms can affect the transport of hot electrons**
- **Spin valve structure is used to easily study of spin-dependent transport and/or phenomena of hot electrons by controlling magnetizations**
- **Combination of MTJ, spin valve and Schottky barrier forms our magnetic tunnel transistor used to investigate new ways of manipulating electronic spin**

Chapter II: Hot electrons transport

II. Hot electrons transport

II.1 – Introduction

The experimental study of the hot electron properties with energies several eV above the Fermi level is not an obvious task. Even the use of BEEM that can be implemented with tools available in the laboratory is difficult and faces many experimental issues : injection of spin polarized electrons, stability of the tunnel junction, etc. An interesting alternative to BEEM is the use of a magnetic tunnel transistor (MTT). In the framework of my PhD the devices conceived for the precession at Institut Jean Lamour to study spin precession[1] are appropriate candidates to explore the physics of spin-polarized hot electrons. So far, experimental results for our samples had only been considered under the scope of electronic spin precession[1]. However, the dependence of the Transfer Ratio (TR) on several parameters (materials, energy, temperature,…) gives insights on electron spin-polarized transport. In the 2000s, few groups have used such structures to investigate spin-dependent charge carriers transport[82,84–89]. Given that our MTT enable spin-polarized hot electron injection into complex spin-valves, unusual transport effects can be expected.

In our case, we used samples used for inducing spin precession that have been statured under applied field to be in the full parallel configuration and the stack multilayer is the following:

Pt(5)/IrMn(7.5)/Co(2)/Ta(0.5)/CoFeB(2)/MgO(2.5)/CoFeB(y)/Cu(3.5)/[Ni(0.6)/Co(0.2)]x5/Ni(0.6)/Cu(5)/Ta(1)/Cu(5)//Si(100)

where numbers in brackets indicate the layer thicknesses in nm. In order to only collect hot ballistic electrons, a Cu/Si Schottky barrier is built up by an chemical treatment called hydrofluoric acid (HF) cleaning of the Si substrate before entering the substrate in the Physical Vapor Deposition (PVD) machine and Cu deposition in Ultra High Vacuum (UHV) conditions. Measurements have been performed on two different CoFeB thicknesses y: 1nm and 4nm. High magnetic field (1T) was applied to saturate magnetizations in plane[90] and have a parallel configuration (Fig.II.1.d).

Figure II.1 a) and b) shows measured currents both at the tunnel junction (I_{tun}) and the Schottky barrier (I_c). In both cases, the considered current shows a monotonic increase with injection voltage (V_{inj}). For tunneling current, this increase can be understood based on Figure I.7. While for low bias ($<U_0 \sim 0.5eV$)[91], electrons tunnel through the whole barrier, giving a non-linear energy dependence of the current. Figure II.1.a) shows almost similar tunneling current for the two stacks studied. Therefore, similar injection can be assumed, independently of the CoFeB thickness deposited. The difference of maximum voltage between both experiments is due to the breakdown voltage of the MgO barrier. Samples have been pushed to their limits to explore hot electron physics. For such high voltages compared to the barrier height, breakdown can happen at any time with probabilities increasing with injection energy.

Unlike $I_{tun}(V_{inj})$, hot electron current characteristics show a huge difference depending on the CoFeB thickness. For an applied voltage of -2V, the collected current is twenty times higher in the case of 1nm CoFeB layer compared to that of 4nm. Such difference can be either explained by increased scattering while crossing the spin valve or by change in the Schottky barrier from one device to the other. The latter hypothesis is unlikely to take place as both the height ($\sim 0.65eV$) and the 5/2 power law energy dependence is the same for the two samples.

Therefore, difference of I_c can be attributed to enhanced scattering with increasing thickness of CoFeB.

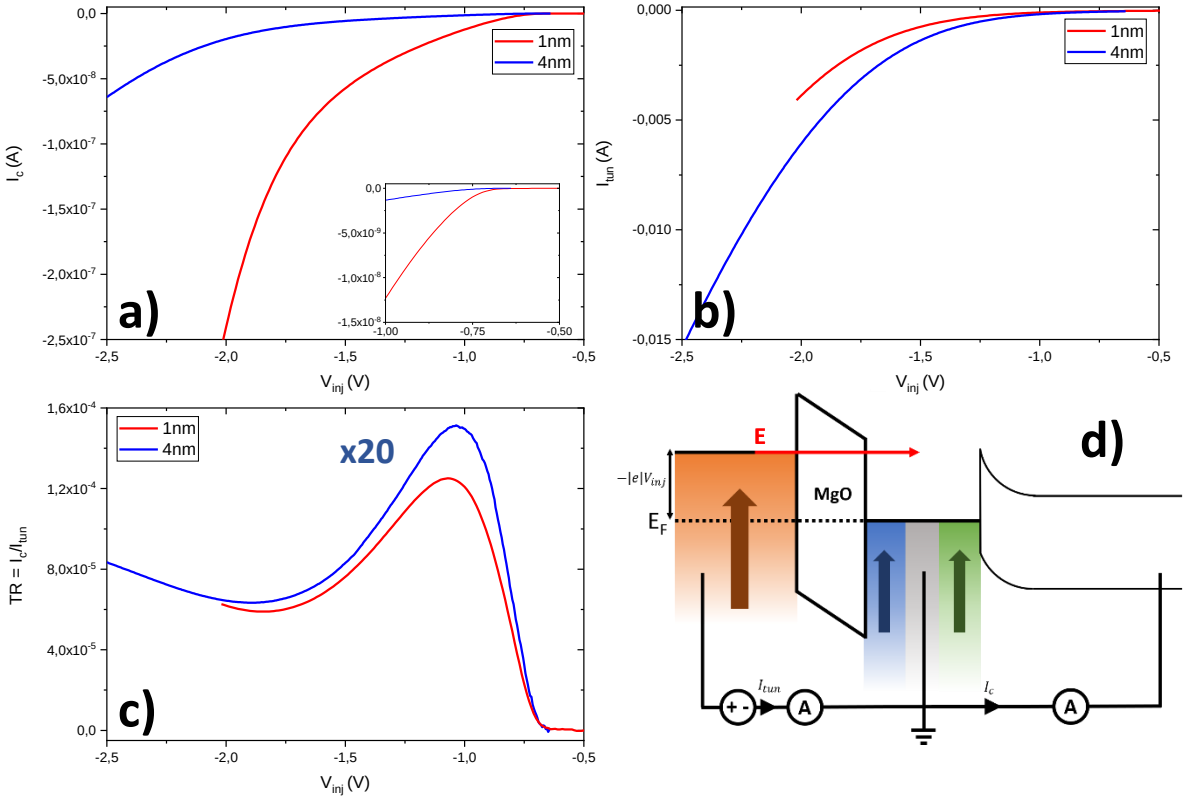

Figure II.1: a) Collected and b) tunneling currents of two MTT with different CoFeB thickness. c) The ratio between both measurements gives the transfer ratio. d) Magnetic configuration of the saturated MTT.

Figure II.1.c) shows the transfer ratio ($TR = \frac{I_c}{I_{tun}}$) as the function on injection voltage. The twenty multiplying factors previously mentioned for the collected current is also found for transfer ratios. The non-monotonic behavior for this transport measurement demonstrates the presence of competing effects that overcome each other during voltage increase. Literature concerning hot electrons transport in such devices (BEEM, SVT, MTT) gives information on how scattering with different particles (see section I.2-3) can translate into hot electrons spectroscopy specific features.

Indeed, first measurements using a BEEM structure (injection with a STM tip) was performed by Kaiser and Bell[62]. Figure II.2 shows the I_c-V_{inj} spectrum for a Au/n-Si(100) sample. Associated I_c corresponds to our TR as the tunneling current is kept constant in the case of BEEM. No specific feature can be observed after overcoming the Schottky barrier height ($\sim 0.82V$) on Figure II.2.b). Theoretical predictions (dashed and solid lines) well describe experimental data over the range of energy explored. In this study, Kaiser & Bell only deposited 10nm of Au on top of a semiconductor to form a Schottky barrier height. This thickness remains below the mean free path for electrons in these materials (few tens of nanometers). Therefore, this measurement can be considered as a scattering-less spectrum of hot electrons.

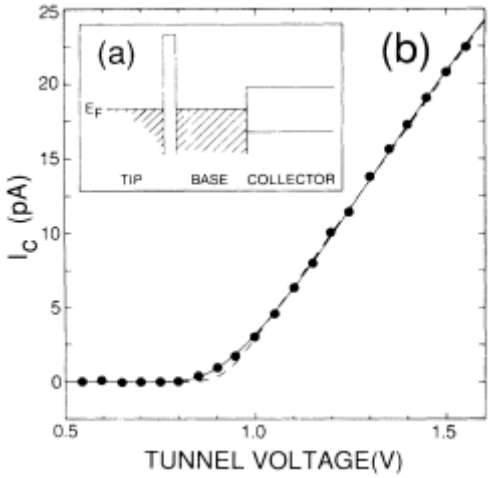

Figure II.2: a) Energy-band diagram of a three-terminal BEEM measurement configuration. b) BEEM Ic-V_{inj} spectrum for a Au/n-Si(100) structure. Dashed and solid lines correspond to theorical models fitting experimental data. From Kaiser and Bell[62].

Few years after, studies[57] have explored hot electrons transport based on BEEM structure with various metal/semiconductor interfaces. Figure II.3. shows I_c-V_{inj} measurements performed using n-GaP(110) as a collector. For most materials and the thicknesses deposited, the collected current increases slower than theoretical model at high injection voltage. This can be understood if scattering of hot electrons becomes stronger than the initial predicted of the model. Therefore, the latter deviates from experimental data. However, for ultrathin Ni/n-GaP(110) both curves match perfectly. This could be interpreted as a mean free path much higher than the film thickness, resulting in a similar trend as the study of Kaiser and Bell on Au/n-Si(100).

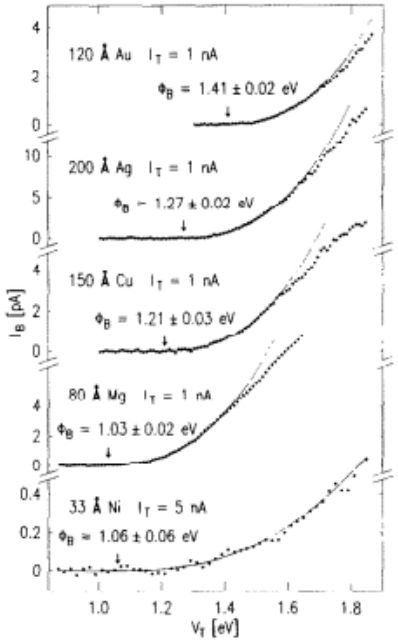

Figure II.3: BEEM spectra for several metal/n-GaP(110) structures with constant tunneling current. Collected currents are plotted as a function on injection voltage. For some samples, theoretical model (dashed) fail to reproduce experimental data (dots). From Prietsch and Ludeke[57].

Later, BEEM measurements have been performed at even higher voltages up to 5eV[92]. Figure II.4 shows experimental BEEM spectrum using n-GaP(110) semiconductor. Injection energies are as high as 5eV which enable careful observation of features related to hot electrons transport. Above 2-3eV, higher than previously mentioned studies, TR (here, relative BEEM current) stagnates for all studied samples and even decreases for 5nm-thick Mg/n-GaP(110) stack. In the case of Au(12Å) and Mg(12Å), the TR rises again after increasing energy of injected electrons.

To account variations of the TR, Monte Carlo simulations were based on a four-step model: tunneling from tip to metal, transport through the base, transmission at the Schottky interface and impact ionization in the semiconductor. To interpret energy features of the spectra, Bauer *et al.* highlighted the importance of electron-electron interactions by including energy-dependent inelastic mean free path. In the case of electrons with high enough energy, possible electron-hole pair creation by impact ionization was also considered to contribute to TR. The Monte-Carlo model was able to reproduce the main spectral features of the measurement. On figure II.4, energy-dependent inelastic mean free path results in a decrease of the contribution of ballistic electrons for high energies. Secondary electrons generated by electron-electron generation then compensate the loss of those primary electrons. Such results have also been reported by Cuberes *et al.* for Au/Si(111) at high voltages[93]. Therefore, these features are supposed to be independent on the semiconducting material used for collection.

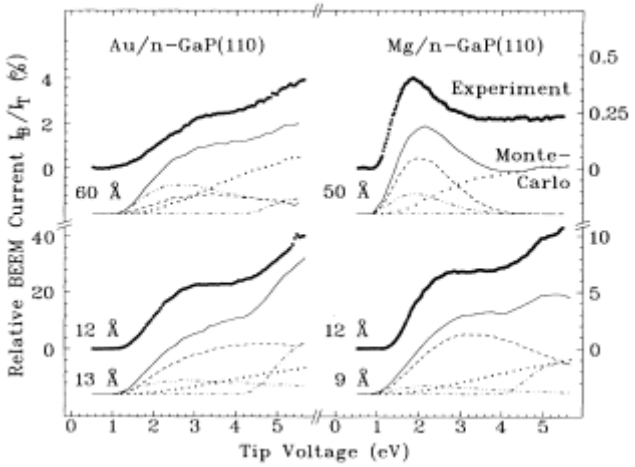

Figure II.4: BEEM spectra and results of Monte Carlo simulation (solid curves) for various film thicknesses of Mg and Au on n-GaP(110). Theoretical curves are decomposed into ballistic, elastically or inelastically scattered electrons and electrons generated by impact ionization. From Bauer et al.[92].

The spectrum of Mg/n-GaP(110) on figure II.4 for BEEM experiment is similar to that of our MTT samples with a complex stack structure (see Fig.II.1.c)). Therefore, the specific features of our measurements could be attributed to inelastic interactions. Results presented both on figure II.3 and figure II.4 demonstrate that the spectra obtained through energy spectroscopy of the devices are dependent on the material studied and the thickness. Adding additional layers with various elements, crystallographic directions could deeply modify the transport of electrons towards the Schottky barrier. Furthermore spin-dependent effects could also account for some hidden characteristics of our measurement.

Several groups have studied spin-dependent transport of hot electrons either by injecting a non-polarized hot electrons current into a spin-valve with a MTT (see Fig.II.5 – a) or a BEEM structure (see Fig.II.5 – b). Metallic structure investigated in both cases are multilayers of transition-metal alloys and noble metals (Cu, Au), similar to our own stacks. The same energy range is also explored with applied voltage up to 2-2.5V to inject hot electrons into the base. The main difference between all studies is the choice for the collector material. Indeed, while a n-Si(100) was used in our device, Van Dijken *et al.* used a n-GaAs collector and Heindl *et al.* deposited the layers on top of a n-GaAsP substrate[74,94].

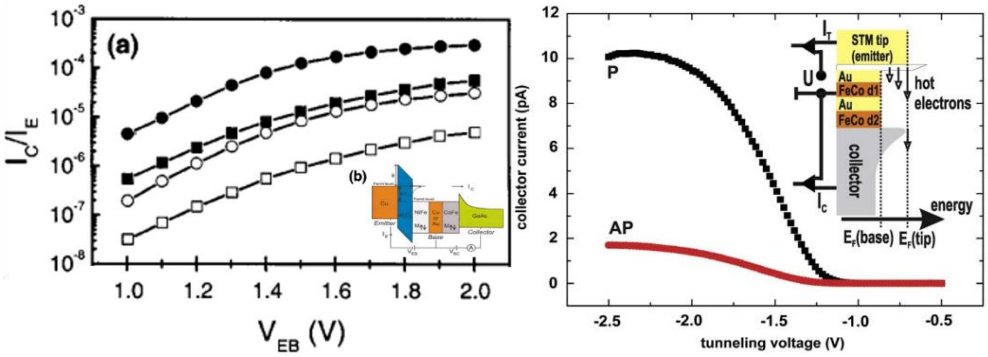

Figure II.5: a) Transfer ratio of a MTT with a NiFe/Cu(circles)-Au(squares)/CoFe spin-valve for parallel (solid symbols) and antiparallel (open symbols) configuration. b) Collected current spectra in parallel (P) and antiparallel (AP) configurations for Au/FeCo/Au/FeCo structure for a constant tunneling current. Insets show structure associated to each measured devices. From Van Dijken et al.[94] *and Heindl* et al.[74].

Above the Schottky barrier, electrons start getting collected in the semiconductor. The collected current (or $TR = \frac{I_c}{I_{tun}}$) is increasing with higher applied voltage. However past a given energy, this increase slows down and collected current even decreases in the case of figure II.5.b), giving a typical bell-shaped curve. Therefore, experimental data once again deviate from the theoretical $\frac{5}{2}$ power law introduced earlier (Eq. I.27). The mechanism associated with this deviation are supposed to be electron-electron inelastic interactions.

Prietsch tried to give a qualitative description of electron-electron interactions impact on the hot electrons transport[59]. Figure II.6 shows hypothetical BEEM spectra obtained in three different current a) low, b) intermediate and c) high coverages, depending on the inelastic scattering intensity. This coverage corresponds to the inelastic scattering compared to several parameter: the metallic base length, elastic mean free path, inelastic mean free path. High coverage corresponds to the situation where inelastic mean free path is shorter to the two others. In such case, much hot electrons go under electron-electron collisions generating secondary electrons. Therefore, inelastic contribution will be dominant at high voltage compared to primary electrons or elastically scattered ones.

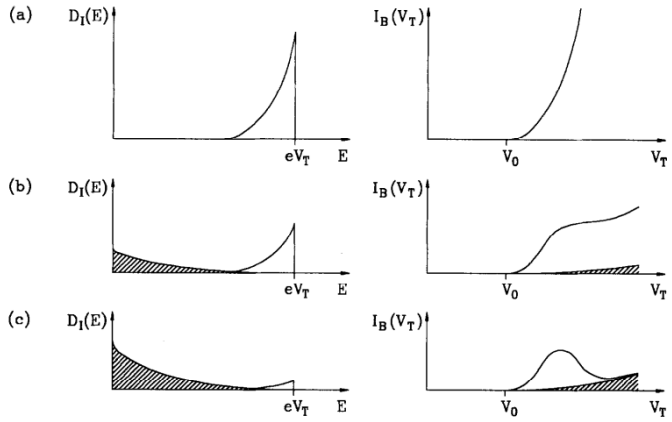

Figure II.6: Schematic plot of the energy distribution of the electrons in the metal film at the interface (left) and corresponding collected current for BEEM measurement (right). a) At extremely low coverages, where inelastic scattering is negligible, measured current follow the theoretical 5/2 power law. b) at intermediate and c) high coverages where inelastic scattering is strong, the current bends with increasing voltage. The contribution of secondary electrons resulting from inelastic scattering, is indicated by hatched areas. From Prietsch[59].

Only one study[88] using MTT presents Transfer ratios like that of our structure, with this bell-like shape followed by an increase of TR for higher voltages (see Fig. II.7). In this paper, TR (noted as α) is exclusively associated with ballistic primary electrons. Therefore, the signal is theoretically descripted with a simple exponential attenuation with the base thickness. Attenuation length (λ) is plotted for a given injection voltage of 1.5V, thus no discussion about its dependence on energy was proposed. The bump in the TR is considered as an anomaly due to Interfacial Resonant States at the Fe/semiconductor for all three materials used as substrate.

Still, explanation based on secondary electrons collection generated by electron/electron collisions was not discussed. Considering a short inelastic mean free path for Fe(100) around 1-2eV, such shape could be explained as described in figure .II.6. The shift of the bump obtained by changing the collector materials would result by the difference of Schottky barrier height. When ϕ_{sch} is increased, the energy required for ballistic electrons to overcome the barrier is higher as well as for the inelastically scattered ones. Thus, inelastic contribution to the TR is also expected to be shifted, resulting in a change in the bump position.

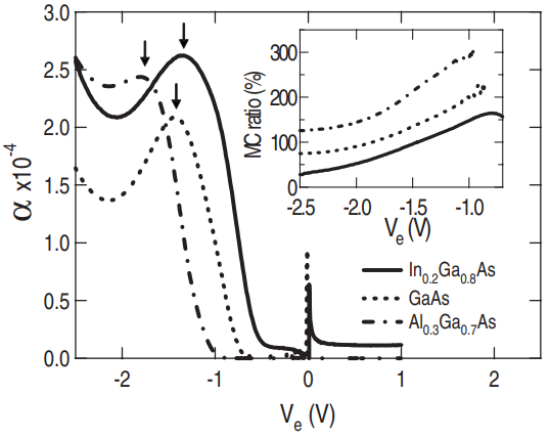

Figure II.7: Transfer ratio (a) for various MTT a based on a Fe/MgO/Fe(100) on different collector materials. Inset is the plots of MC as a function of injection voltage. From Nagahama et al.[88].

Resonant effects are unlikely to explain our bell-like shape results. First, Interface Resonant States created at the Fe/semiconductor interface do not exist in our structure. Nagahama *et al.* grew their sample by molecular-beam epitaxy which enable deposition quality leading to such effect. On the contrary, our stacks were deposited by magnetron sputtering. Even though, deposition conditions and annealing temperature were optimized to preserve the Schottky barrier interface, conditions are not that of an epitaxial growth.

Furthermore, bulk resonant states cannot take place in our system considering the total length of the metallic base with several interfaces to be crossed. In our study, Schottky barrier nature is always kept the same (Cu/Si(100) interface) and only the active layer material below the tunnel barrier is changed. Over all samples we measured (and also from the literature shown here) at high voltages, only CoFeB leads to such voltage dependent feature. This might be due to low mean free path of this material in comparison to the deposited thicknesses in the experiments shown here. Thus, we believe this specific material to have properties that gives bumps in the transfer ratio around -1.2V with an increase at even higher voltages.

Results of Nagahama *et al.* could also be explained in term of electron/electron scattering. If the local maxima in the transfer ratio arises from a competition between thermalized electrons from the primary beam and collection of secondary electrons, then changing the Schottky barrier does not affect the physics inside the base but rather the height allowing secondary electrons to be collected. A higher Schottky barrier height then leads to a shift of the local maxima towards higher voltages which can be seen on figure II.7.

All studies concerning hot electrons transport in metallic bases tend to show that electron-electron interactions are often not considered in models and that a simple power law energy-dependence is usually taken without further details. Yet, they have a direct impact on underlying processes that enable collection of hot electrons, or symmetrically, generation of scattered electrons. With this work, theoretical grounds concerning description of electron-electron interactions are proposed. Then, these concepts are integrated into a model aiming at explaining experimental measurement of figure II.1 in order to confirm/invalidate previously made assumptions. Further approaches are proposed to predict impact of elastic spin-flip in our hot electron measurement. Lastly, transport measurements based on a planar MTT structure are proposed to study the spin-dependence underlying mechanism with a single electron-electron collision.

II.2 – Low-energy hot electrons transport

II.2 – 1. Electron/electron interaction

Fermi Liquid theory

Studies concerning electron transport in metals have been extensively carried out in the 50s[95–97]. Different materials were investigated by fast electron beam (several tens of eV) and outcoming electrons escaping from the surface were used to understand processes happening in the metal. High energy of injected electrons led to intense inelastic scattering of the hot electrons. This gave a framework to model scattering of primary electrons injected with electrons from the free-electron gas, thus generating secondary electrons. However, due to the high energy of the injected beam, this theoretical work cannot be applied to explain low energy electron/electron interactions. This is especially true concerning momentum repartition

between the two electrons during a collision. In the high energy case, low energy transfer due to the strong asymmetry in energy leads to small deviations of the incoming hot electrons[96].

Unlike the high energy range, exclusion principle applies strongly in the case of electron/electron scattering at low energies. For low energy hot electrons going under an electron-electron interaction, the scattering process is spherically symmetric with half its energy transferred after each collision[97]. Quinn made explicit calculation of the energy-dependence of mean free path of electrons[98]. He considered the mechanism of hot electrons interacting with conduction electrons for energies below that of plasma excitations. Thus, based on electron/electron interactions model and exclusion principle for energies close to the Fermi level he gave a variation of the mean free path as the inverse square of the excitation energy.

While for low energies the two secondary electrons generated by an electron-electron interaction share by half the total energy of the primary electron due to exclusion principle making it impossible for scattered electrons to fall within the Fermi sphere, increasing energies make screening more and more important[97]. Incoming hot electrons will keep more energy after a scattering event, thus moving from a ½ energy repartition coefficient to a higher one. The spread in energy is also expected to increase as the repartition deviates from a 50/50 behavior.

Experimental observations of e^-/e^- interaction

Shortly after Quinn's model for the mean-free path of hot electrons due to electron-electron interactions, studies have investigated these effects on attenuation lengths of several materials[99,100]. A qualitative agreement between Quinn's theory and measured attenuation lengths could be found, thus tending to prove the importance of electron-electron interactions to explain energy-dependence of the mean free paths. However, discrepancies with expected values from the theory make difficult to draw conclusions. Sze *et al.* showed the importance of decorrelating the different mean-free paths contributing to experimental attenuation length[101]. In the case of purely ballistic electrons, energy-dependence of the attenuation length matches perfectly that of the electron-electron mean free path.

Yet, Quinn's result failed to fully describes experimental measurements on Cu. This triggered intensive work using time-resolved two-photon photoemission (TR-2PPE) on this material to understand the energy-dependence of hot electrons lifetime. Several studies[102–104] pointed out the importance of the d-band in electron-electron scattering. These strongly localized orbitals were not considered in initial model developed by Quinn. Therefore, they influence scattering twofold. First, d-band electrons contribute to an additional screening effect that modifies interaction between electrons. Thus, calculations taking into account the band structure of Cu fit better experimental lifetimes of hot electrons. Then, the presence of d-band buried below the Fermi level can also lead to additional scattering mechanisms when it becomes accessible. Additional features observed through TR-2PPE experiments are also supported by theoretical calculations[73].

Lastly, spin-dependence of the electron-electron interaction was not considered in initial theories. Scattering rates of spin-up and spin-down are assumed to be the same. However, even if exchange interaction is weaker than Colombian interaction, it should still lead to a spin-asymmetry in the scattering. Penn concluded that exchange interaction can compensate partially electron-electron interactions at low energies[105], thus leading to longer mean-free path for spin-up electrons compared to that of spin-down. Spin-resolved TR-2PPE measurements were

performed by Aeschlimann *et al.* on fcc Co[106]. While theory qualitatively describes the energy-dependence of the lifetime in Co, further analyze of its spin-dependence appears to be complex. Spin-asymmetry seems to be weak at low excitations but increases with increasing energies. Description of hot electrons inelastic scattering lies somewhere between Quinn's and Penn's theoretical works. Further details on the spin-resolved band structure of the material are required to give a better description of hot electron transport.

Integration of band structure effects

Model for electron/electron interaction proposed by Quinn[98] is based on the free-electron model. No band structure effects are included. However, the presence of some features can have a significant effect on the mean free path. Experimental results[99] for Cu led to deviations from Quinn's prediction. Screening contribution of the d-band electrons affect hot electrons and modify inelastic mean free path. Thus, some corrections should be brought to distinguish interactions between each band of transition-metals typical band structure.

Furthermore, anisotropy of the material band structure also leads to anisotropic electron-electron scattering. In the case of Cu, distortion of the Fermi surface from a spherical one results in higher rate of scattering in the high-density "neck" of the Fermi surface[107,108]. Symmetrically, low-density regions or gap in the band structure will lead to reduced electron-electron scattering in specific directions and/or energies that can be correlated with features in energy-dependent lifetime of materials[109]. However, expression of the mean-free path which reproduces screening from the band structure on the electron-electron interactions can be implemented with first-principles calculations[110].

II.2 – 2. Model for hot electrons transport at low energies

Hot electrons measurements can be explained using first-principles description of electronic transport in several materials[70,110,111]. Different features concerning band structure effects of metals can be modeled and included *ex post* in transport equation. However, this does not give a full description of transport. Despite the first model proposed by Bell and Kaiser[61] succeeds to explain experimental energy-dependence of BEEM hot electrons current, its simplicity makes it difficult to draw conclusions concerning more complex systems. In order to go further, several groups have used Monte-Carlo (MC) simulations[65,92,112] to describe ballistic hot electron transport. Here, we drew inspiration from MC-based works to develop a more traditional method using approximation of integrals and/or experimental measurements. Three main steps are distinguished and are treated independently: injection of electrons, transport into the base and collection at the Schottky barrier.

Injection

In a first step, hot electrons are extracted from the tunnel barrier into the base. This generates an electronic distribution peaked around $|e|V_{inj} - E_F$ at the base entrance (e is the elementary charge, V_{inj} the voltage applied to the tunnel barrier and E_F the Fermi level (see Fig. I.1). Injected electron beam is considered as mono-kinetic due to the narrow energy distribution of injected electrons[113]. Moreover, wave vector **k** is taken perpendicular to the interfaces considering that a sufficiently thick tunnel barrier filters non-perpendicular wave vectors. The measured tunneling current $I_{tun}(V_{inj})$ is used to evaluate the transfer ratio $\left(TR = \frac{I_c}{I_{tun}}\right)$.

Previously made hypothesis about electrons participating to the current are used to simplify expressions and/or to solve integrals in the rest of the model.

Transport in the base

In a second step, charge carriers transported through the base are described within the free-electron approximation, with the mean free path depending linearly on the lifetime of electrons. With metallic layer thicknesses smaller or of the same order of magnitude as attenuation lengths, scattering can be described using exponential decay of the ballistic electron population while traveling along the base. Matthiessen's rule provides an expression for the attenuation length considering all the different scattering processes involved (see section I.2 – 3):

$$\frac{1}{\lambda} = \frac{1}{\lambda_e(E)} + \frac{1}{\lambda_{ph}(T)} + \frac{1}{\lambda_{mag}(T, \boldsymbol{S})} + \frac{1}{\lambda_{def}}. \qquad (II.1)$$

where λ stands for the attenuation length in the material and λ_i are respectively the electron-electron, electron-phonon, electron-magnon and electron-defect attenuation lengths.

Among all scattering processes listed in equation II.1, only electron-electron interaction is strongly inelastic. Others are not energy-dependent nor result in significant energy loss for the hot electrons, but it rather leads to a momentum transfer. Electrons deviated from their initial trajectory are ejected out the Schottky diode acceptance cone[114]. Unlike other elastic effects, electron/magnon interaction affect the spin of the charge carriers, **S** (see section I.2 – 3. **Electron-magnon interactions**). As the temperature-dependence of electron-phonon and electron-magnon interactions is much stronger than that of electron-electron one, we can assume λ_e to be independent on T. electron-electron mean free path is then only affected by injection energy E.

The frame of the Fermi-liquid theory offers a description of single excited electrons interacting with conduction electrons from the Fermi sea (see section II.1 – 1). Electron-electron scattering will be modeled by a simple expression of the mean free path corrected by previous studies made on transition and noble metals whose d-band make contribute to the electronic decay[71]. Thus, from Fermi-liquid theory and assuming a free-electron behavior, energy-dependence of the inelastic mean free path can be described as:

$$\lambda_e(E) = \lambda_0 \frac{\sqrt{E}}{(E - E_F)^2 + \varrho(E - E_F - \omega^{\uparrow})^2} \qquad (II.2)$$

where λ_0 stands for a characteristic value of the electron-electron interaction. E is the electron energy, E_F the Fermi level, ϱ a unitless coefficient related to the d-band density and, $\omega^{\uparrow}$ the energy shift between the upper part of the spin-up d-band and the Fermi level.

As it was previously stated, for low enough injection energies only ballistic electrons can be collected. Thus, a single scattering event prevents a hot electron from entering the semiconductor. This means that a low energy range, attenuation length given by equation II.1 matches the mean-free path of the material. This justifies the use of equation II.2 to calculate energy-dependence of λ for each material. If scattered electrons generated after an elastic or an inelastic event is being collected, attenuation length describing the exponential decay and physical mean-free path will no longer match. In this study, we tend to show the possibility of

describing the transport of secondary electrons from electron/electron interaction with expression of the mean-free path of equation II.2 for an energy roughly divided by two.

Collection of ballistic electrons

In the last step of this model, electrons overcoming the Schottky barrier height are collected in the semiconductor conduction band. Previous studies on BEEM showed that collected current scales with a 5/2 power law of the injection energy (see equation I.34 in section I.3 – 2. **Angular distribution**). As the Schottky barrier height and the energy of injected electrons are low (few eVs), both impact ionization in the semiconductor and backscattering phenomena due to optical phonons at the Schottky interface are not considered in this model[115].

General expression of TR for the low energy range

From all previous hypotheses made for each step of the hot electrons transport, the TR can be written as:

$$TR(T, V_{inj}) = \frac{\left(|e|V_{inj} - \phi_{Sch}(T)\right)^{\frac{5}{2}}}{I_{tun}(V_{inj})} . T_{el}(T) . T_{inel}(V_{inj}) \qquad (II.3)$$

where $\phi_{Sch}(T)$ is the Schottky barrier height. $T_{el}(T) = T_0 . \Gamma^n . e^{-d_{base} \cdot \left(\frac{1}{\lambda_{ph}} + \frac{1}{\lambda_{mag}}\right)}$ stands for all the elastic processes with phonon and magnon attenuation lengths taken as effective values for the whole base stack. T_0 is a constant that considers the scattering induced by defect, Γ is a scattering coefficient accounting for the n interfaces present between each layer of the base, d_i represents the thickness of the individual layer indexed *i* and $d_{base} = \sum d_i$ is the total thickness of the base. $T_{el}(T)$ strongly depends on temperature but not on the electron energy (see Eq. II.1). $T_{inel}(V_{inj}) = \prod e^{-\frac{d_i}{\lambda_e^i}}$ accounts for all the inelastic electron-electron interactions which depend on the electron energy but not on the temperature (see Eq. II.1), for all layers of the base.

II.2 – 3. Parameters for the model

Copper

Extensive work has been done using time-resolved 2 photons photoemission (TR-2PPE) to understand transport of hot electrons in Cu experimentally[102–104,116]. These results have also been supported with theoretically considerations[109,117,118]. Some experimental studies show a deviation from the Fermi-liquid theory with higher measured lifetime at low excitation. Nevertheless, experiments performed by Hertel *et al.* found an energy-dependence scaling that of the Fermi-liquid theory[119]. Cascade processes could contribute to TR-2PPE signal and cause this increase of bump in the measured lifetime of hot electrons.

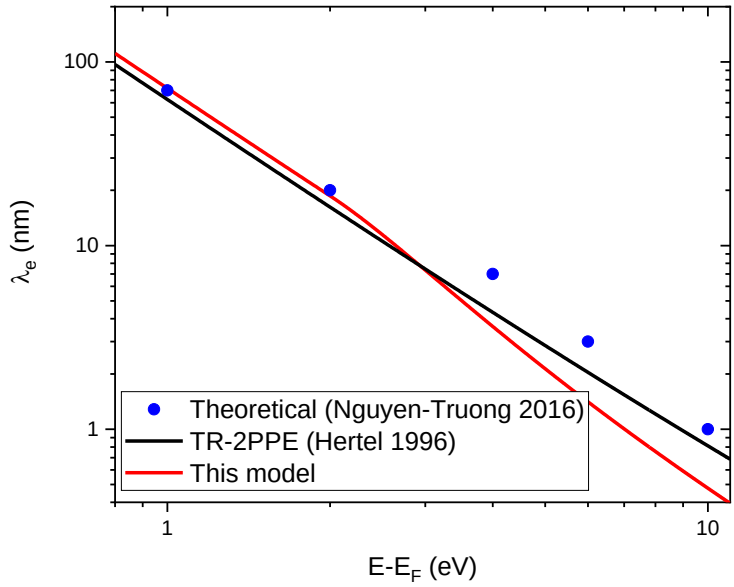

Figure II.8: Electron inelastic mean free path for copper. Solid black line corresponds to Fermi-liquid theory based fit of TR-2PPE measurements from Hertel et al.[119] *and blue dots represent values calculated by Nguyen-Truong using a dielectric approch*[118]*. Our model in red solid line correspond to equation II.2 with* $\lambda_0 = 20nm.eV^{3/2}$ and with $\rho = 1.5$ and $\omega^{\uparrow} = 2eV$ given by réf.[71].

Inelastic mean free path can be expressed based on equation II.2. Values for the parameters ρ and $\omega^{\uparrow}$ can be found in the literature[71], 1.5 and 2eV respectively. In order to find a proper value for λ_0 in copper, expression II.2 is compared to results from other studies. Figure II.8 shows inelastic mean free path from a fit of TR-2PPE experiments (solid black line)[119] and calculated values (blue dots)[118]. Our model with $\lambda_0 = 20nm.eV^{3/2}$ is plotted with a red solid line. This model seems to be consistent with other studies until 4eV. Contribution from the d-band in copper seems to be overestimated, leading to a faster decrease of λ_e at higher energies. As this study does not tackle this energy range, our model will include equation II.2 with a value of $20nm.eV^{3/2}$ for λ_0.

CoFeB

Hot electrons transport in CoFe samples has been studied from the angle of spin-asymmetry of the relaxation processes. As mentioned earlier in this section, exchange interaction between parallel spins may affect the resulting description of the transport through longer inelastic mean free path compared to theoretical ones. The presence of the d-band also results in screening of incoming hot electrons. Van Dijken *et al.*[84] investigated spin-dependent transport of hot electrons in a MTT. By sending a spin-polarized hot electrons current in a $Co_{84}Fe_{16}$ base, they could see asymmetry of the current collected at GaAs-based Schottky barrier depending on the relative configuration of electrodes magnetizations.

The shift of the majority d-band below the Fermi level is obtained through *ab initio* calculation. From DOS plotted on figure II.9, $\omega^{\uparrow} = 0.5eV$. The value for ρ taken for CoFeB is 0.28. This corresponds to that of Co given by Zarate *et al.*[71]. We will suppose this value to remain the same for all transition metal. Comparison of our model with equation II.2 with other studies is made to get λ_0 for CoFeB. Figure II.10 shows attenuation lengths data from Van Dijken experiments (orange dots)[84] and calculated values with *ab initio* method (green dots)[120] and dielectric constant approximation (blue dots)[121]. Our model with $\lambda_0 = 3.5nm.eV^{3/2}$ is

plotted with a red solid line. The description of the electron-electron means free path is rather good. Discrepancies between this model and Van Dijken experiments can be explained by other source of hot electrons scattering. Thus, energy-dependence of their attenuation lengths differs from that of the mean-free path.

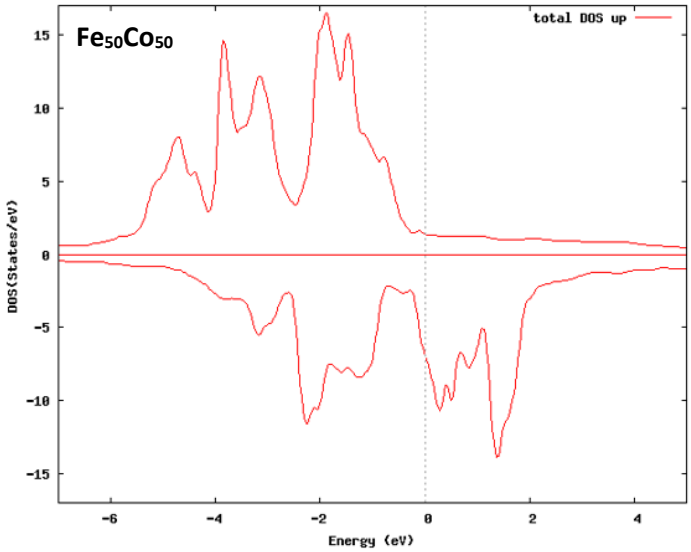

Figure II.9: Spin-resolved density of state for CoFe.

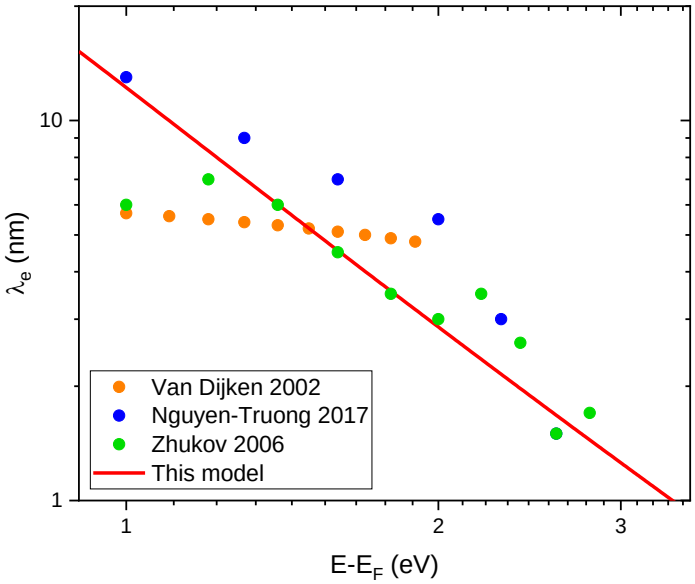

Figure II.10: Electron inelastic mean free path for CoFe. Orange dots correspond to MTT measurements of Van Dijken et al.[84]*, blue dots represent values calculated by Nguyen-Truong using a dielectric approch*[121] *and green dots* ab initio *calculations by Zhukov* et al.[120]*. Our model in red solid line correspond to equation II.2 with* $\lambda_0 = 3.5nm.eV^{3/2}$ *and with* $\rho = 0.28$ *given by réf.*[71]*.* $\omega^{\uparrow} = 0.7eV$ *is estimated from ab initio calculations of the DOS for CoFe.*

[Co/Ni]

No studies of hot electrons transport in [Co/Ni] multilayers or CoNi alloys could be found in the literature. Therefore, we decided to base our model with results from Ni films and NiFe alloys. DOS of fcc-Ni is obtained by *ab initio* calculation. The d-band of majority spins

lies about 0.5eV below the Fermi level (see Fig. II.11). It should be noted that the largest contribution to the d-band lies much deeper in the band structure of the material.

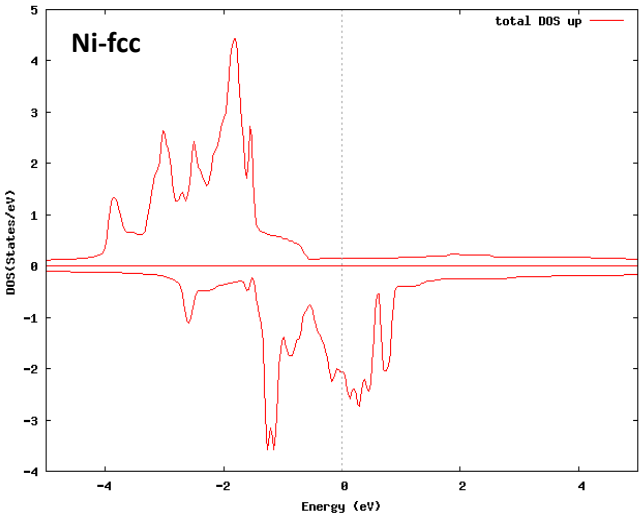

Figure II.11: Spin-resolved density of state for fcc Ni.

Concerning the electron-electron mean free path, we compared the model of equation II.2 with the same references as for CoFeB. Indeed, Van Dijken *et al.* studied spin-dependent hot electrons transport in $Ni_{81}Fe_{19}$-based MTT[84]. Associated attenuation lengths are reported on figure II.12 (orange dots). Calculations from Zhukov *et al.* (green dots)[120] and Nguyen-Truong (blue dots)[118] are also added on the figure. Solid red line describes our model with $\lambda_0 = 5nm.eV^{3/2}$. The studies reported in the literature seem to suggest a flatter variation of the electron-electron mean-free path with energies. This might be due to difference of the velocity energy-dependence that deviates from the one in square-root of the energy predicted by free-electron model.

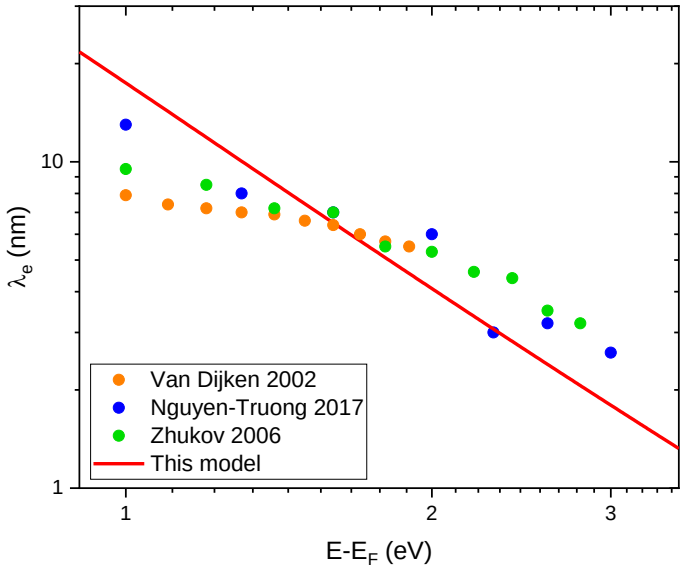

Figure II.12: Electron inelastic mean free path for Ni. Orange dots correspond to MTT measurements of Van Dijken et al.*[84], blue dots represent values calculated by Nguyen-Truong using a dielectric approch[118] and green dots* ab initio *calculations by Zhukov* et al.*[120]. Our model in red solid line correspond to equation II.2 with* $\lambda_0 = 5nm.eV^{3/2}$ *and with* $\rho = 0.28$ *given by réf.[71].* $\omega^{\uparrow} = 0.5eV$ *is estimated from ab initio calculations of the DOS for Ni.*

II.2 – 4. Fits of experimental measurements

Model to compute the transfer ratio was applied to reproduce experimental measurements performed on our MTT in the magnetic saturated state (see Fig. II.1.d) as a function of the temperature. Figure II.13.a) shows comparison between data for temperature ranging from 30K to 230K and fits following our model given by equation II.3. Measured curves show the same trend no matter the temperature: after overcoming the Schottky barrier height around 0.6eV, TR increases monotonously over the whole range of energy explored. After passing an inflexion point around 0.72eV, TR increase starts to slow down, and the signal tends to take a bell-like shape.

Solid lines on figure II.13.a) describe fits associated to each measurement. As energy-dependence of TR is explicit in our model given by equation II.3, only temperature-dependent Schottky barrier height $\phi_{Sch}(T)$ and elastic transmission coefficient $T_{el}(T)$ are free parameters. Concerning figure II.13.a), our model gives a rather good description of energy-dependence of TR for all the temperature studied.

Fitted parameters associated are reported on figures II.13.b) and II.13.c). The Schottky barrier height on figure II.13.b) reaches almost 0.6eV, in agreement with similar results in the literature[122] slightly decreases with increasing temperature (about 4%). A linear behavior can be found from 90K to 230K, as described by the solid red line on figure II.13.b). The slope associated with this linear fit of $\phi_{Sch}(T)$ is -165µeV/K. This value is similar to what was reported in previous studies of Cu/Si Schottky barrier height[123]. This confirms both the quality of our Schottky contact and the reliability of our model at low energy.

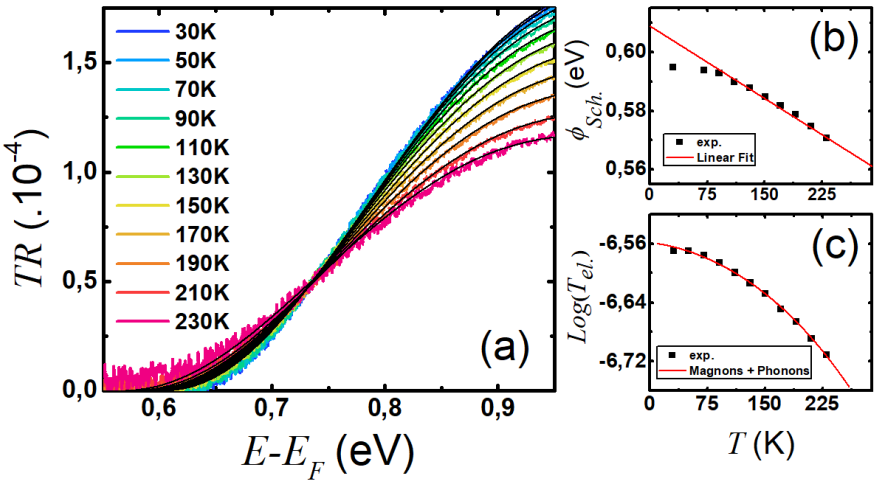

Figure II.13: (a) Experimental TR(E-E_F) of CoFeB(1) sample for several temperatures with associated fits. (b) Temperature dependence of Schottky barrier height with linear fit over the [90K,230K] region. (c) Temperature dependence of elastic transmission coefficient A. Theoretical model including magnons and phonons contribution is displayed.

Figure II.13.c) shows logarithm of the elastic transmission coefficient introduced in equation II.3. The logarithm enables a separation of terms with temperature-independent scatterings (defects and interfaces) lying in the intercept and temperature-dependent electron-phonon and electron-magnon scattering being described by the power law. Thus, both source of scattering can be disentangled and a fit using a T^{-2} dependence for λ_{ph} and λ_{mag} is applied.

This dependence has been theoretically and experimentally found in the case of metallic thin films for temperatures up to 100K[124–126], matching with the low temperature range of our study.

As a result, by the used of reasonable values for $\phi_{sch}(T)$ and $T_{el}(T)$, our model is able to accurately and quantitatively reproduce TR(V_{inj}) for a wide range of temperatures when low-energy injected electrons are considered. Our model shows that simple addition of both elastic and inelastic mean-free path contribution to Kaiser and Bell original model[62] gives accurate prediction for hot electrons transport in such structure.

II.3 – Hot electrons transport at higher energies

II.3 – 1. Transition to higher energies

While figure II.13 shows that experimental data are well reproduced through our model based on equation II.3, it fails describing hot electrons transport at higher energies. Both measured TR (solid line) and model of equation II.3 (dashed line) are plotted on figure II.14. Maximum of the TR lies around 1.05eV in both cases. Above this injection energy, TR decreases with increasing energy. If our model based on primary electrons collection also shows a decrease of TR passed this maximum, the slope of the decrease is too strong compared to experimental data. Moreover, our model does not predict a second increase of the signal around 2eV.

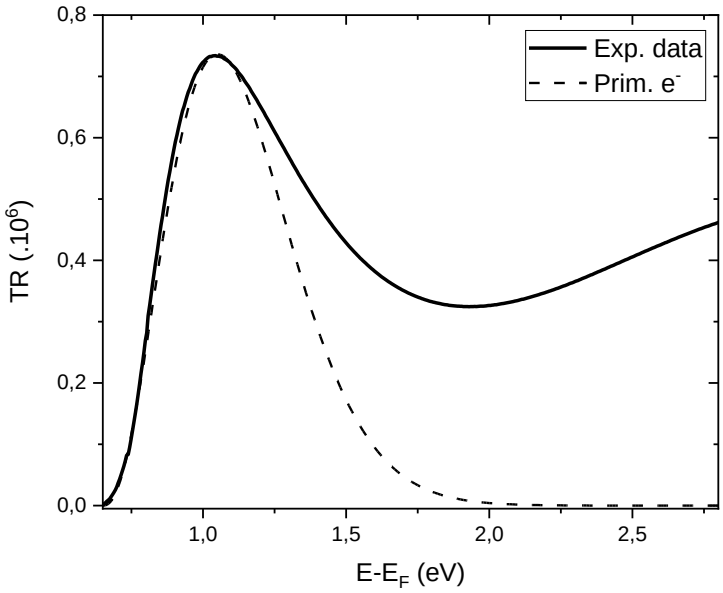

Figure II.14: Experimental TR(E-E_F) values of the CoFeB(4) sample measured at 50K. Solid line shows experimental data and dashed line the theoretical contribution of primary hot electrons.

Discrepancies between our theoretical model and the experimental data suggest that another channel of hot electrons collection appears and compensates, in the collected current in the base, scattered incoming primary hot electrons at higher voltages. The literature review reporting similar bell-like shape of the TR at the beginning of this chapter tends to point out the role of secondary electrons resulting from an electron-electron interaction.

II.3 – 2. Model for secondary electrons collection

In a first place, we will include secondary electrons in our model as described by Quinn's model. Exchange interaction, taking place between two adjacent electronic spins[127], is

taken into account in the same manner for spin-up and spin-down electrons so that electron-electron interactions are indifferent to the spin of electrons involved in the scattering process. Furthermore, details of the band structure of the materials will not be taken into account, so that only electrons close to the Fermi-level belonging to sp-bands can interact with incoming hot electrons.

Assuming all scattering events are modeled in equation II.1, the probability of an electron NOT to be scattered over the base of thickness d, is given by $e^{-d/\lambda}$. As Matthiessen's rule is applied, previous exponential expression can be decomposed as a product related to each possible interaction. Thus, the probability of an electron NOT to be scattered of the base thickness d is $\prod_i e^{-d/\lambda_i}$, where i represents each possible interaction. The different exponential factors given in the product correspond to the probability of an electron NOT being scattering by the i interaction over the distance d. Therefore, the probability of an electron being scattered by an electron-electron interaction AND NOT any other interaction is expressed as:

$$\left(1 - e^{-\frac{d}{\lambda_e(E)}}\right)\prod_j e^{-\frac{d}{\lambda_j}} \qquad (II.4)$$

where j represents each possible interaction except electron-electron one.

Expression of the inelastic mean-free path given by equation II.2 implicitly contains two term: an original $1/(E\text{-}E_F)^2$ that relates to interaction with sp-band and a correction for d-band contribution to the electronic decay passed a given energy with a $1/(E\text{-}E_F\text{-}\omega^{\uparrow})^2$. Yet, we wish first to only consider the former term in the secondary electrons generation. Thus, probability of each interaction to happen can also be decoupled following Matthiessen's rule, so that the probability of an electron to suffer an electron-electron interaction ONLY with a sp-band close to the Fermi level is given by:

$$\left(1 - e^{-\frac{d}{\lambda_e^{sp}(E)}}\right)e^{-\frac{d}{\lambda_e^{d}(E)}}\prod_j e^{-\frac{d}{\lambda_j}} \qquad (II.5)$$

With each electron-electron mean-free path that can be written with the typical expression:

$$\begin{cases} \lambda_e^{sp}(E) = \frac{\lambda_0^{sp}\sqrt{E}}{(E-E_F)^2} \\ \lambda_e^{d}(E) = \frac{\lambda_0^{d}\sqrt{E}}{\left(E-E_F-\omega^{\uparrow}\right)^2} \end{cases} \qquad (II.6)$$

If one takes λ_0^d equals to $\frac{\lambda_0^{sp}}{\varrho}$, equation II.2 is retrieved as a combination of both expressions in equation III.6 with $\lambda_0 = \lambda_0^{sp}$.

Following Quinn's theory, an incoming hot electron being scattered with an electron from the Fermi sea is supposed to transfer half its energy. Thus, if electrons are injected with an energy E above the Fermi level, secondary electrons generated have an energy E/2. This means that this additional channel participating to hot electrons collection appears when

primary electrons are injected with an energy above twice ϕ_{Sch}. Below this, they cannot satisfy conditions to enter the semiconductor.

The mean-free path of a secondary electron is supposed to be that a primary electron with an energy $\frac{E}{2}$ above the Fermi level, E being that of the incoming hot electron that created the secondary one. This means that the semiconductor has less available states to host this electron compared to primary ones. The same expression for the electron-electron mean-free path is applied. Electron-electron interaction is supposed to lead to a strong anisotropy in scattered electrons ejection. While one of the two generated electrons is propagated backward, the other one travels perpendicular to the planes direction, so that their parallel wavevector can be considered negligible. As a consequence, elastic transmission coefficient T_{el} taking into account other interactions is kept unchanged.

To simplify, we will focus on generation of secondary electrons in CoFeB. As this layer is the first to be crossed by hot electrons and it has the shortest electron-electron mean-free path (see section II.1 – 3), most inelastic scattering should take place in the first 4nm of CoFeB. The total transfer ratio related to the channel activated after $E - E_F = 2\phi_{Sch}$, for secondary electrons from electron-electron interactions with sp-band of CoFeB(4), can then be written as:

$$TR_{sp}^{CoFeB}(V_{inj}) = \frac{\left(\frac{|e|V_{inj}}{2} - \phi_{Sch}\right)^{\frac{5}{2}}}{I_{tun}(V_{inj})} . T_{el} . \left(1 - e^{-\frac{t_{CoFeB}}{\lambda_d^{CoFeB}(V_{inj})}}\right) e^{-\frac{t_{CoFeB}}{\lambda_{sp}^{CoFeB}(V_{inj})}} \prod_j e^{-\frac{d_j}{\lambda_e^j\left(\frac{|e|V_{inj}}{2}\right)}} \quad (II.7)$$

Figure II.15 show both contributions from primary electrons (black dashed line) and scattered generated by an interaction with sp-band (dashed and dotted red line) from equations II.3 and II.7 respectively. The sum of these two contributions is also plotted in dashed red line. The additional contribution added by equation 4 fails correcting our initial model in two ways: first, this channel is activated too late as the total TR still follow fast decrease from the primary electrons model until 1.5eV. Then, sp-band contribution becomes much higher than experimental TR at higher energies. It even decreases at higher energies while, the measured signal keeps increases steadily.

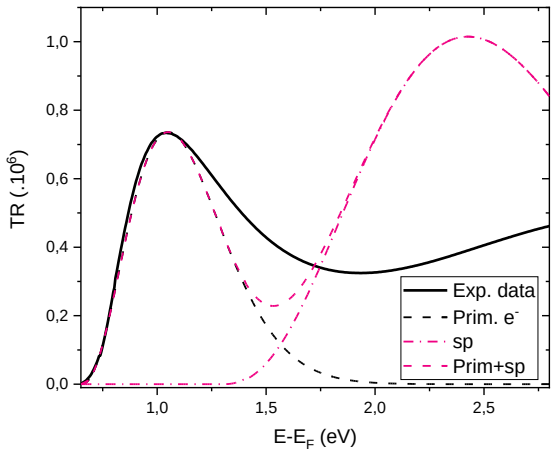

Figure II.15: Experimental TR(E-E_F) values of the CoFeB(4) sample measured at 50K. Solid black line shows experimental data, dashed black line the theoretical contribution of primary hot electrons, dashed and dotted red line the theoretical contribution of sp-band given by equation 4 and dashed red line the sum of both contributions.

Energy repartition coefficient

A possible explanation for the delayed increase of secondary electrons can be found in the effect of exchange interaction. Theoretical work predicted a change of the final energy repartition of secondary electrons due to electron-electron collisions[105,128]. Due to spin-spin interaction the electronic collisions are attenuated. Thus, secondary electrons with higher energy could be generated and enter the Schottky diode before $2\phi_{Sch}$ ($E_{sec} > \frac{E}{2}$). Ritchie and Ashley[128] applied perturbation theory to evaluate scattering of low-energy excited electrons with and without exchange interaction. They showed the energy repartition coefficient to lie between $\frac{1}{2}$ and $\frac{2}{3}$, energy of the scattered electron corresponding to *coefficient* x *initial energy*.

Figure II.16 shows TR modeled based on equations II.3 and II.7 with energy repartition coefficients different from one-half. Several conclusions can be drawn on the effect of this coefficient on the total TR. As the coefficient gets higher, the maximum value reached above 1.5eV decreases while the local minimum in-between increases. The position of both particular points moves towards lower energy with increasing coefficient values. For $\frac{2}{3}$, contribution of secondary electrons happen so early that it shifts the local maximum associated with only primary electrons collection, around 1eV.

In term of transport, hot electrons scattered through electron-electron interactions transfer a lower part of their energy to the Fermi sea. Thus, they can be collected before $2\phi_{Sch}$. Yet, they also can undergo inelastic collision. Their electron-electron mean-free path is shorter than in the case of half-energy scattered electrons. As injection energy is increased, they get scattered faster, explaining the shift of extrema seen on figure II.16.

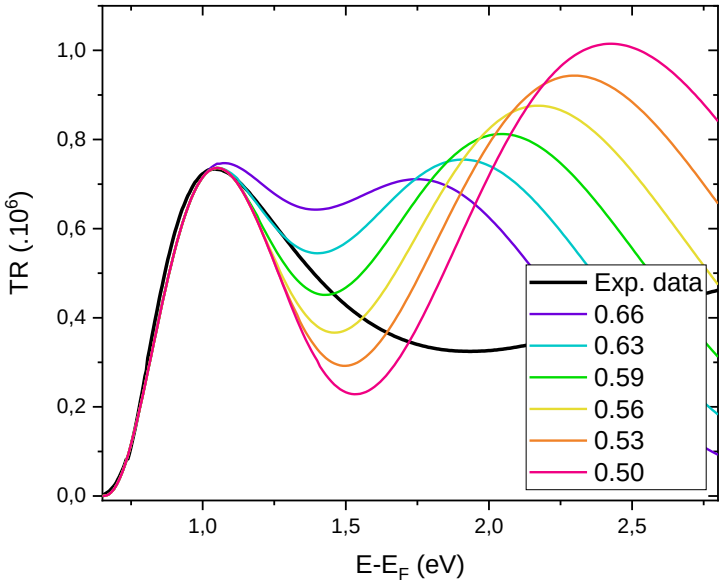

Figure II.16: Comparison of models based on equation 4 using different values for the energy repartition coefficient between $\frac{1}{2}$ and $\frac{2}{3}$.

Scattering cone of ejection

However, models shown on figure II.16 are not satisfactory, no matter the value of the repartition coefficient. The second bump happening at higher voltages is almost as high as the first one. However, experimental data shows a local minimum of the TR. This means that the amount of collected electrons at the Schottky barrier is overestimated by our model. One strong hypothesis made earlier was to suppose each scattered electrons to travel perpendicular to the interfaces. We propose to modify this assumption by having a closer look on angular distribution resulting from electron-electron interactions. Conservation of both energy and momentum is supposed:

$$\begin{cases} \vec{k} + \overrightarrow{k_F} = \overrightarrow{k_1} + \overrightarrow{k_2} \\ 2E_F + |eV_{inj}| = E_1 + E_2 \end{cases} \quad (II.8)$$

where $\vec{k}$ is the incoming hot electron wave vector, $\overrightarrow{k_F}$ that of electron at the Fermi level and $\overrightarrow{k_1}$, $\overrightarrow{k_2}$ the resulting wave vectors after scattering associated with energies E_1 and E_2 respectively.

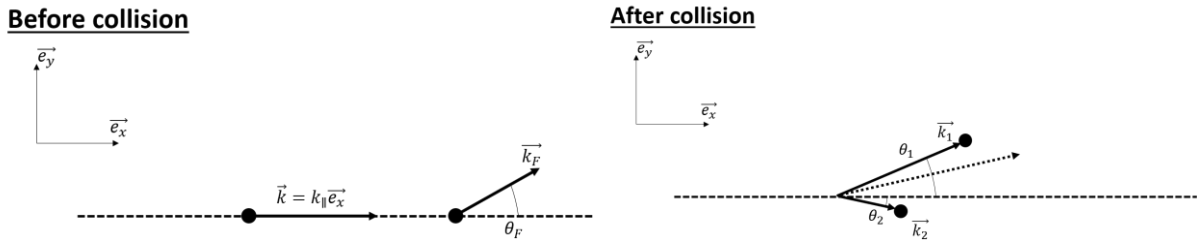

Figure II.17: Diagram for a inelastic collision between a hot electron with a wave vector $\vec{k}$ and an electron at the Fermi level. Scattered electrons are labelled 1 and 2 after the interaction. They propagate along the direction of wave vectors $\overrightarrow{k_1}$ and $\overrightarrow{k_2}$ with associated angle of scattering θ_1 and θ_2 .

Figure II.17 shows two diagrams describing an electron-electron collision. On the left one, an incoming electron with a wavevector $\vec{k}$ perpendicular to the interfaces. Electron at the Fermi level has an associated wave vector $\overrightarrow{k_F}$ in some random direction. On the right, the diagram shows the two scattered electrons propagating in new directions with wave vectors $\overrightarrow{k_1}$ and $\overrightarrow{k_2}$. Two angles θ_1 and θ_2 indicate propagation direction with respect to the initial propagation direction of the incoming electron.

At first glance, system of equations II.8 has four unknown parameters for the two equations: E_1, E_2, θ_1, θ_2. Thus, resolution cannot be made straightforward. Yet, a relation between energies was assumed earlier through the energy repartition coefficient. In the case of equipartition of energy between scattered electrons, as the total energy of the system {hot electron, electron at E_F} is conserved during interaction, the first equation of II.8 gives:

$$E_1 = E_2 = E_F + \frac{|eV_{inj}|}{2} \quad (II.9)$$

So now, momentum conservation equation $\vec{k} + \overrightarrow{k_F} = \overrightarrow{k_1} + \overrightarrow{k_2}$ can be expressed as a function of angles and energies by projection on $\overrightarrow{e_x}$ and $\overrightarrow{e_y}$:

$$\begin{cases} (cos(\theta_1) + cos(\theta_2))\sqrt{2m\left(E_F + \frac{|eV|}{2}\right)} = \sqrt{2m(E_F + |eV|)} + \cos(\theta_F)\sqrt{2mE_F} \\ (sin(\theta_1) + sin(\theta_2))\sqrt{2m\left(E_F + \frac{|eV|}{2}\right)} = 0 + \sin(\theta_F)\sqrt{2mE_F} \end{cases} \quad (II.10)$$

For a given θ_F the system II.10 has a unique pair (θ_1, θ_2) solution of these equations. Figure II.18 shows the solution of system II.10 as a function of θ_F. After an electron-electron interaction one electron propagates perpendicular to the interfaces ($\theta_i \approx 0°$) while the other will be deviated towards higher angles. For some values of θ_i, one scattered electron can reach the metal/semiconductor interface with a low enough angle to be collected (solid red line). The others cannot pass the Schottky barrier and will be thermalized in the base.

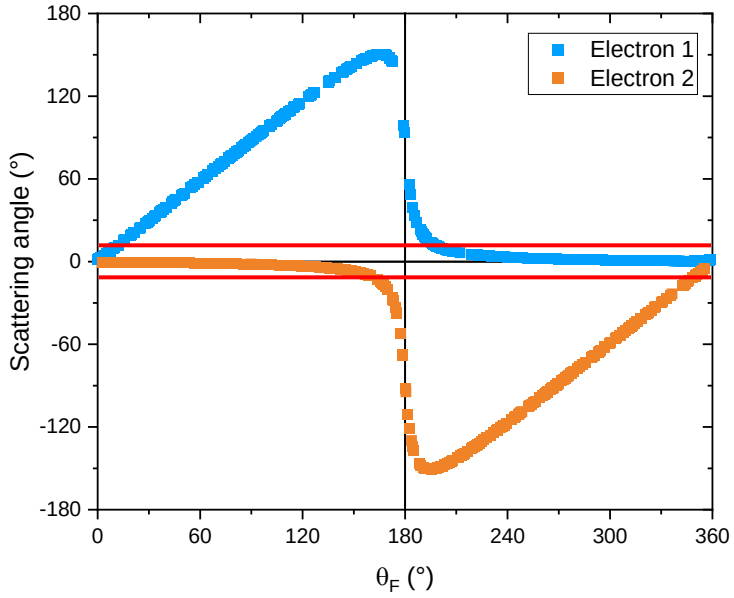

Figure II.18: Resulting scattering for each electron after an electron-electron interaction with the Fermi sea, as a function of θ_F. Injection energy is taken equal to 1eV and the Fermi level, 12eV. Equipartition of energy between both electrons is assumed. Electron 1 and 2 are undistinguishable. The red solid lines represents the maximum acceptance angle of the Schottky barrier at 1V.

Thus, there is only a fraction of the scattered electrons that can be collected. Assuming a spherical Fermi surface, probability distribution for θ_F is uniform over 360°. Coefficient C_{sp} represents the ratio of collected electrons of the total number of scattered electrons for an interaction with an electron from a sp-band. For the energy range of our study [1eV,3eV], the values for this coefficient are lying around 0.36 for C_{sp} with only a weak energy dependence and no change with the energy repartition coeffecient. This value corresponds to integration of accessible secondary electrons contained in the two red lines shown on figure II.18, taking into account momentum filtering coming from our Schottky barrier.

Equation 4 can be expressed with the modifications brought to the model:

$$TR_{sp}^{CoFeB}(V_{inj}) = \frac{(s.|e|V_{inj} - \phi_{Sch})^{\frac{5}{2}}}{I_{tun}(V_{inj})}.T_{el}.C_{sp}.\left(1 - e^{-\frac{t_{CoFeB}}{\lambda_{sp}^{CoFeB}(V_{inj})}}\right)e^{-\frac{t_{CoFeB}}{\lambda_{d}^{CoFeB}(V_{inj})}}\prod_j e^{-\frac{d_j}{\lambda_e^j(s.|e|V_{inj})}} \quad (II.11)$$

where s represents the energy repartition coefficient for an electron-electron interaction. Equation II.7 is a specific case of equation II.11 with $s = \frac{1}{2}$ and $C_{sp} = 1$. Figure II.19 shows the comparison between models based on equation II.11 and experimental TR. The shape of modeled transfer ratios agrees more with experimental data. Even though the decrease of the theoretical signal is still much faster in the [1eV, 1.5eV] range, a further increase happens after the local minimum with reasonable values, smaller than experimental ones. This is expected as only secondary electrons from CoFeB were considered in the model. Others can also be produced in Cu or in $[Co/Ni]_{x5}$ but in fewer quantities, thus explaining discrepancies between this model and experimental data.

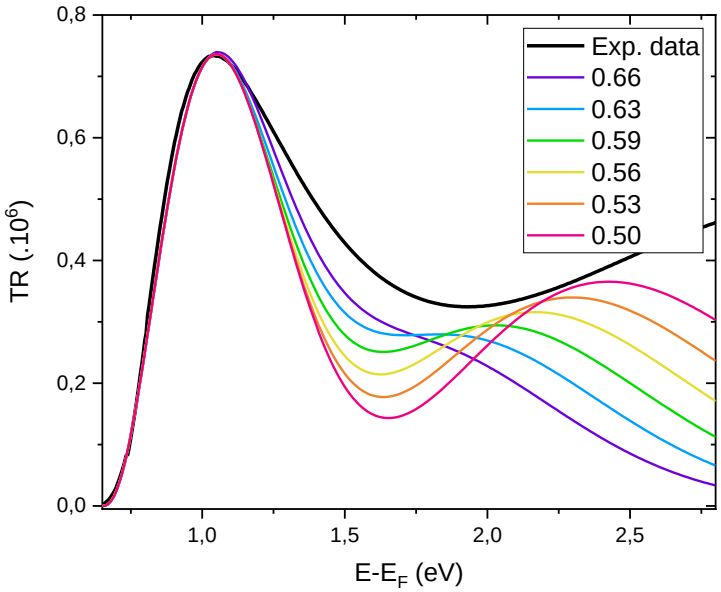

Figure II.19: Comparison of models based on equation II.11 with $C_{sp} = 0.36$ using different values for the energy repartition coefficient between $\frac{1}{2}$ and $\frac{2}{3}$.

II.3 – 3. Secondary electrons from d-band scattering

Photoemission experiments showed that d-bands of metals do not only affect electron-electron interactions through screening effect[102,104,106] but also lead to additional scattering mechanism in addition to that from sp-band. Expression used for describing electron-electron mean-free path (Eq. II.3) in our model includes the presence of sp-band and d-band contributions in the change of λ_e. Therefore, two kind of secondary electrons (sp and d) can be generated through electron-electron interactions, while only sp ones have been taken into account so far.

Figure II.20 shows a density of state diagram describing electron-electron interactions in a transition metal. DOS is approximated by boxes with constant densities over a given energy region. Red rectangles are associated with sp-band while blue ones correspond to d-band. The latter is shifted in energy with that of majority spin electrons lying lower in energy compared to that of minority spin electrons. All states are empty above the Fermi level of the metal. On figure II.20, two mechanisms are shown: white circles at the highest energy describes hot electrons suffering an electron-electron interaction of different type. The one on the left is scattered by an electron from a sp-band at the Fermi level. Therefore, assuming an equipartition

of energy between the two scattered electrons, the resulting state lies at $\frac{E}{2}$ above the Fermi level (see section II.3 – 2).

The one of the right is interacting with an electron from deeper d-band of majority spin. Even though the band lies well below the Fermi level and thus, it is partially screened, the high density of states for this band makes the interaction likely to happen. The incoming hot electron is scattered by an electron from this d-band at an energy E_F-$\omega^{\uparrow}$. Therefore, the resulting energy for both secondary electrons is $\frac{E-\omega^{\uparrow}}{2}$ above the Fermi level. Furthermore, this interaction cannot take place if E is lower than the energy shift $\omega^{\uparrow}$ of the d-band as the resulting state for scattered electrons would lie below E_F. For CoFeB, $\omega^{\uparrow}$ was taken equal to 0.5eV. Thus, this contribution appears around 2eV which also corresponds to the missing high-energy contribution of the secondary electrons.

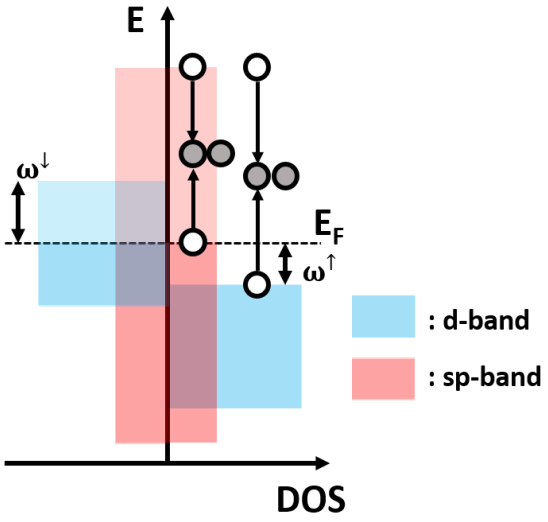

Figure II.20: Hot electrons above the Fermi level interact with electrons below E_F (white circles). This interaction generates two electrons at an intermediate energy (grey circles). Here, the final state of both electrons is the same energy which depicts the case s = 0.50.

Following equation II.7, an additional term can be added to take into account scattering from this d-band mechanism:

$$TR_d^{CoFeB}(V_{inj}) = \frac{(s.(|e|V_{inj} - \omega^{\uparrow}) - \phi_{Sch})^{\frac{5}{2}}}{I_{tun}(V_{inj})} . T_{el} . C_d . \left(1 - e^{\frac{-t_{CoFeB}}{\lambda_d^{CoFeB}(V_{inj})}}\right) e^{\frac{-t_{CoFeB}}{\lambda_{sp}^{CoFeB}(V_{inj})}} \prod_j e^{-\frac{d_j}{\lambda_e^j(s.(|e|V_{inj}-\omega^{\uparrow}))}} \quad (II.12)$$

Equation II.12 gives expression of the associated transfer ratio for energies higher than $\frac{\phi_{Sch}}{s}$, s being the energy repartition coefficient introduced earlier. Here, only electrons which interacted specifically with d-band from CoFeB are taken into account. Coefficient C_d is calculated in the same way as C_{sp} in section II.3 – 2. **Scattering cone of ejection**. Value found for this coefficient is 0.43 and is different from that of sp-band because the energy state of the scattered electrons is not the same.

Figure II.21 shows models with different energy repartition coefficient with contribution of the d-band scattering described by equation II.12. The increase of TR due to TR_d^{CoFeB} is stronger in the case of equipartition of energy (s=0.50) rather than for other values. Indeed, red

curve is above all other models plotted on figure II.21 for high energies. The same happens with hot electrons scattered by sp-band (see Fig. II.20). As secondary electrons travel through Cu and [Co/Ni] with lower energies, their mean-free path is longer and thus, they suffer less interactions until reaching Schottky barrier.

Qualitative agreement can be found between our model with an energy repartition coefficient lying around 0.60 as the total modeled TR follows the shape of experimental transfer ratio. As it was mentioned earlier discrepancies between measurement and our model can be explained by the fact that CoFeB was assumed to be the only source of secondary electrons collected in our MTT. Other can be produced in fewer quantities in [Co/Ni] or Cu.

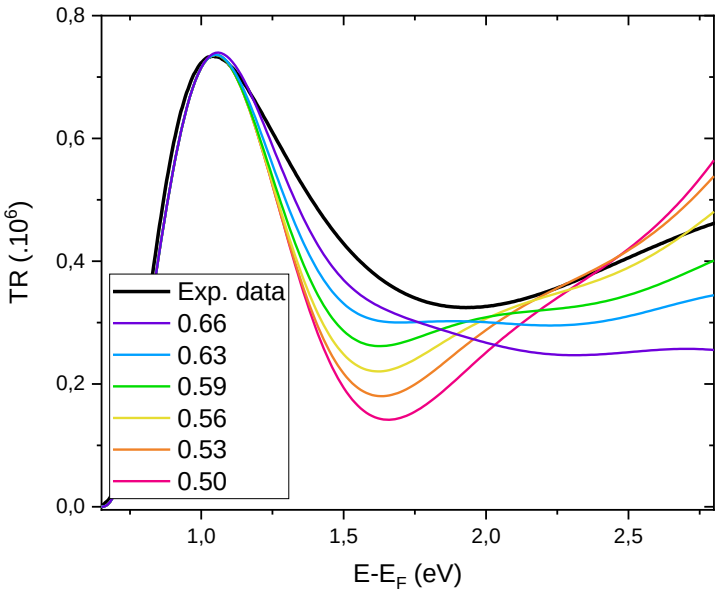

Figure II.21: Comparison of models for several energy repartition coefficient and including collection of both hot electrons scattered by electrons from sp-band or d-band.

A similar measurement was performed on a CoFeB(1) MTT with energies up to 2eV (see Fig. II.1.c). Both experimental curves show the same behaviour with this bell-like shape followed by an increase at higher energies (see Fig. II.22). It should be noted that in the case of CoFeB(1), we assume the signal to follow the same trend. A huge difference of agreement between experimental and modelled transfer ratio depending on CoFeB thickness is seen on figure II.22. Our model assumes CoFeB to be the main source of secondary electrons generation. As soon as its thickness is reduced, less interactions take place in this layer and [Co/Ni] or Cu may become dominating in term of electron-electron scattering.

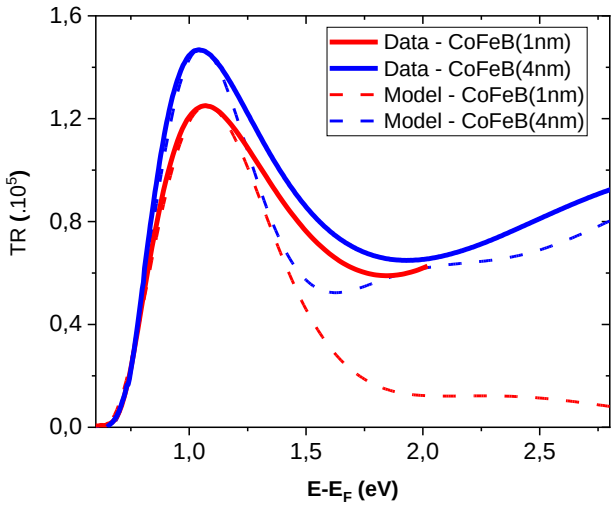

Figure II.22: Experimental and modeled TR for two MTT with different CoFeB thicknesses. Energy repartition coefficient is equal to 0.59 for both models.

II.4 – Spin-dependence of electron-electron interactions

So far, spin-dependence on hot electrons mean-free path was ignored. Only majority spin electrons were supposed to be injected in the metallic base and their interaction with conduction electrons to generate only majority spins electrons. Yet, these assumptions can be questioned. First, TMR lies around 50% corresponding to a polarization just below 50% according to Jullière's formula. Thus, 75% of injected electrons correspond to majority spins ones while the remaining 25% are associated with minority spin. This differs from the full polarization electron beam initially taken in our model. The hypothesis to take only majority electrons can be assumed for low energies as minority spin electron-electron mean-free path is too short for those electrons to cross the base. However, at higher energies more and more scattering could lead to spin-flip or other processes leading to minority spins to enter the Schottky diode. In the following section, we will project estimations of spin effects on hot electrons transport in the scope of previously introduced electron-electron scattering processes.

II.4 – 1. Spin-dependent transport of hot electrons

Energy-dependent mean-free paths reviewed in section II.2 – 3 was done only for majority spin electrons. Minority spin electrons have a much shorter inelastic mean-free path compared to majority spins ones. Figure II.23 shows experimental measurements of Van Dijken *et al.* of minority spin electrons IMFP in a CoFe-based MTT structure[84]. Here, λ_{min} is less than 1nm for the whole energy range explored. Furthermore, the ratio between spin-up over spin-

down mean-free paths lies around 6, showing that minority spin electrons suffer much more interactions in the base.

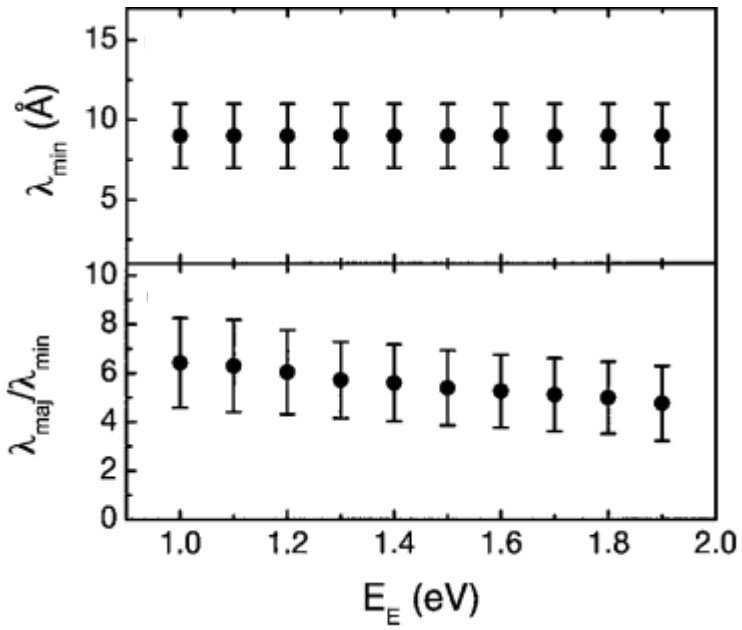

Figure II.23: Attenuation length of minority electrons in $Co_{84}Fe_{16}$ (top) and attenuation lengths ratio (bottom). From Van Dijken et al.[84].

In order to understand the physical origin of this difference, several mechanisms have to be taken into account: screening effects, scattering mechanisms, impact of exchange interaction, band structure of the material, etc. To simplify the picture, we can decompose expression of the mean-free path as a function of energy into two spin-dependent terms, namely electrons velocity and lifetime:

$$\lambda_\sigma(E) = v_\sigma(E).\tau_\sigma(E) \qquad (II.13)$$

with σ represents the spin of electrons. Equation II.13 summarizes the two contributions of asymmetry of the mean-free path depending on electrons spin. Velocity is associated with the motion of electrons in the metal while the lifetime corresponds to probabilities of scattering events.

Figure II.24 shows calculations performed by Zhukov *et al.* of spin-dependent velocities as a function of energy in Fe and Ni[129]. While almost no spin-asymmetry is observed in the case of Ni as the two curves follow the same trend, that of Fe is much different. The energy-dependence of majority spin velocity corresponds to that of free-electrons in Fe. Yet that for minority ones is much lower and has a completely different shape with almost constant $v_\downarrow(E)$ up to 2eV. Explanations can be found in spin-resolved band structure calculations[129] as in Fe, majority spin electrons occupy free-electron-like states while minority spin electrons are in 3d-like ones over this energy range.

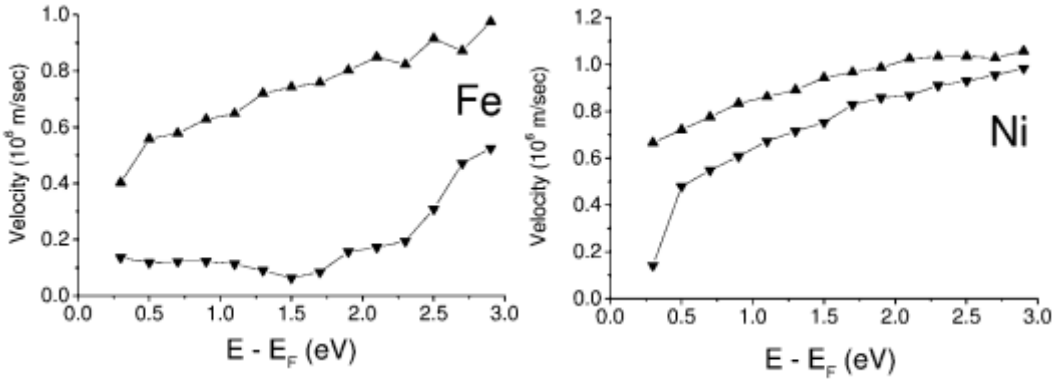

Figure II.24: Spin-dependent velocities for Fe (left) and Ni (right). Up triangles are for majority spin electrons and down triangles for minority spin electrons. From Zhukov et al.[129].

Spin-dependent scattering events filtering out preferential spin orientation were investing through measurement of the spin-dependent lifetimes with TR-2PPE technique[106]. Figure II.25 shows spin-resolved inelastic lifetime measurement in Co as a function of energy. A difference of these inelastic lifetimes is found as the ratio of both of them increases from about 1 at 0.6eV to almost 2 around 1.1eV. Explanation given by Aeschlimann *et al*. is related to Co density of states (see inset on Fig. II.25). They suggest a relaxation process for which excited minority spin electrons can decay much faster due to the presence of empty d-band states until 1.3eV above the Fermi level. On the other hand, majority spins could only relax in fewer quantities of unfilled majority spin states. Therefore, minority spin electrons are scattered out at a faster rate than majority spin ones.

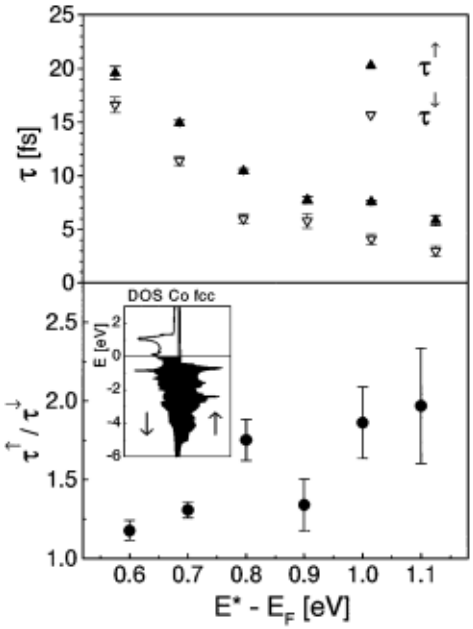

Figure II.25: Spin-resolved inelastic lifetime of hot electrons in Co (top) and spin lifetime ratio (bottom). Inset shows the spin-resolved density of states of fcc Co. From Aeschlimann et al.[106].

II.4 – 2. Spin-asymmetry in electron-electron interactions

Results of Aeschlimann *et al.* shown on figure II.25 highlights the importance of density of states and band structure when analyzing spin-dependent hot electrons transport. Yet, it gave only a qualitative indication on dependence of spin on inelastic scattering. Moreover, secondary

electrons generated through Auger or cascades mechanisms may contribute to measured relaxation times and thus, affect the resulting experimental lifetime.

As mentioned in section I.2 – 1, Ritchie and Ashley[128] first considered interaction of hot electrons by including exchange effect. They showed this effect to reduce the interaction between two electrons with parallel spins. Thus, a first step to include spin into electron-electron interactions was done. Years later, Penn[105] continued this work for low-energy interacting electrons by proposing a calculation of the electron mean-free path with spin dependence of the scattering. His work gives a ratio of scattered electrons in the parallel configuration over that in the antiparallel configuration. His expression gives ratios ranging from 2 to 10, depending on corrections brought in the calculation. These values are comparable to ratios measured experimentally (see Fig. II.25).

Zarate *et al.* proposed a model describing excitations of hot electrons by taking into account mechanisms related to the density of states of the metals[71]. We already used their results in section II.2 – 3 for the electron-electron mean-free path of noble and transition metals. Here, the main discussion about their result will be about detailed transitions between incoming hot electrons and that at the Fermi level and the influence of d-band in these processes. Results from theoretical model is compared to Aeschlimann *et al.* measurements on hot electrons lifetimes in Co (see Fig. II.26).

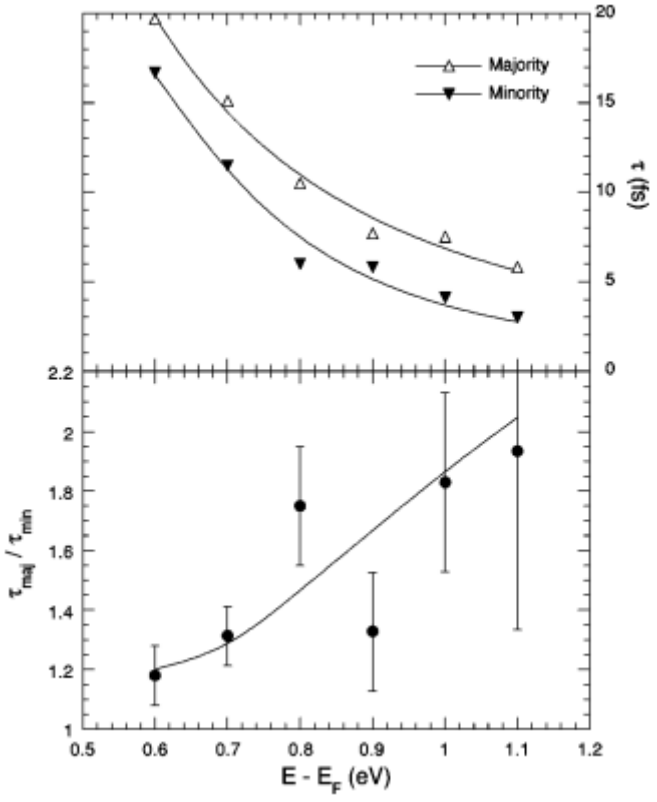

Figure II.26: Spin-dependent lifetimes in Co and associated spin lifetime ratio. From Zarate et al.[71].

A general and explicit expression of hot electrons lifetime can be given by the following expression first introduced by Berglund and Spicer[130]:

$$\frac{1}{\tau(E)} = \frac{\pi}{\hbar}\rho_s^3 |M|^2 (E - E_F)^2 \qquad (II.14)$$

where ρ_s stands for the density of state and M, the matrix element describing scattering processes between initial and final states. The latter is supposed to be constant. Expression given by equation II.14 is based on the same assumptions as those used in this study. Quinn's result can be retrieved in the low-energy limit and assuming a free-electron[98]. Yet in order to include d-band and spin effects in the model, matrix element M has to be modified in order to describe a more complex density of states.

To do so, a box model of the density of state is assumed as it was done in figure II.27. Matrix element written as $\left|M_{l_f k_f}^{l_i k_i}\right|$ is related to an incoming hot electron going from band l_i to band l_f while a secondary electron goes from band k_i to band k_f. d-bands are only accessible for given energies as they are not as extended as sp-bands (see Fig. II.28). The shift of the top of these bands with respect to the Fermi level is given by ω^σ where σ stands for the spin of electrons. The bottom of d-bands is too deep in the DOS of the metals to become accessible at energies studied in our work (several eVs below E_F).

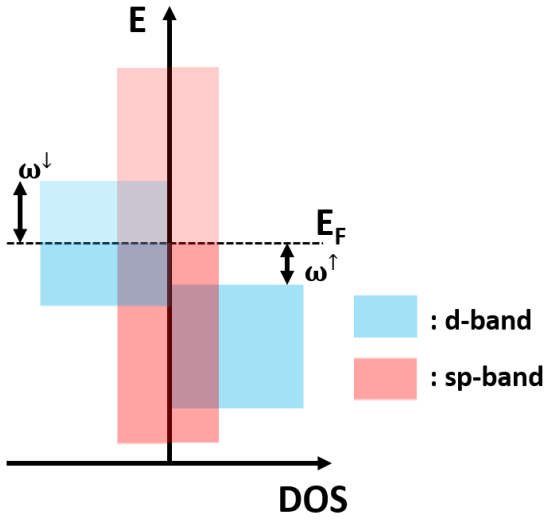

Figure II.27: Box model of the DOS for a transition metal. High density d-bands are shown in blue while low density sp-bands are in red. The left side of the diagram describes density for minority spin electrons while right side stands for density of majority spin electrons. $\omega^\uparrow$ (resp. $\omega^\downarrow$) gives the shift of the d-band with respect to the Fermi level.

Assuming interacting electrons cannot change their spin, either coming from higher energy and relaxing or being excited during the scattering, few mechanisms describing spin-dependent lifetimes can be identified. Table II.1 presents the four main transition for electron-electron scattering and secondary electron generations. The appropriate way to describe depends on two considerations: spin of incoming hot electrons and initial energy above the Fermi level.

For a spin-up hot electron injected in the base, associated state corresponds to sp-band as no majority spin d-band empty state are available above the Fermi level. At low energies ($E - E_F < \omega^\uparrow$), only minority spin electrons from both d-band or sp-band and majority from sp-band can be excited. As the density of state for the former process is much higher than the others, it can be assumed to be the main way to generate secondary electrons (Top-left case in table II.1). At higher energies ($E - E_F > \omega^\uparrow$), additional processes may occur: majority spin d-

band electrons can also be scattered into empty states (Top-right case in table II.1). Thus, an additional contribution described by $|M_{ss}^{sd}|$ participates to secondary electrons generate along with the one at lower energies.

Concerning minority spin hot electrons, they are supposed to be injected into d-band above the Fermi level due to the great number of empty states. When looking at secondary electrons generation, similar processes take place: at low energies, only d-band minority spins are excited (Bottom-left case in table II.1) and at higher energies, additional majority spins from buried d-band can participate to generation of secondary electrons (Bottom-right case in table II.1).

	$E - E_F < \omega^{\uparrow}$	$E - E_F > \omega^{\uparrow}$
Majority spin hot electrons	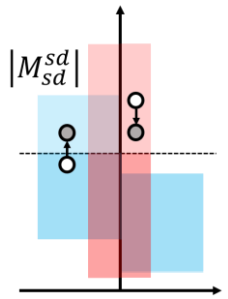	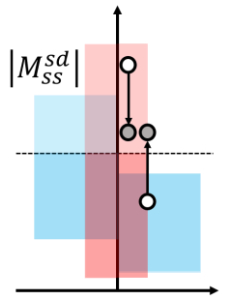
Minority spin hot electrons	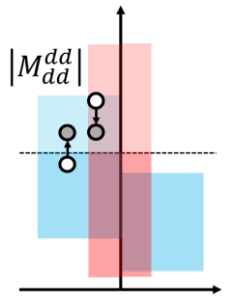	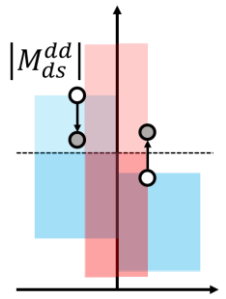

Table II.1: Different electron-electron scattering mechanisms depending on incoming hot electron spin orientation and initial energy. The first line corresponds to majority spin electrons while the second stands for minority spin ones. The first column describes the only mechanism available for hot electrons to decay inelastically as majority d-band is not available yet. Passed a given energy, transitions shown by figures of the second column gives new way for hot electrons to be scattered. The corresponding matrix element to each process is shown next to associated figure.

Based on this description, Zarate *et al.* describes spin-dependent lifetime with:

$$\begin{cases} \frac{1}{\tau^{\uparrow}(E)} = \frac{2\pi\rho_d^3}{\hbar}\left[\frac{1}{2}\left(\frac{\rho_s}{\rho_d}\right)|M_{sd}^{sd}|^2(E-E_F)^2 + \frac{1}{2}\left(\frac{\rho_s}{\rho_d}\right)^2|M_{ss}^{sd}|^2\left(E-E_F-\omega^{\uparrow}\right)^2\right] \\ \frac{1}{\tau^{\downarrow}(E)} = \frac{2\pi\rho_d^3}{\hbar}\left[\frac{1}{2}|M_{dd}^{dd}|^2(E-E_F)^2 + \frac{1}{2}\left(\frac{\rho_s}{\rho_d}\right)|M_{ds}^{dd}|^2\left(E-E_F-\omega^{\uparrow}\right)^2\right] \end{cases} \quad (II.15)$$

Which is used to fit experimental data from Aeschlimann *et al.* as shown on figure II.26.

II.4 – 3. Additional spin-flip processes and spin-polarization phenomenon

As there is a spin-dependence of the lifetime of hot electrons some electrons are preferentially scattered, thus leading to a change in the spin-polarization of the initial hot electron beam. Yet, secondary electrons can also have spin oriented in a given direction. Indeed, according to the work of Zarate *et al.* secondary electrons produced at low energies (first column in table II.1) are supposed to mainly be minority spin occupying empty d-states, independently of the incoming hot electrons spin. Thus, a spin-polarized electron beam could be produced even by injecting a non-polarized one through a ferromagnetic layer with appropriate thickness and energy.

Kisker *et al.* experimentally measured spin-polarization of low-energy secondary electrons from Fe and Co[131]. Figure II.28 is the results of these measurements when sending 60eV light on a Fe sample. The energy distribution associated with this measurement is peaked around 3eV with a long tail going up to 20eV. This measurement shows that for energies above 5eV, spin-polarization corresponds to the average magnetization of the 3d and 4sp electrons (dashed line on Fig. II.28). Importance of the band structure of the materials concerning scattering mechanism and spin-polarization of secondary electrons is shown. In addition, the linear increase of secondary electrons was interpreted in the scope of transition between minority/majority d and sp-bands, taking account possible spin-flip. This latter process was not considered in the model of Zarate *et al.*

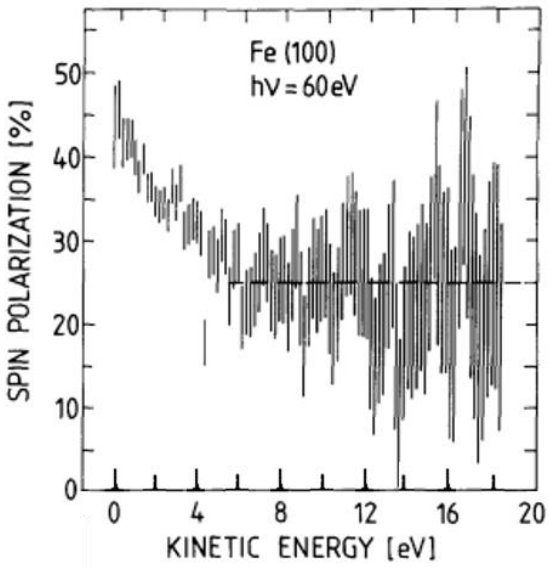

Figure II.28: Spin polarization of secondary electrons for Fe(100) excited with 60eV light. From Kisker et al.[131].

Disagreement about spin-flip contribution to electron-electron scattering was tackled years later with *ab initio* calculation of excited electrons lifetime in ferromagnet. Zhukov *et al.* investigated these interactions based on DOS of Fe and Ni[129]. Figure II.29 shows their calculation with an asymmetry function defined as

$$A_\sigma(\omega) = \frac{\left|Im\Delta\Sigma_\sigma^{nsf}(\omega)\right| - \left|Im\Delta\Sigma_\sigma^{sf}(\omega)\right|}{\left|Im\Delta\Sigma_\sigma^{nsf}(\omega)\right| + \left|Im\Delta\Sigma_\sigma^{sf}(\omega)\right|} \qquad (II.16)$$

with imaginary parts being related to lifetimes and nsf (resp. sf) standing for the non-spin-flip (resp. spin-flip) contribution. ω is the excitation energy. Their calculation show that inelastic electron-electron scattering is mainly dominated by nsf processes for both materials above 2eV. However, in the case of Fe minority spin electrons have a higher probability to spin-flip with suffering a collision with another electron at lower energy.

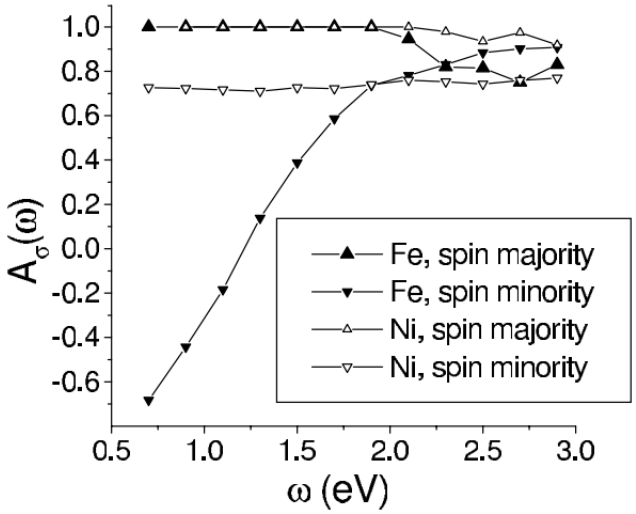

Figure II.29: Calculated spin asymmetry of excited electron decay in Fe and Ni. From Zhukov et al.[129].

While spin-dependent transport of hot electrons was investigated in previously mentioned studies, experimentally and theorically, no definitive conclusion can be drawn for this energy range. The model presented in this chapter can be extended to include spin-dependence of interacting electrons with mechanism presented in table II.1.

II.4 – 4. Planar MTT for spin-polarization at low energies

Model for spin-dependent transport

Equation describing electron-electron mean-free path for minority spin hot electrons has to be implemented in order to model spin-dependent transport. Equation II.2 (see section II.2 – 2. **Transport in the base**) is supposed to describe hot electrons transport for both spin orientation. Parameters given in the section II.2 – 3 correspond to that of majority spin electrons. The same method is applied to evaluate $\lambda_0^{\downarrow}$ and $\rho^{\downarrow}$, the characteristic value for electron-electron interaction and coefficient related to d-band density respectively, for both CoFeB and [Co/Ni]. These coefficients are calculated with values extracted by Zarate *et al.*[71]. The coefficient $\rho^{\downarrow}$ is around 3.8 from experimental data of Aeschlimann *et al.* on Co. It is supposed to be the same for all transition metal alloys. Concerning $\lambda_0^{\downarrow}$, values for CoFeB and [Co/Ni] taken are as 1.5nm.eV$^{3/2}$ and 1nm.eV$^{3/2}$ respectively. These values give inelastic mean free paths about the same order of magnitude as attenuation lengths measured in CoFe and NiFe alloys by Van Dijken *et al.*[84].

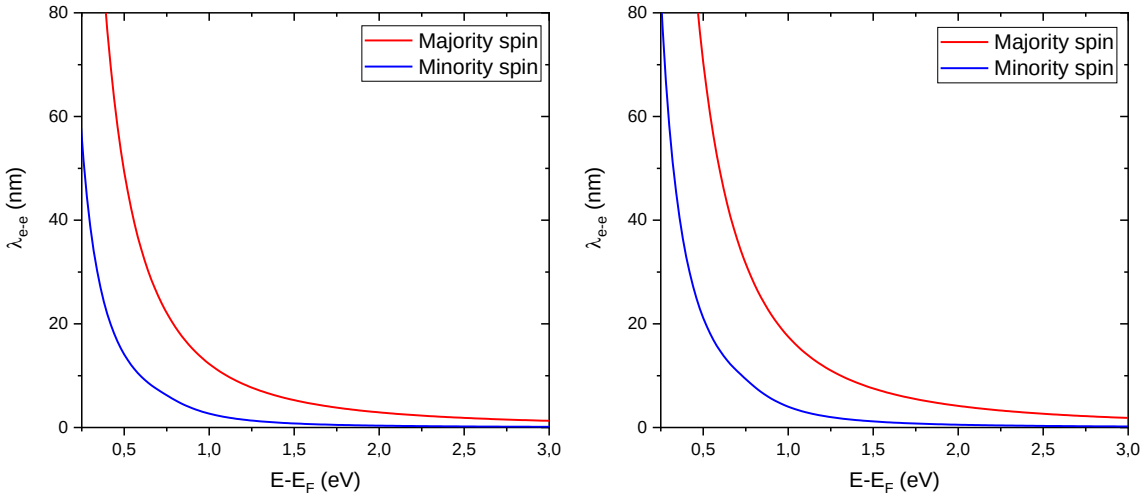

Figure II.30: Electron-electron mean-free path of both spin orientations as a function of energy for CoFeB (left) and [Co/Ni] (right).

Figure II.30 shows a comparison between electron-electron mean-free path for both CoFeB and [Co/Ni] as a function of energy for both spin orientation. The mean-free path for minority spin electrons is well below the value for that of opposite spin as observed experimentally. As a free-electron behavior is assumed for all hot electrons, energy-dependence of the ratio between spin-up and spin-down electron-electron mean-free path is that of the lifetime in our model, *i.e* the denominator in equation II.2. The main difference in term of energy dependence between both expressions comes from the effect of the d-band with the ρ coefficient. The value chosen leads to an increase of the spin-up over spin-down ratio with increasing energy as experimentally shown by TR-2PPE experiments on Co[106]. Yet, it contradicts measurements of a CoFe-based MTT obtained by Van Dijken *et al.* who found a decrease of this ratio[84]. The latter result could arise from collection of non-ballistic electrons. Thus, measured characteristic length value corresponds to attenuation lengths and not mean-free paths, explaining this difference.

Electron-electron mean free paths are now included in our model. Two spin channels are considered with 75% of injected electrons being spin-up and 25% being spin-down. The two channels are treated independently for the whole transport through the base. As described in section II.4 – 2. (see Table II.1), electrons can suffer different kind of electron-electron scattering. These interactions can produce secondary electrons with different spin orientation and different energy depending on the mechanism considered. The probability of scattering is given by exponential expression as introduced in section II.1 – 2 (see Eq. II.3). Thus, these probabilities now depend also on the spin of incoming electrons in addition to energy (see Table II.1). We also consider possible the collection of secondary electrons excited from the conduction band in addition to the scattered initial hot electron. Therefore, for each mechanism

presented on table II.1, one of the two electrons generated can be collected. Secondary electrons are still assumed to be produced in the CoFeB(4) layer.

New terms added to equation III.3 to describe contribution of secondary electrons to transfer ratio can be expressed with a general expression such as:

$$TR_k^{\sigma\to\sigma'}(V_{inj}) = T_{sch}\left(\frac{V_{inj}-\omega_k}{2}\right).T_{el}.C_k.\left(1-e^{\frac{-t_{CoFeB}}{\lambda_k^{\sigma}(V_{inj})}}\right)e^{\frac{-t_{CoFeB}}{\lambda_{k'}^{\sigma}(V_{inj})}}e^{\frac{-t_{\left[\frac{Co}{Ni}\right]}}{\lambda_{\left[\frac{Co}{Ni}\right]}^{\sigma'}\left(\frac{V_{inj}-\omega_k}{2}\right)}}e^{\frac{-t_{Cu}}{\lambda_{Cu}\left(\frac{V_{inj}-\omega_k}{2}\right)}} \qquad (II.17)$$

Where a secondary electron of spin σ' is generated after a hot electron of spin σ scattered through a mechanism with a k-band. ω_k describes the energy shift of the band considered. It equals 0 in case of an interaction with a sp-band (first column of Table II.1) and 0.5eV in case of an interaction with a majority d-band (second column of Table II.1). It should be noted that the energy repartition coefficient is supposed to be equal to 0.5 in order to simplify the model. The coefficient C_{sp}/C_d is supposed to be independent of the spin, with the same values as that used in sections II.3 – 2 and II.3 – 3.

Figure II.31 shows TR given by this model with contribution from the primary electrons for low energies and that of secondary electrons at higher energies. Presence of minority spin electrons in injected current does not change much the first part of the curve as they are totally scattered in the base with no possibility of collection. Thus, energy-dependence of this part is mainly due to that of majority spin electrons. For secondary electrons contribution, only three of them were plotted on figure II.31. All other processes lead to negligible contributions to the TR in regard of the others. Only one mechanism contributing to our model involves minority spin electrons : $TR_{sp}^{\uparrow\,to\,\downarrow}$. For $TR_d^{\uparrow\,to\,\downarrow}$, the electron-electron mean-free path in [Co/Ni] for minority spin electrons is so short that almost all those electrons are being scattered again. Moreover, $TR_{sp}^{\uparrow\,to\,\downarrow}$ (dashed green line) reaches its maximum much earlier than $TR_{sp}^{\uparrow\,to\,\uparrow}$ (dashed orange line) with much lower values for the former one. It is the sign that this contribution is limited due to the short mean-free path for minority spin electrons crossing the second ferromagnetic layer. Figure II.31 also shows the absence of scattering mechanism for spin-down injected electrons contributing for the modeled transfer ratio. This can be understood as the mean-free path for those of minority spin hot electrons being so short in CoFeB that multiple scatterings are expected for them for energy range considered. Yet maybe expression for $TR_d^{\downarrow\,to\,\uparrow}$ given by equation II.17 is not appropriate to describe transport related to this scattering mechanism. Indeed, difference in term of transport when the scattered electron considered goes from minority to majority spin is huge. Thus, if this electron interacts in the first nanometer of

the CoFeB layer and becomes a spin-up electron, it can cross the rest of the base much easily than what is predicted by our model.

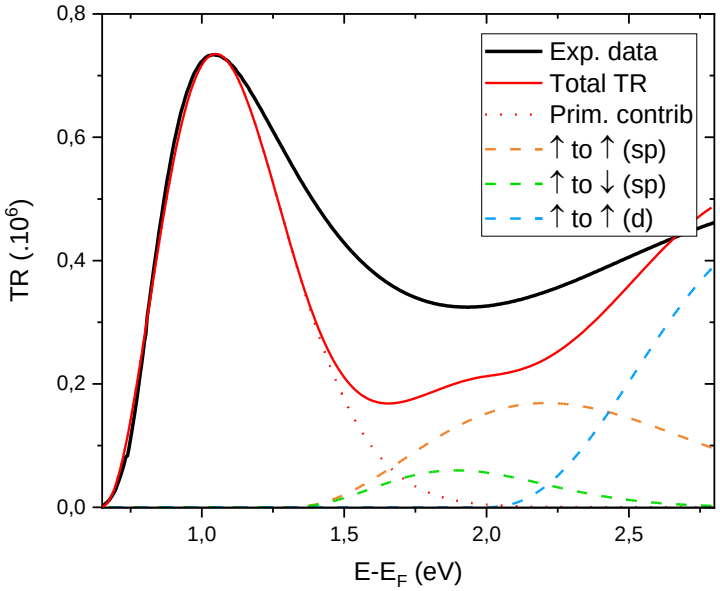

Figure II.31: Model for TR taking spin-dependence of the scattering into account. Dotted red line shows primary electrons contribution, dashed orange line that of spin-up to spin-up electron generation with a sp-band, dashed green line that of spin-up to spin-down with a sp-band and dashed blue line that of spin-up to spin-up with a d-band. Total TR modeled is described by the red solid line.

This model is an extension of that shown in section II.3. Indeed, if one considers that only secondary electrons corresponding to incoming majority spin electrons are collected (transitions from spin-up to spin-up), this model tends reproduce the trend shown in figure II.21 with orange and blue dashed lines. Knowing which secondary electron is collected is a difficult question. Both secondary electrons are supposed not to be undistinguishable. Yet, due to exchange interaction both energy and spin asymmetries arise between those secondary electrons. Therefore, it might be possible to tackle this question if the different mechanisms contribution to TR are disentangled.

To conclude about this extended model, no clear improvement concerning the description of experimental transport is seen by adding contributions of mechanisms shown in table II.1 in equations (see Eq. II.17). A new channel of collected minority spin electrons (green dashed line on Fig. II.31) appears at the cost of initial mechanism (orange dashed line on Fig. 31). Absence of other scattering processes associated with minority spin electrons is due to a short mean-free path for theses electrons. It is supposed to be so short that electrons can suffer several interactions before crossing the base.

Another question not considered yet is a possible spin-flip associated with an electron-electron interaction. Most studies considered interacting electrons to remain in their respective spin channel (no spin-flip). Yet, theoretical work[77,129] introduced a possible spin-flip mechanism following an electron-electron interaction depending on both spin and energy (see Fig. II.29). In our MTT, both ferromagnetic layers have Ni-like DOS. Thus, for both spin-up and spin-down electrons, interactions are supposed to be dominated by non-spin-flip mechanism. Even by considering that minority spin electrons are turning into majority ones, modeled TR shown on figure II.31 is not affected much. Yet as explained earlier, this model

may not perfectly take into account a spin-flip mediated process described by $TR_{sp}^{\downarrow to \uparrow}$ for the same reasons as $TR_{d}^{\downarrow to \uparrow}$.

To further understand a possible spin-flip contribution to electron-electron scattering and also to observe a possible contribution related to minority spin electrons, another device has to be designed. In a planar MTT, all magnetizations are lying in the plane of the sample and magnetic configurations can be switched to favor transport of different spin populations (minority/majority).

Experiments on planar MTT

In order to further investigate the physics described by our model, we designed a planar MTT with a similar structure as that shown on figure II.1 – d). Contrary to the MTT presented so far in this study with non-colinear magnetizations, a planar device have all three anisotropy axes lying along the same axis. Thus with different coercive fields for each ferromagnetic layer, it becomes possible to switch a given magnetization without affecting the two others. This means that 4 new states (PPP, PA_PP, PPA_P, PA_PA_P) are now accessible as opposed to our current device which only gives one state (PPP). By comparing hot electrons transport measurements in these four configurations at low energy (<1eV), it is possible to confirm that spin-dependent electron-electron mean-free paths taken in this model matches that of the literature. Furthermore by applying our model for energies above twice the Schottky barrier height in these four different configurations, it should be possible to verify multiple assumptions made so far: presence of a d-band mechanism contributing to electron-electron scattering, collection of scattered initial hot electron instead of that from the Fermi level, absence of spin-flip process participating to hot electrons transport.

To do so, we deposited a stack based on similar structure:

Pt(5)/IrMn(7.5)/Co(2)/Ta(0.5)/CoFeB(2)/MgO(2.8)/CoFeB(y)/Cu(3.5)/Co(3)/IrMn(3)/Cu(5)/Ta(1)/Cu(5)//Si(100)

Here, the [Co/Ni] multilayer is replaced by a Co(3)/IrMn(3) layer. As mentioned earlier in this manuscript, IrMn is an antiferromagnetic layer that couples to the adjacent ferromagnetic layer to increase and shift the coercivity of the latter one. So, both the top electrode and this Co(3) analyzer layer are biased by a coupling with IrMn. The thickness of each IrMn layer is different (7.5nm and 3nm respectively) in order to change intensity of the coupling. Therefore, the Co(3) can be switched without switching the top electrode. Bottom CoFeB(y) electrode remains not biased, so that only a weak magnetic field is required for its reversal.

Figure II.32 shows hysteresis loop measured with VSM on a CoFeB(3) thin film in an in-plane configuration. On this figure, three minor loops can be distinguished and associated with each ferromagnetic layer. The first one centered around 0Oe is supposed to correspond to the CoFeB(3) layer as there is no bias. A second around between -150Oe and -70Oe is attributed to the top electrode. Here, the exchange bias is the most significant. The remaining loop that lies between -80Oe and 0Oe shows the reversal of the bottom Co(3) analyzer layer. The fact that the jump for this reversal is so high in comparison to that of the CoFeB(3) with same thickness may suggest a possible coupling between the two layers. A study with variation of CoFeB thickness was made to minimize this effect.

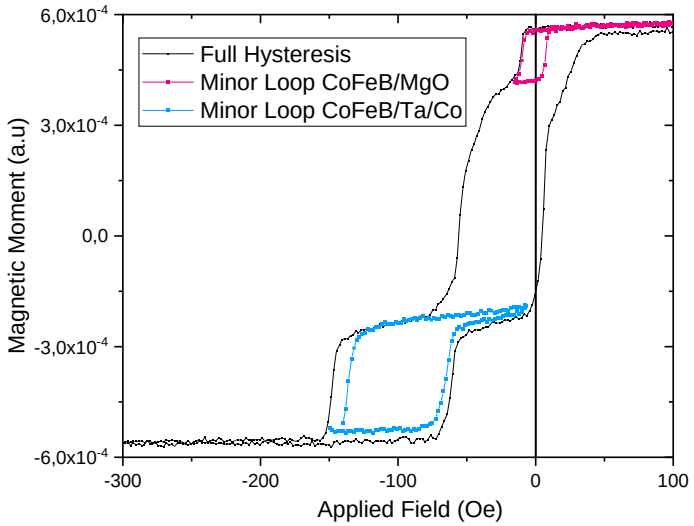

Figure II.32: Magnetic moment as a function of applied field in IP configuration. This sample corresponds to a CoFeB(3) thin film with stack structure given in the text.

This stack was then patterned using a four steps UV-lithography process to enable three-terminals measurements of the device. In order to check properties of the tunnel junction, tunnel resistance of the MTJ part in the MTT was characterized. Figure II.33 shows such measurements performed at 50K for an applied voltage of +10mV. Associated TMR is around 60% which is great considering that growth and annealing process were optimized for the Schottky barrier quality instead of the MgO barrier. Figure II.35 shows several switching fields: 0Oe, 250Oe, 500Oe. The former one is associated with the bottom CoFeB(3) electrode. This layer magnetization reverses for low field values as seen on figure II.35. The other loop lying between 250Oe and 500Oe correspond to the switching of the top electrode. Exchange bias observed here is much stronger than that of thin films using VSM (see Fig. II.32). Yet, decoupling of the two layers is clear enough to stabilize both parallel and antiparallel configurations of the magnetizations.

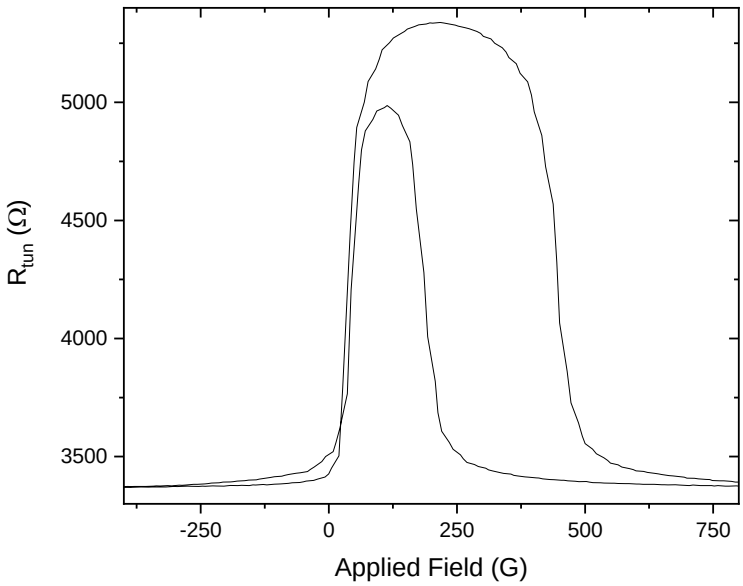

Figure II.33: Tunnel resistance R_{tun} measurement at 50K performed on a CoFeB(3) planar MTT with stack structure mentioned in the text.

The only remaining layer yet to characterize in the full structure is the Co(3)/IrMn(3) layer. As this layer lies deep in the base, the only way to observe its switching is through hot electron measurements. Magneto-current exceeding 2000% was experimentally observed on MTT with a magnetic base with in-plane magnetizations developed at Institut Jean Lamour[81]. Thus, reversal of the Co(3)/IrMn(3) is expected to induce a huge change in the hot electron current. By observing at the same time variations of TMR of the tunnel junction and TR in the base, contribution from each magnetization reversal should be disentangled.

Figure II.34 shows hot electrons measurement for two temperatures, 25K (left) and 100K (right). A magnetic field is applied in the sample plane, in the bias direction. Applied voltage for injection is -1V. this value is well above the Schottky barrier height in order to collect enough hot electrons to have a proper signal, but low enough not to collect secondary electrons. The applied field does not exceed +250Oe in order not to observe the switching of the pinned top electrode of the MTJ. Therefore, changes in the measured signals can be only attributed to CoFeB(3) and Co(3)/IrMn(3) magnetization reversals.

Measurements for temperatures shown on figure II.34 have the same variation with magnetic field. The TMR signal (red solid line) goes from its lowest to highest value around 0Oe. Thus, sharp changes in the TR (black solid line) for the same field values can be attributed to the reversal of the CoFeB(3) layer. Identification for the effect of the Co(3)/IrMn(3) layer is more difficult. Around -150Oe and -100Oe for 25K and 100K respectively, a change about 15% of TR can be observed. Considering that this change is far from 0Oe, it could be attributed to a biased layer. Yet, 15% is far from the expected 2000%.

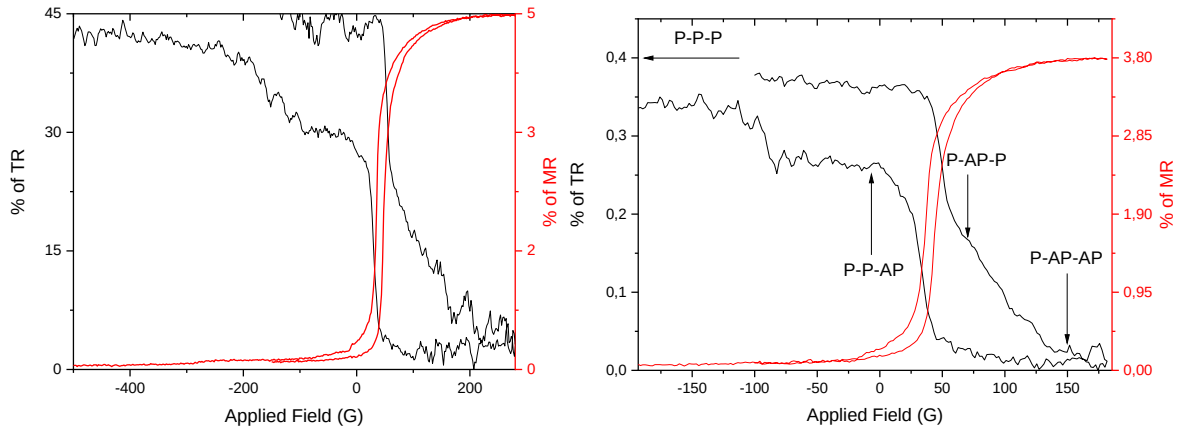

Figure II.34: Hot electron measurements for a CoFeB(3) planar MTT at 25K (left) and 100K (right). Injection voltage is set at -1V for both measurements. Black line corresponds to TR while red one stands for TMR of the tunnel junction.

Figure II.35 shows TR measurement at 25K for the three different magnetic states indicated by arrows on figure II.34 – right. A distinct variation with injection voltage shows that differences in TR of figure II.35 are not artifacts. Still, another strange detail can be observed on figure II.35. The Schottky barrier height associated with this measurement is around 0.78eV. It is much higher than what was seen on our similar Cu/Si(100) Schottky barriers deposited for this work. Contamination of the Schottky contact with diffusion of Mn could affect the height of the barrier. Schottky barrier using Mn/Si(100) contact is indeed expect to be higher than our Cu/Si(100) one. Such a contamination of the Schottky barrier could also induce non-conservation of the wave vector while hot electrons are entering the semiconductor.

Therefore, electrons are not ballistic anymore and transport cannot be interpreted as previously. Moreover, the presence of an antiferromagnetic IrMn can also affect spin-dependent hot electron transport by reducing the magnetocurrent of the device. This latter explanation would explain low TR variation but not the high Schottky barrier height value.

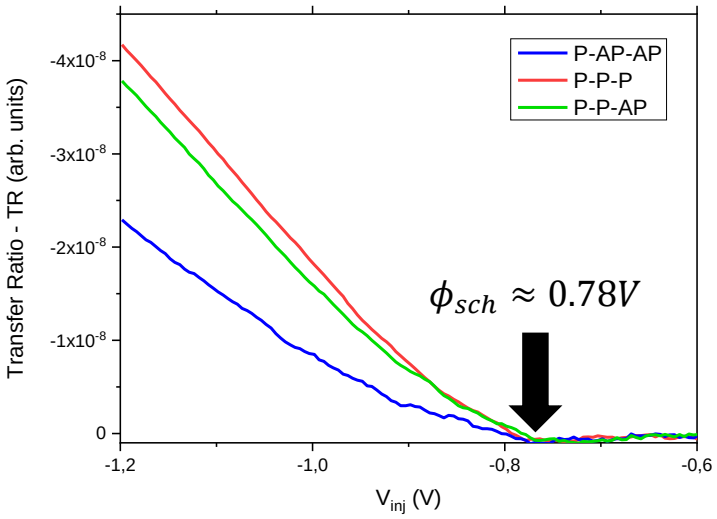

Figure II.35: Transfer ratio at 25K as a function of injection voltage for the three magnetic states identified on Fig. II.34.

Key takeaways for Chapter II:

- **Contribution of inelastic scattering allows a quantitative description of hot electrons transport for low energies**
- **For high energies, secondary electrons generated by electron-electron interactions are good candidates to explain increase of transfer ratio**
- **Our model gives a qualitative description of transport considering collection of majority spin electrons**
- **Addition of spin-dependent scattering mechanisms shows no improvement of our model**
- **A planar magnetic tunnel transistor can help measuring complex scattering processes. Yet, no device could be achieved to answer these questions**

Chapter III:
Spin precession in CoFeB

III. Spin Precession in CoFeB

III.1 – Context

Modern magnetoelectronic devices are based on the control of electron spin direction and its injection into an adjacent layer to either store, read or transfer information. In the early hours of spintronics, spin valves[132,133] and magnetic tunnel junctions[16,23] were used for their spin filtering effects with conventional collinear magnetizations structure for electronic devices. Yet, structures based on non-colinear configurations can be interesting for applications as long as the spin orientation can be controlled between 0° and 90° while exiting a ferromagnetic layer[20]. Therefore, further understanding and control of this degree of freedom is essential to enable the development of ultralow energy spintronic devices.

Previous studies showed the possibility of controlling the spin polarization direction of an electron current using external parameters such as applied voltage or magnetic field[134–136] for several class of materials. In each case, the spin precesses under the presence of an effective field. Moreover, transport has to take place over several micrometers due to low values of the molecular field in studied structures. Full rotation of electronic spin over few nanometers is desirable in order to limit scattering mechanisms and also to all integration in spintronic devices. In the case of ferromagnet, spin polarization could be controlled through an internal molecular field as demonstrated by Weber *et al.*[137]. This molecular field is related to the exchange interaction and gives rise to the magnetization of the ferromagnet. Concerning ferromagnets, the molecular field reaches hundreds of Teslas[1,137] much higher than values obtained with macroscopic magnets. Therefore, the distance required for rotating spins can be reduced from micrometers to nanometers. It allows manipulation of electronic spin in perpendicular structures composed of ultrathin multilayers. Such phenomena can be integrated into existing CMOS-compatible devices with only a single layer used for control of the spin orientation. Yet, values of the molecular field experimentally observed in this energy range is still too high[1] compared to that of actual applications. Tailoring a ferromagnetic layer with a tunable molecular field of reduced intensity could enable the use of precession phenomenon to manipulate electronic spin.

III.1 – 1. Electronic spin precession

Volume precession

In order to evaluate the motion of a spin associated to an electron with an energy E ($>E_F$) travelling through a (magnetic) metallic base, the time dependent Schrödinger equation has to be solved:

$$i\hbar\frac{\partial}{\partial t}|\psi(t)\rangle = \widehat{H}|\psi(t)\rangle \qquad (III.1)$$

Where $\psi(t)$ is the electron quantum state. Considering that $|\uparrow\rangle$ and $|\downarrow\rangle$ are the stationary solutions of the spin state associated to $E_\uparrow$ and $E_\downarrow$ energies respectively, the solution of this Schrödinger equation is given by:

$$|\psi(t)\rangle = C_\uparrow(t).e^{+i\frac{E_\uparrow}{\hbar}t}|\uparrow\rangle + C_\downarrow(t).e^{-i\frac{E_\downarrow}{\hbar}t}|\downarrow\rangle \qquad (III.2)$$

Where $C_{\uparrow(\downarrow)}(0)$ depend on the initial spin state entering in region where precession occurs and the time evolution is linked to the spin filtering effect. A time dependent dephasing between the two spin states will occur that leads to a precession motion. The time dependent precession is given by $\frac{E_\uparrow - E_\downarrow}{\hbar} t$ that can be converted in a space dependent precession $\frac{E_\uparrow - E_\downarrow}{\hbar} \frac{d}{v(E)} = \varepsilon^*.d = \varepsilon$ where d is the layer thickness (considering propagation perpendicular to the interface) and $v(E)$ is the velocity at the injection energy.

The components of the polarization vector resulting from the precession can be calculated using the product of the initial density matrix ρ (describing the initial polarization) and Pauli matrix σ_i $(i = x, y, z)$ in the state $\psi(t)$:

$$\boldsymbol{P} = \frac{\langle\psi(t)|\rho\sigma|\psi(t)\rangle}{\langle\psi(t)|\psi(t)\rangle} \qquad (III.3)$$

This equation III.3 describs the rotation of the polarization vector **P** starting from an initial state given by density matrix ρ, under the effect of the local magnetization described by the Pauli matrix σ. In the case of a fully saturated ferromagnetic layer whose magnetization is oriented in the z direction, equation III.3 describes the rotation of **P** around this axis. Therefore, we obtain from equation III.3:

$$P = \begin{cases} 2\frac{P_0 C_\uparrow C_\downarrow}{C_\uparrow^2 + C_\downarrow^2} cos\left(\frac{E_\uparrow - E_\downarrow}{\hbar} t\right) \\ 2\frac{P_0 C_\uparrow C_\downarrow}{C_\uparrow^2 + C_\downarrow^2} sin\left(\frac{E_\uparrow - E_\downarrow}{\hbar} t\right) \\ P_0 \frac{C_\uparrow^2 - C_\downarrow^2}{C_\uparrow^2 + C_\downarrow^2} \end{cases} = \begin{cases} P_0\sqrt{1-A^2}\cos(\varepsilon) \\ P_0\sqrt{1-A^2}\sin(\varepsilon) \\ P_0 A \end{cases} \qquad (III.4)$$

By introducing the asymmetry factor A = $\frac{C_\uparrow^2 - C_\downarrow{}^2}{C_\uparrow^2 + C_\downarrow{}^2}$. Coefficients $C_\uparrow$ and $C_\downarrow$ are proportional to transmitted currents for both spin channels in the precession layer. As the transport is perpendicular to interfaces, the population of ballistic electrons in the metallic base decays following a $\exp\left(-\frac{d}{\lambda_{\uparrow(\downarrow)}}\right)$ law along the layer thickness, where $\lambda_{\uparrow(\downarrow)}$ is the mean free path of spin-up (resp. spin-down) electrons. The spin asymmetry can then be rewritten as : $A = \tanh\left(\frac{d}{2\lambda^-}\right)$ where $\frac{1}{\lambda^-} = \frac{1}{\lambda_\downarrow} - \frac{1}{\lambda_\uparrow}$.

Thus, by combining equations III.4 and that of the asymmetry factor A, we obtain an expression of the polarization vector as a function of the two rotation angles θ and ε, along with material parameter d and λ^-:

$$P = \begin{cases} P_0\cos(\theta)\cos(\varepsilon) \\ P_0\cos(\theta)\sin(\varepsilon) \\ P_0\sin(\theta) \end{cases} = \begin{cases} P_0\cos(\varepsilon)/\cosh\left(\frac{d}{2\lambda^-}\right) \\ P_0\sin(\varepsilon)/\cosh\left(\frac{d}{2\lambda^-}\right) \\ P_0\tanh\left(\frac{d}{2\lambda^-}\right) \end{cases} = \begin{cases} P_0\cos(\varepsilon^*.d)/\cosh\left(\frac{d}{2\lambda^-}\right) \\ P_0\sin(\varepsilon^*.d)/\cosh\left(\frac{d}{2\lambda^-}\right) \\ P_0\tanh\left(\frac{d}{2\lambda^-}\right) \end{cases} \qquad (III.5)$$

The two introduced rotation angles θ and ε describe orientation of the polarization vector with respect to the precession layer magnetization and to the initial polarization vector. Futher description related to these angles is given by figure III.1 (see below).

Interfacial precession

An additional precession term can arise when an electron is travelling through a magnetic junction, the molecular field of the right electrode may affect the direction of its spin. If both magnetizations are not collinear, an additional dephasing occurs at the interface. Interfacial spin precession was already demonstrated considering reflection from ferromagnetic surfaces, but for higher energies[138].

Taking Slonczewski's work[20] (see I.1-2 and I.1-4) to model spin-dependent tunnel transport through a MTJ, the wave-function in the second electrode can be written as a superposition of the two spin states:

$$\psi_3 = r_\uparrow e^{i\varphi_\uparrow}|\uparrow\rangle + r_\downarrow e^{i\varphi_\downarrow}|\downarrow\rangle \qquad (III.6)$$

From this equation, two rotation angles can be determined:

$$\begin{cases} \varepsilon^{int} = \varphi_\uparrow - \varphi_\downarrow \\ \theta^{int} = Arctan\left(\dfrac{|r_\uparrow|^2 - |r_\downarrow|^2}{2|r_\uparrow||r_\downarrow|}\right) \end{cases} \qquad (III.7)$$

Both expressions related to an interfacial rotation have a similar form as that for the volume. The filtering angle θ^{int} depends on reflection/transmission coefficient at the MgO/Ferromagnet interface. The precession expression can be expressed as a function of incoming wavevectors:

$$\varepsilon^{int} = Arctan\left(\frac{k_\uparrow^2 - k_\downarrow^2}{2\kappa k_\uparrow}\right) - Arctan\left(\frac{k_\uparrow k_\downarrow - \kappa^2}{\kappa(k_\uparrow + k_\downarrow)}\right) \qquad (III.8)$$

where k_σ is electron wave vector associated with a σ spin in the ferromagnetic layer where precession takes place and κ, the imaginary wave vector of electrons inside the tunnel barrier.

Therefore, this interfacial precession will depends on injection energy, barrier potential and exchange energy in the ferromagnet. From equations III.5 and III.11, contributions from both volume and interfacial terms can be discussed when interpreting precession signals.

III.1 – 2. How to access spin precession at low energy

Measuring principle

Following the formalism introduced in section I.2-2. and I.2-3., we can now express the measured transfer ratio after filtering of the analyzer layer :

$$TR = TR^{\perp}(1 + MC^{\perp}\boldsymbol{P}\cdot\boldsymbol{m_{an}}) \qquad (III.9)$$

Where **P** is the hot electron spin polarization vector after crossing the active layer and $\mathbf{m_{an}}$ is a unit vector pointing along the magnetization direction of the analyzer[83]. $TR^{\perp}$ represents the of the transfer ratio in a crossed geometry, while $MC^{\perp}$ (defined in Eq. I.39) accounts for spin-filtering.

The projection of the polarization vector is given by $\boldsymbol{P} \cdot \boldsymbol{m_{an}} = P_0 \cos(\theta) \sin(\varepsilon)$ where θ is the filtering angle and ε the precession angle. Using equation III.5 in different configurations, the two previous angles can be obtained: parallel ($\parallel$), clockwise ($\circlearrowright$) and counter-clockwise ($\circlearrowleft$) are needed as presented on figure III.1.

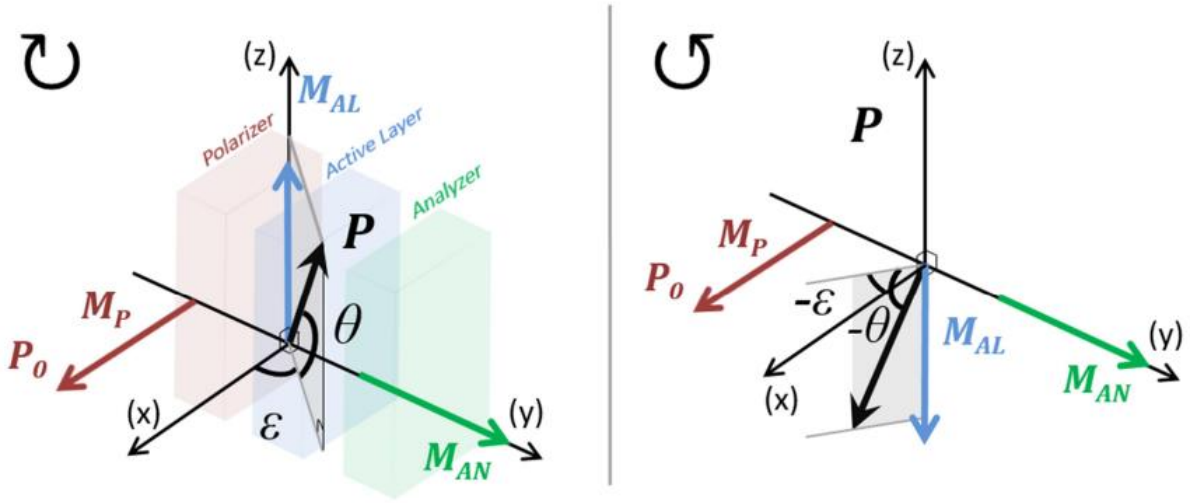

Figure III.1: Angles of precession (ε) and filtering (θ) of the spin polarization vector of an electron beam injected into a magnetic layer with a magnetization $\boldsymbol{M_{AL}}$. From Vautrin et al.[1].

Associated transfer ratios can be expressed as $TR^{\parallel} = TR^{\perp}(1 + MC^{\perp}P_0)$ and $TR^{\circlearrowright/\circlearrowleft} = TR^{\perp}(1 \pm MC^{\perp}P_0 \cos(\theta) \sin(\varepsilon))$. Thus, the product $\cos(\theta) \sin(\varepsilon)$ (also denoted as Δ_{rel}TR) can be expressed as a function of experimental quantities:

$$\Delta_{rel}TR = \cos(\theta) \sin(\varepsilon) = \frac{TR^{\circlearrowright} - TR^{\circlearrowleft}}{2TR^{\parallel} - (TR^{\circlearrowright} + TR^{\circlearrowleft})} \qquad (III.10)$$

Two additional magnetic configurations can be obtained using the switch of $\mathbf{m_{an}}$ as will be shown in the next paragraph.

3D Structure

The 3D structures used are similar to that designed by Vautrin *et al.*[1,83]. Hot electrons injection is ensured by the CoFeB/MgO/X tunnel barrier, with X being a ferromagnetic layer (CoFeB, CoAl or CoCu). The CoFeB/MgO interface is supposed to bring higher spin-polarization of the hot electrons due to symmetry filtering during tunneling (see section I.1-7.).

In the very simple Julliere model, the polarization can be expressed from the TMR measured in the MTJ (see Eq. I.5). In the case of a symmetric CoFeB/MgO/CoFeB junction grown in this study, the TMR lies around 50% indicating a spin polarization of about 75% of injected electrons. The smaller value obtained for the TMR compared to the literature[139] can be explained by the low temperature of annealing (for preserving the Schottky diode and the perpendicular magnetic anisotropy in the [Co/Ni] analyzing layer) and by the [111] texture of the bottom layers that does not favor the growth of the tunnel barrier[90]. Hot electrons collection with both k and energy selection is made by a Cu/Si Schottky barrier. The height of the barrier is directly measured by the hot electron current and evaluated to be around 0.65eV.

In order to stabilize each configuration needed for measuring the precession signal of equation III.7, specifications concerning the MTT magnetic layer anisotropies are required. Since it is easy to define an in plane anisotropy through deposition conditions or shape of the electrode of the tunnel barrier, the precession layer will be in plane. So, a large variety of materials can be tested as precession material in our MTT structure.

To get crossed magnetizations across the MTJ, CoFeB layer used as a polarizer is pinned by an antiferromagnetic adjacent material. The presence of IrMn on top of the polarizer fixes the direction of the polarizer when no external field is applied. This exchange coupling is highest in the case of a [111] texture of the IrMn layer. Thus, to promote this texture, a Ta/Co stack is deposited on top of the CoFeB electrode. The amorphous Ta enables both the growth of Co along its close packed planes and the coupling of CoFeB and Co magnetizations. The final structure for the polarizer is :

IrMn(7.5)/Co(2)/Ta(0.5)/CoFeB(2)/MgO(2.8)

where numbers in parenthesis are the deposited thicknesses in nanometers. The magnetic bias induced by exchange coupling of IrMn is initiated through an annealing at 200°C for one hour. A 600Oe external magnetic field is applied in the film plane during annealing so that when the sample is cooling down below Néel temperature of IrMn, the bias is fixed in the magnetic field direction. The use of IrMn ensures the presence of an unidirectional anisotropy that makes the magnetization of the CoFeB always in the same position whatever the magnetic history needed to orient the precession layer.

A [Co/Ni] multilayer is used as spin analyzer. The stack was optimized by Vautrin *et al.* to optimize both the perpendicular magnetic anisotropy and the magneto-current for a CoFeB/Cu/$[Co/Ni]_{xN}$ structure.

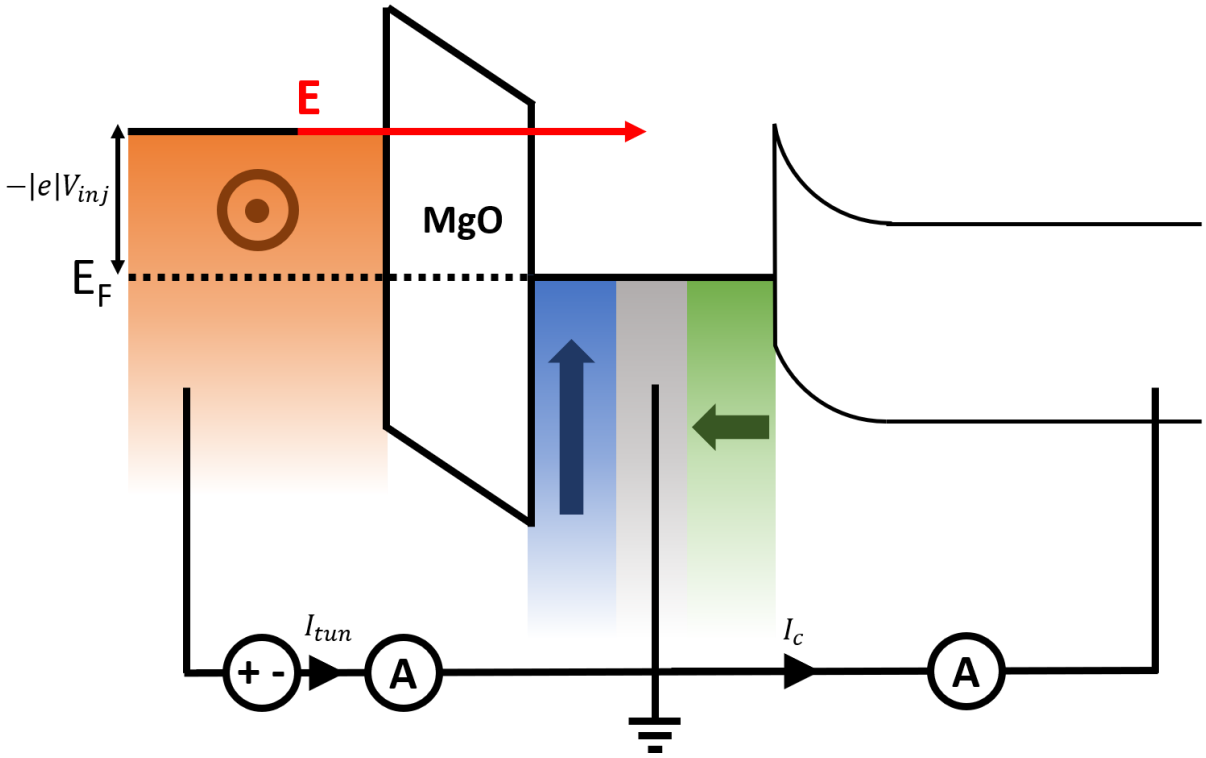

Figure III.2: MTT structure used for spin precession measurement. Orange layer represents the top electron (IrMn/Co/Ta/CoFeB), blue the precession layer and green the analyzer ([Co/Ni]$_{x5}$/Cu/Ta/Cu). A direct configuration of the magnetizations is shown on the figure.

In precession measurements performed by Vautrin *et al.* on similar MTT structures, the magnetization of the [Co/Ni] multilayer was stabilized perpendicular only in one configuration. Thanks to an additional magnet added on our experimental set-up, the perpendicular analyzer magnetization could now be reversed, that allows to measure two additional magnetic configurations. As a consequence, in equation III.6, $\mathbf{m_{an}}$ can be switched from +1 to -1.

Figure III.3 shows the results of the measurement of $\Delta TR = TR^{\circlearrowright} - TR^{\circlearrowleft}$ keeping the magnetic configuration of the injection and precession layers and reversing the magnetization of the [Co/Ni] multilayer. While the energy-dependence of ΔTR is related to that of $TR^{\perp}, MC^{\perp}, \ldots$ the change of sign is directly related to $\boldsymbol{P} \cdot \boldsymbol{m_{an}}$ as reversing the [Co/Ni] magnetization reverses the sign of the projection. However value of ΔTR is not strictly the same. This raises the question of the role of misalignments relative to the perfect crossed configuration on the measurement of filtering and precession angles.

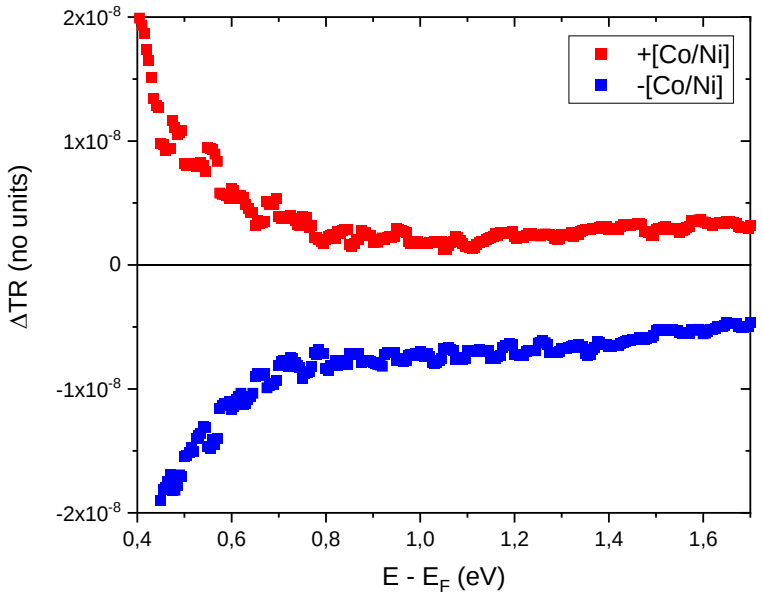

Figure III.3: Measurement of the precession signal $\Delta TR = TR^{\circlearrowright} - TR^{\circlearrowleft}$ as a function of injection energy for each [Co/Ni] magnetization direction with respect to direct orientation of the 3D configuration. The lack of symmetry between the two ΔTR can be explained by measurements fluctuations.The measurement is performed at 50K.

Misalignement

In the paragraph, we will check the impact of misalignments relative to a perfect cross configuration. Indeed, as zero-field state differs from the crossed configuration, a small magnetic field ($\sim 50Oe$) is applied in the film plane to reach the right configuration. Tunnel resistance measurement enables an estimation of the angle between the two electrodes magnetizations. Once tunnel resistance associated with crossed configuration is reached, precession measurements are performed. Still, the precession magnetization could realign during the hot electrons measurement, resulting in a signal different from the expected value if perpendicular state was achieved.

Around 90°

In the following, we will quantify the effects of angular misalignment errors and their potential impact on the precession angles. Therefore, we used a MTT with a CoFeB(1) precession layer to get currents as high as possible and limit the noise in the current measurement. Noise effects can come from different sources. One hand, static noise comes from measuring instruments and the overall environment. This was tackled by optimizing parameters of acquisition while measuring picocurrents. On the other hand, physical effects such as electron-phonon or electron-magnon scattering also affects transport and are inherent in the sample. However, lowering temperature of the measurements to 50K can limit such effects. At lower temperature, charge effects at the Schottky interface can affect measured signals[81].

For a precession measurement, three transfer ratio measurements need to be performed. Misalignment relative to a perfect cross configuration can be present in one of the clockwise or counterclockwise measurement. Thus, we start by studying such misalignment on one transfer ratio in the perpendicular configuration (here clockwise) while the other one is kept in the ideal

90°configuration. Therefore, the precession signal can be expressed as follow with Δγ being the deviation to 90°:

$$\Delta_{rel}TR(\Delta\gamma) = \frac{TR^{\circlearrowright}(\Delta\gamma) - TR^{\circlearrowleft}}{2TR^{\parallel} - (TR^{\circlearrowright}(\Delta\gamma) + TR^{\circlearrowleft})} \qquad (III.11)$$

Figure III.4 shows a diagram of the different magnetizations projected on the sample plane. The magnetic configuration corresponds to a clockwise one. Δγ indicates a slight deviation from perfect crossed configuration. Magnetization **M**$_{AL}$ is tilted by this Δγ angle from this position. As angle between electrodes magnetizations (**M**$_P$ and **M**$_{AL}$) are directly related to the relative angle between the two[140], alignment error Δγ can be interpreted as a variation of tunneling resistance compared to that in the perpendicular configuration.

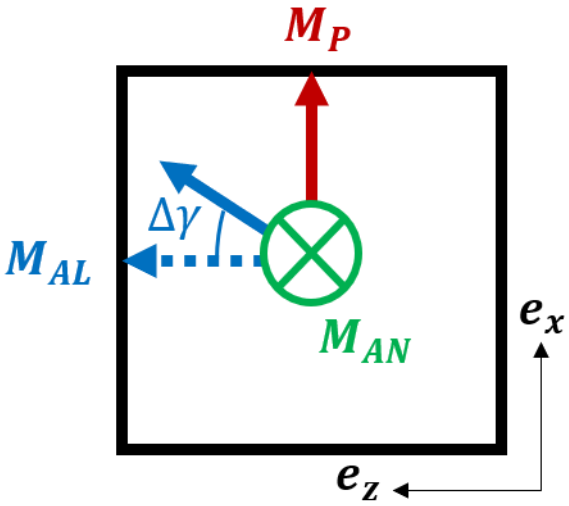

Figure III.4: Schematic top-cross view of a MTT. Each color and indication correspond to that of Fig. III.1. Misalignment error is indicated by Δγ in this clockwise magnetic configuration.

Figure III.5 shows the experimental results of a given range of misalignment angles. These measurements have been performed for the two [Co/Ni] analyzer configurations. Once again, for a crossed state with no misalignment, the precession is around the same absolute value but opposite while switching the [Co/Ni] magnetization. Around the crossed state ($\Delta\gamma = \pm 10°$), the precession signal $\Delta_{rel}TR$ is found to decrease linearly with the misalignment angle (see dashed lines) in both analyzer configurations.

By introducing an additional misalignment error in the counterclockwise configuration measurement, interactions between both errors can be evaluated. Thus, following equation III.11 of precession signal dependence on the misalignment, we now have:

$$\Delta_{rel}TR(\Delta\gamma_1, \Delta\gamma_2) = \frac{TR^{\circlearrowright}(\Delta\gamma_1) - TR^{\circlearrowleft}(\Delta\gamma_2)}{2TR^{\parallel} - \left(TR^{\circlearrowright}(\Delta\gamma_1) + TR^{\circlearrowleft}(\Delta\gamma_2)\right)} \qquad (III.12)$$

with $\Delta\gamma_1$ and $\Delta\gamma_2$ being misalignment errors corresponding to clockwise and counterclockwise magnetic configurations respectively. They are defined in the same manner as $\Delta\gamma$ on figure III.4.

A similar decrease was found as showed in figure III.5. Figure III.6 summarizes all the precession signals measured for each combination of misalignment angles. Experimental data

acquired have been used to perform an interpolation resulting in this colored map. Value and sign of the precession are represented by the shade and the color (red/blue) of the area.

Influence of the [Co/Ni] magnetization orientation can be observed. The left map corresponding to negative saturation of the analyzer is dominated by the red area while the right map for positive saturation is dominated by blue area. The linear trend previously mentioned is retrieved on the maps: starting from given angle in the counterclockwise configuration, increasing misalignment in the clockwise measurement (from left to right) induces a decrease of the signal (from red to blue). The map also shows some symmetry. The diagonal going from the bottom left corner to the top right corner describes constant values for $\Delta_{rel}TR$. On the opposite, the error is the highest when the misalignment is of opposite sign (from top left corner to bottom right corner).

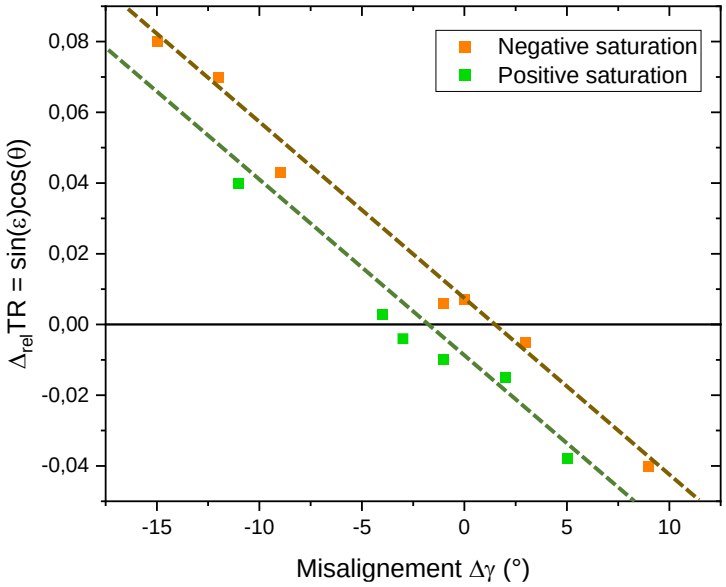

Figure III.5: Experimental measurement of the relative transfer ratio $\Delta_{rel}TR = sin(\varepsilon)\,cos(\theta)$ as a function of misalignment angle for the clockwise measurement (counterclockwise is kept crossed configuration). Dashed lines are a visual guide describing the linear variation of $\Delta_{rel}TR$ with the misalignment angle. For the perpendicular configuration ($\Delta\gamma$ = 0°) is opposite for the two saturation states of the [Co/Ni] analyzer.

As a conclusion of this study, one can state that impact of a misalignment error is minimized in the case the same error is repeated for both clockwise and counterclockwise configurations. In other words, if the same resistance state is verified before performing a measurement. A next step is to check the evolution of Δ_{rel}TR for higher angle deviations. Indeed, if the two electrodes magnetizations are collinear, the precession signal should be zero.

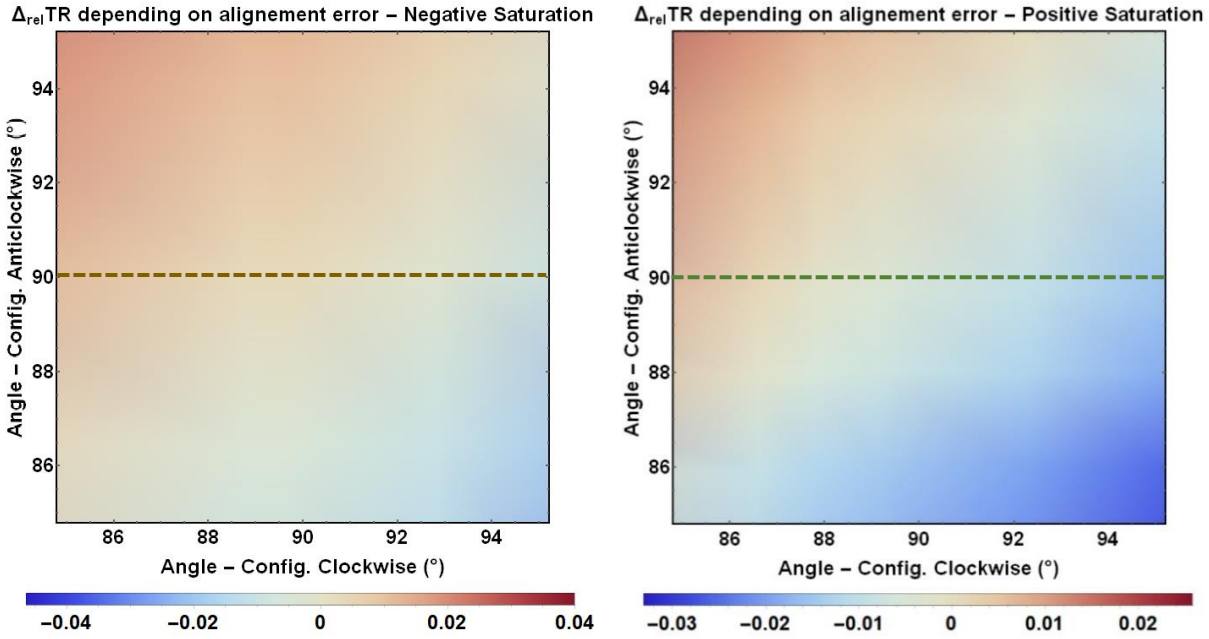

Figure III.6: Maps of the relative transfer ratio $\Delta_{rel}TR = sin(\varepsilon)\,cos(\theta)$ as a function of alignment errors in both clockwise and counterclockwise configurations for the two analyzer configurations. All the measurements have been performed on a CoFeB(1) MTT at 50K. Orange and green dashed lines corresponds to that of Fig. III.5.

At higher angle deviations

The misalignment is now considered to be the same for clockwise and counterclockwise configurations. Therefore the angle between the spin polarization vector and the precession layer is the same. In term of tunnel transport, this results in same resistance states in both configuration. This means the diagonal with constant value Δ_{rel}TR of figure III.6 is further explored for high values of misalignment.

Measurements were performed with the device and the same conditions used for figure III.5 and figure III.6. The misalignment goes now from -90° (parallel configuration) to +90° (antiparallel configuration). Two figures related to hot electron transport are plotted on figure III.7. On the left panel, $TR_{denom} = 2TR^{\parallel} - (TR^{\circlearrowright} + TR^{\circlearrowleft})$ is shown as a function of $\Delta\gamma$. TR_{denom} increases with higher misalignment angles from -60° to 90°. A discontinuity of this curve occurs at $\Delta\gamma = -90°$ (not shown here) as the value equals zero whereas all experimental measurements lie between $1{,}4.\,10^{-4}$ and $2{,}4.\,10^{-4}$. The red line represents a fit of the data using a A+B*sin(Δγ) function, with $A = 1{,}85.\,10^{-4}$ and $B = 0{,}45.\,10^{-4}$. The signal is well described by this sinus dependence on the misalignment angle.

The right panel of figure III.7 shows the precession signal $\Delta_{rel}TR = \sin(\varepsilon)\cos(\theta)$ as a function of Δγ. Variation of this value is not monotonous. While reaching zero for high misalignment angles ($\sim \pm$ 90°), $\Delta_{rel}TR$ is maximum between -30° and 0°. The red line serves as visual guide for a possible variation of the precession signal as a function of Δθ. Measured precession signal is almost maximum around perpendicular configuration of the two magnetizations. Errors on obtained values are minimized if one gets closer to the parallel configuration as $\Delta_{rel}TR$ is constant on the [-30°;0°] range.

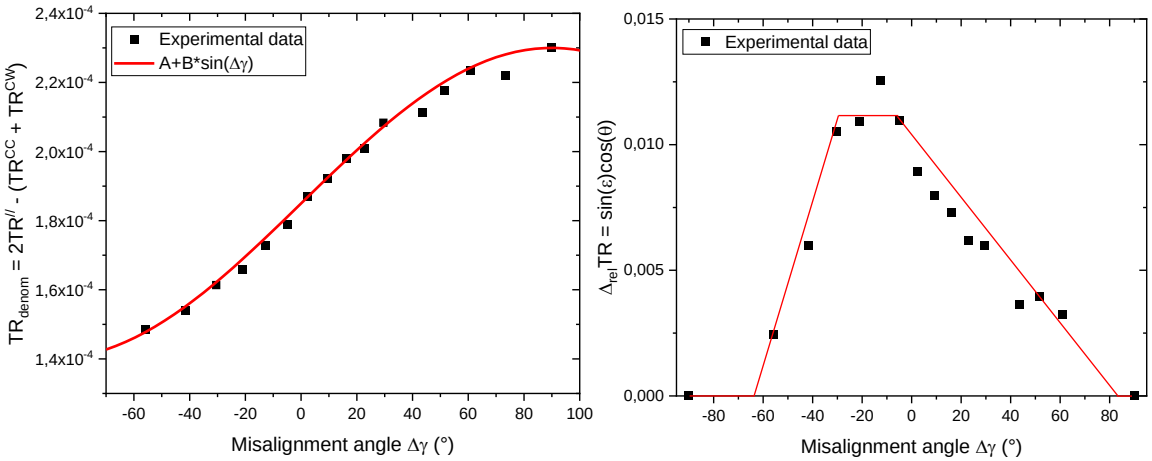

*Figure III.7: TR_{denom} a) and $\Delta_{rel}TR$ b) as a function of the misalignment angle between polarizer and precession magnetizations. a) Red line describes a fit of the data using a function A+B*sin(Δγ). CW stands for clockwise and CC, for counterclockwise. b) Thin red line is shown as a visual guide with a decrease of the signal with increasing angle and a maximum/plateau up to 0°.*

In this section, we showed our 3D MTT allows stabilization of five magnetic configurations. A clear effect of reversal of the [Co/Ni] magnetization on the precession signal was demonstrated. This proves both the reliability of our device for precession measurement and the controlled of the magnetizations orientation in our structure. Impact on misalignment errors was investigated and we showed no modification of the resulting precession signal over a 20° window for these measurements.

III.2 – Experimental measurement of spin precession in CoFeB

III.2 – 1. Introduction

Previous work

Previous work led by Vautrin *et al.* in our team investigated spin precession in ferromagnets for low-energy electrons[1]. This study was a first demonstration of electronic spin precession in the low energy range. Their theoretical calculation predicts an ultrafast precession of hot electrons crossing a ferromagnetic layer of few nanometers. Measurements with devices of several CoFeB thicknesses (1nm, 3nm, 4nm) in this study are explained with this calculation and taking into account roughness. Yet, the three samples cannot reproduce a full oscillation with CoFeB thickness as theoretically forecasted. Here, we focus on CoFeB MTT with a variation of thickness of 1nm, spaced by 0.2nm.

Magnetism

In order to study precession in CoFeB in the same conditions as Vautrin *et al.*[1], the deposition conditions were re-optimized to get the adequate magnetic properties. Vibrating Sample Magnetometer (VSM) measurements were performed on full films at room temperature, for active layer CoFeB thicknesses ranging from 3nm to 4nm, with steps of 0.2nm. Figure III.8 shows the results of those measurements when the magnetic field is applied in the field in-plane (IP) (left) and out-of-plane (OOP) (right). In the case of IP measurement, the field is applied along the direction of the exchange field.

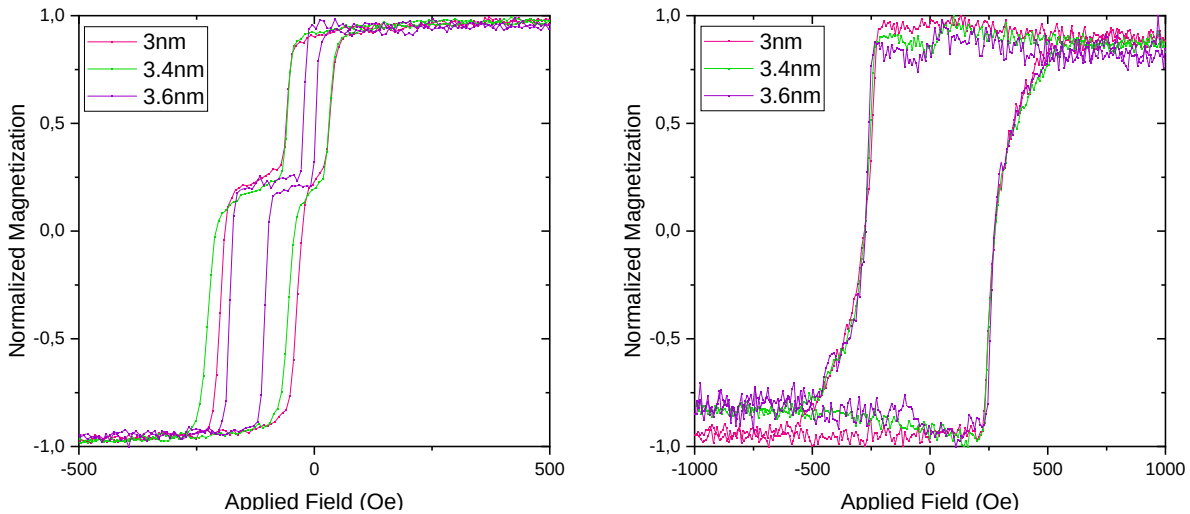

Figure III.8: Normalized magnetization as a function of applied field in IP (left) and OOP (right) configurations. Stacks studied are *Si[HF](100)//Cu(5)/Ta(1)/Cu(5)/Ni(0.6)/[Co(0.2)/Ni(0.6)]$_{x5}$/Cu(3.5)/CoFeB(y)/MgO(2.8)/CoFeB(2)/Ta(0.5)/Co(2)/IrMn(7.5)/Pt(5).*

On the left panel, two hysteresis loops can be observed independently of the thickness of the CoFeB layer. The first one centered around 0Oe, corresponds to the reversal of the soft CoFeB active layer. The second one shifted by -150Oe, corresponds to the magnetic response of the pinned CoFeB(2)/Ta(0.5)/Co(2)/IrMn(7.5) top layer. The coercive field associated with the top magnetic layer is higher than that of the CoFeB active layer because of the IrMn pinning. The magnetic contribution of CoFeB is a slightly lower than that of the top layer.

Only the switching of those two magnetizations with in-plane anisotropies can be observed on the left. Indeed, on the right panel, one can see the reversal of the [Co/Ni] multilayer with perpendicular applied field. This magnetic response confirms the PMA for the analyzer for all three samples with a coercive field around 400Oe. Furthermore, the shape of the hysteresis loop is kept intact while changing the thickness of the CoFeB layer showing that additional deposition has an effect on the magnetism of the [Co/Ni] multilayer.

Tunnel transport

Magnetic tunnel transistors based on the stacks previously measured were built using lithography processes. In a first place, characterizations of the MTJ part of the MTTs were performed in order to verify the magnetic configuration of each layer. Results of those resistance measurements for two temperatures are shown on figure III.9.

Starting from positive field values, the resistance increases as the field reaches 0Oe. However, it peaks and almost instantly goes back to its minimum value when applied field is negative. This corresponds to the parallel configuration of the two magnetizations (see section I.1-1). Now starting from negative field values, tunnel resistance rises again when applied field is around 0. The CoFeB precession layer follows the external magnetic field while the top electrode magnetization is pinned. Thus, the device reaches its maximum resistance value while the magnetizations are antiparallel. Passed a certain field value, the top magnetization is switched back and the parallel resistance state is retrieved.

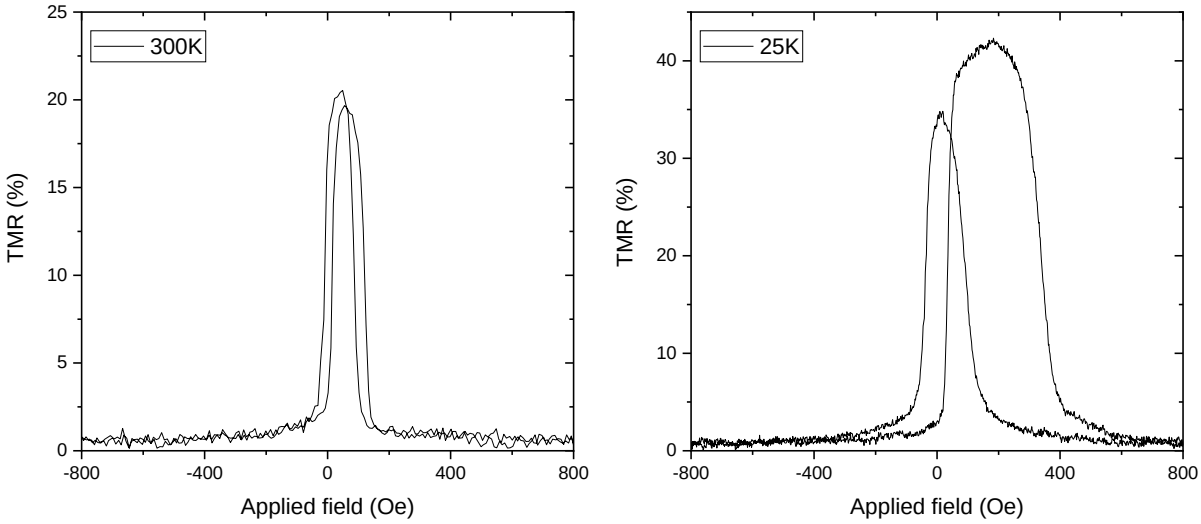

Figure III.9 : Tunnel magnetoresistance for a CoFeB(3.6) MTJ based on a stack similar to that of figure III.8 as a function of applied in-plane field, in the direction of the IrMn exchange field. Applied voltage is +10mV for both measurements and the temperatures are 300K for the left panel and 25K for the right panel.

The change of temperature affects the TMR measurement twofold: first the maximum TMR value increases while the temperature decreases (see section I.1 – 5). Secondly, the pinning and coercive fields of the top magnetizations are enhanced with lowered temperature. This results in an opening of the hysteresis cycle going from antiparallel to parallel configurations.

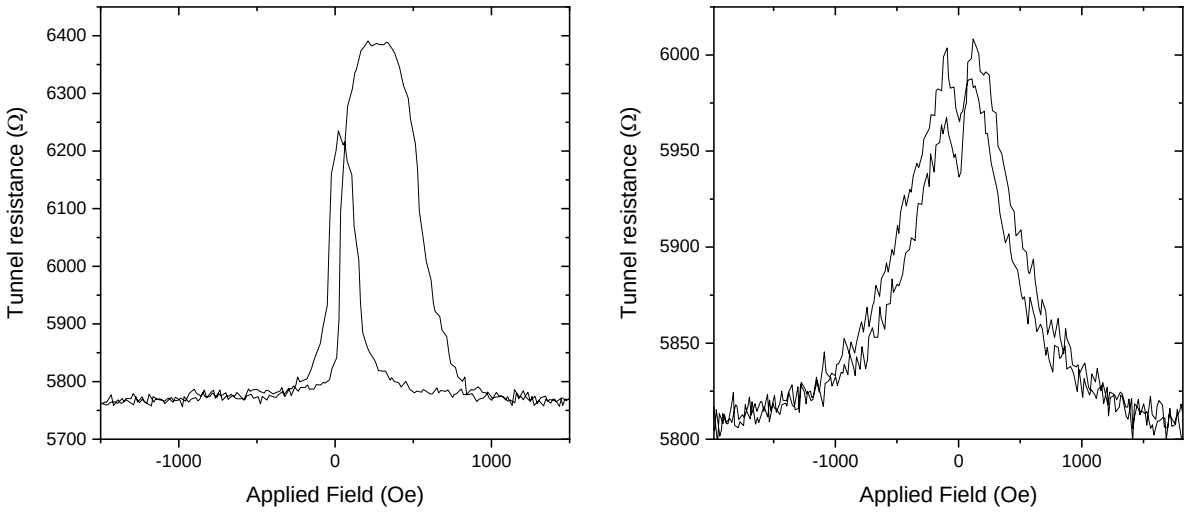

Figure III.10: Tunnel magnetoresistance at 25K with an applied voltage of +10mV for a CoFeB(3.4) device with similar stack structure as Fig. III.9. The left panel corresponds to a magnetic field applied in the exchange field direction and the right panel, in-plane at 90° from this direction.

Figure III.10 shows the comparison between reversal of the magnetizations when the in-place magnetic field is swept in the direction of the exchange field (left panel) or 90° apart from it (right panel). Both measurements were performed on the same device with same conditions. Symmetry of the tunnel resistance measured on the right panel comes from the perpendicular magnetic configuration. The pinned top magnetic layer slowly rotates towards the applied field while its value is increased. Free CoFeB layer switches near 0Oe, when the

top layer is already perpendicular. Therefore, almost no resistance change can be seen. Without the presence of the 0Oe drops, the TMR would reach 50% of its maximum value, thus confirming the presence of a perpendicular magnetizations configuration.

Hot electron transport

Figure III.11 shows two currents measurements performed at the same time on a CoFeB(3) at 50K. On the left panel, tunnel current (I_{tun}) is plotted against injection voltage (V_{inj}) for the three magnetic configurations used for spin precession measurements: clockwise (CW), counterclockwise (CC) and parallel. Red and blue curves associated with CW and CC configurations respectively, are the same. It proves that the injection is equivalent in both measurements. In the parallel configuration, as the resistance is lower than in a perpendicular one, the tunnel current is higher as seen on Fig.III.11 – left. For higher applied voltages, the difference between I_{tun} in parallel and in perpendicular configurations tends to decrease (see section I.1-4).

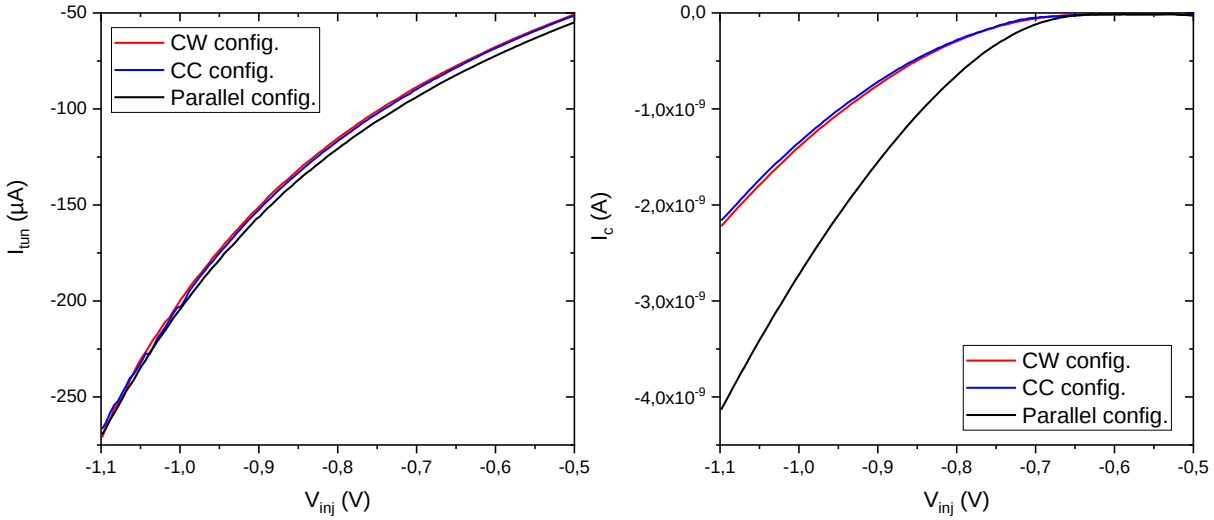

Figure III.11: Tunnel current (left panel) and collected current (right panel) as a function of injected voltage for a CoFeB(3) MTT at 50K in the three magnetic configurations (clockwise, counterclockwise and parallel).

On the right panel, collected current (I_c) is also plotted against V_{inj} for the same three magnetic configurations. The Schottky height corresponds to the voltage / energy for which hot electrons can overcome the barrier. For this device, this corresponds to a voltage around -0.65V. When the applied voltage is above this threshold, collected current starts to increase showing that more and more electrons can enter the semiconductor. A slight difference between CW and CC configurations can be observed (red and blue curves). Since injection currents are similar (see Fig.III.11 – left) this difference can only be attributed to a precession effect. Electron spins precess in the CoFeB layer and end up at the [Co/Ni] multilayer with different orientation leading in a different filtering. Now looking at the parallel configuration curve, the difference with perpendicular ones are greatly enhanced compared to that of injection (Fig.III.11 – left). Once again, this is a demonstration of the filtering affects in the spin-valve. A huge amount of electrons whose spins are not aligned with the [Co/Ni] magnetization gets thermalized and cannot participate to collected current.

III.2 – 2. Thickness dependence

Characterizations of both tunnel and collected currents (I_{tun} and I_c) in all three different magnetic configurations lead to the associated transfer ratios. The Transfer ratios resulting from previously shown currents ($TR = \frac{I_c}{I_{tun}}$) are plotted on figure III.12. All three TR show the same features as the collected currents (Fig. III.11 – right): Schottky barrier height lies around -0.65V, TR is slightly higher in CW configuration than in CC one, filtering effects lead to enhanced TR in the parallel configuration.

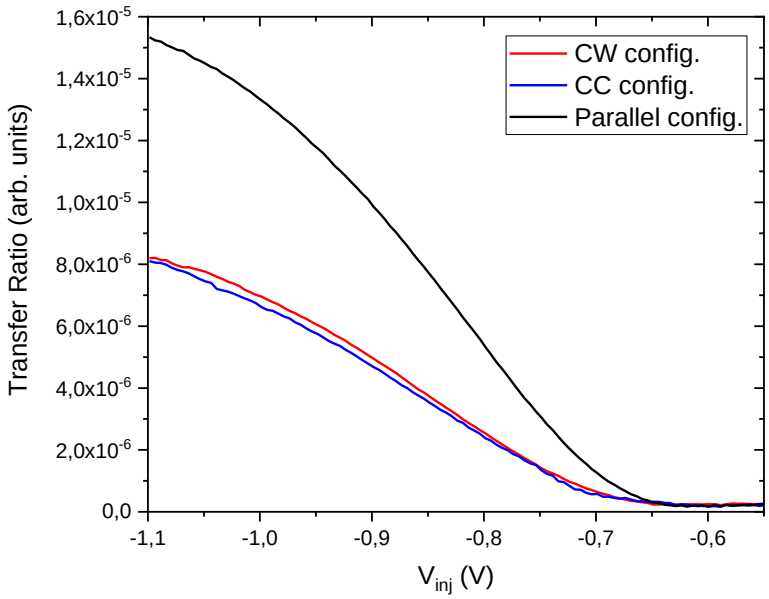

Figure III.12: Transfer ratio as a function of injected voltage for a CoFeB(3) MTT at 50K in the three magnetic configurations (clockwise, counterclockwise and parallel).

From those measurements, $\Delta_{rel}TR$ can be evaluated and sin(ε)cos(θ) can be extracted using (see section III – **Measuring principle**):

$$\Delta_{rel}TR = \sin(\varepsilon)\cos(\theta) = \frac{TR^{\circlearrowright} - TR^{\circlearrowleft}}{2TR^{\parallel} - (TR^{\circlearrowright} + TR^{\circlearrowleft})} \qquad (III.13)$$

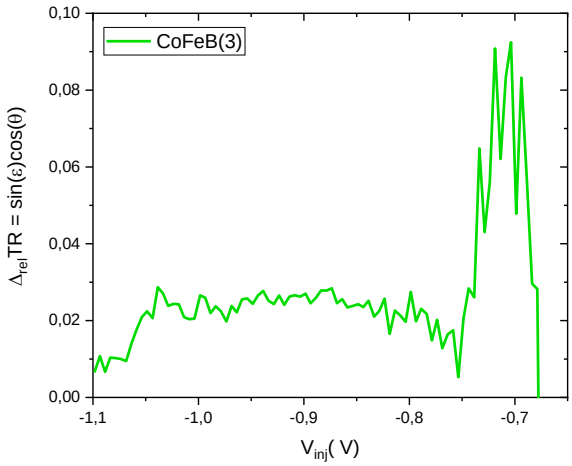

Figure III.13: Precession signal $\Delta_{rel}TR$ as a function of injection voltage V_{inj} for a CoFeB(3) MTT at 50K. Plotted signal is calculated using the transfer ratios of Fig.1.

Figure III.13 shows precession signal $\Delta_{rel}TR$ as a function of injection voltage V_{inj} calculated with transfer ratios of Fig. III.12 for a CoFeB(3) MTT at 50K. $\Delta_{rel}TR$ variations with V_{inj} on figure III.13 can be divided into three separate regions: From the Schottky barrier height -0.65V to -0.75V, the collected currents are too weak to extract a reliable precession signal. Past this voltage, values of $\Delta_{rel}TR$ stabilizes around 0.025 (in a direct orientation of the three magnetizations). At higher energies (<-1.5V), the precession signal tends towards 0. Taking in considerations secondary electrons generation detailed in chapter II, one can assume that the precession signal coming from ballistic primary electrons beam is attenuated by the collection of secondary electrons.

Since the precession angles are huge, we can assume that total precession signal arises from a bulk effect (see III – **Volume precession**), the precession angle is proportional to the thickness of the precession layer: $\varepsilon = \varepsilon^*.d$ with d the layer thickness in nm and ε^*, the precession angle per nanometer in °/nm. Figure III.14 shows the results of measurements for five different thicknesses from 1nm to 4nm over the [-1V, -0.8V] range where the precession signal remains almost constant (see Fig. III.13).

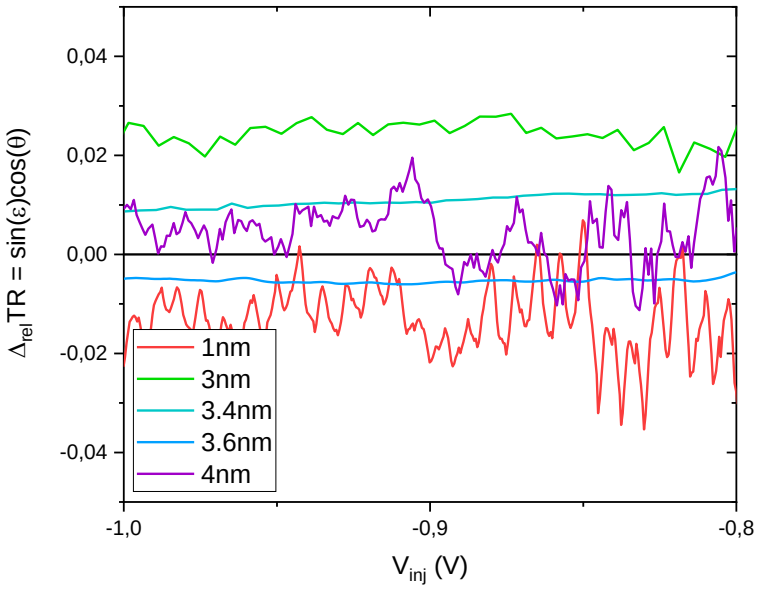

Figure III.14: Precession signal $\Delta_{rel}TR$ as a function of injection voltage V_{inj} for several CoFeB thicknesses at 50K.

The 1nm and 4nm samples are the same samples studied by Vautrin *et al.*[1]. During our work, we re-measured the values of $\Delta_{rel}TR$ with the same procedure of configuration stabilization used for the sample made during this PhD. The values are slightly different than those obtained in Vautrin's work.The explanation for this difference can be twofold: either the aging of the sample with time changed the magnetic properties of the CoFeB of the precession layer or the thickness little variations from one device to the other modifies the obtained precession signal. We will see later that this signal is very dependent on the layer thickness and that few Å can totally change its value or its sign. To be noted that fact that the two oldest samples (1nm and 4nm) are also the ones whose signal fluctuates the most (compared to 3nm, 3.4nm, 3.6nm).

As the precession signal can be rewritten as a function of volume precession parameters (see Part III – **Volume precession**), we have:

$$\sin(\varepsilon)\cos(\theta) = \sin(\varepsilon^* d)\cosh\left(\frac{d}{2\lambda^-}\right)^{-1} \qquad (III.14)$$

where ε^* is the precession angle per nanometer in °/nm and λ^- is related to the spin asymmetry in the mean free path in nm.

Value obtained by Vautrin *et al.* concerning λ^- was evaluated at 0.56nm in accordance with similar measurements performed by Van Dijken *et al.*[84]. As the full spin filtering occurs for 5nm in the CoFeB ($\cos(\theta) \simeq 0$), the precession signal decreases quickly with the thickness. The spin asymmetry length λ^- varies slightly with energy over the window studied as pointed out by Nechaev *et al.*[141]. Indeed, the value of λ^- is mainly determined by the small value of $\lambda_\downarrow$ that does not change much with energy.

Vautrin *et al.* proposed an alternative explanation for these unexpected precession angles. Considering expression of the precession speed in the case of a bulk effect (see III – **Volume precession**), ε* can easily be expressed as a function of incoming wave vectors. Therefore, we have:

$$\varepsilon^*(E) = k_\uparrow - k_\downarrow \qquad (III.15)$$

with $k_{\uparrow(\downarrow)}$ being the wave vector for spin-up (resp. spin-down) electrons, at energy E. Thus, precession angle per nanometer is related to the band structure of the material considered.

Figure III.15 shows theoretical considerations based on *ab initio* calculations. The band structure of CoFe(100) crystallographic orientation in the Δ direction is shown on figure III.15 – a). Below 1.95eV, only the majority spin band is accessible. Then, equation III.15 is simplified in $\varepsilon^* = k_\uparrow$. Figure III.15 – b) shows the manifestation of the CoFe band structure into precession angle per nanometer values. For this low energy range, theoretically predicted ε* is expected to be around 800°/nm. This theoretical prediction is also in agreement with Weber *et al.* for higher energies[137].

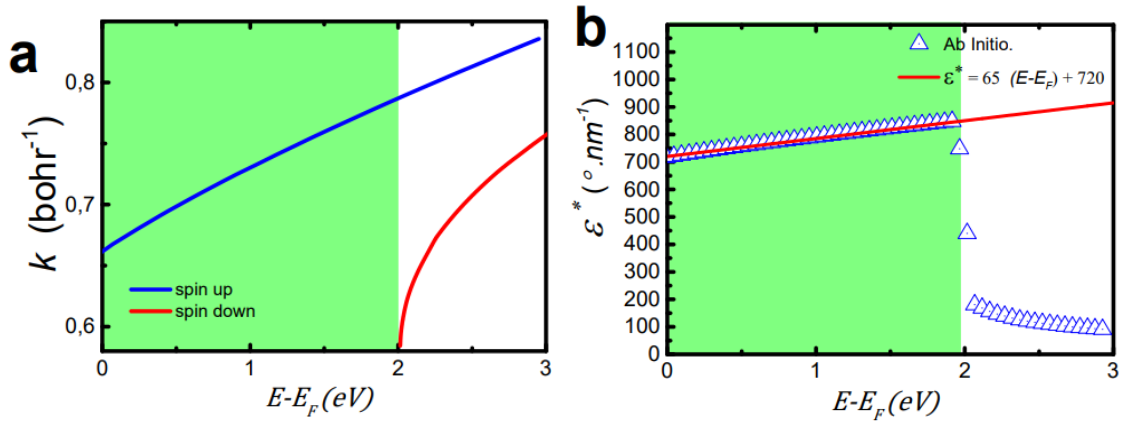

Figure III.15: a) Ab initio *computation of the band structure along the Δ direction in the CoFe(100). b) ε* vs. E-E*F *from* ab initio *computation for CoFe(100). From Vautrin* et al.[1].

Explanation between this difference between experimental measurements made by Weber *et al.* and this *ab initio* calculation lies in the access of the minority spin band above 1.95eV. From this energy, the difference between spin-up and spin-down is quickly reduced resulting in a fast decay of the precession speed. As Weber's measurements were performed at 7eV above the Fermi level, ε* is reduced in comparison with low energies measurements.

Concerning interpretations of experimental data presented on figure III.14, a precession speed evaluated at 800°nm would induce quick changes in the precession angles with varying thicknesses, especially signals of opposite signs. However, measurements should allow observations of precession angles close to ±90° while experimental results only show angles close to 0°. Vautrin *et al.* also took roughness of samples into consideration to link theoretical ε* values to experimental precession angles[1].

In real samples, there are fluctuations of the hot electron travel distance even in the ballistic hypothesis. The roughness at the interface with adjacent layers leads to small variations of the CoFeB thicknesses. Considering the high precession speed predicted, even a few Å difference can induce huge changes in the final precession angles of incoming electrons. Therefore, formula of equation III.5 needs to be modified to interpret the precession signal as a mean value of precession angles:

$$\sin(\varepsilon)\cos(\theta) = \frac{1}{\Delta d}\int_{d}^{d+\Delta d} \frac{\sin(\varepsilon^* t)}{\cosh\left(\frac{t}{2\lambda^-}\right)} dt \qquad (III.16)$$

where the travel distance is varying from d, the layer thickness, to d+Δd, the roughness.

Figure III.16 shows the comparison between averaged experimental values (see Fig. III.14) and model (see Eq. III.16). Injection energy and spin asymmetry length were taken at 1eV and 0.56nm respectively. The associated roughness was estimated to be at 0.4nm by Vautrin *et al.* which also seems reasonable for new samples taking into account similar deposition conditions. Additional thicknesses to the work of Vautrin *et al.* fits very well the model.

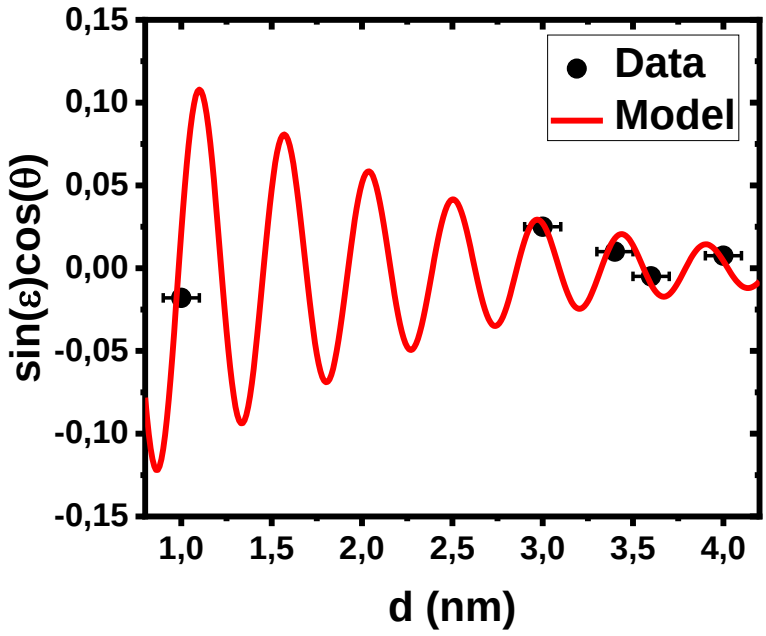

Figure III.16: Mean sin(ε)cos(θ) vs. thickness for an energy E-E_F = 1eV along with corresponding experimental values (dots). All measurements were performed at 50K.

This work confirms the high precession speed induced volume effect in CoFeB with the same model parameters as that used by Vautrin *et al*. Furthermore, these results are more reliable accounting the full control of magnetic configurations as demonstrated previously with

experimental data following a single oscillation between 3 and 4nm. Yet, we shows a limitation of using CoFeB to accurately manipulate electronic spin: precession is changing too fast that required thickness steps are too low to modify electronic spins by less than 90°.

III.2 – 3. Energy dependence

Low energy precession

Now that spin precession phenomenon has been demonstrated as a function of thickness for energy around 1eV, its energy dependence can be further investigated. From *ab initio* calculation (see Fig. III.15), the precession angle per nanometer for a given CoFeB is expected to increase with increasing energy up to 1.95eV. Even though an average of the precession angle is performed due to interfaces roughness, the energy dependence should still be present. Figure III.17 – left shows $\Delta_{rel}TR$ calculated with equation III.16 taking into account *ab initio* calculations and interface roughness of the samples. Curves plotted for three different CoFeB thicknesses (1nm, 3nm and 4nm) show a different behavior compared to results observed in figure III.17 - right. Here, the precession signal is not constant with injection. Sign change is expected for CoFeB(3) around 1.2eV and in the case of CoFeB(1), the precession signal is almost tripled from 0.8eV to 1.5eV.

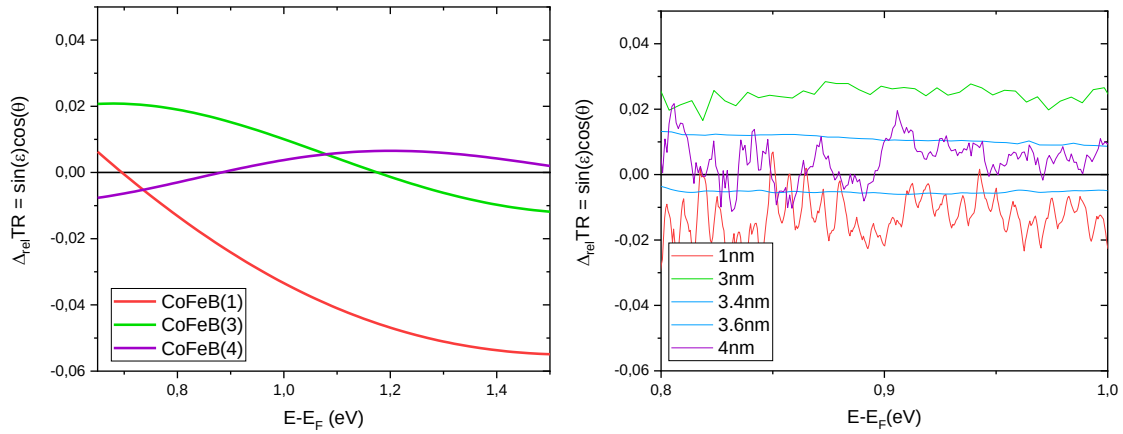

Figure III.17: Mean sin(ε)cos(θ) as a function of energy for three different CoFeB thicknesses: 1nm, 3nm and 4nm (left). Interface roughness is taken equal to 0.4nm. Experimental results shown on Fig. III. 14 (right). The two curves do not have the same energy scale in order to show trends predicted by the model.

In order to further investigate the energy dependence of the precession signal in CoFeB MTT, $\Delta_{rel}TR(E - E_F)$ was measured for different precession layer thickness at higher voltages. These measurements were performed after getting results on low-energy spin precession due to the barrier breakdown more likely to happen at high voltages. Figure III.18 shows the results in the case of CoFeB(1) at 50K for injection energies up to 1.5eV. The precession signal was acquired in two times: a first measurement from below the Schottky barrier height to 1.1eV and a second one from 0.9eV to 1.5eV. This procedure was used for higher voltages measurements in order to limit the time spent constraining the tunnel junction by applying a voltage and also to ensure the continuity from one measurement (low energies) to another (medium energies).

As mentioned previously, the precession signal is still noisy (few hundreds of mV) after the Schottky barrier height. Once fluctuations of $\Delta_{rel}TR$ are reduced, experimental signal

indeed decreases with high energies. At an energy of 1.5eV, $\Delta_{rel}TR$ reaches -0.015 which remains much lower than what was predicted by our model with -0.06 (see Fig. III.17). On figure III.18, a scaling coefficient equal to 0.22 was implemented in order to compare the shape of the decrease of the experimental data and that of the model. Apart from this scaling coefficient, the decay itself seems to be similar.

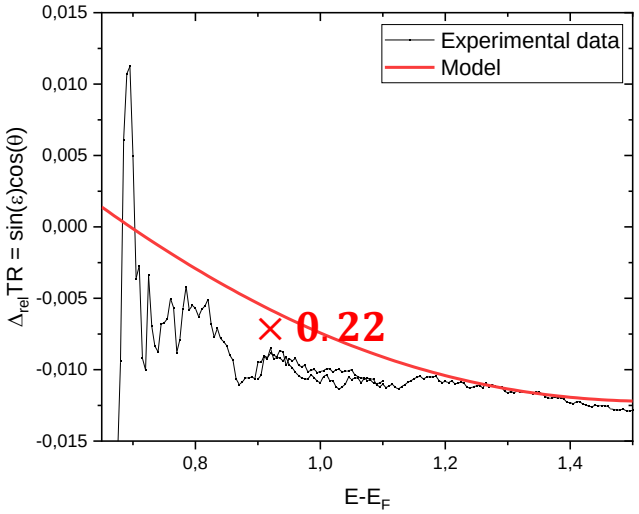

Figure III.18: Mean sin(ε)cos(θ) as a function of injection energy. Measurement was performed at 50K on a CoFeB(1) sample. Red solid line described the decrease of the signal predicted by the model with a scaling coefficient equal to 0.22 to compare both decays.

Figure III.19 shows similar measurements acquired on a CoFeB(4) MTT at 50K. As in the previous figure, the measurement was performed in two times to preserve the tunnel barrier from breakdown. Energy range explored goes from the Schottky barrier height (0.65eV) to 1.5eV. Below 0.8eV, the precession signal $\Delta_{rel}TR$ fluctuates between positive and negative values due to the low signal over noise ratio for these energies. Then, the precession signal increases and reaches a value of 0.005 as predicted by our model (see Fig. III.17). For higher energies, the precession signal starts to decrease following a similar decay as our model.

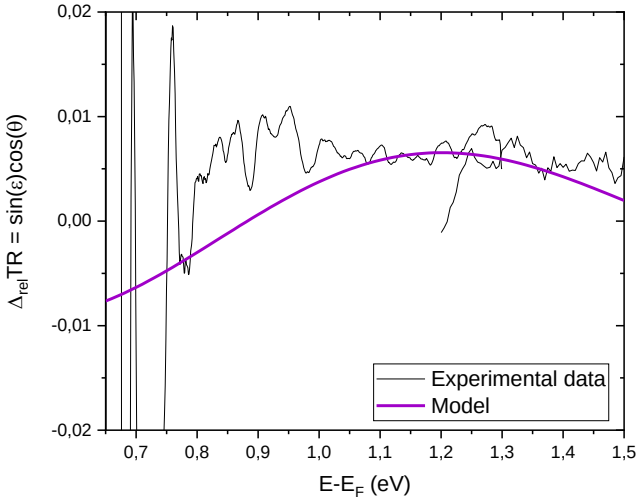

Figure III.19: Mean sin(ε)cos(θ) as a function of injection energy. Measurement was performed at 50K on a CoFeB(4) sample. Purple solid line described the decrease of the signal predicted by the model. No coefficient was required to scale model values to experimental data.

Due to the complexity of acquiring precession measurements at such high voltages (tunnel barrier breakdown), $\Delta_{rel}TR(E-E_F)$ could not be measured for more samples. However, it is already possible to formulate hypothesis concerning the energy variation of the precession signal. For the two extreme thicknesses studied (1nm and 4nm), the energy variation of $\Delta_{rel}TR$ seems to be roughly similar between experiments and model. Yet, a scaling coefficient is required in the case of CoFeB(1) to get the same order of magnitude for $\Delta_{rel}TR$ at higher energies (see Fig. III.18), whereas there is no need for it for the CoFeB(4) MTT (see Fig. III.19).

Precession signal as a function of the signal showed that our data is described very well by the ε* from *ab initio* calculations. As the period of the sinusoidal curve corresponds to that of our measurements, difference in the precession angle cannot explains deviations in the energy dependence of $\Delta_{rel}TR$. However, the filtering angle could explain the difference in $\Delta_{rel}TR(E-E_F)$ in the case of CoFeB(1). So far, we considered the filtering only coming from the CoFeB volume with a asymmetry length $\lambda^{-}=0.56nm$. If possibility of interface induced filtering (see III – **Interfacial precession**) is now taken into account, θ could be underestimated for the lowest thickness sample.

A new resulting expression for the filtering angle would be:

$$\theta=\theta_{vol}+\theta_{int} \qquad (III.17)$$

where θ_{vol} is the filtering angle associated with volume effect and θ_{int}, a filtering angle induce at the MgO/CoFeB interface. For thicker CoFeB MTT, the first term may have a stronger contribution to equation III.14 while for CoFeB(1), it may be the second one. An angle of θ_{int} equals to 35° is enough to remove the scaling coefficient.

The effect of secondary electrons have not been considered in this part. Still, study of secondary hot electrons of Chapter II. showed that over this energy range those electrons can overcome the Schottky barrier height. At this point, we have no further information on how they would affect the precession signal. However, it seems to be possible to correlate spin precession measurements at higher energies with the energy dependence of the model based on *ab initio* calculations.

High energy precession

Below 1.95eV, only the majority band is accessible resulting in a small energy variation of the precession angle per nanometer. This energy-dependence further vanishes with averaging induced by roughness. Above 1.95eV, the minority band becomes accessible and thus, the precession angle per nanometer falls drastically with energy. In this case, a huge variation of the experimental precession signal is expected. Such energy dependence was already studied by Weber *et al.* experiments, with a $\frac{1}{\sqrt{E}}$ dependence[137].

Figure III.20 shows calculations of precession signal with energy and focuses on possible change after the minority band in CoFeB becomes accessible (around 1.95eV on Fig. III.15). Passed this energy, a blue line shows expected precession signal when the decrease of ε* at higher energy follows a $\frac{1}{\sqrt{E}}$ dependence. In this case, the period of Δ_{rel}TR with energy is much shorter than for low energies and the maximum values of the signal increase.

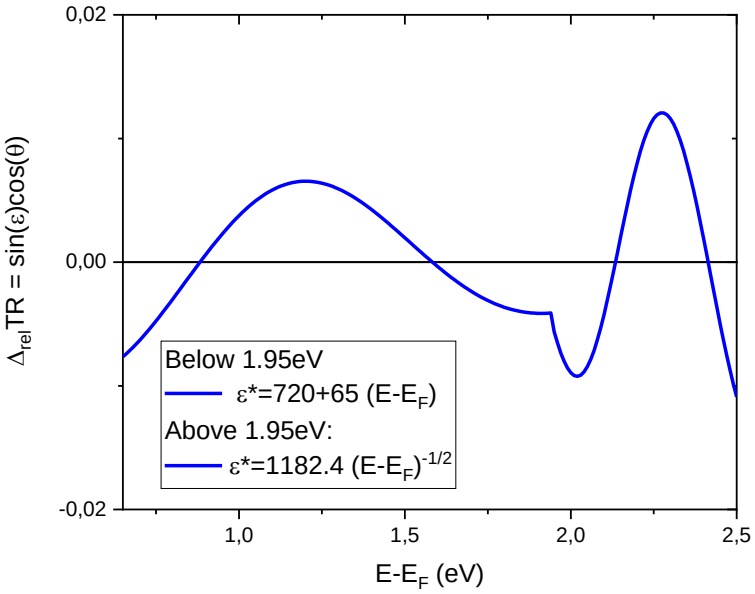

Figure III.20: Mean sin(ε)cos(θ) as a function of energy. Model depicted with a blue line describe what happens past 1.95eV in the CoFeB. Theoretical spin precession follows a root square decrease of Δ_{rel}TR as observed by Weber et al.[137].

By further increasing applied voltages to our devices, both majority and minority bands could become accessible. An interesting idea would be to do high energy measurement and compare experimental data to the sharp precession signal variation around 1.95eV (see Fig. III.20). Once again, we see decreasing noise as the voltage of the measurements is increased. Precession signal reaches a maximum of 0.006 similarly to the model shown on figure III.20, before decreasing. Passed -1.6V, the precession signal Δ_{rel}TR starts again to slowly increase up to 0.005V at the maximum voltage applied (-2.5V).

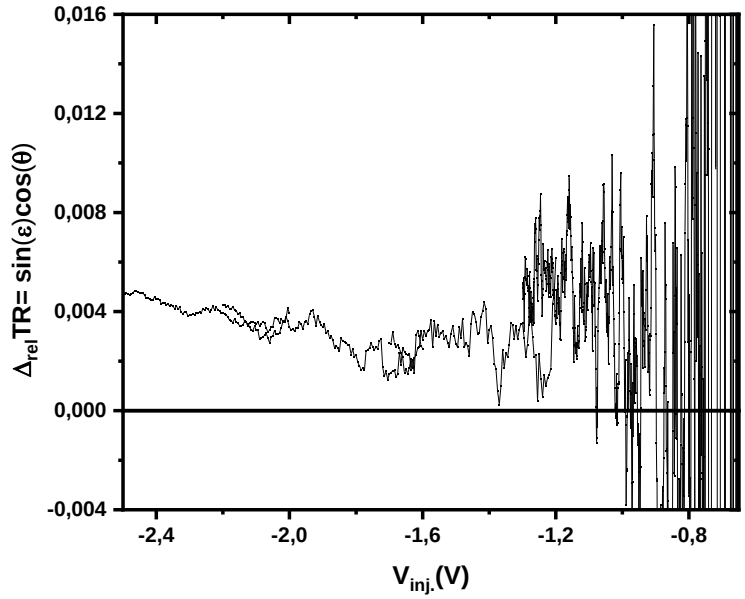

Figure III.21: Mean sin(ε)cos(θ) for highest energy range explored (up to -2.5V). Measurement was performed at 50K on a CoFeB(4) sample.

Comparison between figures III.20 and III.21 show clear discrepancies. While theoretical model predicts a fast change of sign for the signal with higher voltages past 1.95eV,

experimental data on figure III.21 remains positive. These results do not match with theory. One explanation can be that our device is not appropriate for such measurement.

A too low Schottky barrier height compared to injected energies leads collected electrons beam dominated by secondary electrons which underwent an electron-electron interaction. This could lead to dilution of the precession signal resulting in a change of the energy dependence of the signal. At this point, we have no information about the spin-polarization of scattered electrons. Therefore, we cannot model further the contribution of secondary electrons to precession signal.

Key takeaways for Chapter III:

- **5 magnetic configurations can be stabilized in our 3D MTT**
- **Misalignment errors are shown to have a limited impact on precession signal**
- **New CoFeB devices confirmed results from Vautrin *et al.***
- **Precession angles in CoFeB are too high to accurately control the polarization vector of hot electrons crossing the layer**
- **No demonstration of minority band access around 1.95eV could be achieved**

Chapter IV: Manipulation of H_{mol} with temperature

IV. Manipulation of H_{mol} with temperature

IV.1 – Spin precession in CoAl

IV.1 – 1. Introduction

Motivation

Spin precession results obtained with CoFeB samples opened new perspectives: is it possible to control electronic spins within a single device ? Spin precession phenomenon is induced by the presence of internal molecular field in the ferromagnetic precession layer. Therefore, tuning the value of this field would lead to a modification of the resulting ε angle. Temperature seems to be a good candidate to control the molecular field. Indeed, in Weiss theory of magnetism, molecular field is proportional to the magnetization of a sample. Then, alloying transition-metal and non-magnetic elements lead to paramagnetic-ferromagnetic transition with a reduced Curie temperature. Therefore, choosing a T_C close to the working temperature of our MTT enables sharp variation of the molecular field and thus, of the precession angle with temperature.

State of the art – Structure

Co_xAl_{100-x} alloys crystallize into cubic structure (CsCl) for stoichiometric composition (see Fig. IV.1). For concentration between 57% and 50% of cobalt, Co atoms replace substitutional Al atoms [142]. Magnetism was further studied for this specific structure, for Co concentration close to the stoichiometric composition. Co excess can deeply affect the transport properties by affecting band structure and spin order. This is due to charge transfer and hybridization of the electric states between Co and Al atoms.

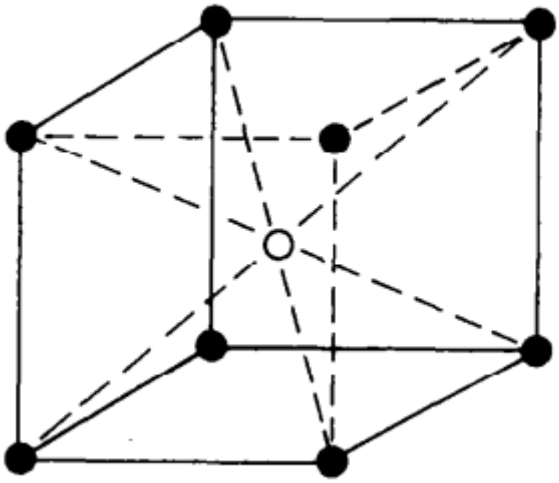

Figure IV.1: Bcc structure (CsCl type) of stoichiometric CoAl. The white sphere represents an Al atom with 8 nearest neighbor Co atoms in black. From Sellmyer and Kaplow[142].

Concerning the structure of crystallization of these transition-metal aluminides, while "late" Transition Metals (TM) on the right side of the periodic table like Fe, Ni or Co, favors a bcc structure, early TM on the left side of the periodic table (Ti, V, Mn) rather induce a face-centered $L1_0$ structure. As stabilization of each phase results from bonding between Al and Co

elements, it would remain possible to stabilize a metastable phase of CoAl grown on a fcc multilayer oriented in the [111] direction deposited by a sputtering system. Both crystalline structures would be considered while investigating x-ray diffraction analysis.

State of the art – Magnetism

Magnetism of Co_xAl_{100-x} alloys was studied by Butler *et al.* for a composition range over which the bcc ordered structure is stable[143]. Figure IV.2 shows magnetic susceptibility and saturation magnetization for as-deposited Co_xAl_{100-x} samples as a function of Al concentration. Only Co-rich samples (x>50) shows ferromagnetism. The saturation moment per excess cobalt atom is around $2\mu_B$ for the range of composition studied by Butler *et al.*

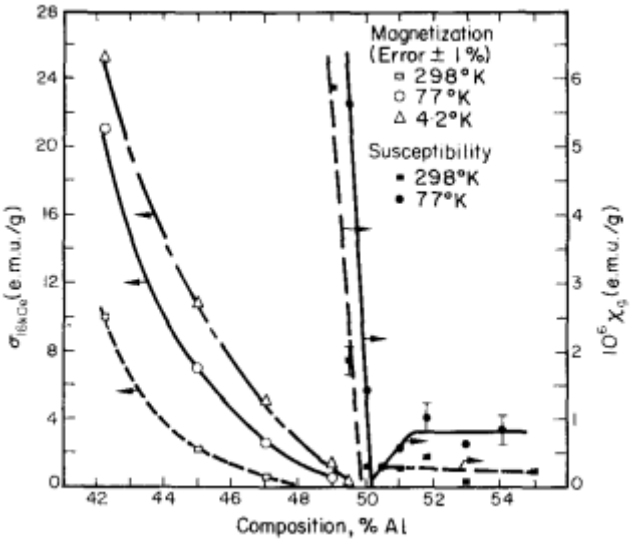

Figure IV.2: Magnetic susceptibility and saturation magnetization of as-deposited CoAl samples. From Butler et al.[143].

They developed a simple model to explain both the paramagnetic behavior of Al-rich CoAl samples and paramagnetic-ferromagnetic transition at higher Co concentration[143]. As an Al atom is surrounded by its eight nearest Co atoms neighbors in a bcc structure in a stoichiometric composition (see Fig. IV.1), bounding occurs only between Al and Co. Thus, Co atoms give 2 electrons to the sp-band of Al and the Co d-band is now t^6e^1 (see Fig. IV.3) with t and e designating orbitals. No magnetism can occur in an alloy with equicomposition. When additional Co atoms are added, they replace Al atoms and this leads to an enhancement of the net magnetic moment by $2\mu_B$ per Co atoms added. The same description was also applied by Butler *et al.* to NiAl alloys to explain their measurements on this alloy, thus showing the reliability of this model for TM-Al.

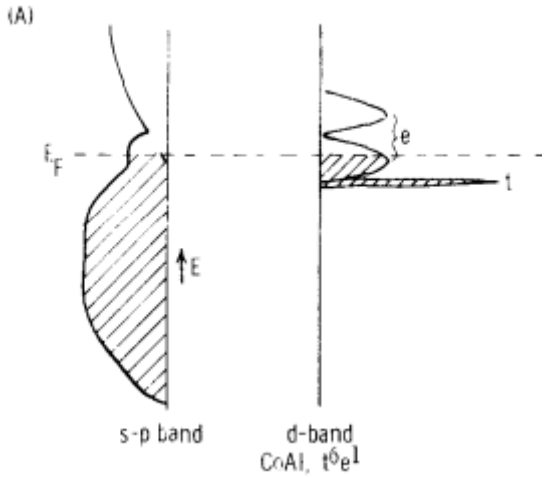

Figure IV.3: Schematic density of states for stoechiometric CoAl. From Butler et al.[143].

Sellmyer *et al.* investigated TM-Al properties as a function of temperature. The treatment of the ferromagnetism (localized vs. itinerant) in Co-rich alloys has been discussed in the litterature[142]. Their experimental results show that at low temperature, excess Co atoms behave like localized magnetic impurities interacting with conduction electrons through s-d interactions. By increasing the Co concentration and lowering the temperature, interactions between localized magnetic moments becomes stronger.

State of the art – Electrical properties

Both structural and electronic properties affect transport properties. Sellmyer *et al.* showed a minimum in the electrical resistivity for an equicomposition CoAl alloy (see Fig. IV.4 – top-left). A sharp increase of the resistivity can be observed while increasing or decreasing the Co content of the alloy. These results were similar to that found by Butler *et al.*. This can be explained by a modification of the internal structure of the lattice as an excess/deficiency of Co can increase the scattering rate of conduction electrons. However, the slope of each side of $50\%_{Co}$ is different. This means that excess Co atoms scatter much more than Co vacancies. This can be related to spin scattering from the additional sites[144].

Local minima appear for Co-rich samples around 40K which do not exist for Al-rich alloys (see Fig. IV.4 – bottom-left). A possible explanation for these minima would be localized magnetic moments interacting with conduction electrons by s-d scattering. These result could also be explained in term of band structure, as in previous section. By changing the Co content, E_F is shifted from a high density of states region to a lower one, thus resulting composition-dependence resistivity of the sample[145].

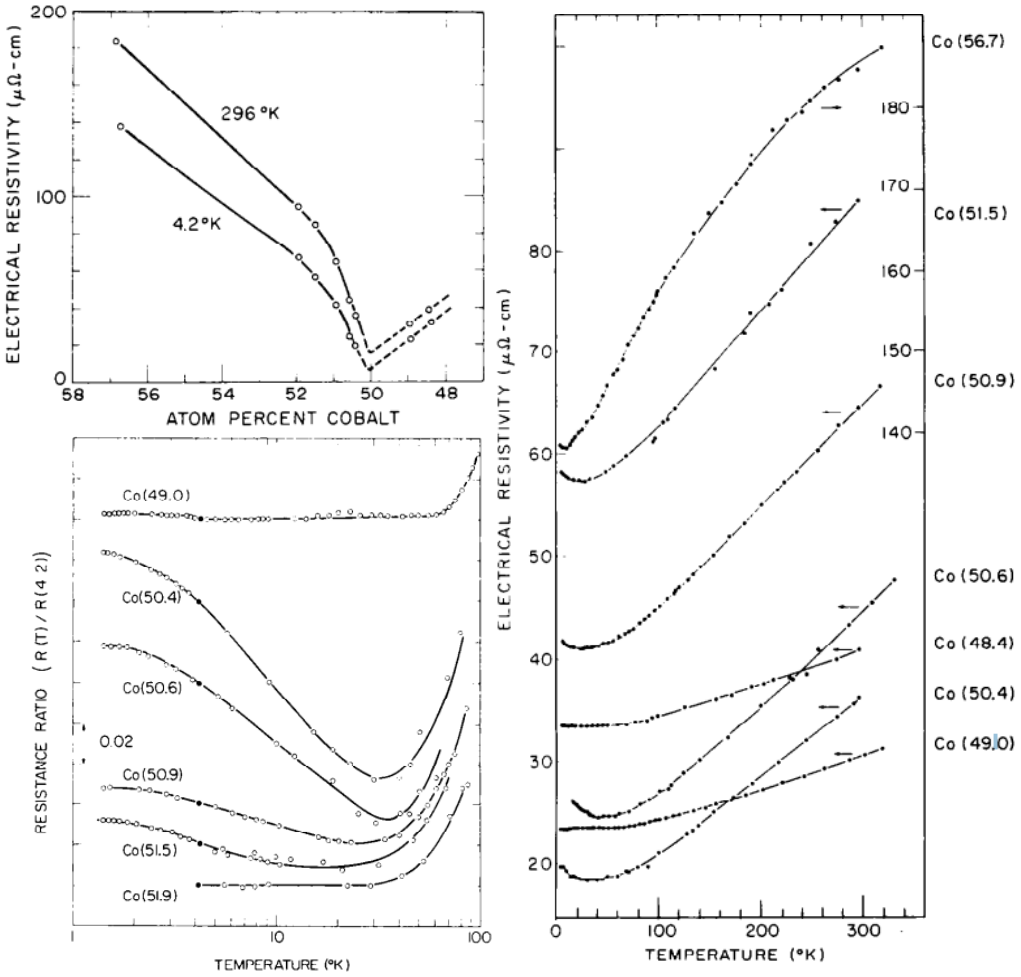

Figure IV.4: Electrical resistivity as a function of Co concentration (top-left). Normalized resistance to that at 4.2K as a function of temperature for several alloy composition, vertical placement is arbitrary (bottom-left). Temperature dependence of electrical resistivity of Co_xAl_{100-x} alloys between 4.2K and 300K (right). From Sellmyer et al.[142].

State of the art – Band structure

The simple energy-density scheme introduced by Butler *et al.* was further supported by theoretical calculations. Several electronic structure calculations of TM have investigated the role of orbitals hybridization in these alloys properties[146,147]. Figure IV.5 – right shows that hybridization deeply affects the band structure of the alloy and leads to high density peaks in the DOS. The Fermi level lies in a pseudo-gap with low density for equiatomic CoAl alloys. For higher Co concentration, the DOS at the Fermi is enhanced showing a shift towards the closer peak.[146] This phenomenon is also responsible for the bcc phase stabilization of CoAl[147].

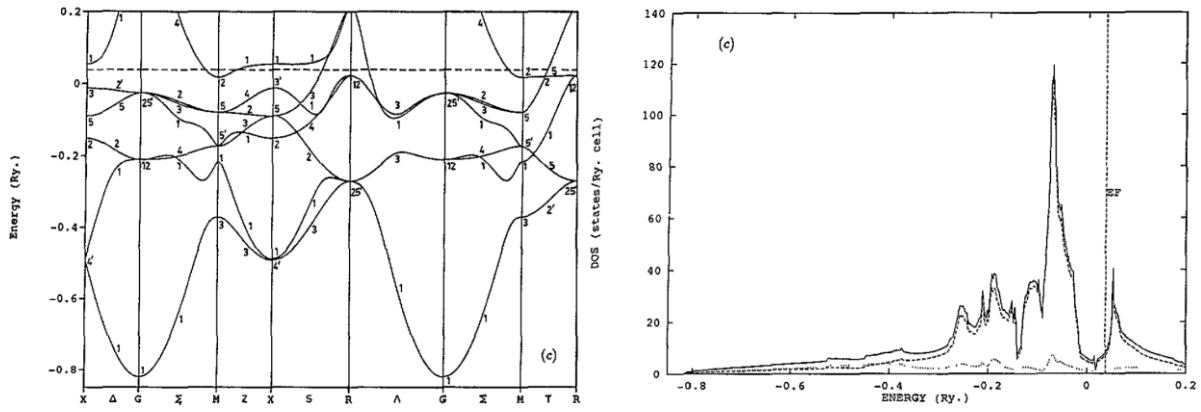

Figure IV.5: Band structure for $Co_{50}Al_{50}$ along certain symmetry directions (left) and DOS for $Co_{50}Al_{50}$ (right). Continuous line gives the total DOS while partial DOS from Al and Co are represented by dotted and dashed lines respectively. From Sundarajan et al.[148].

Literature concerning Co_xAl_{100-x} suggests that an alloy with equicomposition of each element is supposed to have a paramagnetic-ferromagnetic transition close to room temperature. Therefore, exploring alloys close to this concentration is interesting to make a tunable ferromagnetic layer. Concerning electrical properties, alloys in this range of concentration can show a metallic to semiconducting-like behavior with a change in the resistivity temperature-dependence. This feature can be related to electronic states of CoAl alloy with a pseudo-gap lying close to the Fermi level.

IV.1 – 2. Characterization

Room temperature magnetism

In order to control the magnetic response of the Co_xAl_{100-x} samples, magnetic properties were first investigated at room temperature. C. Vautrin studied magnetism of thin films based on typical stacks: Si//Ta(5)/Pt(5)/Co_xAl_{100-x}(40)/Pt(5) for Co composition of the alloys going from 60% to 93%. CoAl alloy is grown on Pt oriented in the [111] direction thanks to the presence of an amorphous Ta layer. Thus, CoAl can grow in a similar condition as that in the MTT with a [111] orientation of the [Co/Ni]/Cu multilayer.

Vautrin's study shows a ferromagnetic behavior of CoAl alloys at room temperature, for compositions with more than 65% of Co. These results are different from those obtained by Butler *et al.*[143], where they found a paramagnetic-ferromagnetic transition at room temperature for 50% of Co. Still, a possible explanation could be a difference of deposition techniques (High temperature arc melting for Butler *et al.* and room temperature sputtering for Vautrin *et al.*) or also by a size effect as this study was made on nanometric thin films.

Saturation magnetization measured at room temperature from VSM cycles is plotted against Co concentration on figure IV.6. Saturation magnetization of the alloy increases monotonously with the Co content up to the theoretical value for bulk cobalt (1400emu/cm^3). For a Co composition of 60%, the sample is no longer magnetic at room temperature. Since we are seeking for a transition temperature from paramagnetic to ferromagnetic state to be in the range of temperature in which our device is working properly (50K-200K for a Schottky barrier that is not leaking), samples were investigated at lower temperatures to find both modification of $T_c(\%_{Co})$ and $M_s(T)$ for each concentration.

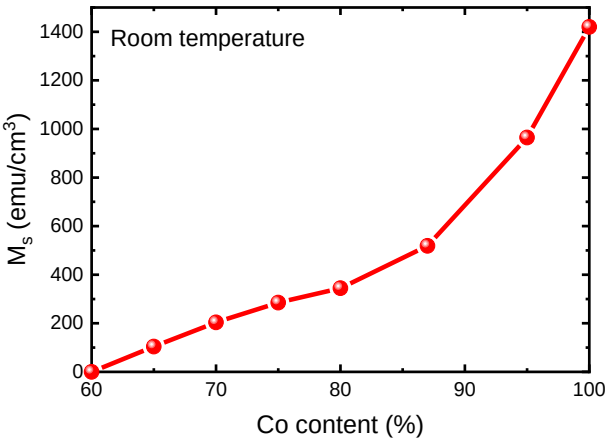

Figure IV.6: Saturation magnetization M_s at room temperature as a function of Co content. From C. Vautrin PhD thesis.

Low temperature magnetism

SQUID measurements were performed on samples measured at room temperature (see Fig. IV.7) and new thin films with lower Co content with the same stack structure as previously. For each temperature, a magnetic field was applied in-plane up to 2T to observe and remove all magnetic responses from the substrate and of the VSM sample holder. Therefore, values of magnetization while the sample is saturated are reported on figure IV.7. Samples studied can be divided in two categories (Fig. IV.7 – left). On one hand, samples with more than 60% of Co are still ferromagnetic at room temperature. Their saturation magnetization as a function of temperature correspond well to that of ferromagnets with M_s slowly saturating at low temperature. Concerning samples with less Co which are paramagnetic at 300K, M_s values measured are lower compared to alloys richer in Co. Figure IV.7 – right focuses on specific concentrations of Co_xAl_{100-x} whose saturation magnetization does not exceed 40emu/cm^3. All samples studied show a quasi-linear variation of M_s with temperature from 50K to T_c.

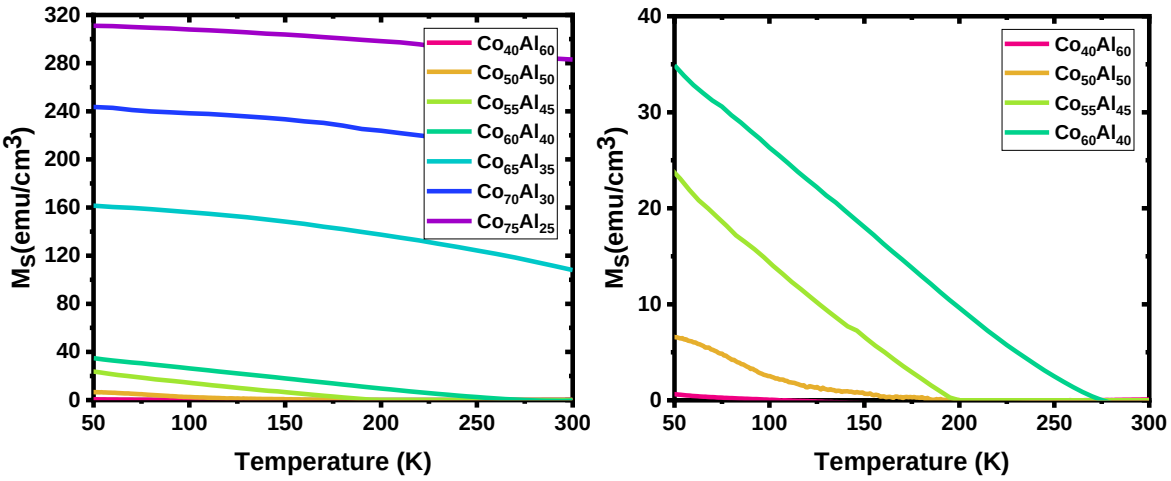

Figure IV.7: Left - Saturation magnetization as a function of temperature for various Co_xAl_{100-x} alloys measured by SQUID. Right – Focus on Co content ranging from 40% to 60% with low magnetization.

Curie temperature increases linearly with the Co content, from 40% with T_c around 100K to 60% with a T_c measured at 280K. Alloy with $\%_{Co}$=40% is almost not ferromagnetic event at 50K (less than 1emu/cm^3) The saturation magnetization at the lowest temperature

measured increases along with the cobalt concentration. Considering our MTT working range to be [50K,200K], we chose to deposit samples with 50%, 55% and 60% for further study of CoAl alloys due to the Curie temperature lying in this window.

X-ray diffraction

In order to have further information on the crystalline growth of CoAl in our sample, we performed X-Ray Diffraction (XRD) experiments on thin films. The stacks studied is similar to that patterned for MTTs structures:

$$Si[100](HF)//Cu(5)/Ta(1)/Cu(5)/Ni(0.6)[Co(0.2)/Ni(0.6)]_{x5}/Cu(3.5)/Co_xAl_{100-x}(10)/MgO(2.8)/CoFeB(2)/Ta(0.5)/Co(2)/IrMn(7.5)/Pt(5)$$

with 10nm of Co_xAl_{100-x} instead of 5nm to increase the X-ray signal of this particular layer in the multilayer stack. The value for the cobalt concentration is equal to 50%. The θ/2θ spectra was acquired using a copper anode for x-rays emission (λ_{Cu}=1.54Å).

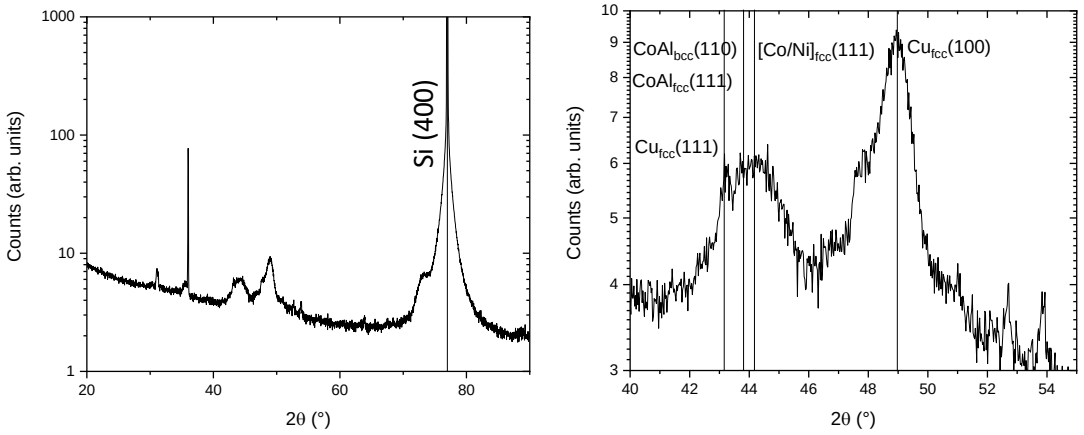

Figure IV.8: Out-of-plane XRD scan for a stack with $\%_{Co}$ = 50% described previously (left). Zoom over of the XRD scan over the [40°,55°] region (right). Two peaks can be distinguished, one centered on 44° and another around 49°. The two CoAl phases considered lie in the first of the two peaks.

On the spectra plotted on figure IV.8, several peaks can be observed. Theoretical positions of deposited materials whose crystallinity and orientation are well-known in our stacks are indicated. The theoretical position for the CoAl(110) peak in a bcc structure is lying close to that of the [Co/Ni](111) multilayer. The peak of highest intensity for a bcc structure CoAl corresponds to the [110] direction. The position of CoAl(111) peak in a fcc structure would be close to the previous ones around 44°, along with that of Cu(111). Therefore, it is difficult to conclude about the crystallography of our alloy. XRD spectra taken with high Co concentration do not show additional features compared to that of figure IV.8.

Stack observations

In order to draw conclusions concerning the crystallinity of our CoAl alloy, a Transmission Electron Microscopy was used to get further information. A $Co_{50}Al_{50}$(10) stack with previously mentioned structure was analyzed. This investigation was carried out by the microscopy team at the IJL using a JEM – ARM 200F Cold FEG TEM/STEM, operating at 200kV and equipped with a spherical aberration probe and image correctors. The point resolution of this microscope is 1.2Å in TEM mode and 0.78Å in Scanning TEM (STEM) mode. 50-60nm thick cross sections were prepared by a focused ion beam etching with Ga ions. With such thickness, electrons with a 200keV energy cross the whole section.

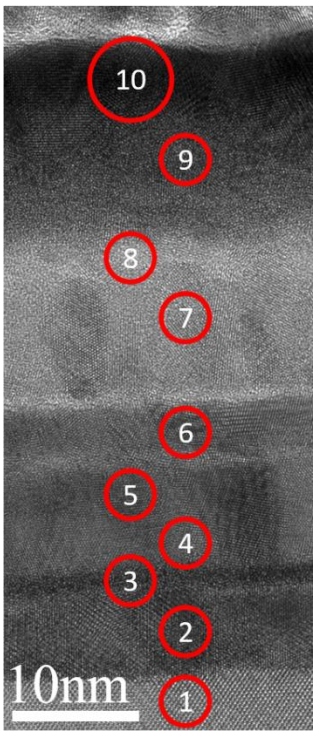

10. Pt

9. CoFeB/Ta/Co/IrMn

8. MgO

7. CoAl

6. Cu

5. ~$[Co/Ni]_{x5}$

4. ~Cu

3. Ta

2. Cu

1. Si(100)

Figure IV.9: High-resolution TEM image of the cross-section of a $Co_{50}Al_{50}$(10) MTT stack. Circled numbers gives associated deposited materials indicated on the right. Layers labeled 4 and 5 cannot properly be distinguished on this image.

Figure IV.9 shows a high-resolution TEM image of the studied stack. Each layer is labeled with a number. This image shows a single crystal 1.Si(100) substrate used to grow our structure. Both 2./ 4.Cu and 5.$[Co/Ni]_{x5}$ layers seem to be well crystallized with an apparent texture that is left to be determined by Fast Fourier Transform (FFT). Concerning the 7.CoAl region, some grains can be distinguished showing that the alloy is rather polycrystalline. Indeed, their orientation seems to change from one grain to another. Layers deposited on top of 7.CoAl do not retrieve good crystalline quality. As far as we go higher in the stack, grains tend to get smaller until amorphous Pt is reached.

Furthermore, a bright area lies between 6.Cu and 7.CoAl which cannot be attributed to deposited elements. It could result from either local misorientation of the material, leading to diffraction condition different to that of the 7.CoAl volume. It could also be induced by some local oxidation at this specific interface. In order to answer this question, element mapping using x-ray on STEM mode was performed.

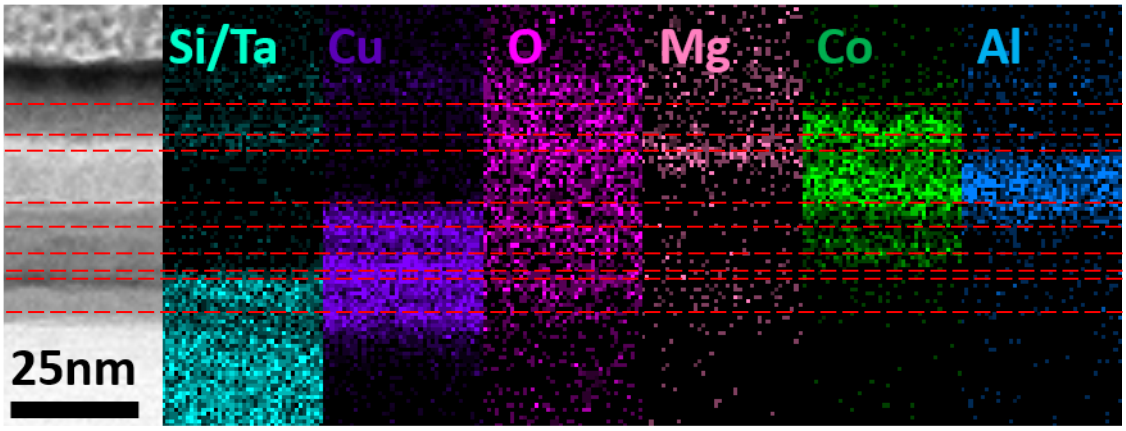

Figure IV.10: STEM x-ray mapping of the stack cross-section for several elements present in the film with corresponding bright-field image. Dashed lines indicates separation of each deposited layers.

Results of this STEM x-ray mapping is shown on figure IV.10. Corresponding bright-field image is added on the left. Dashed lines indicates the separation of each layer from what can be observed from this BF image. Most important elements are shown on this figure. First, we see that the Ta layer separates well the two Cu(5) grown on top of the Si substrate. This can also be guessed on figure IV.9 as the second 4.Cu layer crystalizes following its own orientation. Presence of three distinct Co layers is also confirmed with one for the top electrode, one corresponding to the CoAl alloy and finally, trace of Co in the $[Co/Ni]_{x5}$ multilayer. Concerning the CoAl alloy itself, both Co and Al lie in the same regions showing that the alloy is well defined. Diffusion phenomenon happening with this material will be discussed later in this section. Finally, O atoms seem to be present in all the stack with higher concentration at the tunnel barrier, as expected. The presence of oxygen everywhere can be explained by inevitable oxidation of deposited layers after being cut.There is no specific present of oxygen at the 6.Cu/7.CoAl interface. Therefore, the bright area seen on figure III.32 can be attributed to change of crystalline orientation between these two materials.

FFT was performed over HR TEM image in order to define crystalline orientation of the different layers. Figure IV.11 shows FFT made on 5 different regions: Si(100) (red), Cu (orange), $[Co/Ni]_{x5}$ (green), Cu (blue) and CoAl (purple). The growth follows the direction perpendicular to the interfaces. This direction can be easily taken from the [100] direction of the single crystal substrate. Preferential directions align in the same direction, *i.e.* perpendicular to interfaces. While the first Cu layer grows with a fcc structure oriented in the [100] direction initiated by the substrate, the following layers which are grown on amorphous Ta are oriented in the [111] direction, that of minimum energy. Patterns obtained by FFT is different between the two Cu layers (orange and blue) confirming this trend.

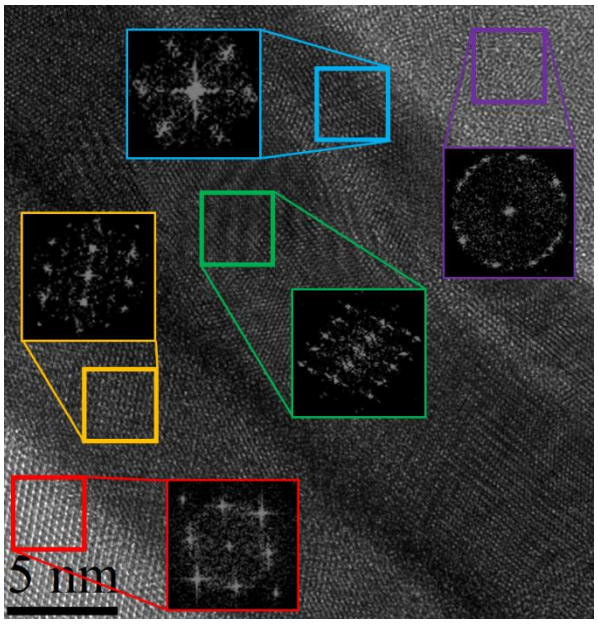

Figure IV.11: HR TEM image over the bottom of the thin film. FFT performed over different regions of the stack are shown with colored edges for each materials.

Structural analysis

More specific attention was given to the CoAl layer. Figure IV.12 – left shows a bright field TEM image centered on the region of interest. On this image, local crystallized grains of CoAl can be observed. However, those grains seem not to have a common orientation, as the crystalline planes are not aligned along the same direction. FFT was performed on different regions of this image (red squares on Fig. IV.12 – left). The combination of these FFT is shown on figure IV.12 – right. Orientation of the Si substrate is shown with a red arrow to indicate the orientation of the sample.

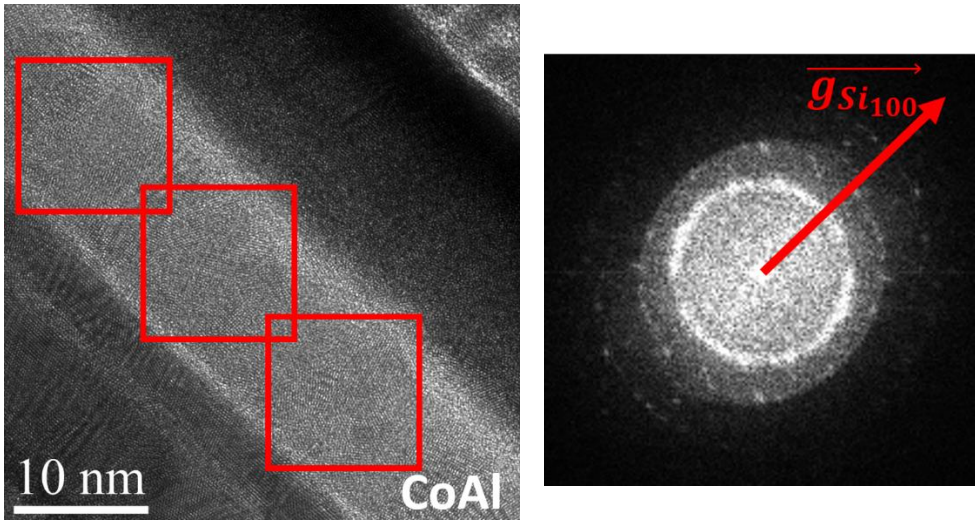

Figure IV.12: BF TEM image of our multilayer (left). CoAl grains can be identified in the red regions. FFT image of the TEM image over the CoAl region (right). Si[100] direction is shown.

While a mono-crystalline layer would give bright spot corresponding to the specific orientation of the material, figure IV.12 – right only shows a bright ring corresponding to a distance of 2.09Å, identified with the [110] direction of CoAl in a Bcc structure or [111] direction in a fcc structure. FFT made on local grains to isolate bright individual spots

discriminated the two possibilities and confirmed the bcc structure. The fact that CoAl did not follow the [111] direction in a fcc structure could be due to the bright interface between Cu and CoAl on figure IV.12 – left. CoAl favored a bcc structure which is more stable rather than create a possible metastable fcc phase. From figure IV.12, CoAl layer seems to be polycrystalline. To confirm the lack of texture, we performed angle analysis of the FFT image.

Figure IV.13 – left shows previous FFT image with indication of the ring integration. Two red circles delimit the radius of integration while two dashed lines described the angular parameter that goes from 0° to 360° (horizontal line is the reference). Intensity is integrated on 5° sectors. Figure IV.13 – right is the plot of these integrated intensity as a function of the polar position. Integration over a sector is made between θ and θ+5°. Textured material would result in a more intense direction corresponding to the growth of a favored orientation of the grains, yet misaligned. However, figure IV.13 – right shows no particular direction. We can conclude that CoAl is polycrystalline (5nm-sized grains) with no specific orientation.

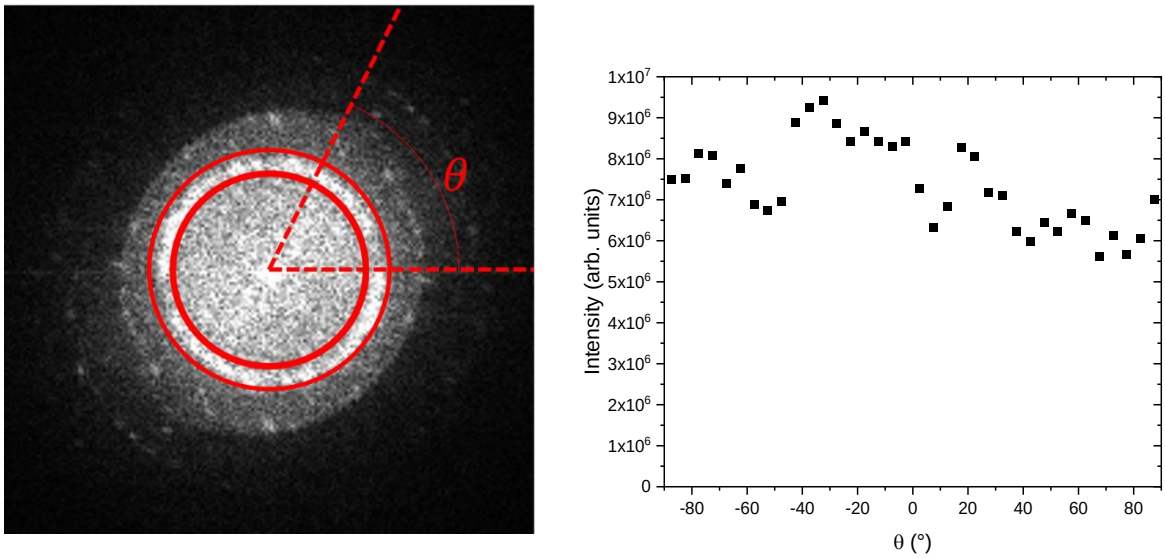

Figure IV.13: Intensity integration over 5° sectors of previous FFT image (left). Intensity of integrated sectors as a function of their angular position on the CoAl[110] ring (right). Reference is taken with the horizontal line.

Elements mapping of figure IV.10 can be used in order to evaluate the roughness at the CoAl interfaces. However, brightness contrast between CoAl and MgO/Cu makes it difficult to define the edge of the alloy. To overcome this issue, X-ray mapping presented on figure IV.11 can define a clearer limit for the CoAl alloy. As precession happens as soon as Co is present in the material, this sounds like a reasonable method to evaluate the roughness. Figure IV.14 shows STEM x-ray mapping corresponding to Co atoms over a wider region (see Fig. IV11). Edges of the alloy is defined by searching a sharp decrease of the Co density on the image. The two red lines on figure IV.14 delimit both interfaces. The thickness of this layer corresponds to the 10nm of CoAl deposited by sputtering.

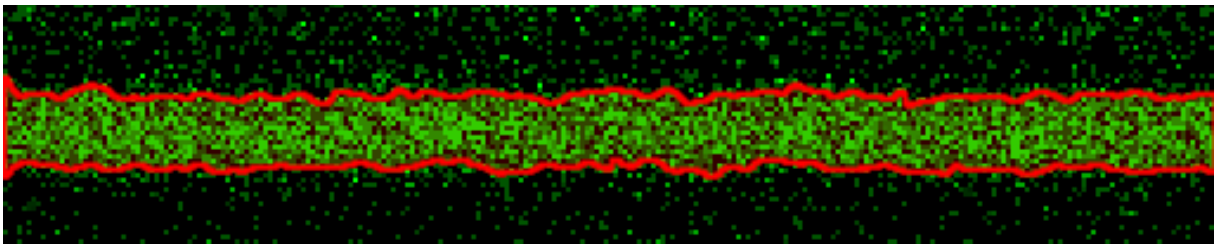

Figure IV.14: STEM x-ray mapping of Co over the same region as figure III.33. Green dots correspond to Co atoms. Red line indicates the edge of the alloy defined by a nearest neighbors method.

Each red line is matched with a corresponding function $f_i(x)$ which returns the profile of the i interface, where x stands for the abscissa of figure IV.14. The thickness of the layer at abscissa x is then defined as the difference between the two function $f_i(x)$. Arithmetic roughness giving a value for the whole cross-section shown on figure IV.14 is expressed as follows:

$$R_a = \frac{1}{L}\int_L |\Delta f_i(x) - \mu|\, dx \qquad (IV.1)$$

with L being the total length integrated and μ, average thickness of the layer. Equation III.14 returns a deviation of local thickness to its average value. Integration using this formula leads to $R_a = 0.6$. This value means that the thickness changes by around 0.6nm. This value can then be used for integration of the precession signal.

Chemical analysis

Another important study to perform on our CoAl is the chemical analysis of the layer. Due to the presence of MgO on top of the alloy, possible segregation/diffusion phenomena can occur to see the formation of alumina oxide. Figure IV.15 – left shows a HR BF image of the sample with each material being indicated. A red rectangle covers the CoAl/MgO region. This corresponds to the region where a chemical analysis by Energy Dispersive X-Ray (EDX) was performed. Associated chemical profile is plotted on figure IV.15 – right with four elements of interests detected in this zone: Al, O, Co and Mg.

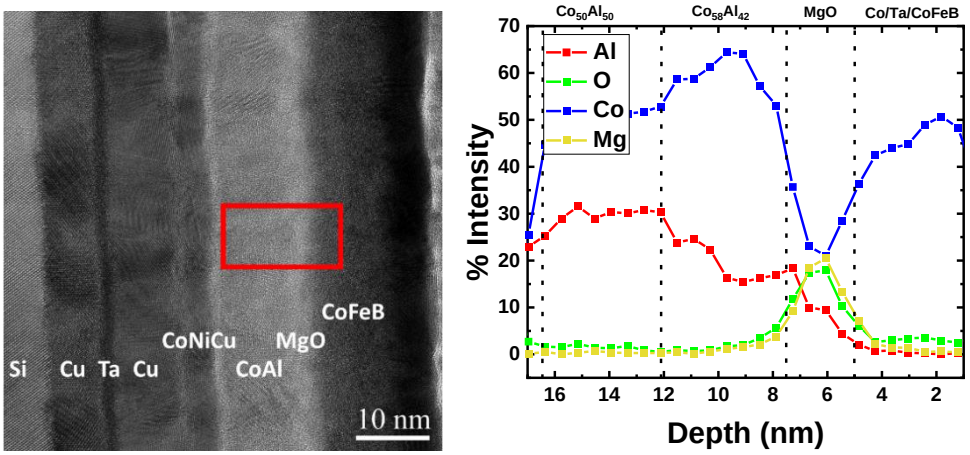

Figure IV.15: Bright field micrograph of studied sample (left) and chemical analysis by Energy Dispersive X-Ray analysis of the CoAl(10)/MgO/CoFeB interface made in the red rectangle (right).

Intensities of detected elements vary while crossing the sample section. Several regions can be identified and associated with deposited layers. A first zone from the beginning of the measurement up to 5nm sees a uniform presence of Co. This corresponds to the Co/Ta/CoFeB top electrode. Then, intensity of Co decreases while that of Mg and O rises, showing that oxide tunnel barrier is detected. From this chemical analysis, its thickness can be evaluated around 2.5nm, close to the deposition parameter for MgO (2.8nm). As both Mg and O signals are rising simultaneously, formation of the tunnel barrier seems to be well done. Then from 7.5nm to 16.5nm (almost the 10nm deposited) depth, intensities for Co and Al stay around 60% and 20%. This corresponds to the analysis of the CoAl layer.

However, two level of both signals can be observed in the CoAl part on figure IV.15 – right. Far from the MgO barrier (12nm to 16.5nm), Co and Al intensities lie at 50% and 30% respectively. By getting closer to the MgO layer, intensities respectively increases and drops around 60% and 20%. This change in intensity is attributed in Al diffusion if the first part of layer towards MgO, resulting in an Co enrichment of the alloy over the first 4.5nm. Assuming the CoAl with stable intensities remained stochiometric, the averaged composition for the first alloy would be $Co_{58}Al_{42}$.

Pumping of Al towards MgO can be understood considering the Gibbs formation energies which gives the possible chemical reactions in standard conditions and underline those which are thermodynamically favored. At the CoAl/MgO interface, pumping of Al from the $Co_{50}Al_{50}$ in order to form Al_2O_3 (Δ_fG^*=-1582 kJ/mol) that is far more stable than MgO (Δ_fG^*=-569 kJ/mol)[149]. Consequently, a segregation phenomenon leading to the formation of Co-rich CoAl alloy is expected at the interface.

Transport in thin films

Resistivity of CoAl thin films was measured as a function of the temperature. Figure IV.16 shows normalized resistivity to the resistivity at room temperature for all three compositions used for MTT structures (50%, 55% and 60%). Thickness of thin films were the same as that used for magnetometry (40nm of CoAl). Variation of resistivity depicts an unusual behavior with a transition from a semiconducting-like to metallic transition happening between 100K and 200K for all studied samples. This can be the sign of the presence of a pseudo-gap in the band structure of the material[145]. Local minima found here are located at higher temperature than previous studies (see section IV.1 – 1. **State of the art – electrical properties**). Difference between samples in term of deposition conditions and compositions makes it difficult to give a definitive conclusion of this pseudo-gap explanation.

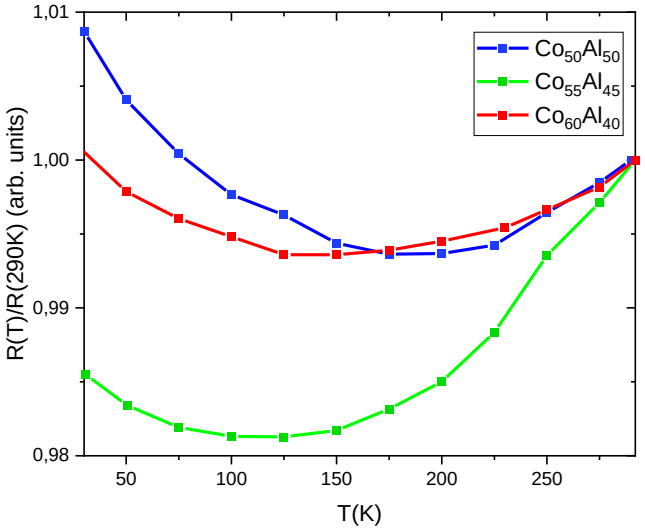

Figure IV.16: Normalized resistance compared to that at 290K as a function of temperature for all three alloy compositions.

Tunnel transport

Magnetic tunnel transistors were patterned using the same lithography processes as mentioned previously. Characterization of the tunnel magneto-resistance (TMR) as a function of the applied field was made for different temperatures both to check on tunnel transport through the barrier in the device and to relate magnetism results to evolution of TMR with temperature. Figure IV.17 shows comparison of TMR (see Eq. I.1) for four temperatures: 40K, 80K, 120K and 160K. The limited TMR value is attributed to the polycrystalline CoAl structure that does not allow symmetry filtering as observed in CoFeB-based MTJs. Therefore, minority spins electrons probably contribute to the tunnel current, reducing the overall TMR of our device. Decrease of temperature affects magnetic properties of the MTJ. While temperature is increased, both coercive and pinning fields of the top electrode magnetization are reduced. Indeed, the main loop associated with CoFeB/Ta/Co/IrMn reversal gets thinner and shifts as the same time. As for CoFeB (see section III.1.1 – **Tunnel transport**), tunnel resistance of the device decreases with increasing temperature.

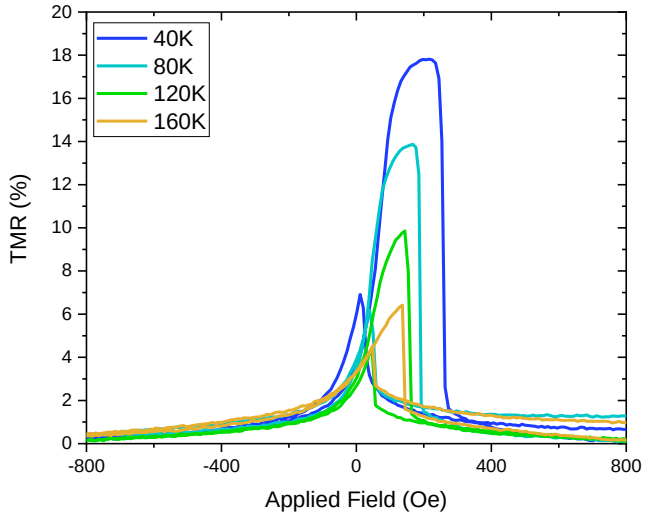

Figure IV.17: TMR as a function of applied field for 40K, 80K, 120K 160K. Measurements have been performed on the CoFeB/MgO/$Co_{50}Al_{50}$ MTJ part of the associated MTT, with a voltage of +10mV.

Similar measurements have been performed for a wide range of temperature going from 20K to 240K. The maximum values of TMR were plotted against temperature on figure IV.18. Experimental data shows two separate trends: from low temperatures up to 180K, TMR decreases linearly with temperature. Above 180K, TMR remains almost constant even at room temperature with a value around 4%. This latter fact was surprising knowing that CoAl with almost stoichiometric composition is supposed not to be ferromagnetic anymore at 300K. Therefore, no magnetoresistance effect was expected.

Concerning the linear variation of TMR(T) at lower temperature, it could be related to several mechanism. As in CoFeB, TMR is expected to change with temperature (see section I.1 – 5). Here, we tried to relate this change to magnetism of the CoAl electrode. Following expression of the TMR based on Jullière's model (see Eq. I.5), TMR is expected to depends on each electrode polarization. While polarization of CoFeB is almost constant as its Curie temperature is far from room temperature[150], the polarization of CoAl is dependent on the temperature (see Eq. I.11). Indirect estimation of the polarization in CoAl based on TMR measurements can then be correlated with the variation of magnetization of the same material. In both cases, we observe a linear variation of the signal with temperature. Isolating this linear trend of the TMR leads to a possible value of the Curie temperature around 225K. This value of T_C is consistent with what is obtained through SQUID measurements (see Fig. IV.7).

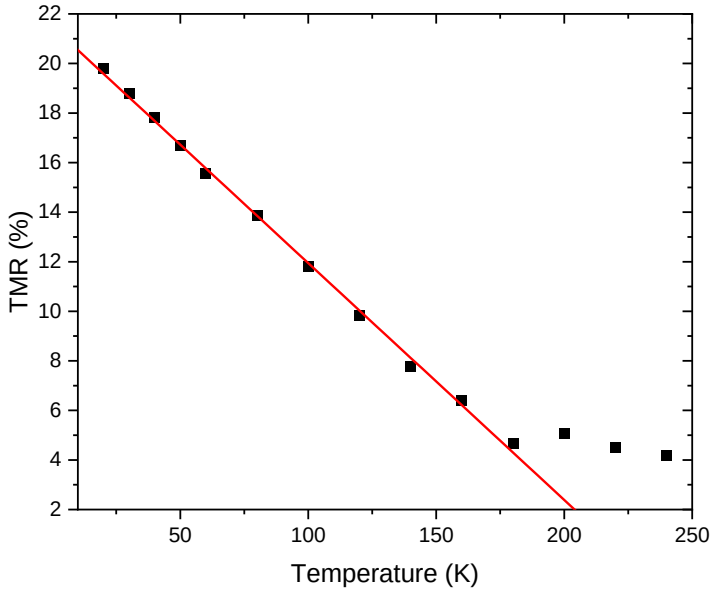

Figure IV.18: Maximum TMR values as a function of temperature for an injection voltage of +10mV. Measurements were performed on the same device as Fig.III.37. Red solid line shows a linear dependence of the TMR with temperature over the [10K,180K] range. Associated Curie temperature with this model is 225K.

Hot electrons transport

Both tunnel and collected currents were characterized to have information on the transport of hot electrons injected from the tunnel barrier to the base. Figure IV.19 shows the two currents measurements performed on a $Co_{50}Al_{50}$(5) MTT at 50K. On the left panel, tunnel current (I_{tun}) is plotted against injection voltage (V_{inj}) for the three magnetic configurations (clockwise, counterclockwise and parallel). Red and blue curves are associated with CW and CC configurations respectively and the black curve with parallel one. If superposition of red

and blue curves show a similar injection in both perpendicular configurations of the electrodes magnetizations, the fact that the black one is so close to the others is a result of the decreasing TMR with increasing voltages (see III.1.2 – **Tunnel transport**).

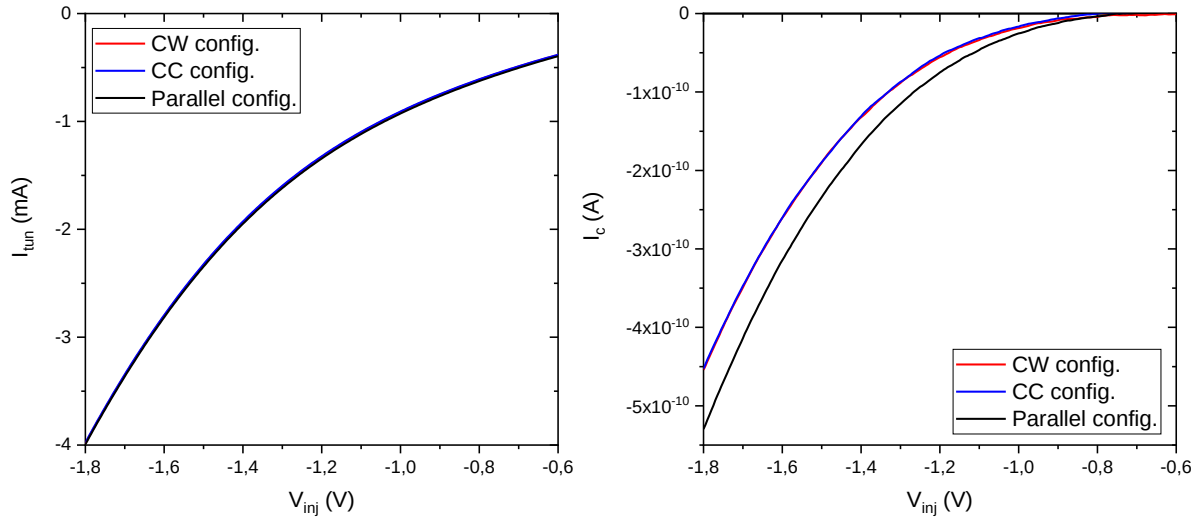

Figure IV.19: Tunnel current (left panel) and collected current (right panel) as a function on injected voltage for a $Co_{50}Al_{50}$(5) MTT at 50K in the three magnetic configurations (clockwise, counterclockwise and parallel).

On the right panel, collected current (I_c) is also plotted against V_{inj} for the same three magnetic configurations. In this device, the Schottky barrier height corresponds to a voltage of -0.7V. The three collected currents increase for higher voltages as electrons start overcoming the Schottky barrier. Unlike for tunneling current, a slight difference between CW and CC configurations can be observed. From a single measurement, it remains hard to distinguish precession effect from electrical noise contributions to this difference. Therefore, collected currents measurements such as plotted on figure IV.19 – right were performed several times to give a value for precession signals. Concerning the parallel configuration, here, black curve is clearly separated from red and blue ones. As this difference does not come from injection, it can be attributed to the spin filtering with the CoAl/Cu/[Co/Ni] spin-valve.

IV.1 – 3. Temperature-dependent spin precession

Mesures

Transfer ratio (TR) as a function of injection voltage (V_{inj}) is calculated in all three magnetic configurations based on previously shown I_{tun} and I_c curves (see Fig. IV.19) and is plotted on figure IV.20. All three TR are increasing with voltage, once the Schottky barrier height is passed around -0.7V, close to the value for CoFeB MTT. Values for the TR are much lower compared to that for CoFeB (see Fig. III.12). Here, for the parallel configuration, the signal is reduced by a factor 300. Knowing that the only difference between the two samples are the material chosen for the precession layer (CoFeB vs. CoAl) and that the bottom of the stack is well crystallized, the main explanation between this difference in magnitude is the polycrystallinity of the CoAl alloy. While hot electrons have to cross multiple grains with different orientation, they experience more scattering than in the case of a well-crystallized CoFeB layer. Therefore, for a given injection voltage, the TR of the former is reduced.

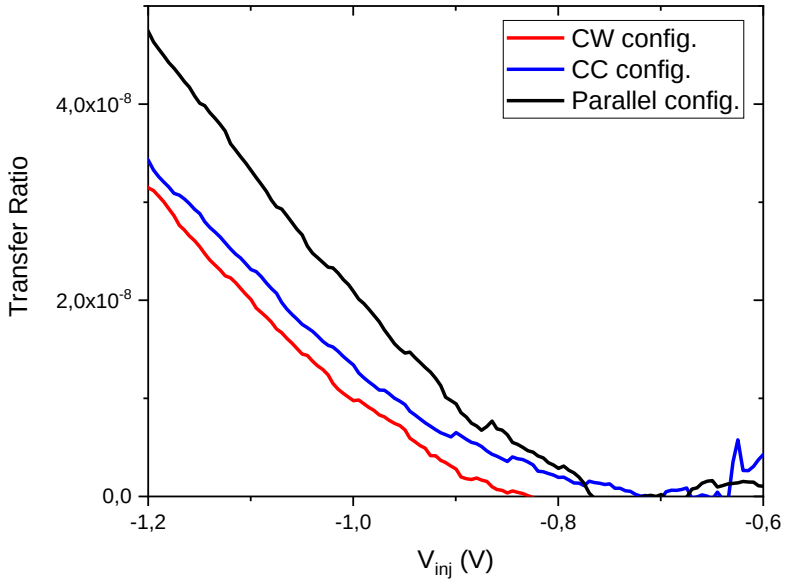

Figure IV.20: Transfer ratio as a function of injection voltage for a $Co_{50}Al_{50}$(5) MTT at 50K in three different magnetic configurations (clockwise, counterclockwise and parallel).

TR associated with parallel configuration is higher than that for crossed configuration.. Concerning red and blue curves for perpendicular cases, a gap between those two corresponds to a signature of the precession phenomenon. This difference looks more important in the case of CoAl scaled with the TR values (compared to CoFeB on Fig. III.12). It can be noted that in this case, TR for the CW configuration is lower than that for CC configuration (unlike Fig. III.12). This corresponds to a negative precession angle, between -180° and 0°. However, results from figure IV.20 have to be interpreted carefully. Indeed, noise of the measurements induce a huge uncertainty on the TR values and thus, on the precession signal. This noise on calculated TR results from the low values of I_c acquired, reaching instrumental limits of our set-up. Few years ago, instruments in place on this set-up for hot electrons precession measurements were not enough to distinguish a signal on the same CoAl devices. Addition of a picoampeter with further precision and of an optimized filtering of the signal led to these improved measurements. On figure IV.20, negative values for the TR below -0.8V makes the curve for CW configuration off the chart. In order to reduce the impact of these noises as much as possible, precession signals extracted as function of the temperature have been averaged over ten measurements.

From TR of figure IV.20 and expression of the precession signal $\Delta_{rel}TR$ of equation III.10 (see section III – **Measuring principle**), it is possible to connect experimental measurements to the precession (ε) and filtering (θ) angles. Calculated values for this $Co_{50}Al_{50}$(5) device is plotted on figure IV.21. As for CoFeB, precession signal highly diverges until few hundreds of mV above the Schottky barrier height (-0.7V). Around -0.9V, $\Delta_{rel}TR$ lies in the [-1, 1] window for all measurement performed and does not leave it anymore. Therefore, we can assume that the measurement of the precession signal is reliable above this voltage, as it was already the case for CoFeB. Figure IV.21 shows an increasing precession signal with increasing voltage.

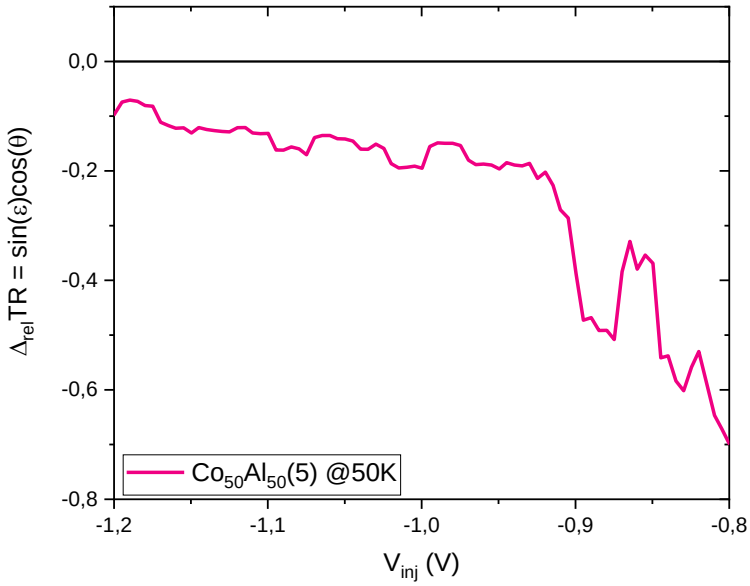

Figure IV.21: Precession signal Δ_{rel}TR as a function of injection voltage V_{inj} for a $Co_{50}Al_{50}$(5) MTT at 50K. Plotted signal is calculated using the transfer ratios of IV.20.

Similar measurements have been performed for a wide range of temperature. Δ_{rel}TR for six different temperatures from 50K to 140K is reported on figure IV.22. No repetition of the measurements have been made in order to reduce the noise. All precession signals follow the same trend: going from high values (close to ± 1), they decay quickly towards a lower value, which depends on the temperature. For each 20K-30K temperature increase, sign of Δ_{rel}TR is changing. This predicts a periodicity with temperature as it was with thickness in the case of CoFeB.

Highest values of the precession signal for CoAl-based devices for -1.2V are around 0.1 (see 120K on Fig. IV.22). This value is 5 times higher compared to that of CoFeB precession (see Fig. III.13 in section III.2.2). Explanation can be twofold: either the precession angle per nanometer is low enough for the roughness to have a limited impact on the measured signals or the spin filtering (higher λ^{-}) is reduced, both resulting in an increase of the sin(ε)cos(θ) product. Answer of this question will be given once model associated with spin precession in CoAl is given in the following parts.

Measurements of Δ_{rel}TR shown on figure IV.22 were extended at higher voltage, up to -1.8V. For each temperature studied, the value of the signal slowly decreases. Δ_{rel}TR almost stabilizes at its value for -1.2V for 50K measurement. As for CoFeB, it remains difficult to interpret experimental data for high precession energy due to the presence of secondary electrons. No study has been made to quantify the contribution of secondary electrons to the TR signal. Nevertheless, for each temperature a finite non-zero value is obtained.

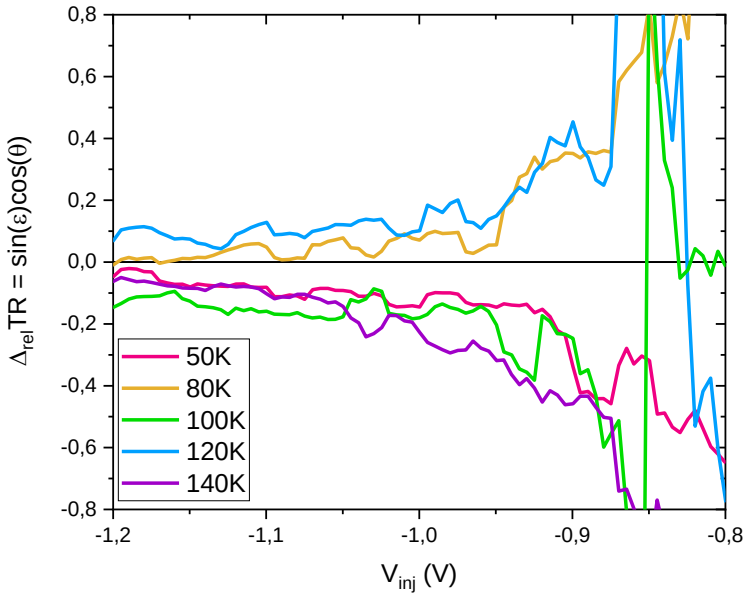

Figure IV.22: Precession signal $\Delta_{rel}TR$ as a function of injection voltage V_{inj} for several temperatures.

The same measurements have been performed over a 70K window, from 50K to 120K. Experimental data is plotted on figure IV.23 along with associated error bars. These uncertainties come from standard deviations after several repetitions of the same measurements for a given temperature. Considering that the whole data acquisition took place over a whole month, great care was given to make sure the tunnel barrier was not affected by the hot electrons measurements (no variation of R_{tun}, TMR, TR with time).

Figure IV.22 shows a periodicity in the precession signal as mentioned previously. From 55K where $\Delta_{rel}TR$ is slightly positive, the signal alternates between positive and negative values before going back to its initial one around 120K. Associated period of the signal is evaluated at 65K. A model is proposed to explain the temperature dependence of the sin(ε)cos(θ) product. Considering roughness at each CoAl interface, the precession signal has to be averaged using an integral expression as proposed in equation III.16 (see section III.2.2) for CoFeB.

Here, as the CoAl layer is polycrystalline (see Fig. TEM), expression for the precession angle proposed on equation III.15 cannot be used anymore. ε* has to be integrated over the whole band structure. To do so, Weber *et al.* expression of the precession speed should be applied[151]:

$$\varepsilon^* = \sqrt{\frac{m_e}{2\hbar^2}}\frac{\Delta E_{xc}}{\sqrt{E}} \qquad (IV.2)$$

where m_e is the electron mass, $\hbar$ the Planck constant, ΔE_{xc} the exchange energy of the material and E the energy of incoming electrons (reference taken with the bottom of bands).

Demonstration of equivalence between k-resolved formula and Weber's expression in a Stoner model:

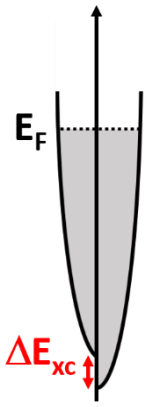

From Eq. III.15 (see section III – **Volume precession**):

$$\varepsilon^* = k^{\uparrow} - k^{\downarrow}$$

$$= \frac{\sqrt{2m_e}}{\hbar}\left(\sqrt{E^{\uparrow}} - \sqrt{E^{\downarrow}}\right)$$

$$= \frac{\sqrt{E}\sqrt{2m_e}}{\hbar}\left(\sqrt{1+\frac{\Delta E_{xc}}{2E}} - \sqrt{1-\frac{\Delta E_{xc}}{2E}}\right)$$ *From Stoner model (Fig. on the left)*

$$= \frac{\sqrt{E}\sqrt{2m_e}}{\hbar}\left(1+\frac{\Delta E_{xc}}{4E} - 1 + \frac{\Delta E_{xc}}{4E}\right)$$ *Taylor expansion for* $\Delta E_{xc} \ll E$

$$= \sqrt{\frac{m}{2\hbar^2}}\frac{\Delta E_{xc}}{\sqrt{E}}$$

Considering a distance of segregation of Al towards MgO in our sample of about 5nm (see Fig. IV.15), which is also the thickness of our CoAl used for precession measurements, we assume that precession happens in an alloy with an atomic cobalt concentration about 58%. In the Weiss theory, the molecular field is proportional to the magnetization, which depends on temperature. For Ni, this has also been forecasted and experimentally verified[152].

We consider here that alloying the Co with Al will bring one additional electron to the Co atom making its electronic configuration close to the one of Ni. Therefore, we modelled the variation of ΔE_{ex} with temperature using the linear variation of magnetization with temperature between curves of $Co_{55}Al_{45}$ and $Co_{60}Al_{40}$ (see Fig. IV.7). As a result, we can rewrite equation IV.2 as:

$$\varepsilon^* = \sqrt{\frac{m_e}{2\hbar^2}}\frac{\Delta E_{ex}}{\sqrt{E}} = \varepsilon^*(E, 0K)\left(1 - \frac{T}{T_C}\right) \qquad (IV.3)$$

with T_C being the Curie temperature of the material, evaluated around 225K (see Fig. IV.7).

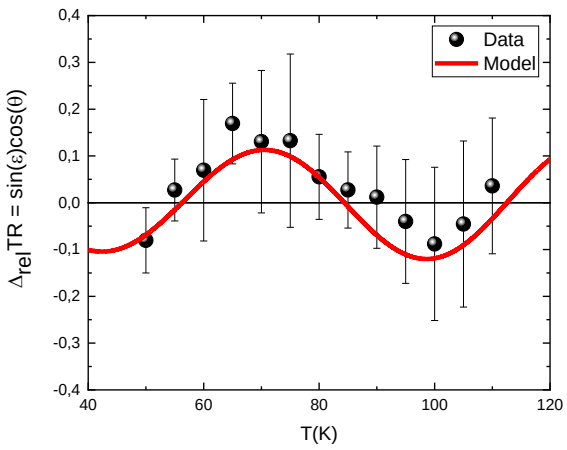

Figure IV.23: Mean sin(ε)cos(θ) vs. temperature for an injection voltage of -1V. Dots with error bars represent experimental data with the red solid line describes associated model for precession. Fit parameters: ε^*=289°/nm, λ^-=0.93nm and interface dephasing equals to zero.

Experimental data plotted on figure IV.23 could be fitted using the model based on equations III.16 and IV.3. Presented model reproduces well the sinusoidal behavior of the experimental data with a period around 55K. Two parameters can be extracted from the fit of the experimental, namely precession speed at 0K, $\varepsilon^*(E, 0K)$, and the spin asymmetry length λ^-. For the fit shown on figure IV.23, the calculated parameters were ε^*=289°/nm and λ^-=0.93nm.

The same procedure was applied for energies between 0.9eV and 1.2eV. The highest energy being lower than twice the Schottky barrier height to avoid the contribution of secondary electrons. Experimental data with associated model are shown on figure IV.24. Amplitude of $\Delta_{rel}TR$ is globally decreasing with higher voltages as the maximum values of the precession signal goes from $\pm$0.2 for V_{inj}=-0.9V to $\pm$0.1 for V_{inj}=-1.2V. The period of the sinusoid is not affected much by energy as we observed the same oscillation of the signal being measured over all panels of figure IV.24.

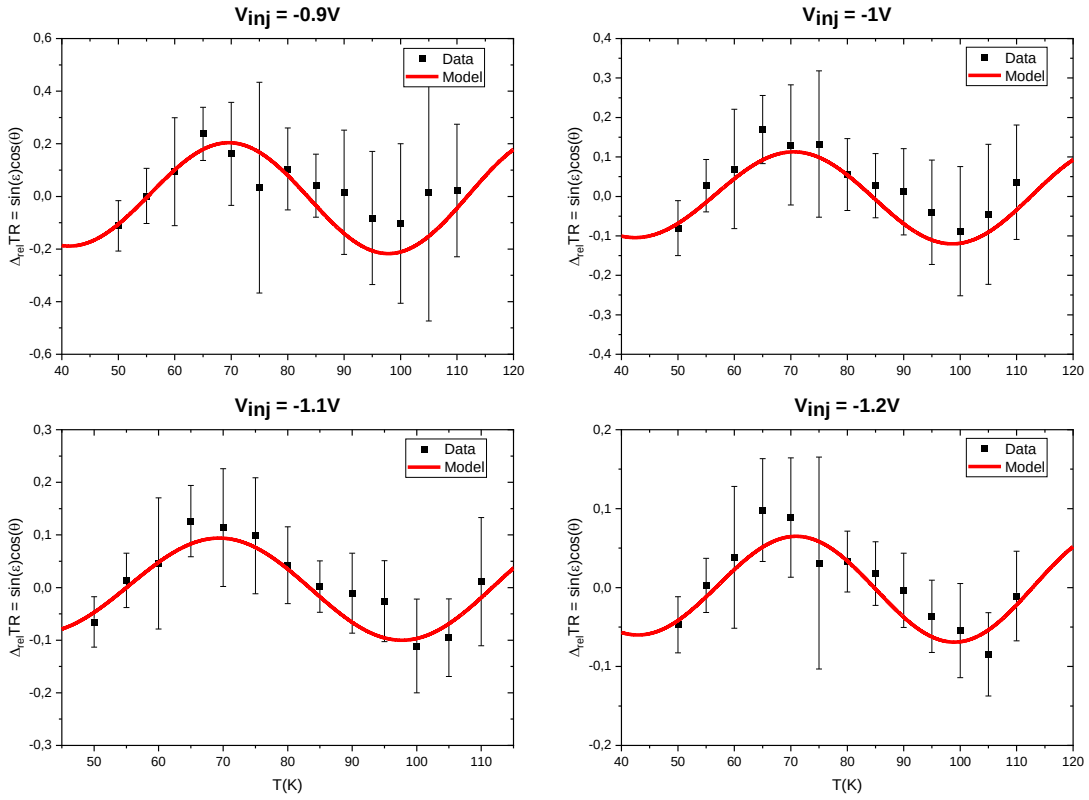

Figure IV.24: Precession signal $\Delta_{rel}TR$ as a function of temperature for each injection voltage measured.

Fitted parameters for each injection energy are reported on figure IV.25 with associated error bars given by standard deviation of $\varepsilon^*(E, 0K)$ and λ^-. Values extracted for λ^- from measurements of figure IV.24 are plotted as a function of energy on figure IV.25 – right. Spin asymmetry length is expressed as $\frac{1}{\lambda^-} = \frac{1}{\lambda_\downarrow} - \frac{1}{\lambda_\uparrow}$ ($\lambda_{\downarrow/\uparrow}$ being the minority/majority inelastic mean free path). From our analysis and for the range of interest [-1.2V, -0.9V], λ^- lies between 0.7nm and 1.5nm, decreasing when energy increases. Reported values of λ^- in the literature using different Co-based alloys[1,84,137] are consistent with values found in this study. However, these values are higher than that reported for CoFe (0.56nm) and close to what was found for Co (1.4nm) which is expected considering Al has a much higher mean free path than Co and that

the magnetic moment of CoAl is much lower than the one of Co or CoFe. Energy dependence of λ^- could be reproduced assuming Colombian inelastic interactions between hot electrons described using:

$$\lambda_{\downarrow/\uparrow} = \lambda^0_{\downarrow/\uparrow} \frac{\sqrt{E}}{(E - E_F)^2} \qquad (IV.4)$$

By leaving only $\lambda^0_{\downarrow/\uparrow}$ as only free parameters, inelastic mean free path for minority (resp. majority) electrons is 0.95nm (resp. 18.3nm) for E-E_F=1eV (see Fig. IV.25 – right). Obtained values do not strongly depends on the other fitting parameter $\varepsilon^*(E, 0K)$. λ^- decays quickly with energy, resulting in the decrease of the precession signal amplitude (see Fig. IV.24). If such a fast decrease can be observed compared to that of CoFeB (see Fig. III.18), this is due to the longer minority/majority mean free paths of CoAl. Therefore, λ^- is higher and its variation with energy can be sharper than that of CoFeB.

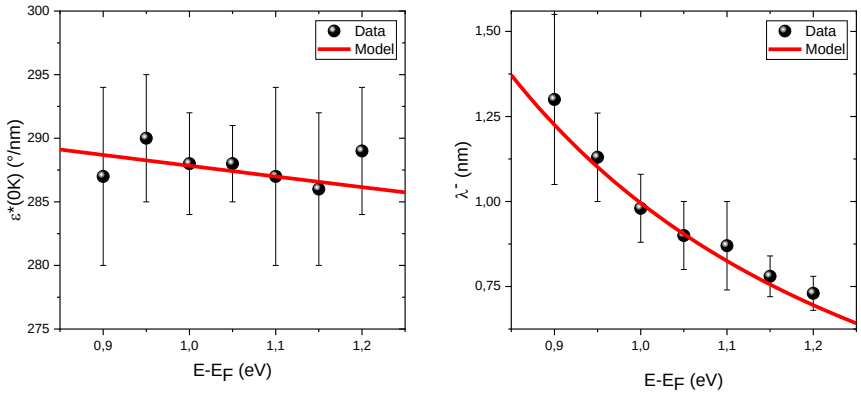

Figure IV.25: Precession speed at 0K (left) and spin asymmetry length (right) as a function of energy. Both parameters were extracted from fits using Eq. III.13 and Eq. IV.3.

Figure IV.25 – left shows the precession speed at 0K extracted from measurements using different injection energies. ε*(E,0K) obtained by the fitting procedure described previously is mostly constant over [0.9eV, 1.2eV] with a value around 287°/nm. This value is more than two times lower than the one measured in CoFe which was close to 700°/nm. As no phase change is considered at the MgO/CoAl interface, which is in accordance to theoretical predictions in magnetic multilayers[51], energy dependence of ε*(E,0K) can be fitted using Weber's formula (Eq. IV.3). The Fermi level is supposed to be that of bulk Co (11.9eV[153]) with respect to the bottom of the bands. A slight variation of the Fermi level position by adding an electron from Al has little impact on the value of the exchange field fitted with this model. Based on equation IV.3, the model predicts a slow decrease of ε*(E,0K) with increasing energies which fits experimental data. Considering an effective electron mass equal to 1, the value for ΔE_{xc} obtained in this study is 6.92eV, much higher than the exchange splitting of Co d-bands[154].

Transition metal aluminides with a stochiometric composition are known to host a semiconducting like resistivity versus temperature behavior[145]. This behavior has also been measured in our sample (see III.2 – **Transport in thin film**). Band structure calculations predict flat density of states in the energy range of our study (see III.2 – **State of the art - Band structure**). As a result, it is not excluded that the effective mass is much higher than 1, making that an overestimation of ΔE_{xc} using equation IV.3 is done if m_e=1 is assumed.

Lastly, precession measurements were performed for higher temperature close to the estimated T_C of our CoAl sample. Chosen temperatures are 200K, 220K and 240K for a T_C around 225K. Once T_c is reached, the precession signal is expected to be equal to zero as the precession layer is not ferromagnetic anymore. Still, 220K and 240K cannot be exploited due to fluctuations in the precession signals.

Measurement of $\Delta_{rel}TR$ for a temperature 200K is shown on figure IV.26. Experimental data of the precession signals fluctuates during the measurement within [-1, 1] limits for sin(ε)cos(θ) product. Here, CoAl alloy is supposed to be still magnetic. Therefore, the denominator doesn't reach zero. The precession signal itself takes both positive and negative values during the measurements. As $\Delta_{rel}TR$ is centered around 0, it can be assumed that there are fluctuations of the $TR^{\circlearrowright/\circlearrowleft}$ measurements. This is also in agreement with our model taken a Curie temperature of 225K. Indeed, decreasing the temperature by half a period leads to sin(ε) being equal to zero. This highest temperature measurement, close to both the Curie temperature and the working range of our MTT seems to confirm the reliability of our theoretical model.

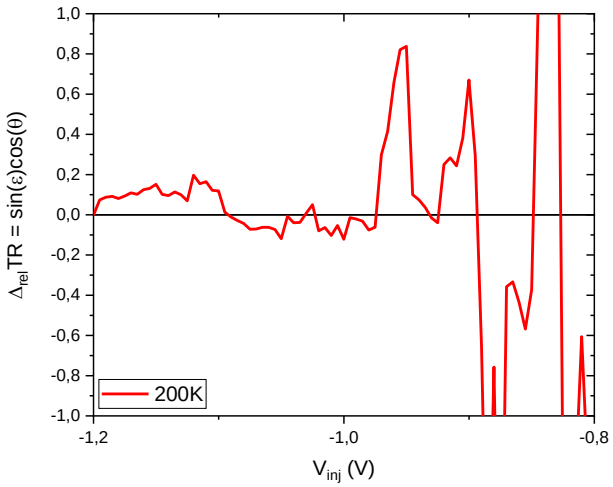

Figure IV.26: Precession signal $\Delta_{rel}TR$ as a function of injection voltage for a temperature of 200K.

In this study, first manipulation of the molecular field in CoAl was demonstrated. The precession phenomenon could be measured over a 60K window in the working range of our device. Even though, precession angle per nanometer is much lower in CoAl than in CoFeB, it remains unexpectedly high. Band structure calculations could explain these values by enhanced effective mass for electrons injected at 1eV above the Fermi level

IV.2 – Spin precession in CoCu

IV.2 – 1. Introduction

Motivation

Our study on spin precession in CoAl alloys showed that it was possible to reduce the precession angle per nanometer and control its values through variation of temperature. However, hybridization between Co and Al atoms leads to an unusual band structure with a pseudo-gap close to the Fermi level. The presence of this pseudo-gap makes hot electrons deviate from free-electron model, thus resulting in a potential explanation for high precession speed (about 300°/nm). Furthermore, the chemical affinity of Al to O led to diffusion of Al towards the tunnel barrier, making the control of the CoAl layer composition difficult. We aim

at reaching a value of ε* low enough to control precession angle from 180° to 0° over the working temperature range of our device and, if possible, to see extinction of the precession signal with a T_C below 200K. Following the same strategy adopted for CoAl, Co was alloyed with Cu in order to reduce its molecular field and decrease its Curie temperature.

State of the art - Structure

Excitement around Giant Magnetoresistance (GMR) brought considerable attention to CoCu systems either structured in multilayers or granular thin films. Indeed, segregation of Co in this alloy leads to the precipitation of ferromagnetic nanoclusters embedded in a non-ferromagnetic Cu matrix (see Fig. IV.27 – right) with a typical size between 5nm and 20nm. Both elements have a cubic fcc crystal structure making it possible to create a solid solution. Yet, miscibility of Co in Cu is very limited (see Fig. IV.27 – left). This system showed a maximum solubility of cobalt in copper around 21%. Above this concentration, formation of Co nanoclusters during sputtering deposition is expected with further diffusion caused by an annealing treatment. We chose to investigate further this alloy to see if we could extend the composition range of a metastable solid solution.

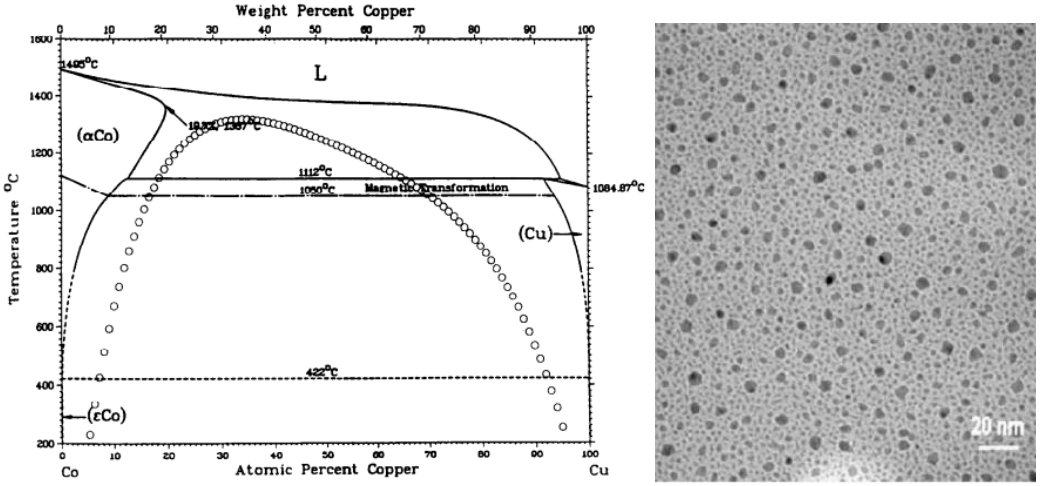

Figure IV.27: Binary Cu-Co phase diagram (left). From Bernardi[155]. BF TEM image a $Co_{45}Cu_{55}$ annealed thin film (right). From Mebed and Howe[156].

Unlike these studies on GMR on CoCu alloys, our purpose is to have a single phase CoCu thin films with homogenous magnetic properties. Work of Errahmani *et al.* on this material deposited with sputtering technique showed the alloys to stabilize into a fcc structure with a lattice parameter being directly proportional to the Co content[157]. This proves the creation of a solid solution.

State of the art – Magnetism

In the case of granular system, GMR is induced by spin-dependent scattering of electrons with Co particles embedded in the Cu matrix[158]. Formation of nanoclusters can be evidenced by a change of magnetoresistance as seen on figure IV.28. Typical magnetoresistance for granular CoCu systems reaches several percent. By comparing magnetoresistance of our thin films to that of the literature, additional information concerning the presence of Co nanoclusters can be given. As we expect to have a solid solution of CoCu alloy, description of the magnetism is different. Here if dilution of Co in Cu is low enough, description of magnetism can be different from that of classic itinerant electrons model. Thus,

one needs to look at the resulting electronic structure of isolated Co atoms in a Cu matrix treated as magnetic impurities.

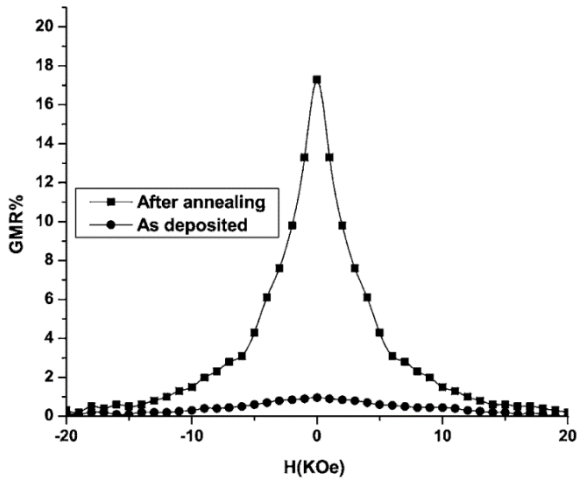

Figure IV.28: Room temperature magnetoresistance of a $Co_{45}Cu_{55}$ film annealed in the same condition as Fig. IV.27 – right. From Mebed and Howe[156].

State of the art – Electronic structure

Properties of the TM – noble metals alloys were deeply studied in the 50s, especially in the scope of their electronic structure. Friedel proposed a model to explain electrical properties of alloys with low concentration of TM in a solid solution[159]. This model was later applied on Mn alloyed with Cu to explain magnetic properties of the material[160]. This description seems to give a qualitative picture of the electronic structure of such system.

When alloying Co with Cu, d states of the transition metal are overlapping with conducting states of the matrix. As both have similar energies, a resonance phenomenon takes place. A d state of Co combines with a conducting state k of Cu to give two new states that will also resonate with others of similar energies (see Fig. IV.30 – left). At the end, a zone located around the magnetic impurities host high amplitude d states (see Fig. IV.30 – right). The resulting local excess of charge is called a virtual bounding state.

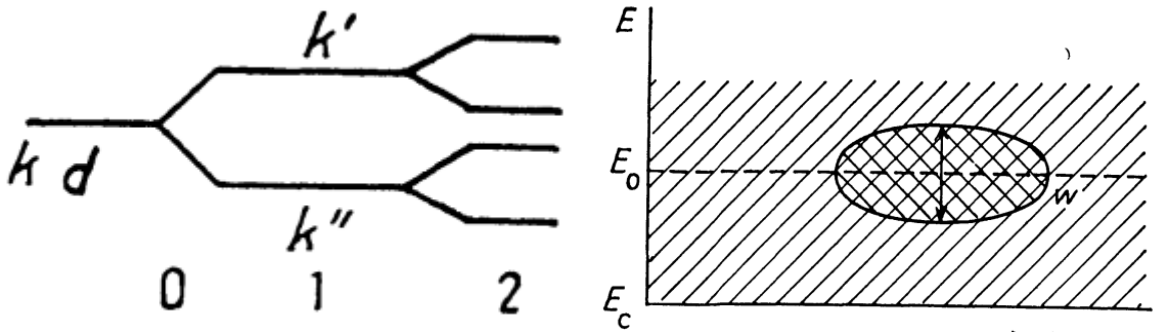

Figure IV.30: Resonance phenomena leading to a virtual bounding state (left). Diagram of a virtual bounding state in a space-energy representation (right). From Friedel[161].

Electrons participating to these virtual states can be decoupled into spin-up and spin-down populations (see Fig. IV.31 – left). The position of the local additional contribution of Co

atoms to the density of states is splitted between minority and majority electrons. Thus, depending on the spin asymmetry in the number of electrons at the Fermi level, an additional contribution to the exchange energy can be added (see Fig. IV.31 – right). For this TM – noble metal system in a fcc structure, there is a critical concentration limit around 20% of the TM which gives the influence of impurities magnetic moments on one another[160]. Below that limit, they do not interact and can be treated independently. Above that limit, interaction between neighboring impurities becomes strong enough to lead to ferromagnetism.

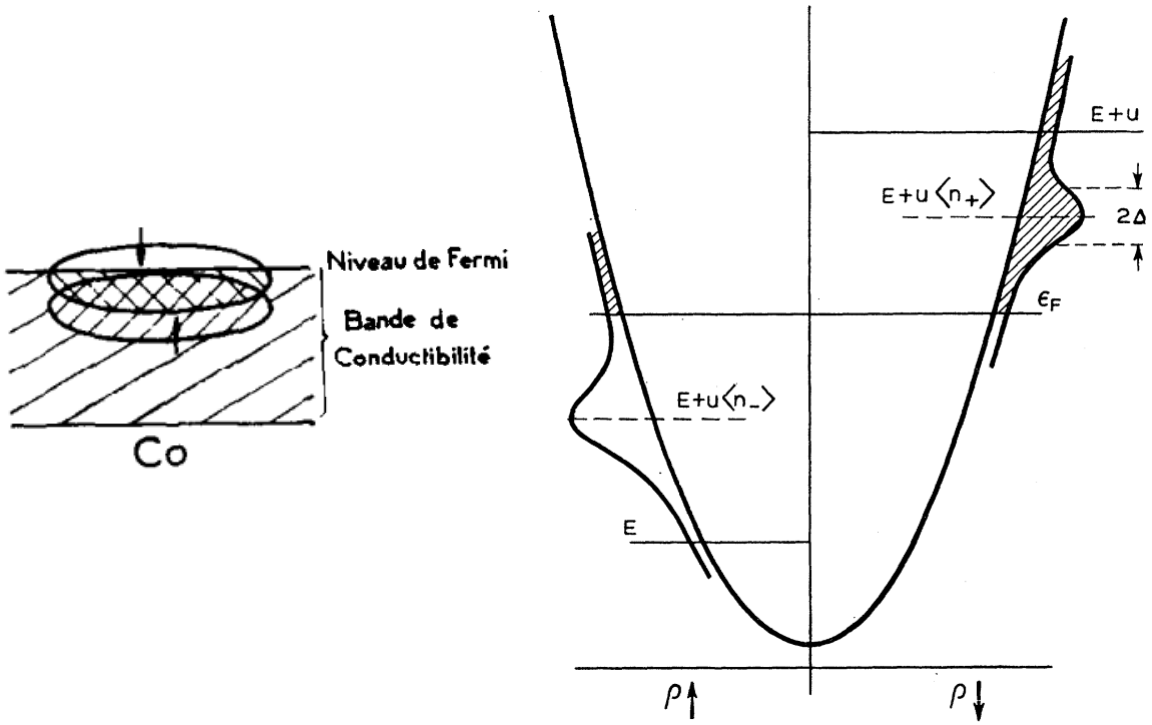

Figure IV.31: Electronic structure of Co atoms in a Cu matrix (left). From Daniel[162]. Density of state for Co impurities in a Cu matrix (right). The "humps" are the virtual d levels. From Anderson[163].

IV.2 – 2. Characterization

Room temperature magnetism (Ms)

As it has been evoked in the case of CoAl, we need in a first step to optimize the magnetic response of our CoCu alloy and especially design it to get the paramagnetic-ferromagnetic transition at temperatures around 100-200K. Therefore, Si//Ta(3)Co_xCu_{100-x}(40)/Pt(3) with Co compositions ranging from 10% to 60% have been grown by co-sputtering at room temperature. A 40nm thickness has been chosen to have enough magnetic signal for VSM measurements. Unlike CoAl thin films for magnetic measurements, no Pt seed layer was added in the stack because CoCu alloys naturally tends to order into a fcc structure with the [111] orientation. Therefore, 3nm of amorphous Ta should be enough to break the [100] direction of Si substrate and enables the growth of CoCu in this orientation.

Saturation magnetization measured at room temperature from VSM cycles is plotted against Co concentration on Fig.1. As clustering effects were reporting in the literature (see section IV.1 - 1), comparison between as-deposited and annealed samples properties was made. Black dots on Fig.1 correspond to as-deposited Co_xCu_{100-x} thin films while the red ones indicate

M_s for the same sample after an annealing. We applied the same annealing procedure for the thin films as we did for all our MTT: 1h at 200°C under vacuum with an in-plane applied magnetic field. No significant change of saturation magnetization could be observed for studied thin films (see Fig. IV.32). This can be attributed to a uniform deposition of Co and Cu elements over the whole layer with no effect of annealing. A Curie temperature around room temperature is obtained for a Co content around 20%. Therefore, samples with a concentration of Co below 20% were studied in order to determine both their Curie temperature and the temperature dependence of their saturation magnetization.

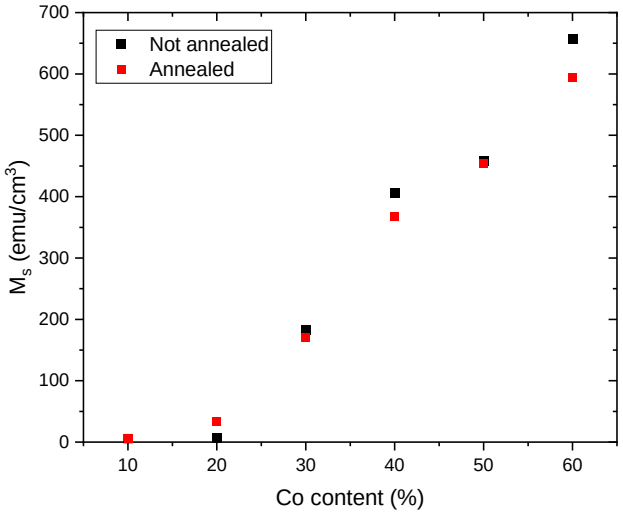

Figure IV.32: Saturation magnetization M_s at room temperature as a function of Co content. Black dots correspond to measurements for as-deposited samples and red ones for those after annealing.

Room temperature magnetism (Mr)

Contrary to CoAl samples, CoCu shows a remanent magnetization different from 100%. Even though an in-plane easy axis could be observed as shown on figure III.56 – left for $Co_{60}Cu_{40}$(40) at room temperature, magnetization at 0Oe does not reach its maximum value while the sample is saturated. As precession measurements are performed with almost no applied field, the magnetization of the CoCu thin film will be closer to $M_r(H_{app}=0Oe)$ than M_s. Magnetization hysteresis loops centered near 0Oe for different Co content are plotted on figure IV.33 – right. From 30%, remanence starts to decrease from 80% to 45%. It can be expected that at lower temperatures, the same trend appears for lower Co concentration alloys. Therefore, magnetization values associated with measured precession signals are much lower than M_s.

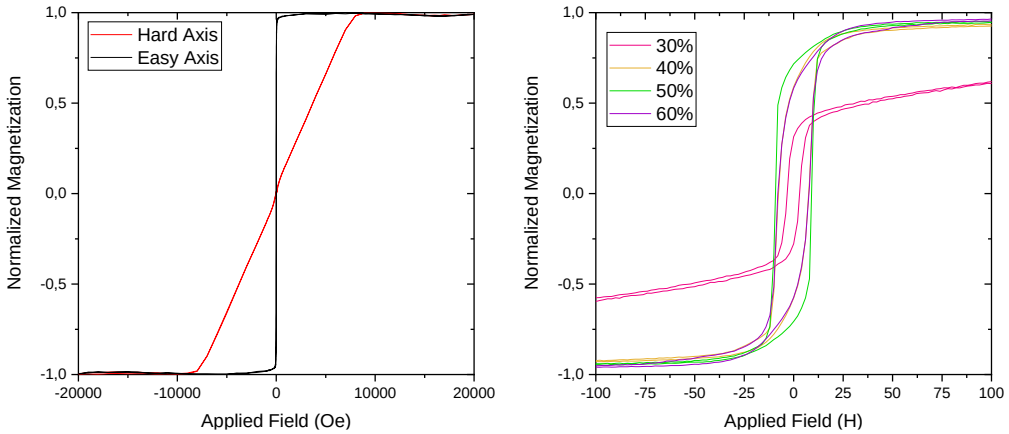

Figure IV.33: VSM measurements of $Co_{60}Cu_{40}$(40) sample in-plane (easy axis in black) and out-of-plane (hard axis in red) configurations at room temperature (left). VSM measurements of Co_xCu_{100-x}(40) along its easy axis (right). Range of applied field is [-100Oe, 100Oe]. Remanence is not 100% for those samples and tends to decrease with lowered Co concentration.

X-ray diffraction

CoCu alloy is expected to crystallize in a fcc structure oriented in the [111] direction. XRD experiments were performed on thick CoCu thin films. The annealed stacks studied were that of room temperature VSM measurements: Si[100]//Ta(3)/Co_xCu_{100-x}(40)/Pt(3). Even though crystalline structure could be affected by adjacent seed layers or by reduced thickness, those thin films were a first step to investigate orientation of the Co_xCu_{100-x} as a function of the Co content. In case of an inhomogeneous alloy due to the presence of clusters in a Cu matrix, deviations from the Vegard law should be observed.

Associated spectra are plotted on figure IV.34 for Co content ranging from 10% to 60%. First peaks observed on figure III.58 can be associated with Pt(111), Co_xCu_{100-x}(111) and Si(400) from the substrate. Inset of figure III.58 shows a zoom of the spectra around the reflection associated with Co_xCu_{100-x}(222) for all samples. A shift of the peaks position can be observed as cobalt content increases. Assuming that CoCu alloy behaves as a solid solution due to the close atomic radius of Co and Cu, Co atoms are replacing Cu atoms in the initial fcc structure. As Co atomic radius is shorter than that of Cu, the averaged cell parameter for Co_xCu_{100-x} is expected to decrease with increasing x.

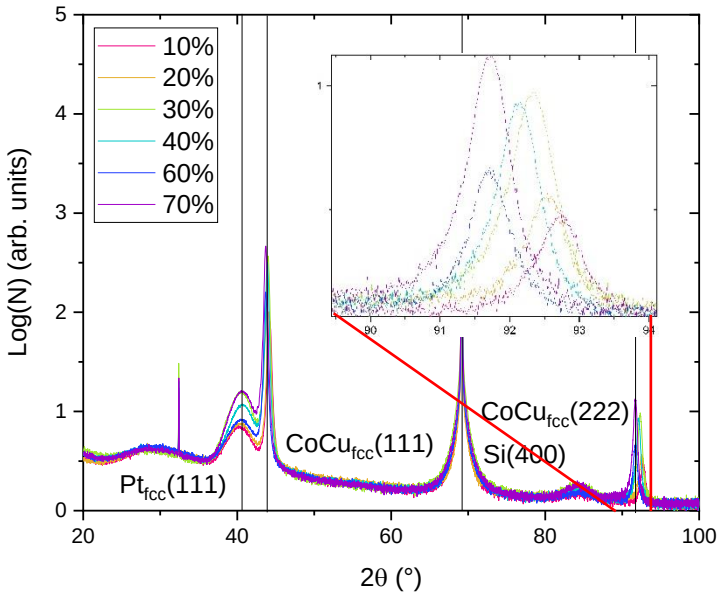

Figure IV.34: Out-of-plane XRD scan for a full film for several Co concentrations. N represents the number of counts for each angle explored. Inset: zoom around the reflection of Co_xCu_{100-x}(222). Peaks are shifted with the cobalt concentration.

Figure IV.35 shows cell parameters corresponding to Co_xCu_{100-x} diffraction peaks as presented on figure IV.34. Black dots is associated to as-deposited samples and white dots, to annealed samples. Red solid line describes theoretical Vegard law for a solid solution. According to Vegard law, cell parameter of an alloy follows a weighted mean law of the cell parameter of the two constituents. Thus, value for $\%_{Co}$ = 0% (resp. %Co = 100%) corresponds to the lattice parameter of Cu (resp. Co) in a fcc phase.

Both as-deposited and annealed follow a linear trend of d versus Co concentration. Therefore, it can be assumed that CoCu behaves like a solid solution. Still, annealed samples are off the mean law given by the red solid line. Experimental dots are shifted from theoretical model by 10% in Co content. A possible explanation would be that some Co segregate to form clusters in copper-rich matrix, leading to a decrease of the cobalt in this matrix. However, such phenomenon was not observed above 20% of Co[155]. Moreover, diffraction peaks on figure IV.34 are well defined. No side peaks corresponding to Cu can be observed. Thus, this deviation cannot be attributed to the crystalline quality of the CoCu layers. Measurement errors taking place during the XRD scan has to be considered, such as the positioning of the sample in the scanning place.

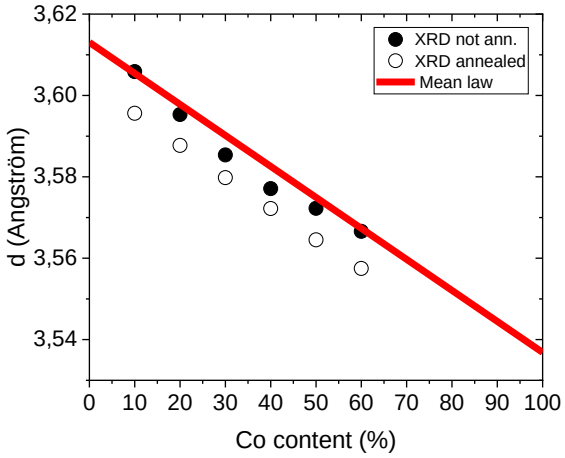

Figure IV.35: Cell parameter d extracted from XRD measurement on as-deposited (black dots) and annealed (white dots) samples as a function Co concentration. Red solid line describes theoretical Vegard law.

Transport in thin films

Transport measurements were performed in order to check the temperature dependence of the resistivity. An unusual R(T) was observed for CoAl thin films which associated with a semiconducting-like transition due to the presence of a pseudo-gap in the band structure of the material[146–148]. Therefore, we made sure of the metallic behavior of our alloys before going to patterning step.

Figure IV.36 shows the variation of resistance of Co_xCu_{100-x} thin films as a function of the temperature for x=20% (red) and x=50% (blue). Both samples were deposited in the same series of samples and patterned in a Hall cross of same geometry and size. Measurements were made on the same stacks used for magnetometry: Si//Ta(3)/Co_xCu_{100-x}(40)/Pt(3). Two contact points were taken on the full film to perform this measurement with about 1cm gap. Figure IV.36 shows that both thin films see their resistivity decrease with decreasing temperature, a behavior typical for metals.

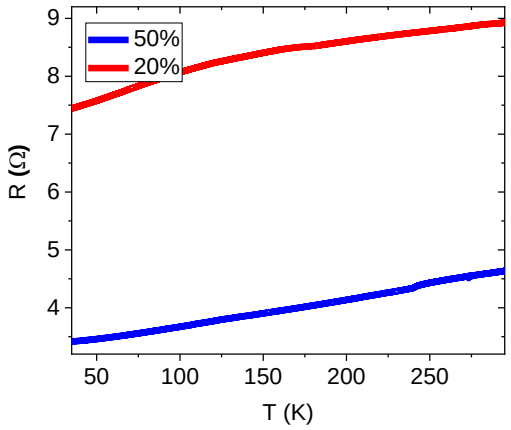

Figure IV.36: Resistance as a function of temperature for $Co_{20}Cu_{80}$(40) (red) and $Co_{50}Cu_{50}$(40) (blue).

Additional resistance measurements have been made on the same thin films at room temperature. Applying a magnetic field in the plane of the thin film can lead to a reorientation of the magnetization. If the magnetization is parallel to the direction of the injected current, the resistance is maximum while it will be minimum in the case they are perpendicular to each

other. This magneto-resistance effect is due to Anisotropic Magneto-Resistance (AMR) and arises from the orientation of the magnetization and spin-orbit interaction.

Magnetic anisotropy of Co_xCu_{100-x} thin films is known to be in-plane through VSM measurements (see Fig. IV.33 – left). Therefore, applying a magnetic field perpendicularly to the anisotropy axis will lead to a reorientation of the magnetization towards the applied field. Figure IV.37 shows variation of the resistance measured while sweeping the magnetic field in a direction perpendicular of the injected current. The two studied alloys are the same as previously: 50% (blue) and 20% (red) of Co content. The two curves have different variation for the same measurement. Resistance of $Co_{20}Cu_{80}$ is not affected by an applied magnetic field, unlike $Co_{50}Cu_{50}$ which sees its resistance increases around zero field. These two measurements are in agreement with the magnetic characterizations of the alloys. For $\%_{Co}$=20%, magnetization equals zero at room temperature and thus, no magneto-resistance can be observed. Concerning $\%_{Co}$=50%, the material behaves as a normal ferromagnet with the change of the resistance depending on the orientation of its magnetization.

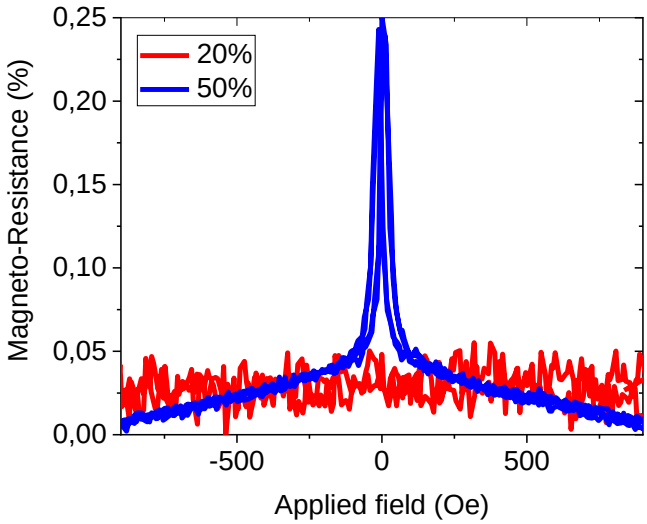

Figure IV.37: Magneto-Resistance measurements at room temperature for $Co_{20}Cu_{80}$(40) (red) and $Co_{50}Cu_{50}$(40) (blue).

Low temperature magnetism (Ms)

For this study additional films with three Co concentrations were deposited as follows: Si//Ta(3)/Cu(10)/Co_xCu_{100-x}(5)/MgO(2)/Pt(3) with x = {15%, 20%, 25%}. In those samples, the thickness of the CoCu layer was reduced from 40nm to 5nm to check a possible size effect and since SQUID is used, 5nm thickness should be enough for sensitivity. Secondly, the Cu and MgO interfaces will make the properties closer to the properties in the MTT. In those new stacks, T_c and M_s(T) were investigated.

SQUID measurements were performed on the three samples along with those with 40nm of CoCu. For each temperature, a magnetic field was applied in-plane up to 2T to observe and remove the diamagnetic components of both susbstrate and quartz rod to the magnetic signal. Therefore, magnetization values while the samples are saturated are reported on figure IV.38. Solid lines corresponds to CoCu(5) samples with different Co content ranging from 15% to 25%. The slope of M_s(T) for 5nm are almost linear over the range of temperature for our MTT. SQUID measurements confirm that a paramagnetic-ferromagnetic transition occurs at room

temperature for $Co_{20}Cu_{80}$ samples. In the case of $Co_{15}Co_{85}(5)$, the Curie temperature lies around 150K. Therefore, inserted $Co_xCu_{x-100}(5)$ precession layers will be deposited with a Co concentration between 15% and 20%.

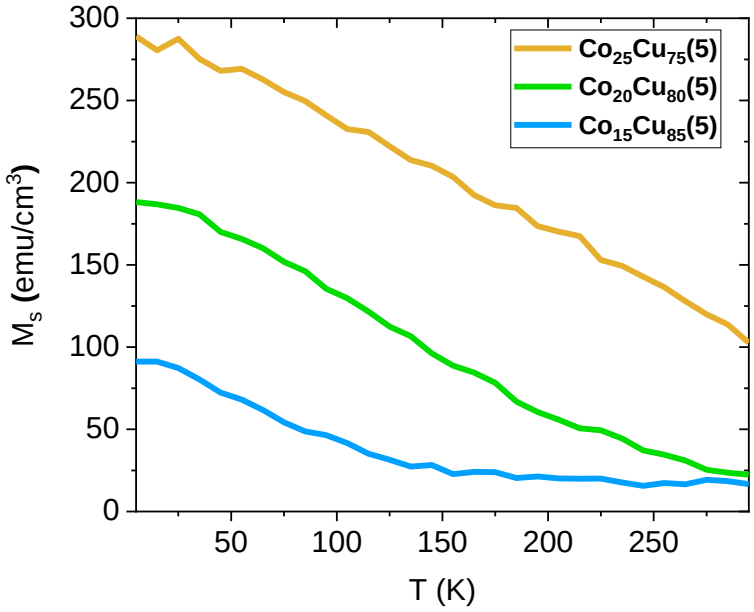

Figure IV.38: Saturation magnetization as a function of temperature for various $Co_xCu_{100-x}(5)$ alloys measured SQUID.

Comparison between SQUID measurements performed on 5nm CoCu thin films before and after annealing is shown on figure IV.39. Dashed lines correspond to as-deposited layers and solid lines to annealed ones. Annealing conditions are the same as previously mentioned. A slight decrease of the M_s is observed after annealing (except for $\%_{Co}$=15%). No clear explanation for this change can be given so far. The difference between two measurements of the same thin film may be due to error on the size of samples characterized. If there was diffusion to an adjacent layer or clustering phenomena of Co, magnetism would be driven by that of the formed Co centers. TEM imaging of our thin films can confirm the presence of such phenomena.

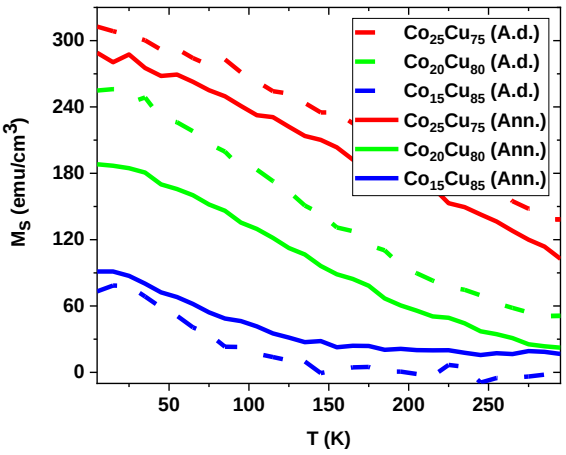

Figure IV.39: Saturation magnetization as a function of temperature for various $Co_xCu_{100-x}(5)$ alloys measured SQUID. Dashed lines indicates as-deposited layers while solid lines correspond to the same samples after annealing.

Low temperature magnetism (Mr)

Figure IV.40 – left shows hysteresis cycle for $Co_{20}Cu_{80}(5)$ centered around 0Oe obtained by SQUID at 70K. This measurements shows a small opening of the loop with a M_r around 14emu/cm^3. Comparing this value with that of M_s(70K) on figure IV.39, a factor ten is obtained. Similar measurements were performed from different temperature on two samples, $Co_{15}Cu_{85}$ and $Co_{20}Cu_{80}$. Experimental data is reported on figure IV.40 – right with blue and red dots respectively. Models describing a (1-T/T_r) law for both M_r(T) is plotted with solid lines of the same color. A linear temperature dependence can be assumed for this alloy. Associated specific temperature T_r for which the small hysteresis cycle of figure IV.40 – left disappears is estimated around 140K and 170K. The temperature for $Co_{20}Cu_{80}$ is much lower than that for its paramagnetic-ferromagnetic transition close to room temperature.

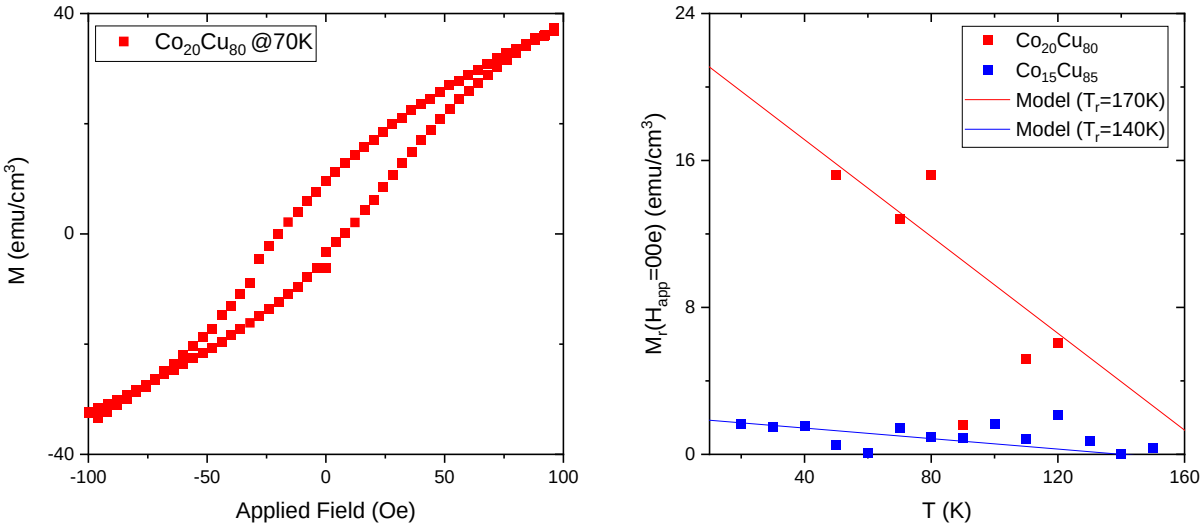

Figure IV.40: SQUID Hysteresis cycle of $Co_{20}Cu_{80}(5)$ centered of [-100Oe, 100Oe] at 70K (left). At zero field, the sample shows only a small remanence with $M_r(H_{app}=0Oe)=14emu/cm^3$. Remanent field M_r plotted as a function of temperature for $Co_{15}Cu_{85}$ and $Co_{20}Cu_{80}$ alloys (right). The two models associated with experimental dots describe linear variation of $M_r(T)$ following a (1-T/T_r) law. Curie temperature were estimated around 140K and 170K respectively.

Stack observations (Structure / Chemistry)

Transmission Electron Miscroscopy was used to get further information on our CoCu sample. A $Co_{17.5}Cu_{82.5}(5)$ stack following previously mentioned structure was analyzed. This investigation was carried out by the same microscope as in the section III.2 – 1. 50-60nm thick cross sections were prepared by a focused ion beam etching with Ga ions. Figure IV.41 shows the resulting high resolution TEM image of the studied stack. Each layer is labeled with a number. 1.Si(100) substrate gives the direction of our sample planes. Each layer until the tunnel barrier seems to be very well crystallized. Layers from the metallic base cannot be distinguished from one another. This is due to all materials crystallizing in the same fcc structure with a similar lattice parameter and all elements being close in the periodic table. Chemical analysis will bring further answer concerning interdiffusion in this structure.

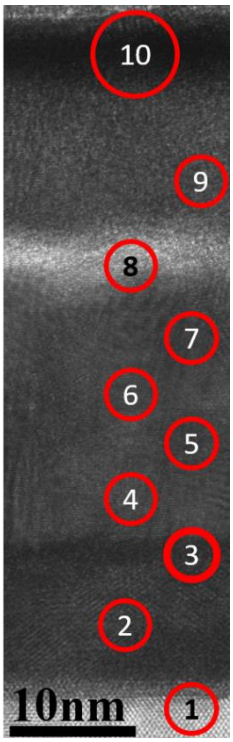

10. Pt

9. CoFeB/Ta/Co/IrMn

8. MgO

7. ~CoCu

6. ~Cu

5. ~$[Co/Ni]_{x4}$

4. ~Cu

3. Ta

2. Cu

1. Si(100)

Figure IV.41: High-resolution TEM image of the cross-section of a $Co_{17.5}Cu_{82.5}$(5) MTT stack. Circled numbers gives associated deposited materials indicated on the right. Layers labeled 4 to 7 cannot properly be distinguished on this image.

As no light element such as Al was critical for chemical investigation, electron energy loss spectroscopy (EELS) technique was used to map our stack with microscope on STEM mode. Colored maps for different elements are shown on figure IV.42 with corresponding STEM high angle annular dark-field (HAADF) image added on the right. Red solid lines are used as a visual guide to give separation between each layer. No interdiffusion seems to take place in our sample as colored dots remain in regions defined by the lines for all investigated elements.

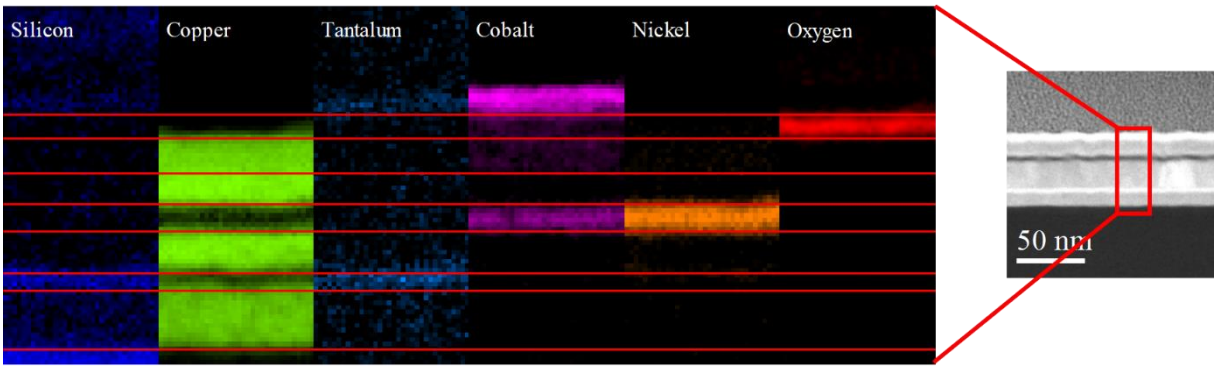

Figure IV.42: STEM EELS mapping of the stack cross-section for several elements present in the film with corresponding STEM HAADF image. Dashed lines indicates separation of each deposited layers.

FFT was performed over HR TEM image in order to define crystalline orientation of the different layers. Figure IV.43 shows FFT made on 5 different regions: 2.Cu (red), 4.Cu.$[Co/Ni]_{x4}$ (orange), Cu/CoCu (green), MgO (blue) and CoFeB/Ta/Co (purple). Direction of the growth corresponds to perpendicular direction with respect to interfaces. While the first Cu layer is rather polycrystalline with no strong apparent [100] texture that should be initiated

by Si(100) as in the case of CoAl sample (see section IV.1 – 1), the following layers are in a fcc structure oriented in the [111] direction. Patterns obtained by FFT is different between the two Cu layers (orange and blue) confirming this trend.

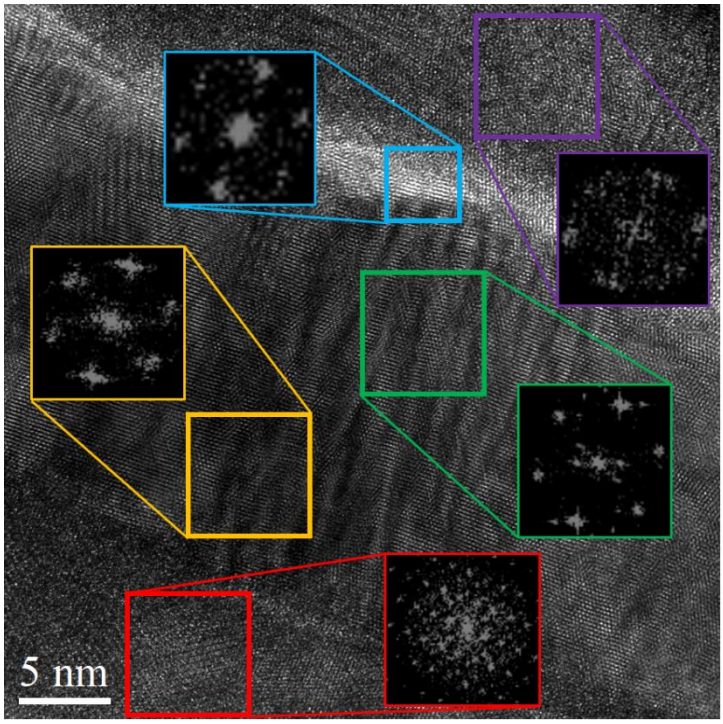

Figure IV.43: HR TEM image over the bottom of the thin film. FFT performed over different regions of the stack are shown with colored edges for each materials.

Chemical Analysis (EDX)

To make sure no diffusion/segregation phenomenon takes place in our sample, chemical profile was plotted for different element in the tunnel barrier region. Figure IV.44 – left shows a STEM BF image of the sample. A red rectangle covers the CoCu/MgO region. This corresponds to the region where a chemical analysis by Energy Dispersive X-Ray (EDX) was performed. Associated chemical profile is plotted on figure IV.44 – right with four elements of interests detected in this zone: Cu, O, Co and Mg.

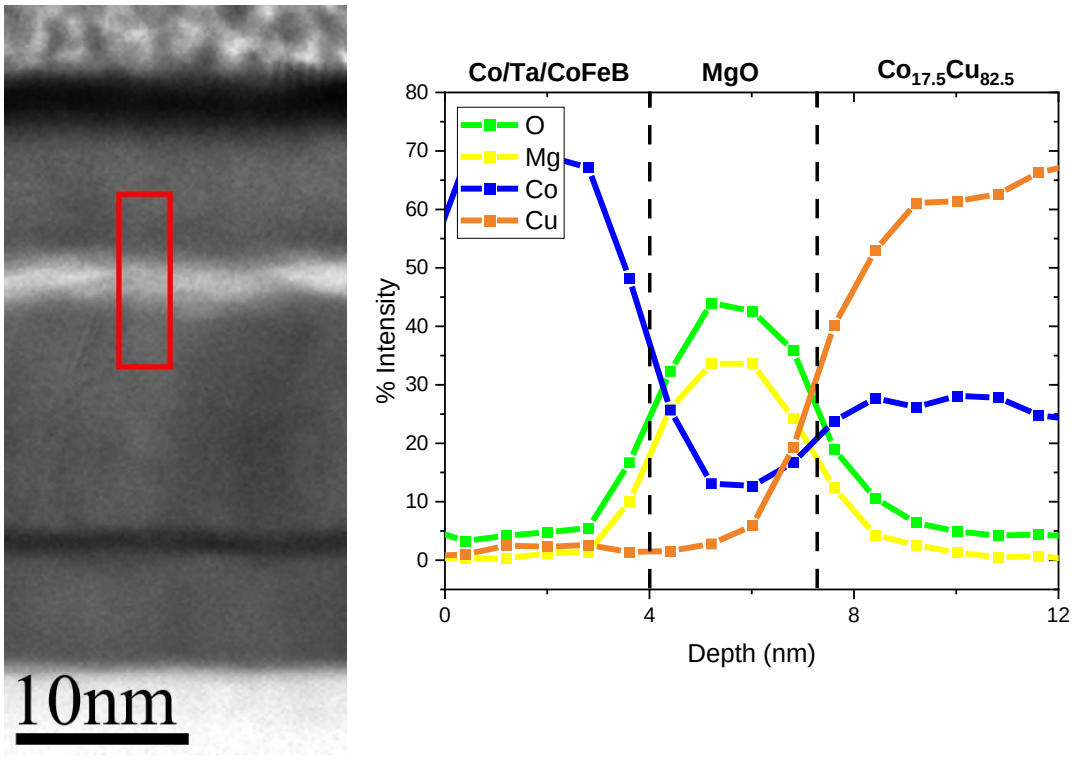

Figure IV.44: STEM BF image of studied sample (left) and corresponding chemical profile by EDX analysis around MgO tunnel barrier made in the red rectangle (right).

A first region from the beginning of the measurement up to 4nm sees a uniform presence of Co. This corresponds to the Co/Ta/CoFeB top electrode. Then, intensity of Co decreases while that of Mg and O rises, showing that oxide tunnel barrier is detected. Its thickness can be evaluated around 3nm, close to the deposition parameter for MgO (2.8nm). Then from 7nm to 12nm (around the 5nm deposited) depth, intensities for Co and Cu stay around 25% and 65%. Concentration of Co and Cu seems to be homogenous over the whole layer as associated intensities remain constant while sweeping the sample.

TEM results are used to confirm absence of Co clusters. Figure IV.45 shows both chemical and structural focus on the CoCu alloy. Literature states that segregation phenomenon leads to most Co atoms leaving the Cu matrix. Resulting clusters size is expected to lie around 5nm and 20nm. Figure IV.45 – left shows rather homogenous Co repartition in the layer. Furthermore, no grains similar to that of figure IV.27 (see III.3.1 – **State of the art - Structure**) can be observed on figure IV.45 – right.

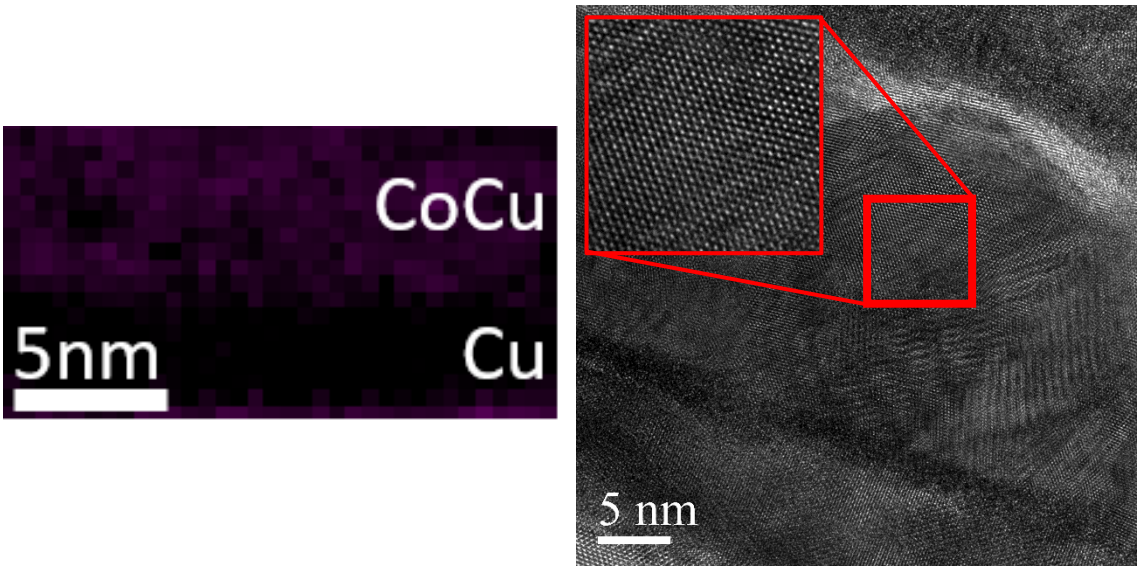

Figure IV.45: STEM EELS mapping of Co atoms of figure 13 (left) and HR TEM image with zoom in on the CoCu region (region).

Transport tunnel

Stacks studied by magnetometry were completed to integrate the full MTT structure for spin precession measurements:

$Si[100](HF)//Cu(5)/Ta(1)/Cu(5)/Ni(0.5)/[Co(0.2)/Ni(0.5)]_{x4}/Cu(3.5)/Co_xCu_{100-x}(5)/MgO(2.6)/CoFeB(2)/Ta(0.5)/Co(2)/IrMn(7.5)/Pt(5)$

with x being equal to 15%, 17.5% or 20%. Deposited thin films were patterned into MTT structure. As no MTJ based on CoCu alloys was reported in the literature, a first characterization of the TMR was made.

Following the same procedure as for CoFeB or CoAl MTJs, TMR of the junction was measured into different direction in the plane of the device for low applied voltage (+10mV). Figure IV.46 – Top-left shows magneto-resistance of a $Co_{17.5}Cu_{82.5}(5)$ device at 65K with three different directions of the applied field: 0° (red), 45° (green) and 90° (blue) with respect to the exchange bias orientation initiated during the annealing. For all measurements, signal is very weak with TMR below 1%. Other panels of figure IV.46 show each measurement zoomed over the [-1000Oe, 1000Oe] window. The weak change of magneto-resistance rises doubts concerning the presence of tunnel magneto-resistance effect in our device or about the magnetism of the CoCu alloy. No hysteresis loop can be observed for the measurement performed in the direction of the exchange bias (Fig. IV.46 – top-right). Only the curve for perpendicular orientation of the in-plane magnetic field (Fig. IV.46 – bottom-right) has the shape expected with a maximum value obtained near zero field and a linear decrease.

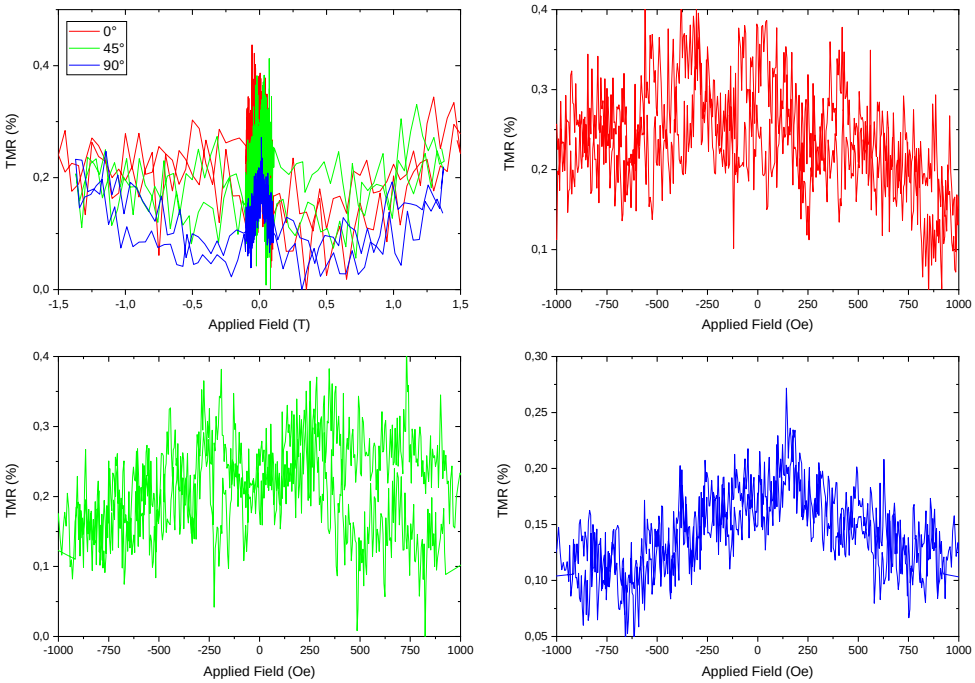

Figure IV.46: TMR of a $Co_{17.5}Cu_{82.5}$(5) MTT at 65K with V_{inj} = +10mV (top-left). Magnetic field is applied in three different directions: 0°, 45°, 90° with respect to the orientation of the exchange bias. Other panels: Zoom of TMR measurements for each direction of the applied field over the [-1000Oe, 1000Oe].

As expected, other measurements performed at higher temperature do not give better results for V_{inj} = +10mV. To go further, we investigated TMR of this device at 65K for different injection voltage. Results are shown on figure IV.47. Six different tunnel magneto-resistance are plotted against applied field for V_{inj} between -500mV and +500mV (convention is the same as that taken in Fig. II.1 – d) with negative voltages corresponding to electrons injected into the spin valve). For all measurements, magnetic field was applied in the direction of the exchange field induced by the IrMn layer, in order to observe transition from parallel to antiparallel configurations of the magnetizations on the MTJ resistance state. Surprisingly, expected hysteresis loop appears for an applied voltage +500mV. For so high voltages, TMR values of tunnel barrier are usually reduced by a huge factor due to scattering processes that help electrons to cross the junction (see section I.1 – 5).

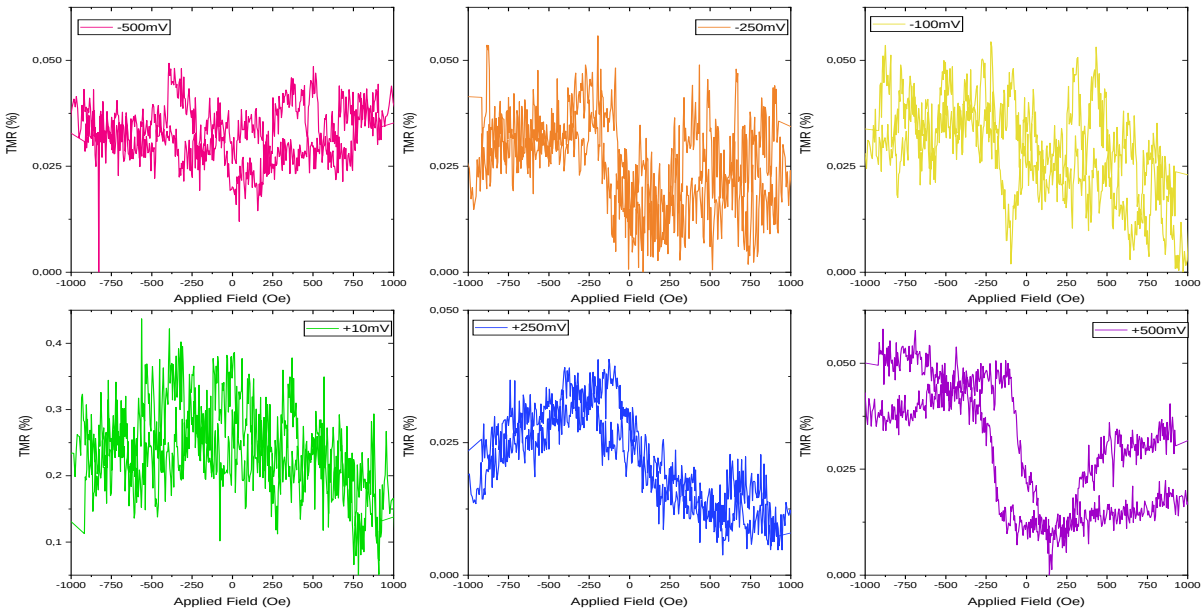

Figure IV.47: TMR of a $Co_{17.5}Cu_{82.5}$(5) MTT at 65K in the direction of exchange bias (0°) for several injection voltages.

TMR measurement at +500mV combines two features that explains that a hysteresis loop can be more clearly observed for this specific injection voltage: first, since the tunnel current increases, the level of noise is reduced while going to higher applied voltage. For lower energies, the level of noise is almost equal to the jump of TMR observed on the last panel of figure IV.47. Secondly, the size of the jump is also higher for this specific voltage of -500mV. In the measurements of +250mV and -250mV, a small cycle opens at the same field values as for -500mV (around -250Oe and 0Oe) but its size is much smaller than that observed for the last measurement.

TMR loop observed for V_{inj} = - 500mV was measured for several temperature from 65K to room temperature. Hysteresis cycle is still present while increasing the temperature. However, experimental TMR is affected in two ways. With higher temperatures, signal/noise ratio decreases. Moreover, the coercivity for the hysteresis loop of figure IV.47 (-500mV) slowly decreases with increasing temperatures. Around 150K, the cycle is totally shrunk and no response can be observed anymore.

Having so weak TMR signal was not expected. The presence of the hysteresis loop is confirmed both with repeated measurements (Fig. IV.48 – left) and with its variation with temperature. Measurement of the TMR but with a magnetic field applied in-plane, perpendicular to the exchange bias direction shows expected triangular signal associated with rotation of the top electrode magnetization, as seen on figure IV.48 – right. We attribute the response of figure IV.48 – left to a reversal of the $Co_{17.5}Cu_{82.5}$ electrode. The switch for AP to P configuration with higher field cannot be observed as the TMR follows a linear variation with magnetic field (see Fig. IV.46). The small response of TMR is probably lost in this contribution. We have no physical explanation for apparition of this hysteresis loop for this specific voltage of -500mV.

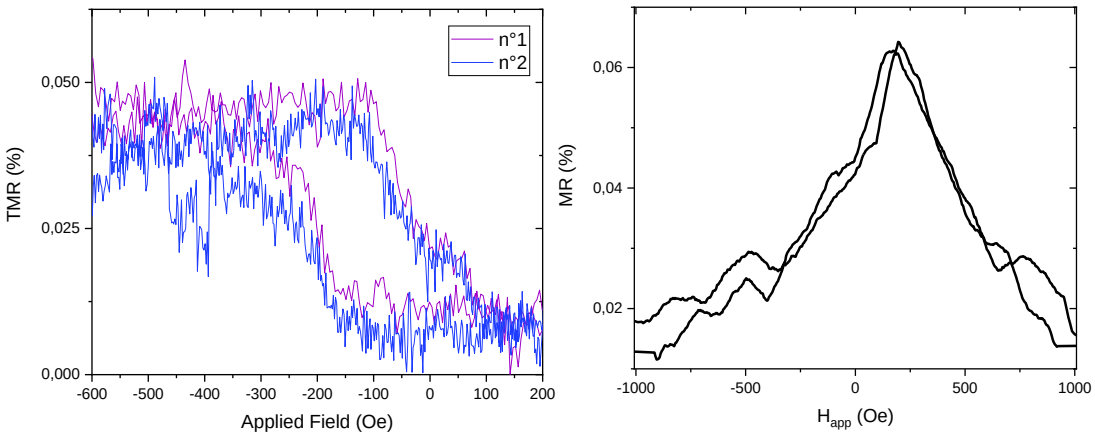

Figure IV.48: TMR of a $Co_{17.5}Cu_{82.5}$(5) MTT at 65K with V_{inj} = +500mV with the magnetic field applied along the exchange bias direction (left). Figure shows two measurements of the device to show persistence of the hysteresis loop. TMR measured in the same conditions with a magnetic field applied in the sample plane, perpendicular to the exchange bias (right).

Considering previous results on magnetometry, magneto-resistance effect observed in our device cannot be associated with M_s but with remanent magnetization M_r close to zero field. The huge difference between M_s and M_r is expected to affect the TMR signal by lowering the value (around 20% in the case of CoAl alloy). Therefore, tiny TMR would be due to the weak magnetic signal of this CoCu alloy. While higher magnetic field is applied (+1T), magnetic moments in CoCu aligns in the same direction. As observed experimentally (not shown on Fig. IV.48), the magneto-resistance signal keeps decreasing while further magnetic field is applied

Considering TMR obtained with CoAl devices (~20%) despite diffusion processes taking place at the MgO interface, such a low TMR in CoCu samples was not expected. Still, this can be understood with the complex magnetism of CoCu alloy that does not reach saturated magnetization with low applied field. Hysteresis loop obtained at +500mV is enough to stabilize magnetic configurations of our MTT. By ensuring a crossed configuration of the magnetizations at this voltage, precession measurements can then be performed at negative injection voltages.

Hot electrons transport

As complex tunneling in our CoCu-based MTJ leaves doubts concerning the CoCu(5) magnetic configurations, we performed hot electrons measurements of a $Co_{15}Cu_{85}$(5) MTT with the same structure as previously described, as hot electrons are very sensitive to the spin valve configuration. Figure III.70 shows the variation of the TR as a function of the magnetic field for an injection voltage of -900mV at 85K. The magnetic field was applied in the MTJ plane with three different orientations: 0°, 45° and 90° with respect to the direction of the exchange bias.

Similar measurements were done in C. Vautrin PhD thesis to demonstrate the crossed configuration for the CoFeB/Cu/[Co/Ni] spin-valve inserted in the MTT. It was possible to corroborate magnetic configurations of each ferromagnetic layer based on measured collected current I_c. Presence of a top electrode polarizing hot electrons injected into the spin-valve makes more complex analysis of the magneto-current. Thus, transfer ratio was studied in order to have a normalized signal. Moreover, changing orientation of the applied magnetic field should allow us to see a possible remaining contribution in the TR signal of the top electrode magnetization.

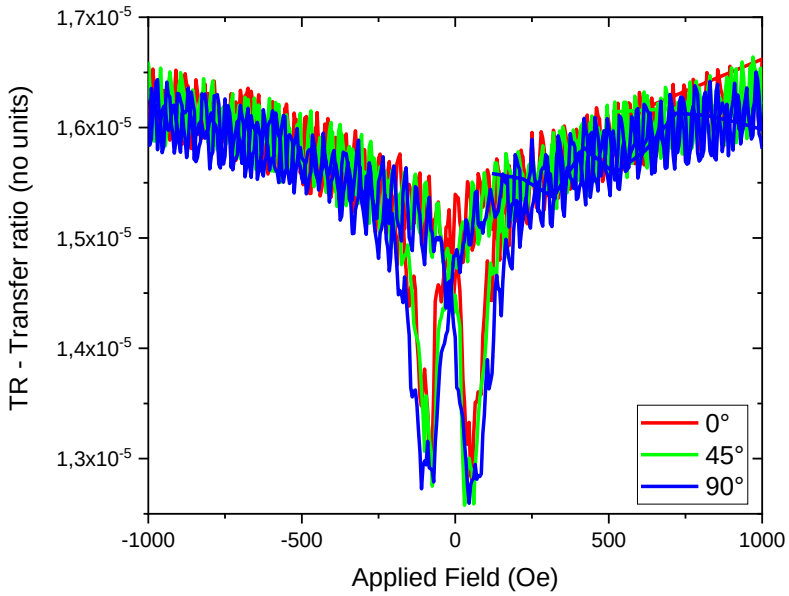

Figure IV.49: Variation of TR measured on a $Co_{15}Cu_{85}$(5) MTT for an injection energy of -900mV at 85K with three different in-plane orientations of the applied field.

Curves plotted on figure IV.49 can be divided into two regions: in the [-100Oe, +100Oe] window, TR varies sharply with magnetic field (~20%). Depending if the magnetic field is swept from positive or negative high field values, the signal dips about the same amount for either positive or negative values. The two peaks are symmetric, centered at almost zero field and are not affected by the orientation of the applied field. Thus, we can attribute this variation of TR to spin-filtering with the spin-valve. With very low field values, CoCu magnetization is reoriented within the plan, breaking the 90° crossed configuration between in-plane CoCu and out-of-plane [Co/Ni]. This can be due to the magnetic anisotropy being influenced by the squared shape of the tunnel junction. Then, the second region above in the $[\pm 500, \pm 1000]$ range, corresponds to an in-plane alignment of [Co/Ni] magnetization and a saturation of CoCu magnetic moments.

Same measurements were performed with a magnetic perpendicular to the exchange bias for different temperatures ranging from 100K to 250K to see an effect of temperature over the TR signal. Experimental data are reported on figure IV.50. As TR is dependent on temperature, a normalized amplitude of TR was plotted to compare the magnitude of the spin-filtering at the spin-valve. Expression of this is expressed as follows: $\frac{TR(H_{app})-TR_{min}}{TR_{min}}$ where H_{app} stands for applied field and TR_{min} refers to the minimum value of TR.

Figure IV.50 – left shows the variation of this normalized amplitude of TR for four different temperatures (100K, 125K, 200K and 250K) with field values ranging from -1.2T to +1.2T. High field values of the normalized amplitude of TR shows a strong dependence on the temperature. For the maximum applied field (1.2T), the signal is reduced from 50% at 100K to 30% at 250K. This can be due to our Schottky barrier being less efficient close to room temperature or also to CoCu becoming paramagnetic (see Fig. IV.40). The remaining signal based on the latter hypothesis could be explained by the fact that incoming hot electrons currents is still spin-polarized.

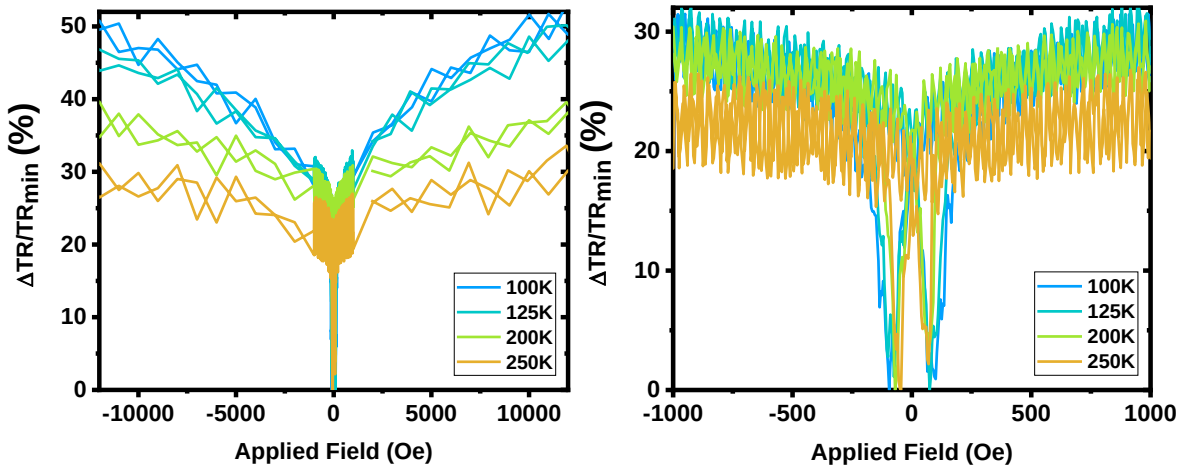

Figure IV.50: Normalized amplitude of TR on a $Co_{15}Cu_{85}$(5) MTT for an injection energy of -900mV for several temperature. The magnetic field is applied in-plane, perpendicular to the bias direction. Normalized amplitude of TR between -1.2T and +1.2T (left) and zoom over the [-1000Oe, +1000Oe] range (right).

Beyond this, values for the normalized amplitude of the TR should be lower than $MC^{\perp}$ (see calculations below). Considering that for a CoFeB/Cu/[Co/Ni], perpendicular magneto-current was about 75%, we can assume to achieve close values for this CoCu-based MTT. This prove an efficient spin-filtering in the spin-valve.

Relation between normalized amplitude of TR and perpendicular magneto-current

$$\frac{TR(H)-TR_{min}}{TR_{min}} \approx \frac{TR(H)-TR^{\perp}}{TR^{\perp}} = \frac{\frac{I_c(H)}{I_{tun}(H)} - \frac{I_c^{\perp}}{I_{tun,P}}}{\frac{I_c^{\perp}}{I_{tun,P}}}$$

In the case where $I_{tun}(H)$ does not change with applied field while the configuration is parallel, we retrieve expression for $MC^{\perp}$. Considering with higher magnetic field, magnetic moments in CoCu align and thus, I_{tun} is increased:

$$I_{tun}(H) > I_{tun,P}(H \approx 0Oe) \; so \; \frac{TR(H)-TR_{min}}{TR_{min}} < MC^{\perp}$$

Having a look over the [-1000Oe, +1000Oe] window plotted on figure IV.50 – right, a change in the two symmetric dips for low applied field can be observed. The two peaks shrink with increasing temperature. This can be attributed to a decrease of the field required to reverse the CoCu magnetization similarly to what was observed for TMR(T). Therefore, TR as a function of the magnetic configuration of our MTT tends to confirm that previously measured TMR hysteresis loop can be associated with a reversal of the CoCu magnetization. With a small magnetic field, crossed configuration between CoCu and [Co/Ni] can be achieved as showed the minimum values for the normalized TR amplitude.

Then, TR was characterized over of temperature and voltage ranges for precession measurements. Figure IV.51 shows TR for a $Co_{20}Cu_{80}$(5) MTT as a function of injection voltage for five temperatures from 50K to 150K. Schottky barrier height can be evaluated around 0.63V, the same value as for CoFeB MTT proving the good quality and reproducibility of our Schottky contact. The shape of TR as function of V_{inj} remains unaffected with the temperature: After a

fast increase of the signal, it slows down for voltages lower than -0.85V. However, no decrease of the TR is observed over this window as it was the case for CoFeB. As the magnitude of the TR for CoFeB is similar (around 10^{-5}), this change in the voltage dependence of transfer ratio can be associated with a longer mean free path for hot electrons injection into CoCu compared to that for CoFeB. This is expected as alloying Co with Cu should increase mean free paths values towards that of Cu.

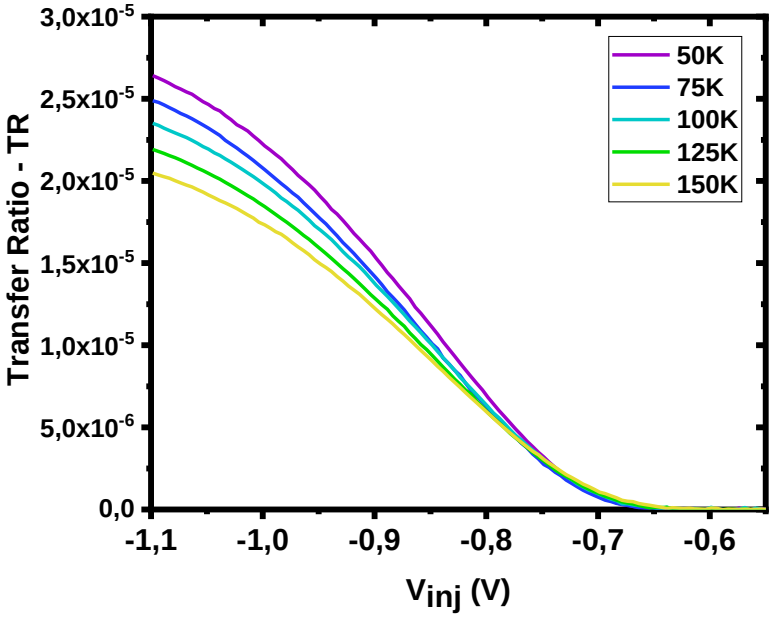

Figure IV.51: Transfer Ratio of a $Co_{20}Cu_{80}$(5) MTT as a function of injection voltage for several temperatures without any magnetic field applied.

Concerning the variation of TR with temperature for a given injection of -1.1V, the TR is decreased by 29% in the case of $Co_{20}Cu_{80}$(5) against 15% for CoFeB(1) while going from 50K to 150K. Moreover, the dependence on temperature of TR is more affected by injection voltage in the case of $Co_{20}Cu_{80}$(5) with the same decrease going from 18% around 0.8V to 29% at -1.1V. As CoCu alloy has a much lower Curie temperature compared to CoFeB, increasing temperature by a same amount leads to much more magnon generation in the former case. Therefore, the temperature dependence is indeed expected to be stronger.

Before measuring spin precession, amplitude of the TR variation with MTJ magnetic configuration needs to be estimated. By comparing TR values for P and AP configurations, an upper bound can be extracted. In the case of pure spin precession motion of hot electrons in the base (*i.e.* without scattering or filtering effect), the difference of TR between P and AP states equals the difference of TR between a 360° and 180° precession of the spin. Figure IV.52 shows TR as a function of injection voltage for three magnetic configurations: fully saturated at +1T (red), P configuration at +200Oe (blue) and AP configuration at -400Oe (green). The two latter magnetic fields correspond to that applied to get the TMR hysteresis loop at +500mV. Once associated resistance states were stabilized, hot electrons measurements of figure IV.52 were performed.

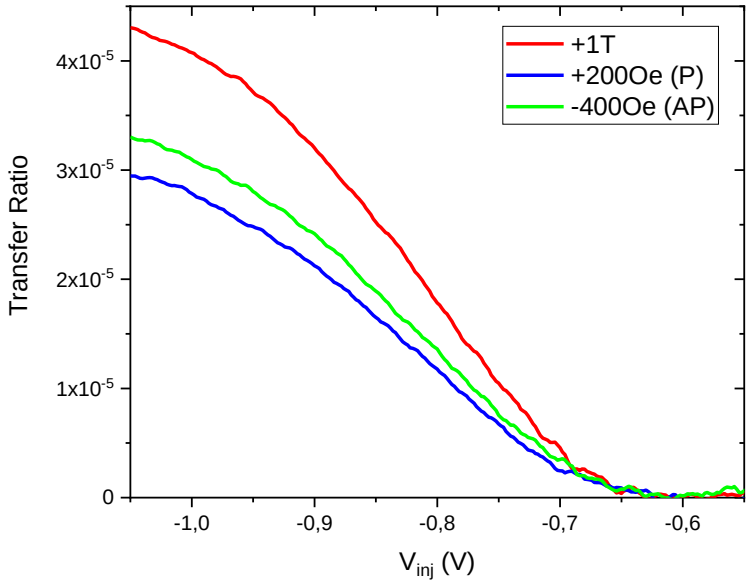

Figure IV.52: Transfer Ratio of a $Co_{17.5}Cu_{82.5}$(5) as a function of injection voltage at 35K for three different magnetic configurations of the MTT: saturated MTT (+1T), parallel configuration for MTJ electrodes (+200Oe), antiparallel configuration of electrodes (-400Oe). P and AP states are associated with minimum and maximum resistance values respectively (see Fig. IV.47).

Surprisingly, higher transfer ratio was found in the so-called AP configuration compared to the P one. This was not expected as such measurements on CoFeB or CoAl led to a reverse ordering of the curves. Physically, this can be understood as electrons having more chance to properly cross MgO barrier by tunnel effect in the parallel configuration compared to the antiparallel state (see Fig. I.8 in section I.1 – 5). Thus, even though TR is normalized signal, injected current may not be equivalent and does not lead to the same scattering resulting in a decreased TR value in AP configuration.

To confirm the origin of this particularity of CoCu MTT, relative tunneling current between P and AP configurations associated with TR measurements of figure IV.52 is shown on figure IV.53. For conventional MTJ, this value usually goes to zero with increasing voltage. Indeed, as electrons overcome the tunnel barrier with more energy, they have higher chances to undergo interactions that flip spins and mix spin-channels. However in the case of $Co_{17.5}Cu_{82.5}$(5), the opposite trends happen. Going from positive values around 500mV, this relative tunneling current decreases until crossing the abscissa line and going towards negative values.

The change of sign with increasing injection voltage explains results of figure IV.52 At higher voltages, AP configuration favors injection of hot electrons into the base compared to P configuration. Detailed mechanisms behind this voltage dependence is too complex to be tackled in this study as many factors are related to these measurements: negative TMR, distribution of injected electrons, scattering effects for tunneling electrons, etc.

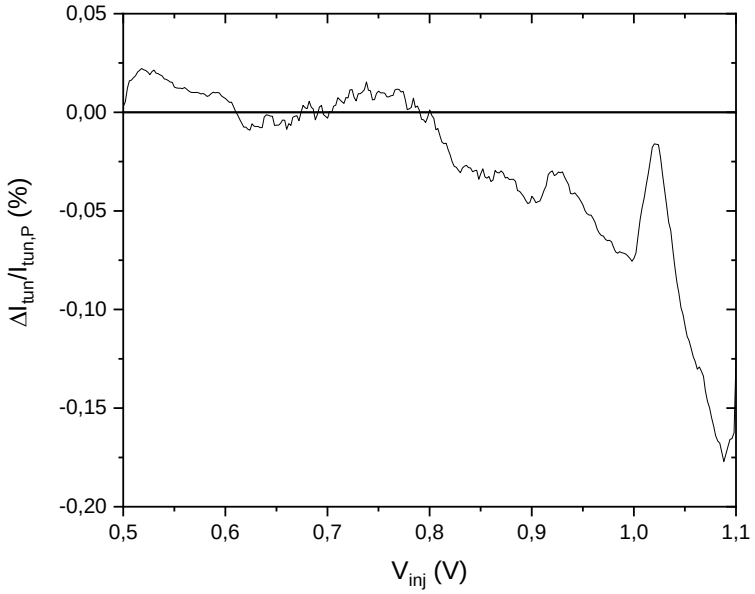

Figure IV.53: Relative tunneling current $\left(\frac{I_{tun,P}-I_{tun,AP}}{I_{tun,AP}}\right)$ *between P and AP configurations as defined previously. This ratio is positive at 500mV, it becomes negative for energy range used for hot electrons measurement.*

IV.2 – 3. Temperature-dependent spin precession

Mesures

Tunnel and collected currents were characterized for this $Co_{17.5}Cu_{82.5}$(5) MTT at 60K. On figure IV.54 - left, tunnel current (I_{tun}) is plotted against injection voltage (V_{inj}) for the three magnetic configurations (clockwise, counterclockwise and parallel). Red and blue curves are associated with CW and CC configurations respectively and the black curve with parallel one. Distinction of the different configurations is difficult due to the extremely low TMR for this device. On figure IV.53 - right, collected current (I_c) is also plotted against V_{inj} for the same three magnetic configurations. In this device, the Schottky barrier height lies around 0.63V. a slight difference between CW and CC configurations can be observed corresponding a spin precession of hot electrons in the metallic base.

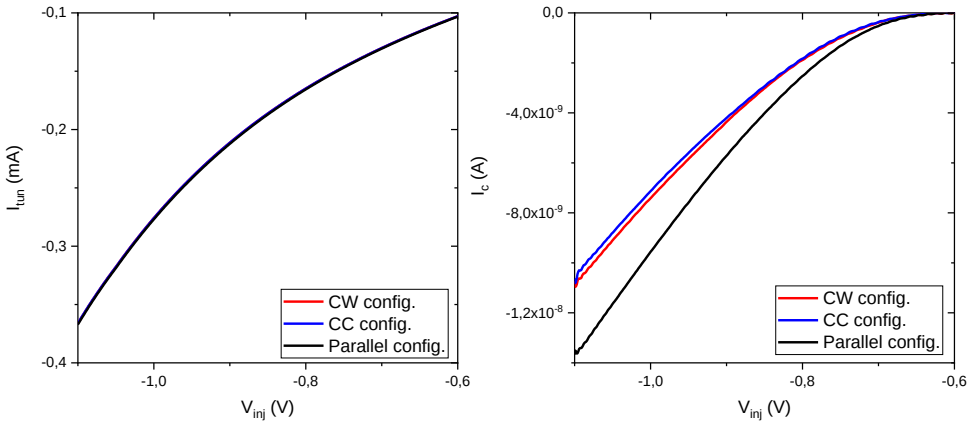

Figure IV.54: Tunnel current (left) and collected current (right) as a function on injected voltage for a $Co_{17.5}Cu_{82.5}$*(5) MTT at 60K in the three magnetic configurations (clockwise, counterclockwise and parallel).*

Considering the three magnetic states – namely clockwise (CW), counterclockwise (CC) and parallel configurations – have been stabilized, TR is plotted as a function of V_{inj} on figure IV.55 based on previously shown I_{tun} and I_c measurements (See Fig. IV.54). The Schottky barrier height can be evaluated around 0.63V, in agreement with that of CoFeB and CoAl MTTs. Values of TR reached for this device is about 3 times higher than that of CoFeB. This enhancement of the signal is expected even though precession layer for this MTT is thicker. The mean free path of CoCu is expected to be higher compared to that of CoFeB due to the Cu alloying. Moreover, number of repetitions for the [Co/Ni] multilayer was decreased to 4 as previously stated. The well-crystallized CoCu layer as seen on TEM images also explains the TR is much higher compared to that of CoAl, which is polycrystalline. The reduced density of states for CoAl may also contribute to the difference between the two materials.

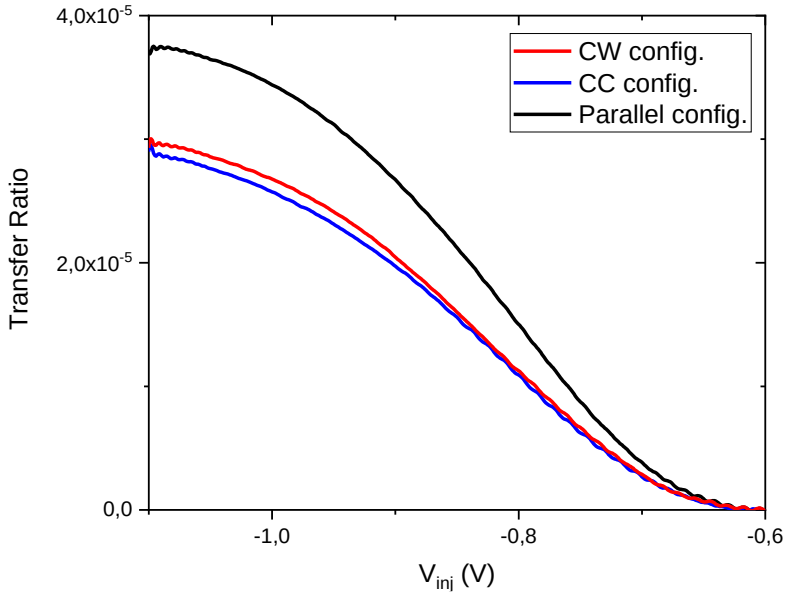

Figure IV.55: Transfer ratio as a function of injection voltage for a $Co_{17.5}Cu_{82.5}$(5) MTT at 60K in three different magnetic configurations (clockwise, counterclockwise and parallel).

Once again, a difference between CW and CC measurements can be associated with a spin precession effect taking place in our active layer. The red curve associated with a clockwise configuration is above the blue one, for counterclockwise configuration. As in the case of CoFeB measurements shown on figure III.12, this corresponds to a positive measured angle, between 0° and 180°. As the signal is much stronger than in the case of CoAl samples, no repetition of the measurements have been made.

Based on expression of the precession signal $\Delta_{rel}TR$ of equation III.10 (see section III – **Measuring principle**), TR signals plotted on figure IV.56 can be used to access both the precession (ε) and the filtering (θ) angles as a function of injection voltage. Calculated values in the case of this $Co_{17.5}Cu_{82.5}$(5) MTT measured at 60K is shown on figure IV.56. Below -0.8V, precession signal switches between high positive and negative values. This part of the graph cannot be used to extract precession angles. Yet, around -0.8V, the signal stabilizes in the [-1, 1] window. To study further the precession phenomenon in this device, precession signal from -1.1V to -0.85V was used. Error bars shown for $\Delta_{rel}TR$ as a function of the temperature and injection voltage results from the local noise of the measurements. Local oscillations of the signal are assumed to induce uncertainty on the extracted values for $\Delta_{rel}TR$.

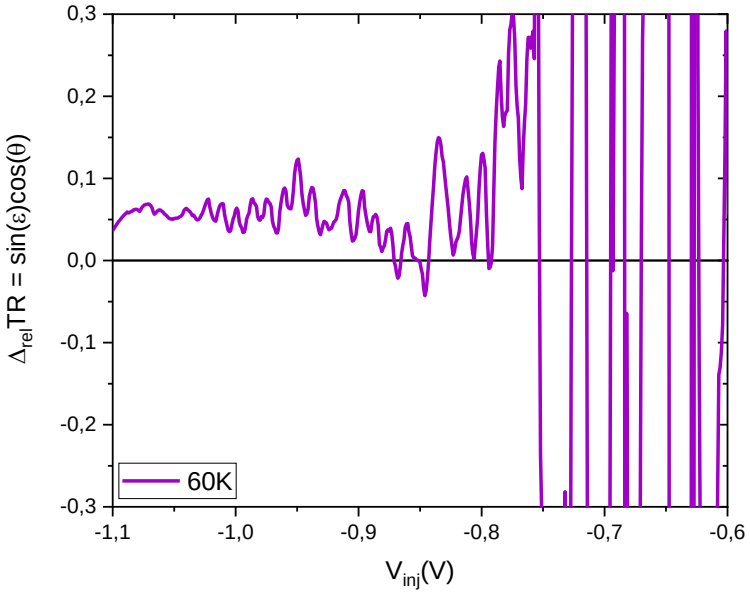

Figure IV.56: Precession signal $\Delta_{rel}TR$ as a function of injection voltage V_{inj} for a $Co_{17.5}Cu_{82.5}(5)$ MTT at 60K. Plotted signal is calculated using the transfer ratios of figure IV.55.

The same measurements have been performed over a wide range of temperature. Figure IV.57 shows $\Delta_{rel}TR$ as a function of injection voltage V_{inj} for four temperature: 60K, 80K, 95K and 115K. Voltage window plotted here was reduced ([-1.1V, -0.8V]) compared to that of figure IV.56 ([-1.1V ,-0.6V]) in order to make the plot clearer for the readers. All precession signals follow the same trend: going from high signal at low energy, the signal is reduced down to given signal for higher injection voltage. $\Delta_{rel}TR$ fluctuates around this value but does not seem to be changing sign for all temperature studied (taking into account noise of the measurements). Precession signal clearly changes its sign with the temperature as $\Delta_{rel}TR$ seems to be positive/negative by 35K intervals. Therefore, a periodicity of the precession signal with temperature can be expected in the same way as CoAl devices.

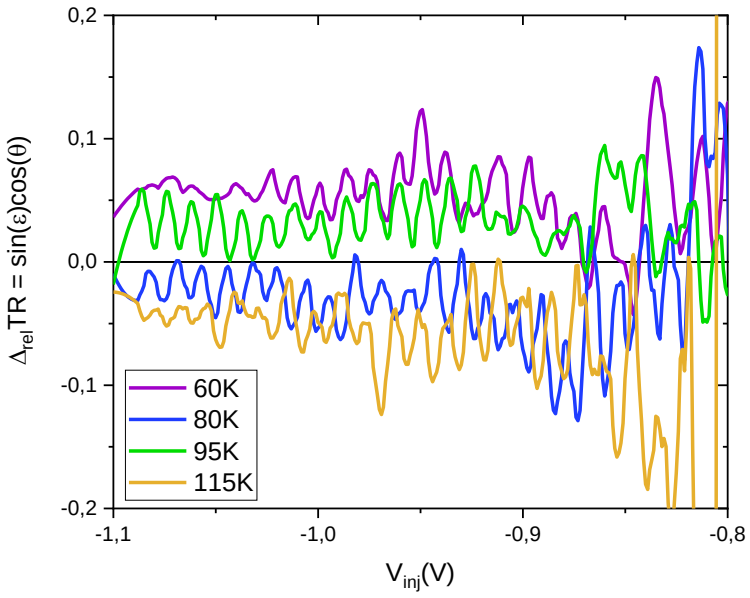

Figure IV.57: Precession signal $\Delta_{rel}TR$ as a function of injection voltage V_{inj} for several temperature.

Values of Δ_{rel}TR lie between -0.1 and 0.1 over the studied energy range. This is comparable to those obtained for CoAl samples. Thus, we can expect mean precession angles and spin length asymmetry obtained for CoCu to be similar to that of CoAl. Additional measurements of TRs were performed at higher injection energy (up to -1.8V) for four different temperatures: 75K, 95K, 115K and 135K. Δ_{rel}TR shows no specific feature for such injection voltage in any temperature studied. Precession signal is slowly decreasing with higher V_{inj} just like for CoAl devices.

The same measurements have been performed from 60K to 150K. Figure IV.58 shows experimental data for V_{inj}=-1V with associated error bars. Periodicity of the precession signal with temperature is found again as Δ_{rel}TR alternates between positive and negative values with increased temperature. Associated period of the signal is around 35K, about half that found for CoAl (65K). The same model as for CoAl was applied here, to explain temperature dependence of $\sin(\varepsilon)\cos(\theta)$ product.

Following the same procedure as in the case of CoAl, roughness at CoCu interfaces could be estimated using images obtained during the TEM investigation. Concerning CoCu alloy, both chemical and structural results had to be used in order to extract a value of R_a (see Eq. IV.1 in section IV.1 – 3). Here, we have R_a = 0.3, about half the value for CoAl. This roughness is reduced for CoCu down to better growth of the system on previously deposited Cu and [Co/Ni] layers which also crystallize into a fcc structure with similar lattice parameters.

Even though CoCu layer is well-crystallized and textured in the [111] direction, lack of information concerning band structure of this material makes it difficult to use expression for the spin precession based on equation III.15 (see section III.2 – 2). Thus, Weber's formula was applied to expressed precession speed ε^* with a temperature dependent exchange energy, as in the case of CoAl. Once again, considering that the molecular field is proportional to the magnetization of CoCu, which is temperature dependent, we obtain ε^* with the same expression as in section IV.1 – 3:

$$\varepsilon^* = \sqrt{\frac{m_e}{2\hbar^2}}\frac{\Delta E_{ex}}{\sqrt{E}} = \varepsilon^*(E, 0K)\left(1 - \frac{T}{T_C}\right) \qquad (IV.5)$$

Here, T_C for $Co_{17.5}Cu_{82.5}$ alloy was evaluated from magnetometry around 135K.

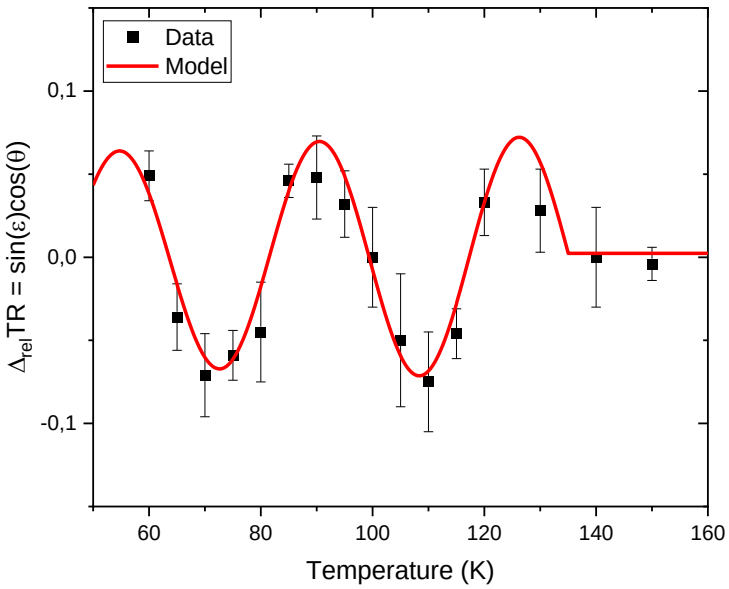

Figure IV.58: Mean sin(ε)cos(θ) vs. temperature for an injection voltage of -1V. Dots with error bars represent experimental data with the red solid line describes associated model for precession. Fits parameters: ε^{*}=274°/nm, λ^{-}=0.78nm and interface dephasing equals to zero.

Model fitting experimental data plotted on figure IV.58 is based on equations IV.3 and equation IV.5. This model still describes well sinusoidal behavior of the experimental data. Contrary to CoAl study, two successive periods can be observed here. Furthermore, two points correspond to temperature exceeding the 135K. The model which predicts extinction of the precession above this temperature also fits these experimental measurements. Two parameters are extracted from fit of figure IV.58: $\varepsilon^{*}(E, 0K)$ and λ^{-}. In the case of figure IV.58, we obtained ε^{*}=274°/nm and λ^{-}=0.78nm.

The same procedure was applied for several injection energies between 0.85eV to 1.1eV. Higher energies were not investigated in order to limit the contribution of secondary electrons. Experimental data and associated models are shown on figure IV.59. Amplitude of $\Delta_{rel}TR$ seems to be slightly decreasing with higher injection voltage. As in the case of CoAl, the period seems not to be affected by injection energy of hot electrons.

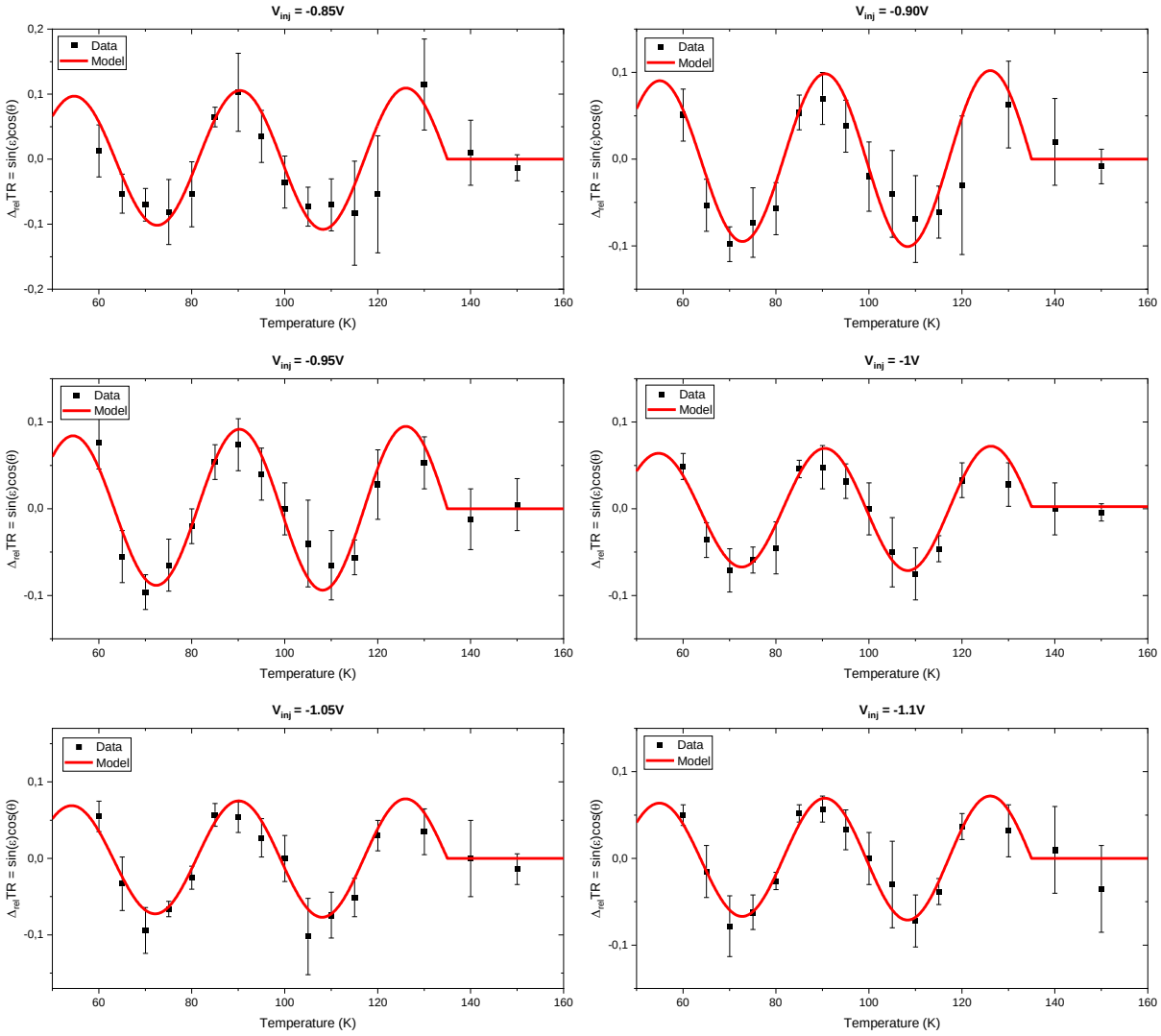

Figure IV.59: Precession signal $\Delta_{rel}TR$ as a function of temperature for each injection voltage measured.

Fitted parameters for each injection energy are reported on figure IV.60 with associated error bars given by standard deviation of $\varepsilon^*(E,0K)$ and λ^-. Values extracted for ε*(E,0K) from measurements plotted on figure IV.59 are given as a function on injection energy on figure IV.60 – left. Fitted precession speed obtained from the fits are mostly constant over this [0.85eV, 1.1eV] window with a value around 273°/nm. This value is similar to that of CoAl samples with 289°/nm. As no phase change is considered at the MgO/CoAl interface, we can use energy dependence in expression of the spin precession of equation IV.2 to extract an exchange energy. This correspond to the model plotted on figure III.81 – left. Fermi level was supposed to be that of Cu (7eV) with little effect of additional Co. Considering an effective electron mass equal to 1, the value for ΔE_{xc} obtained here is around 4.5eV, still much higher than the exchange splitting of Co d-bands.

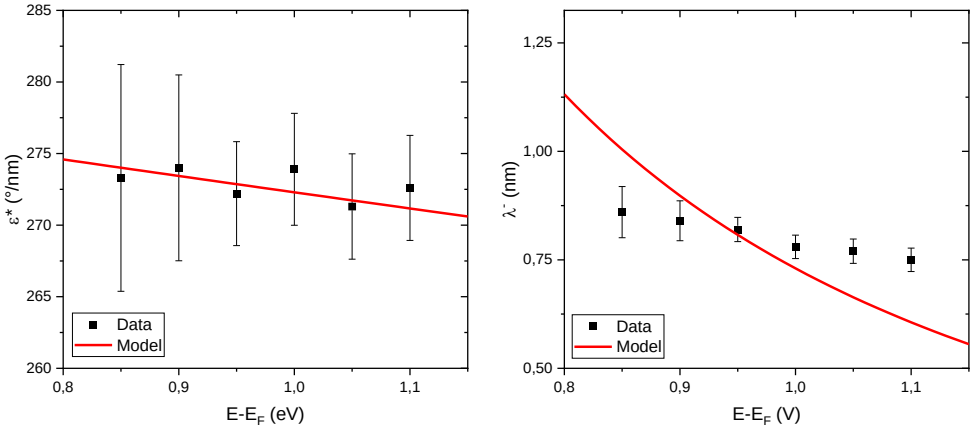

Figure IV.60: Precession speed at 0K (left) and spin asymmetry length (right) as a function of energy. Both parameters were extracted from fits using Eq. IV.2.

Figure IV.60 – right shows spin asymmetry length as a function of injection energy. Data plotted on Figure IV.60 – right correspond to fitted values based on measurements of figure IV.59. λ^- lies around 0.77nm over the whole range of energy considered, slightly lower than what was obtained for CoAl. Extracted values of the spin asymmetry length decrease with increasing injection energy. Model used for fitting the data is the same as what was applied in the case of CoAl. Considering that energy dependence of λ^- results from Coulombian inelastic interactions between hot electrons, we can model its decay with energy. Associated model is shown on figure III.81 – right. At 1eV, minority (resp. majority) inelastic mean free path corresponding to λ^- plotted is about 0.75nm (resp. 20.5nm).

Model shown on figure IV.60 – right does not fit extracted data from experiments. Energy dependence of obtained spin asymmetry length is much weaker than what is predicted by our model. This energy dependence can be affected by band structure of Cu: energy dependence of hot electrons velocity corresponds to that of free-electrons in our model. As there is a well-known gap opening in the [111] direction for Cu, free-electron approximation may not be verified anymore. Therefore strong deviations from this square-root can be expected, inducing a weak energy dependence of the mean free paths.

CoCu alloy was demonstrated to be another candidate for temperature-dependent manipulating electronic spin through precession phenomenon. Solid solution was stabilized for a much wider concentration range than what was observed in the literature. The use of CoCu alloy led to a well crystallized layer without any diffusion precession as in CoAl. Spin precession was measured over a 90K temperature range. A model based on magnetic properties of the sample describes accurately precession variation with temperature. Still, no answer can be given yet to explain the high precession angle per nanometer obtained in this study.

Key takeaways for Chapter IV:

- **CoAl and CoCu are interesting alloys for studying temperature-dependent spin precession as their properties can be adjusted with Co content**
- **Both materials host a variation of the precession signal with temperature according to their magnetic properties, as modeled by Weber *et al.***
- **Oscillations of the precession signals show different period and amplitude comparing both alloys**
- **High $\varepsilon^*(0K)$ found in CoAl can be explained by flat bands hosting hot electrons**
- **No explanation for CoCu high precession angle per nanometer can be proposed yet**

Conclusions & perspectives

During this work, Magnetic Tunnel Transistor (MTT) devices were designed and studied to investigate several aspects of hot electrons transport. Thanks to the MTJ and the Schottky barrier, injection and acceptance cone respectively, enable a strong filtering of scattered electrons. This kind of structure increases the spin diffusion length to tens of nanometers for collected electrons, which allows studies of complex physics. The spin valve inserted in the middle of the MTT gives flexibility to the choice of the active layer. Different spin valve structure can be implemented to stabilize different magnetic configurations.

Hot electrons transport described by the Transfer Ratio (TR) can be explained through expressions for each step in the electrons travel and equations associated with each scattering mechanisms. At low energies, our model reproduces quantitatively experimental results of hot electrons transport in our MTT. At higher energies, the contribution to the collected current of secondary electrons generated from electron-electron interactions is highlighted. Our model shows the necessity of taking the d-band of transition metals into accounts to fully reproduce the shape of our TR. Including additional scattering mechanisms with possible pumping of minority spin electrons does not modify much the conclusion of the study as majority spin electrons are the one contributing the most to the TR. Possible spin-flip processes could come with electron-electron interactions. Yet, they would not produce enough secondary electrons collected at the Schottky barrier to be significant. A planar MTT was designed to specifically investigate the latter questions concerning the role of minority spin electrons. Unfortunately, lack of magneto-current does not allow us to draw conclusion for these measurements.

Pioneering work of Vautrin *et al.* on spin precession in CoFeB was completed with additional deposited devices with CoFeB thickness ranging from 3nm to 4nm. Beyond these new samples, our experimental set-up for spin precession measurement was improved to enable stabilization of the 5 magnetic configurations now accessible. An investigation on the impact of misalignment errors on precession signal showed that it has few effect over a 20° window. New spin precession measurements were accurately described by the model presented by Vautrin *et al.* with identical parameters. These experimental points confirm the oscillatory behavior of precession signal with CoFeB thickness. CoFeB MTT were further used to study energy dependence of the spin precession signal for higher energies. While the model qualitatively agrees with the energy-dependence of the precession angle for a given thickness, we were not able to observe the expected behavior due to the access of minority band of CoFeB around 1.95eV.

While study on CoFeB sample confirmed spin precession phenomenon in ferromagnets, values for precession angle per nanometer was too high to control the electronic spin. In order to reduce this precession angle per nanometer and make it depend on temperature, Co-based alloys were considered as promising candidates. The first one is CoAl alloy. This material was already studied by C. Vautrin but limitations of the measurement set-up prevented him for reaching conclusions concerning the spin precession phenomenon. Here, full characterization of this material both in thin film and in patterned MTT was performed. Chemical analysis performed with a TEM in STEM mode brought answers concerning Al diffusion mechanism towards MgO barrier which explains the temperature-dependence of the TMR. The spin precession was measured for several temperatures ranging from 50K to 110K. The model

developed for CoFeB MTT was applied along with Weber's formula of the precession in the case of polycrystalline samples to fit experimental results. The two extracted parameters follow the predicted energy-dependence. Value of the precession angle per nanometer at 0K is unexpectedly high compared to the lowered magnetization of the sample. A possible explanation can lie in flat bands where hot electrons are injected, which leads to enhanced effective mass for charge carriers.

The second material considered was CoCu alloy. First, a characterization of its growth and structure was required to make sure that the sample was homogenous. Size, interface and annealing effects on CoCu properties was checked. The crystalline quality of this layer was confirmed by TEM imaging. Unexpected low TMR was observed even at low temperature. Yet, the hysteresis cycle was sufficient to stabilize magnetic configurations in order to perform spin precession measurements. Experimental results are ranging over a 90K window. Magnetic properties of CoCu was applied to the spin precession model to fit the data. The period of oscillation of the precession signal with temperature differs from that of CoAl. Moreover precession signal becomes null passed 140K, which corresponds the a paramagnetic-ferromagnetic transition of CoCu. Extracted parameters from these fits are similar to that found in the case of CoAl. The spin asymmetry of the inelastic mean-free path follows a different energy-dependence compared to what is predicted by simple transport equation. Furthermore, the high value for precession angle per nanometer at 0K cannot be explained with the argument as in CoAl. So far, no explanation was brought to explain this result. Therefore, additional theoretical work is required to fully understand our experimental results.

This study has proposed deep insight of hot electron spin-dependent transport in metallic and ferromagnetic layers. While a huge amount of theoretical works are summarized into our model to give a simple but accurate description of electrons transport, the model can still be pushed further to bring answers concerning spin-dependence of the electron-electron interaction. Our all solid state device allowed us to investigate processes related to fundamental physics which would require huge instruments otherwise. The versatility of our lab-on-chip enables tens of measurements using different configuration and/or parameters while accessing desired physical effects by growing a new sample. Our work concerning electron-electron scattering paves the way for further studies on this topic. Achieving a planar MTT with required magnetic configurations can give details on scattering mechanisms. This could have a huge impact on electron-mediated processes. In particular, the role of electron-electron interaction in ultrafast demagnetization process could be better understood. Thus, new perspectives for controlling electronic spins through secondary electrons with a specific energy and/or spin orientation could be considered.

Combining spin precession related to CoFeB band structure in the first study and that of temperature-dependent CoAl and CoCu alloys, it is possible to imagine an MTT based on a ferromagnetic material whose band structure would be tailored for spin precession. By playing with bands of the material to get a low enough precession speed while shifting the Fermi level in order to access a sharp variation of the precession phenomenon (such that at 1.95eV for CoFeB), it would be possible to build a simple device where spin-polarization of hot electrons would be controlled over few degrees by changing the injection energy of electrons.

References

1. Vautrin, C. *et al.* Low-Energy Spin Precession in the Molecular Field of a Magnetic Thin Film. *Ann. Phys.* **533**, 2000470 (2021).

2. Ryzhii, V. & Khrenov, G. High-frequency operation of lateral hot-electron transistors. *IEEE Trans. Electron Devices* **42**, 166–171 (1995).

3. Zeng, C. *et al.* Vertical Graphene-Base Hot-Electron Transistor. *Nano Lett.* **13**, 2370–2375 (2013).

4. Liang, B.-W. *et al.* High-Frequency Graphene Base Hot-Electron Transistor. *ACS Nano* **15**, 6756–6764 (2021).

5. Clavero, C. Plasmon-induced hot-electron generation at nanoparticle/metal-oxide interfaces for photovoltaic and photocatalytic devices. *Nat. Photonics* **8**, 95–103 (2014).

6. Li, W. & Valentine, J. Metamaterial Perfect Absorber Based Hot Electron Photodetection. *Nano Lett.* **14**, 3510–3514 (2014).

7. Li, W. & Valentine, J. G. Harvesting the loss: surface plasmon-based hot electron photodetection. *Nanophotonics* **6**, 177–191 (2017).

8. Kawahara, T., Ito, K., Takemura, R. & Ohno, H. Spin-transfer torque RAM technology: Review and prospect. *Microelectron. Reliab.* **52**, 613–627 (2012).

9. Single-Shot Multi-Level All-Optical Magnetization Switching Mediated by Spin Transport - Iihama - 2018 - Advanced Materials - Wiley Online Library. https://onlinelibrary.wiley.com/doi/abs/10.1002/adma.201804004.

10. Dieny, B. Giant magnetoresistance in spin-valve multilayers. *J. Magn. Magn. Mater.* **136**, 335–359 (1994).

11. Ikeda, S. *et al.* A perpendicular-anisotropy CoFeB–MgO magnetic tunnel junction. *Nat. Mater.* **9**, 721–724 (2010).

12. Ralph, D. C. & Stiles, M. D. Spin transfer torques. *J. Magn. Magn. Mater.* **320**, 1190–1216 (2008).

13. Giaever, I. Electron Tunneling Between Two Superconductors. *Phys. Rev. Lett.* **5**, 464–466 (1960).

14. Meservey, R., Tedrow, P. M. & Fulde, P. Magnetic Field Splitting of the Quasiparticle States in Superconducting Aluminum Films. *Phys. Rev. Lett.* **25**, 1270–1272 (1970).

15. Tedrow, P. M. & Meservey, R. Spin Polarization of Electrons Tunneling from Films of Fe, Co, Ni, and Gd. *Phys. Rev. B* **7**, 318–326 (1973).

16. Julliere, M. Tunneling between ferromagnetic films. *Phys. Lett. A* **54**, 225–226 (1975).

17. Meservey, R., Paraskevopoulos, D. & Tedrow, P. M. Correlation between Spin Polarization of Tunnel Currents from 3 d Ferromagnets and Their Magnetic Moments. *Phys. Rev. Lett.* **37**, 858–860 (1976).

18. Beth Stearns, M. Simple explanation of tunneling spin-polarization of Fe, Co, Ni and its alloys. *J. Magn. Magn. Mater.* **5**, 167–171 (1977).

19. Monsma, D. J. & Parkin, S. S. P. Spin polarization of tunneling current from ferromagnet/Al2O3 interfaces using copper-doped aluminum superconducting films. *Appl. Phys. Lett.* **77**, 720–722 (2000).

20. Slonczewski, J. C. Conductance and exchange coupling of two ferromagnets separated by a tunneling barrier. *Phys. Rev. B* **39**, 6995–7002 (1989).

21. Simmons, J. G. Generalized Formula for the Electric Tunnel Effect between Similar Electrodes Separated by a Thin Insulating Film. *J. Appl. Phys.* **34**, 1793–1803 (2004).

22. Brinkman, W. F., Dynes, R. C. & Rowell, J. M. Tunneling Conductance of Asymmetrical Barriers. *J. Appl. Phys.* **41**, 1915–1921 (2003).

23. Moodera, J. S., Kinder, L. R., Wong, T. M. & Meservey, R. Large Magnetoresistance at Room Temperature in Ferromagnetic Thin Film Tunnel Junctions. *Phys. Rev. Lett.* **74**, 3273–3276 (1995).

24. Zhang, S., Levy, P. M., Marley, A. C. & Parkin, S. S. P. Quenching of Magnetoresistance by Hot Electrons in Magnetic Tunnel Junctions. *Phys. Rev. Lett.* **79**, 3744–3747 (1997).

25. Nowak, E. R., Spradling, P., Weissman, M. B. & Parkin, S. S. P. Electron tunneling and noise studies in ferromagnetic junctions. *Thin Solid Films* **377–378**, 699–704 (2000).

26. Rottländer, P., Hehn, M., Lenoble, O. & Schuhl, A. Tantalum oxide as an alternative low height tunnel barrier in magnetic junctions. *Appl. Phys. Lett.* **78**, 3274–3276 (2001).

27. Zhang, S. Spin-Dependent Surface Screening in Ferromagnets and Magnetic Tunnel Junctions. *Phys. Rev. Lett.* **83**, 640–643 (1999).

28. Stratton, R. Volt-current characteristics for tunneling through insulating films. *J. Phys. Chem. Solids* **23**, 1177–1190 (1962).

29. Shang, C. H., Nowak, J., Jansen, R. & Moodera, J. S. Temperature dependence of magnetoresistance and surface magnetization in ferromagnetic tunnel junctions. *Phys. Rev. B* **58**, R2917–R2920 (1998).

30. MacDonald, A. H., Jungwirth, T. & Kasner, M. Temperature Dependence of Itinerant Electron Junction Magnetoresistance. *Phys. Rev. Lett.* **81**, 705–708 (1998).

31. Åkerman, J. J. *et al.* Criteria for ferromagnetic–insulator–ferromagnetic tunneling. *J. Magn. Magn. Mater.* **240**, 86–91 (2002).

32. Utsumi, Y., Shimizu, Y. & Miyazaki, H. Barrier Height and Film Thickness Dependence of the TMR. *J. Phys. Soc. Jpn.* **68**, 3444–3455 (1999).

33. MacLaren, J. M., Zhang, X.-G. & Butler, W. H. Validity of the Julliere model of spin-dependent tunneling. *Phys. Rev. B* **56**, 11827–11832 (1997).

34. Tedrow, P. M. & Meservey, R. Critical thickness for ferromagnetism and the range of spin-polarized electrons tunneling into Co. *Solid State Commun.* **16**, 71–74 (1975).

35. Moodera, J. S., Taylor, M. E. & Meservey, R. Exchange-induced spin polarization of conduction electrons in paramagnetic metals. *Phys. Rev. B* **40**, 11980–11982 (1989).

36. Moodera, J. S., Gallagher, E. F., Robinson, K. & Nowak, J. Optimum tunnel barrier in ferromagnetic–insulator–ferromagnetic tunneling structures. *Appl. Phys. Lett.* **70**, 3050 (1997).

37. LeClair, P., Kohlhepp, J. T., Swagten, H. J. M. & de Jonge, W. J. M. Interfacial Density of States in Magnetic Tunnel Junctions. *Phys. Rev. Lett.* **86**, 1066–1069 (2001).

38. Binning, G., Rohrer, H., Gerber, Ch. & Weibel, E. Surface Studies by Scanning Tunneling Microscopy. in *Scanning Tunneling Microscopy* (ed. Neddermeyer, H.) 31–35 (Springer Netherlands, 1993). doi:10.1007/978-94-011-1812-5_1.

39. Stroscio, J. A., Pierce, D. T., Davies, A., Celotta, R. J. & Weinert, M. Tunneling Spectroscopy of bcc (001) Surface States. *Phys. Rev. Lett.* **75**, 2960–2963 (1995).

40. Biedermann, A. *et al.* Scanning Tunneling Spectroscopy of One-Dimensional Surface States on a Metal Surface. *Phys. Rev. Lett.* **76**, 4179–4182 (1996).

41. Temple, R. C., McLaren, M., Brydson, R. M. D., Hickey, B. J. & Marrows, C. H. Long spin lifetime and large barrier polarisation in single electron transport through a CoFe nanoparticle. *Sci. Rep.* **6**, 28296 (2016).

42. Sajoto, T. *et al.* Direct Observation of Quasi-Bound States and Band-Structure Effects in a Double Barrier Resonant Tunneling Structure Using Ballistic Electron Emission Microscopy. *Phys. Rev. Lett.* **74**, 3427–3430 (1995).

43. Wunnicke, O. *et al.* Effects of resonant interface states on tunneling magnetoresistance. *Phys. Rev. B* **65**, 064425 (2002).

44. De Teresa, J. M. *et al.* Inverse Tunnel Magnetoresistance in $\mathrm{Co}/{\mathrm{SrTiO}}_{3}/{\mathrm{La}}_{0.7}{\mathrm{Sr}}_{0.3}{\mathrm{MnO}}_{3}$: New Ideas on Spin-Polarized Tunneling. *Phys. Rev. Lett.* **82**, 4288–4291 (1999).

45. Oleinik, I. I., Tsymbal, E. Yu. & Pettifor, D. G. Structural and electronic properties of $\mathrm{Co}/{\mathrm{Al}}_{2}{\mathrm{O}}_{3}/\mathrm{Co}$ magnetic tunnel junction from first principles. *Phys. Rev. B* **62**, 3952–3959 (2000).

46. Butler, W. H., Zhang, X.-G., Schulthess, T. C. & MacLaren, J. M. Spin-dependent tunneling conductance of Fe | MgO | Fe sandwiches. *Phys. Rev. B* **63**, 054416 (2001).

47. Mathon, J. & Umerski, A. Theory of tunneling magnetoresistance of an epitaxial Fe/MgO/Fe(001) junction. *Phys. Rev. B* **63**, 220403 (2001).

48. Callaway, J. & Wang, C. S. Energy bands in ferromagnetic iron. *Phys. Rev. B* **16**, 2095–2105 (1977).

49. Zhang, J., Levy, P. M., Zhang, S. & Antropov, V. Identification of Transverse Spin Currents in Noncollinear Magnetic Structures. *Phys. Rev. Lett.* **93**, 256602 (2004).

50. Stiles, M. D. & Zangwill, A. Anatomy of spin-transfer torque. *Phys. Rev. B* **66**, 014407 (2002).

51. Petitjean, C., Luc, D. & Waintal, X. Unified Drift-Diffusion Theory for Transverse Spin Currents in Spin Valves, Domain Walls, and Other Textured Magnets. *Phys. Rev. Lett.* **109**, 117204 (2012).

52. Ghosh, A., Auffret, S., Ebels, U. & Bailey, W. E. Penetration Depth of Transverse Spin Current in Ultrathin Ferromagnets. *Phys. Rev. Lett.* **109**, 127202 (2012).

53. Manchon, A., Ryzhanova, N., Vedyayev, A., Chschiev, M. & Dieny, B. Description of current-driven torques in magnetic tunnel junctions. *J. Phys. Condens. Matter* **20**, 145208 (2008).

54. Chshiev, M. *et al.* Analytical description of ballistic spin currents and torques in magnetic tunnel junctions. *Phys. Rev. B* **92**, 104422 (2015).

55. Spicer, W. E., Lindau, I., Skeath, P. & Su, C. Y. Unified defect model and beyond. *J. Vac. Sci. Technol.* **17**, 1019–1027 (1980).

56. Rhoderick, E. H. *Metal-Semiconductor Contacts*. (Oxford University Press, 1980).

57. Prietsch, M. & Ludeke, R. BEEM spectroscopy at interfaces of Au, Ag, Cu, Mg and Ni films with n-GaP(110). *Surf. Sci.* **251–252**, 413–417 (1991).

58. Ludeke, R., Prietsch, M. & Samsavar, A. Ballistic electron emission spectroscopy of metals on GaP(110). *J. Vac. Sci. Technol. B Microelectron. Nanometer Struct. Process. Meas. Phenom.* **9**, 2342–2348 (1991).

59. Prietsch, M. Ballistic-electron emission microscopy (BEEM): studies of metal/semiconductor interfaces with nanometer resolution. *Phys. Rep.* **253**, 163–233 (1995).

60. Jansen, R., Banerjee, T., Park, B. G. & Lodder, J. C. Probing momentum distributions in magnetic tunnel junctions via hot-electron decay. *Appl. Phys. Lett.* **90**, 192503 (2007).

61. Bell, L. D. & Kaiser, W. J. Observation of Interface Band Structure by Ballistic-Electron-Emission Microscopy. *Phys. Rev. Lett.* **61**, 2368–2371 (1988).

62. Kaiser, W. J. & Bell, L. D. Direct investigation of subsurface interface electronic structure by ballistic-electron-emission microscopy. *Phys. Rev. Lett.* **60**, 1406–1409 (1988).

63. Hecht, M. H., Bell, L. D., Kaiser, W. J. & Grunthaner, F. J. Ballistic-electron-emission microscopy investigation of Schottky barrier interface formation. *Appl. Phys. Lett.* **55**, 780–782 (1989).

64. Lee, E. Y., Turnew, B. R., Jimenez, J. R. & Schowalter, L. J. Imaging of Metal/Semiconductor Interface by Ballistic-Electron-Emission Microscopy (Beem). *MRS Online Proc. Libr. OPL* **295**, 231 (1992).

65. Schowalter, L. J. & Lee, E. Y. Role of elastic scattering in ballistic-electron-emission microscopy of Au/Si(001) and Au/Si(111) interfaces. *Phys. Rev. B* **43**, 9308–9311 (1991).

66. Bobisch, C. A. *et al.* Conservation of the Lateral Electron Momentum at a Metal-Semiconductor Interface Studied by Ballistic Electron Emission Microscopy. *Phys. Rev. Lett.* **102**, 136807 (2009).

67. Garcia-Vidal, F. J., de Andres, P. L. & Flores, F. Elastic Scattering and the Lateral Resolution of Ballistic Electron Emission Microscopy: Focusing Effects on the Au/Si Interface. *Phys. Rev. Lett.* **76**, 807–810 (1996).

68. Reuter, K. *et al.* Quantum-mechanical analysis of the elastic propagation of electrons in the Au/Si system: Application to ballistic-electron-emission microscopy. *Phys. Rev. B* **58**, 14036–14046 (1998).

69. Reuter, K., de Andres, P. L., Garcia-Vidal, F. J., Flores, F. & Heinz, K. Surface and bulk band-structure effects on ${\mathrm{CoSi}}_{2}/\mathrm{Si}(111)$ ballistic-electron emission experiments. *Phys. Rev. B* **63**, 205325 (2001).

70. de Andres, P. L., Garcia-Vidal, F. J., Reuter, K. & Flores, F. Theory of ballistic electron emission microscopy. *Prog. Surf. Sci.* **66**, 3–51 (2001).

71. Zarate, E., Apell, P. & Echenique, P. M. Calculation of low-energy-electron lifetimes. *Phys. Rev. B* **60**, 2326–2332 (1999).

72. Bauer, M., Marienfeld, A. & Aeschlimann, M. Hot electron lifetimes in metals probed by time-resolved two-photon photoemission. *Prog. Surf. Sci.* **90**, 319–376 (2015).

73. Campillo, I., Pitarke, J. M., Rubio, A., Zarate, E. & Echenique, P. M. Inelastic Lifetimes of Hot Electrons in Real Metals. *Phys. Rev. Lett.* **83**, 2230–2233 (1999).

74. Heindl, E., Kefes, C., Soda, M., Vancea, J. & Back, C. H. Hot electron spin attenuation lengths of bcc Fe34Co66—Room temperature Magnetocurrent of 1200%. *J. Magn. Magn. Mater.* **321**, 3693–3697 (2009).

75. Plihal, M., Mills, D. L. & Kirschner, J. Spin Wave Signature in the Spin Polarized Electron Energy Loss Spectrum of Ultrathin Fe Films: Theory and Experiment. *Phys. Rev. Lett.* **82**, 2579–2582 (1999).

76. Simon, F. *et al.* Generalized Elliott-Yafet Theory of Electron Spin Relaxation in Metals: Origin of the Anomalous Electron Spin Lifetime in ${\mathrm{MgB}}_{2}$. *Phys. Rev. Lett.* **101**, 177003 (2008).

77. Hong, J. & Mills, D. L. Theory of the spin dependence of the inelastic mean free path of electrons in ferromagnetic metals: A model study. *Phys. Rev. B* **59**, 13840–13848 (1999).

78. Electron and Spin Transport. in *Magnetism: From Fundamentals to Nanoscale Dynamics* (eds. Stöhr, J. & Siegmann, H. C.) 637–678 (Springer, 2006). doi:10.1007/978-3-540-30283-4_14.

79. Vlutters, R. *et al.* Modeling of spin-dependent hot-electron transport in the spin-valve transistor. *Phys. Rev. B* **65**, 024416 (2001).

80. Lu, Y. *et al.* Interfacial trapping for hot electron injection in silicon. *Appl. Phys. Lett.* **103**, 022407 (2013).

81. Lu, Y. *et al.* Interfacial trapping for hot electron injection in silicon. *Appl. Phys. Lett.* **103**, 022407 (2013).

82. van Dijken, S., Jiang, X. & Parkin, S. S. P. Comparison of magnetocurrent and transfer ratio in magnetic tunnel transistors with spin-valve bases containing Cu and Au spacer layers. *Appl. Phys. Lett.* **82**, 775–777 (2003).

83. Vautrin, C. *et al.* Thickness and angular dependence of the magnetocurrent of hot electrons in a magnetic tunnel transistor with crossed anisotropies. *Phys. Rev. B* **96**, 174426 (2017).

84. van Dijken, S., Jiang, X. & Parkin, S. S. P. Spin-dependent hot electron transport in ${\mathrm{Ni}}_{81}{\mathrm{Fe}}_{19}$ and ${\mathrm{Co}}_{84}{\mathrm{Fe}}_{16}$ films on GaAs(001). *Phys. Rev. B* **66**, 094417 (2002).

85. Hirose, T. *et al.* Dependence of Hot Electron Transport on Base Layer Thickness of Magnetic Tunnel Transistor. *Jpn. J. Appl. Phys.* **43**, 2479 (2004).

86. Park, B. G. Probing Spin-Polarized Tunneling at High Bias with a Magnetic Tunnel Transistor. D43.005 (2005).

87. Park, B. G., Banerjee, T., Lodder, J. C. & Jansen, R. Opposite Spin Asymmetry of Elastic and Inelastic Scattering of Nonequilibrium Holes Injected into a Ferromagnet. *Phys. Rev. Lett.* **97**, 137205 (2006).

88. Nagahama, T., Saito, H. & Yuasa, S. Hot electron transport in magnetic tunnel transistors with an epitaxial MgO tunnel barrier. *Appl. Phys. Lett.* **96**, 112509 (2010).

89. Li, J. & Appelbaum, I. Inelastic spin depolarization spectroscopy in silicon. *J. Appl. Phys.* **114**, 033705 (2013).

90. Vautrin, C. *et al.* Magnetic tunnel transistor with a perpendicular Co/Ni multilayer sputtered on a Si/Cu(1\hspace0.167em0\hspace0.167em0) Schottky diode. *J. Phys. Appl. Phys.* **49**, 355003 (2016).

91. Schleicher, F. *et al.* Localized states in advanced dielectrics from the vantage of spin- and symmetry-polarized tunnelling across MgO. *Nat. Commun.* **5**, 4547 (2014).

92. Bauer, A., Cuberes, M. T., Prietsch, M. & Kaindl, G. Quantitative study of electron transport in ballistic-electron-emission microscopy. *Phys. Rev. Lett.* **71**, 149–152 (1993).

93. Cuberes, M. T., Bauer, A., Wen, H. J., Prietsch, M. & Kaindl, G. Ballistic-electron emission microscopy study of the Au/Si(111)7×7 and Au/CaF2/Si(111)7×7 interfaces. *Appl. Phys. Lett.* **64**, 2300–2302 (1994).

94. van Dijken, S., Jiang, X. & Parkin, S. S. P. Giant magnetocurrent exceeding 3400% in magnetic tunnel transistors with spin-valve base layers. *Appl. Phys. Lett.* **83**, 951–953 (2003).

95. Baroody, E. M. A Theory of Secondary Electron Emission from Metals. *Phys. Rev.* **78**, 780–787 (1950).

96. Dekker, A. J. & van der Ziel, A. Theory of the Production of Secondary Electrons in Solids. *Phys. Rev.* **86**, 755–760 (1952).

97. Wolff, P. A. Theory of Secondary Electron Cascade in Metals. *Phys. Rev.* **95**, 56–66 (1954).

98. Quinn, J. J. Range of Excited Electrons in Metals. *Phys. Rev.* **126**, 1453–1457 (1962).

99. Crowell, C. R., Spitzer, W. G., Howarth, L. E. & LaBate, E. E. Attenuation Length Measurements of Hot Electrons in Metal Films. *Phys. Rev.* **127**, 2006–2015 (1962).

100. Stuart, R. N., Wooten, F. & Spicer, W. E. Mean Free Path of Hot Electrons and Holes in Metals. *Phys. Rev. Lett.* **10**, 7–9 (1963).

101. Sze, S. M., Moll, J. L. & Sugano, T. Range-energy relation of hot electrons in gold. *Solid-State Electron.* **7**, 509–523 (1964).

102. Ogawa, S., Nagano, H. & Petek, H. Hot-electron dynamics at Cu(100), Cu(110), and Cu(111) surfaces:mComparison of experiment with Fermi-liquid theory. *Phys. Rev. B* **55**, 10869–10877 (1997).

103. Cao, J., Gao, Y., Miller, R. J. D., Elsayed-Ali, H. E. & Mantell, D. A. Femtosecond photoemission study of ultrafast electron dynamics on Cu(100). *Phys. Rev. B* **56**, 1099–1102 (1997).

104. Knoesel, E., Hotzel, A. & Wolf, M. Ultrafast dynamics of hot electrons and holes in copper: Excitation, energy relaxation, and transport effects. *Phys. Rev. B* **57**, 12812–12824 (1998).

105. Penn, D. R. Mean free paths of very-low-energy electrons: The effects of exchange and correlation. *Phys. Rev. B* **22**, 2677–2682 (1980).

106. Aeschlimann, M. *et al.* Ultrafast Spin-Dependent Electron Dynamics in fcc Co. *Phys. Rev. Lett.* **79**, 5158–5161 (1997).

107. Segall, B. Fermi Surface and Energy Bands of Copper. *Phys. Rev.* **125**, 109–122 (1962).

108. Adler, S. L. Theory of the Range of Hot Electrons in Real Metals. *Phys. Rev.* **130**, 1654–1666 (1963).

109. Campillo, I., Pitarke, J. M., Rubio, A. & Echenique, P. M. Role of occupied d states in the relaxation of hot electrons in Au. *Phys. Rev. B* **62**, 1500–1503 (2000).

110. Reuter, K., Andres, P. L. de, Garcia-Vidal, F. J., Flores, F. & Kocevar, P. Hot electron transport in Ballistic Electron Emission Spectroscopy: Band structure effects and k∥-space currents. *Europhys. Lett.* **45**, 181 (1999).

111. de Pablos, P. F. *et al.* Ballistic Electron Emission Spectroscopy Used as a Tool for Determining Accurate Hot-Electron Lifetimes in Metals. *AIP Conf. Proc.* **696**, 829–836 (2003).

112. Appelbaum, I. & Narayanamurti, V. Monte Carlo calculations for metal-semiconductor hot-electron injection via tunnel-junction emission. *Phys. Rev. B* **71**, 045320 (2005).

113. Mead, C. A. Operation of Tunnel-Emission Devices. *J. Appl. Phys.* **32**, 646–652 (1961).

114. Levi, A. F. J., Hayes, J. R., Platzman, P. M. & Wiegmann, W. Injected-Hot-Electron Transport in GaAs. *Phys. Rev. Lett.* **55**, 2071–2073 (1985).

115. Ludeke, R. & Bauer, A. Hot electron transport across metal-semiconductor interfaces probed by ballistic electron emission spectroscopy. *Phys. Scr.* **1994**, 90 (1994).

116. Schmuttenmaer, C. A. *et al.* Time-resolved two-photon photoemission from Cu(100): Energy dependence of electron relaxation. *Phys. Rev. B* **50**, 8957–8960 (1994).

117. Zhukov, V. P., Aryasetiawan, F., Chulkov, E. V., Gurtubay, I. G. de & Echenique, P. M. Corrected local-density approximation band structures, linear-response dielectric functions, and quasiparticle lifetimes in noble metals. *Phys. Rev. B* **64**, 195122 (2001).

118. Nguyen-Truong, H. T. Electron inelastic mean free path at energies below 100 eV. *J. Phys. Condens. Matter* **29**, 215501 (2017).

119. Hertel, T., Knoesel, E., Wolf, M. & Ertl, G. Ultrafast Electron Dynamics at Cu(111): Response of an Electron Gas to Optical Excitation. *Phys. Rev. Lett.* **76**, 535–538 (1996).

120. Zhukov, V. P., Chulkov, E. V. & Echenique, P. M. Lifetimes and inelastic mean free path of low-energy excited electrons in Fe, Ni, Pt, and Au: Ab initio $\mathrm{GW}+\mathrm{T}$ calculations. *Phys. Rev. B* **73**, 125105 (2006).

121. Nguyen-Truong, H. T. Low-energy electron inelastic mean free path in materials. *Appl. Phys. Lett.* **108**, 172901 (2016).

122. Balsano, R., Matsubayashi, A. & LaBella, V. P. Schottky barrier height measurements of Cu/Si(001), Ag/Si(001), and Au/Si(001) interfaces utilizing ballistic electron emission microscopy and ballistic hole emission microscopy. *AIP Adv.* **3**, 112110 (2013).

123. Aboelfotoh, M. O. Temperature dependence of the Schottky-barrier height of tungsten on n-type and p-type silicon. *Solid-State Electron.* **34**, 51–55 (1991).

124. DiTusa, J. F., Lin, K., Park, M., Isaacson, M. S. & Parpia, J. M. Role of phonon dimensionality on electron-phonon scattering rates. *Phys. Rev. Lett.* **68**, 1156–1159 (1992).

125. Echternach, P. M., Gershenson, M. E. & Bozler, H. M. Evidence of interference between electron-phonon and electron-impurity scattering on the conductivity of thin metal films. *Phys. Rev. B* **47**, 13659–13663 (1993).

126. Mathon, J., Wohlfarth, E. P. & Jones, H. The temperature dependence of the spin wave energy in the itinerant electron model of ferromagnetism. *Proc. R. Soc. Lond. Ser. Math. Phys. Sci.* **302**, 409–418 (1997).

127. Zener, C. & Heikes, R. R. Exchange Interactions. *Rev. Mod. Phys.* **25**, 191–198 (1953).

128. Ritchie, R. H. & Ashley, J. C. The interaction of hot electrons with a free electron gas. *J. Phys. Chem. Solids* **26**, 1689–1694 (1965).

129. Zhukov, V. P., Chulkov, E. V. & Echenique, P. M. Lifetimes of Excited Electrons In Fe And Ni: First-Principles GW and the T-Matrix Theory. *Phys. Rev. Lett.* **93**, 096401 (2004).

130. Berglund, C. N. & Spicer, W. E. Photoemission Studies of Copper and Silver: Theory. *Phys. Rev.* **136**, A1030–A1044 (1964).

131. Kisker, E., Gudat, W. & Schröder, K. Observation of a high spin polarization of secondary electrons from single crystal Fe and Co. *Solid State Commun.* **44**, 591–595 (1982).

132. Baibich, M. N. *et al.* Giant Magnetoresistance of (001)Fe/(001)Cr Magnetic Superlattices. *Phys. Rev. Lett.* **61**, 2472–2475 (1988).

133. Binasch, G., Grünberg, P., Saurenbach, F. & Zinn, W. Enhanced magnetoresistance in layered magnetic structures with antiferromagnetic interlayer exchange. *Phys. Rev. B* **39**, 4828–4830 (1989).

134. Datta, S. & Das, B. Electronic analog of the electro-optic modulator. *Appl. Phys. Lett.* **56**, 665–667 (1990).

135. Jedema, F. *Electrical spin injection in metallic mesoscopic spin valves*. (s.n., 2002).

136. Appelbaum, I., Huang, B. & Monsma, D. J. Electronic measurement and control of spin transport in silicon. *Nature* **447**, 295–298 (2007).

137. Weber, W., Riesen, S. & Siegmann, H. C. Magnetization Precession by Hot Spin Injection. *Science* **291**, 1015–1018 (2001).

138. Joly, L., Ha, J. K., Alouani, M., Kortus, J. & Weber, W. Electron Spin Precession upon Reflecting from Ferromagnetic Surfaces. *Phys. Rev. Lett.* **96**, 137206 (2006).

139. Parkin, S. S. P. *et al.* Giant tunnelling magnetoresistance at room temperature with MgO (100) tunnel barriers. *Nat. Mater.* **3**, 862–867 (2004).

140. Jaffrès, H. *et al.* Angular dependence of the tunnel magnetoresistance in transition-metal-based junctions. *Phys. Rev. B* **64**, 064427 (2001).

141. Nechaev, I. A. & Chulkov, E. V. Quasiparticle dynamics in ferromagnetic compounds of the Co–Fe and Ni–Fe systems. *Eur. Phys. J. B* **77**, 31–40 (2010).

142. Sellmyer, D. J. & Kaplow, R. Local-moment model of ferromagnetism in metallic compounds. *Phys. Lett. A* **36**, 349–350 (1971).

143. Butler, S. R., Hanlon, J. E. & Wasilewski, R. J. Electric and magnetic properties of B2 structure compounds: NiAl, CoAl. *J. Phys. Chem. Solids* **30**, 1929–1934 (1969).

144. Coles, B. R. Spin-disorder effects in the electrical resistivities of metals and alloys. *Adv. Phys.* **7**, 40–71 (1958).

145. Barzola-Quiquia, J., Osmic, E. & Häussler, P. The magnetic properties of amorphous Al Fe100− alloys investigated by the atomic structure, magnetoresistance and anomalous Hall effect. *J. Magn. Magn. Mater.* **526**, 167624 (2021).

146. Nguyen-Manh, D. & Pettifor, D. G. Electronic structure, phase stability and elastic moduli of AB transition metal aluminides. *Intermetallics* **7**, 1095–1106 (1999).

147. Zou, J. & Fu, C. L. Structural, electronic, and magnetic properties of 3d transition-metal aluminides with equiatomic composition. *Phys. Rev. B* **51**, 2115–2121 (1995).

148. Sundararajan, V., Sahu, B. R., Kanhere, D. G., Panat, P. V. & Das, G. P. Cohesive, electronic and magnetic properties of the transition metal aluminides FeAl CoAl and NiAl. *J. Phys. Condens. Matter* **7**, 6019–6034 (1995).

149. Lide, D. R. *CRC Handbook of Chemistry and Physics, 85th Edition*. (CRC Press, 2004).

150. Gayen, A., Prasad, G. K., Mallik, S., Bedanta, S. & Perumal, A. Effects of composition, thickness and temperature on the magnetic properties of amorphous CoFeB thin films. *J. Alloys Compd.* **694**, 823–832 (2017).

151. Weber, W., Oberli, D., Riesen, S. & Siegmann, H. C. The electron analogue to the Faraday rotation. *New J. Phys.* **1**, 9 (1999).

152. Kreutz, T. J., Greber, T., Aebi, P. & Osterwalder, J. Temperature-dependent electronic structure of nickel metal. *Phys. Rev. B* **58**, 1300–1317 (1998).

153. Batallan, F., Rosenman, I. & Sommers, C. B. Band structure and Fermi surface of hcp ferromagnetic cobalt. *Phys. Rev. B* **11**, 545–557 (1975).

154. Moruzzi, V. L., Janak, J. F. & Williams, A. R. *Calculated Electronic Properties of Metals*. (Elsevier, 2013).

155. Bernardi, J., Hütten, A. & Thomas, G. GMR behavior of nanostructured heterogeneous M-Co (M=Cu, Ag, Au) alloys. *Nanostructured Mater.* **7**, 205–220 (1996).

156. Mebed, A. M. & Howe, J. M. Spinodal induced homogeneous nanostructures in magnetoresistive CoCu granular thin films. *J. Appl. Phys.* **100**, 074310 (2006).

157. Errahmani, H., Berrada, A., Schmerber, G. & Dinia, A. Comparative study between the effect of annealing and substrate temperature on the magnetic and transport properties of Co20Cu80 granular alloys. *Mater. Lett.* **51**, 48–55 (2001).

158. Rabedeau, T. A. *et al.* Giant magnetoresistance and Co-cluster structure in phase-separated Co-Cu granular alloys. *Phys. Rev. B* **48**, 16810–16813 (1993).

159. Friedel, J. On some electrical and magnetic properties of metallic solid solutions. *Can. J. Phys.* **34**, 1190–1211 (1956).

160. Blandin, A. & Friedel, J. Propriétés magnétiques des alliages dilués. Interactions magnétiques et antiferromagnétisme dans les alliages du type métal noble-métal de transition. *J. Phys. Radium* **20**, 160–168 (1959).

161. Friedel, J. Concept de niveau lié virtuel. *J. Phys. Radium* **23**, 692–700 (1962).

162. Daniel, E. Sur les propriétés électriques et magnétiques d'alliages de métaux de transition dilués dans le cuivre, l'or et le palladium hydrogéné. *J. Phys. Chem. Solids* **23**, 975–983 (1962).

163. Anderson, P. W. Localized Magnetic States in Metals. *Phys. Rev.* **124**, 41–53 (1961).